Scaling Complexity in the Study of Radiation Damage in Biomolecules

Thesis

THE OPEN UNIVERSITY
MILTON KEYNES, MK7 6AA, UNITED KINGDOM

SCALING COMPLEXITY IN THE STUDY OF RADIATION DAMAGE IN BIOMOLECULES

A thesis submitted in partial fulfillment for the degree of Doctor of Philosophy

Faculty:	Science, Technology, Engineering and Mathematics
Department:	School of Physical Sciences
Research group:	Molecular Clusters Group
Supervisors:	Dr. Samuel Eden
	Dr. Jimena Gorfinkiel

Milton Keynes, January 2020 **Jana Bocková**

Abstract

Understanding biological radiation damage on the nanoscale is a major goal in Chemical Physics/Physical Chemistry, with implications in medicine and elucidating the molecular origins of life. A valuable tool for developing new insights involves drawing comparisons between the radiation responses of progressively more complex gas-phase biomolecules. While experimental studies of neutral nucleobases are prevalent, the literature diminishes sharply with increasing molecular complexity. This is linked to escalating thermal lability. In response, this thesis characterises, exploits, and develops a relatively new method, *indirect laser-induced thermal desorption* (ILTD), for the study of neutral gas-phase RNA/DNA constituents.

We present the first in-depth study of ILTD for the production of pure targets of the nucleobase guanine and the nucleosides uridine, thymidine, 2′-deoxyuridine and 5-methyluridine. Except for thymidine, UV multi-photon ionisation (MPI) experiments demonstrated the efficacy of ILTD to produce viable targets without thermal decomposition. This inspired us to design and build a unique set-up for probing dissociative electron attachment (DEA), an important process in radiation damage of nucleic acids, to ILTD targets.

The MPI experiments on uridine showed evidence for changes in isomeric populations as a function of ILTD conditions. Furthermore, they provided the first experimental evidence for the electronic excited state dynamics of uridine being sensitive to the molecule's isomeric form prior to photo-excitation. This highlights the importance of developing methods to produce gas-phase targets that are structurally pure as well as unfragmented.

Finally, the thesis presents an adapted reflectron time-of-flight mass spectrometry technique to analyse the metastable fragmentation and sequential fragmentation pathways. This revealed exceptionally rich metastable dissociation patterns of excited 3-aminophenol ions. We expect MPI-induced metastable dissociation to be highly sensitive to isomeric form, and hence to be a valuable tool in the future development of our research programme.

Acknowledgement

My PhD study at the Open University (OU) has been an extremely rewarding time with respect to my development as a researcher as well as my personal growth. I am grateful for being given the opportunity to carry out my research in the Molecular Clusters Laboratory at the OU, working with a number of friendly, bright and inspiring people who supported me on my way to complete my PhD project. I am taking this opportunity to acknowledge everyone whose input, guidance and support made a positive difference to my PhD study.

First and foremost, I thank my supervisor Dr. Sam Eden for mentoring me and guiding me in my PhD project over the past three years. Sam has always been on hand to offer help and advice, has given me numerous opportunities to attend conferences and introduced me to the scientific community. Thank you, Sam, your input into the research has been invaluable and your encouragement, patience and friendly approach have made it privilege to work with you. Also, I thank my second supervisor Dr. Jimena Gorfinkiel for all her support and guidance throughout my PhD study.

Many thanks to André Rebelo, who worked with me on several experiments during my PhD and on building a new experimental set-up. I really appreciate numerous calculations André carried out to support interpretations of our experimental data. I also acknowledge all the work and efforts of previous PhD students in the Molecular Clusters Laboratory at the OU Bartlomiej Barć, Michal Ryszka and Rahul Pandey in developing the experimental facilities as well as for carrying out their experiments which became a stepping stone for my PhD project. I appreciate contributions from all of the people who were involved in any experiments performed in the Molecular Clusters Laboratory, notably Rebecca Ward, Dr. Violaine Vizcaino, Dušan Mészáros, Dr. Kate Nixon, Irina Jana and Tony Hajj. I acknowledge also Dr. Marvin Weyland for introducing me the velocity map imaging set-up at the OU.

I am very grateful to Dr. Jean-Christophe Poully, who joined us every year for a set of experiments. His passion for science, great experience in our field as well as his sense of humour made his visits always very fruitful and enjoyable times. Great thanks go to Jean-Christophe for his calculations on 3-aminophenol. A great deal of appreciation goes to Prof. Nigel Mason, who introduced me to the OU (also thanks to Dr. Juraj Országh and Dr. Peter Papp) as well as for diverse contributions during my PhD. I also acknowledge

collaboration with Prof. Paulo Limão-Vieira who gave me the opportunity to participate in the vacuum-ultraviolet photoabsorption experiments during his beam time on ASTRID2 apparatus in the Centre for Storage Ring Facilities (ISA), Aarhus, Denmark. I am thankful for valuable professional advice from Prof. Paulo Limão-Vieira and beamline scientist Dr. Nykola Jones as well as contributions from Dr. Khrystyna Regeta during these measurements. I particularly appreciate collaborations with Dr. David Townsend and his group at Heriot-Watt University, and Dr. Peter van der Burgt and his group from National University of Ireland, Maynooth, and their contributions to our common manuscripts.

I am extremely thankful for all technical support at the OU, notably to Chris Hall and later Kevin Dewar and their team from Research Design and Engineering Facility (mechanical workshop), and to Robert Seaton and his colleagues from Intra-Faculty Electronics and Computing Facility (electronics workshop). My special thanks go to Anthony Jones and Michael Abbott who always welcomed me very warmly in their mechanical workshop and whose patience and high-quality work have been both invaluable when dealing with our *urgent* or *super urgent* requests. Big thanks go to David Pound from electronics workshop who patiently kept fixing our old variacs and power supplies, and was irreplaceable when building electronics for the new set-up. His great knowledge and skills in combination with his unmistakeable sense of humour made it pleasure to work with him. I am also grateful for support from laboratory managers Mohammed Shabbir and later Thomas Webley (also in his role of laboratory technician), laboratory technician Elisabeth Moro as well as administrative assistants at the OU. I thank to all *Perry D labs users* for their help, advice and for willingly lending us their spare parts.

I acknowledge the Open University for funding my PhD study, Sir John Mason Academic Trust for the financial support which allowed me to carry out the experiments at ISA, Aarhus, Denmark, as well as the Molecular Physics Group of the Institute of Physics and the Department of Physical Sciences at the OU for co-funding my attendance at POSMOL 2019 conference in Belgrade, Serbia.

Finally, I thank all of my friends who I met at the OU for making my life more enjoyable here in Milton Keynes, notably the ones attending our *12:15 Hub lunches*, the ones staying at *90 Crowborough Lane* and all *Kents Hill gym fellow badminton players*. My special thanks go to Telma, Yadu, Suraj and Nitu. Huge thanks to my family, especially my parents Jozef and Jana, my friends from Slovakia and, last but not least, my partner Matej for their unconditional and endless support.

Contents

List of figures

List of tables

List of acronyms

AIST	Advanced Industrial Science and Technology
B	nucleoBase
$B-H$	nucleoBase minus Hydrogen
$B-2H$	nucleoBase minus 2 Hydrogens
$B-3H$	nucleoBase minus 3 Hydrogens
BBO	Barium BOrate
BH	nucleoBase plus Hydrogen
ChI	Chemical Ionisation
CI	Conical Intersection
CT	Charge Transfer
CW	Continuous Wave
DCM	DiChloroMethane
dCMP	2′-deoxyCytidine 5′-MonoPhosphate
DEA	Dissociative Electron Attachment
DESY	Deutsches Elektronen-SYnchrotron
DFT	Density Functional Theory
DLID	Direct Laser-Induced Desorption
DNA	DeoxyriboNucleic Acid
EG	Electron Gun
EII	Electron Impact Ionisation
ESI	ElectroSpray Ionisation
FAB	Fast Atom Bombardment
Fc	Faraday cup
FC	Franck-Condon
FCU	Frequency Conversion Unit
FFR	Field-Free Region
FrM	Fragment ion resulting from Metastable dissociation
FrP	Fragment ion resulting from Prompt dissociation
GLC	Gas-Liquid Chromatography
HOMO	Highest Occupied Molecular Orbital
HPLC	High-Performance Liquid Chromatography
IC	Internal Conversion
ICol	Ion Collisions
IE	Ionisation Energy
ILT	Indirect Laser-induced Thermally
ILTD	Indirect Laser-induced Thermal Desorption

IR	InfraRed
IRLS	InfraRed Laser Spectroscopy
IRS	InfraRed Spectroscopy
ISC	InterSystem Crossing
KE	Kinetic Energy
LCAO	Linear Combination of Atomic Orbitals
LEE	Low-Energy Electron
LIAD	Laser-Induced Acoustic Desorption
LIF	Laser-Induced Fluorescence
LUMO	Lowest Unoccupied Molecular Orbital
m/z	mass-to-charge ratio
MALDI	Matrix-Assisted Laser Desorption/Ionisation
MB	Molecular Beam
MCP	Micro-Channel Plate
MO	Molecular Orbital
MPI	Multi-Photon Ionisation
mRNA	messenger RiboNucleic Acid
MS	Mass Spectrometer
Nd:YAG	Neodymium-doped Yttrium Aluminium Garnet
NIST	National Institute of Standards and Technology
OU	Open University
Pa	Parent ion
PCol	Potassium Collisions
PDI	Plasma Desorption Ionisation
PEEK	PolyEther Ether Ketone
PEPICO	PhotoElectron-PhotoIon COincidence spectroscopy
PEPIPICO	PhotoElectron-PhotoIon-PhotoIon COincidence spectroscopy
PeS	Photoelectron Spectroscopy
PES	Potential Energy Surface
Pr	Precursor ion
PRI	PRoton Irradiation
QET	Quasi-Equilibrium Theory
REMPI	Resonance-Enhanced Multi-Photon Ionisation
RNA	RiboNucleic Acid
rRNA	ribosomal RiboNucleic Acid
RS	Rotational Spectroscopy
RSD	Relative Standard Deviation
S	Sugar unit of nucleosides
$S-H$	Sugar unit of nucleosides minus Hydrogen
$S-2H$	Sugar unit of nucleosides minus 2 Hydrogens
$S+2H$	Sugar unit of nucleosides plus 2 Hydrogens
S/N	Signal-to-Noise ratio
SD	Standard Deviation
SDBS	Spectral DataBaSe for organic compounds
SH	Sugar unit of nucleosides plus Hydrogen
SHB	Spectral Hole Burning
SHG	Second Harmonic Generation

SIMS	Secondary Ion Mass Spectrometry
SPI	Single-Photon Ionisation
TDC	Time-to-Digital Conversion
TNI	Transient Negative Ion
TOF	Time-Of-Flight
TRIY	Time-Resolved Ion Yield
tRNA	transfer RiboNucleic Acid
TRPP-MS	Time-Resolved Pump-Probe Mass Spectrometry
UV	UltraViolet
UVS	UltraViolet Spectroscopy
VUV	Vacuum-UltraViolet
w.r.t.	with respect to
ZPE	Zero-Point Energy
3-*AP*	3-AminoPhenol
5′-*UMP*	Uridine 5′-MonoPhosphate

Chapter 1

Introduction

1.1 Overview

The overall aim of this PhD thesis is to enhance our understanding of the fundamental processes by which radiation, notably UV photons and electrons, can initiate structural and chemical changes in key biological macromolecules and their subunits. In particular, DNA lesions are understood to be key precursors of lasting biological damage (mutations, cell death and cancer) and a major research effort is currently dedicated to applying nanoscale insights to improve radiotherapies [1, 2]. Elucidating the radiation response of RNA and DNA can have implications for understanding molecular origins and evolution of life on Earth [3–5]. Despite this, the fundamental nanoscale processes by which UV irradiation initiates damage in biological material have not yet been fully elucidated [6]. A *bottom-up* approach is required to link nanoscale chemical physics/physical chemistry to effects in complex biological systems [7–9]. This generally starts with experiments and/or calculations on fundamental building blocks in the gas-phase and then compares the radiation response of sequentially more complex biomolecules.

This PhD thesis tackles the problem of thermal lability of neutral RNA/DNA constituents of greater complexity than nucleobases. This is a great experimental challenge of the *bottom-up* approach and we focus on exploiting and characterising a relatively new vaporisation method, *indirect laser-induced thermal desorption*, for this purpose. Indeed, a key outcome of this work is the development of a unique experimental system for probing dissociative electron attachment processes to relatively large biological molecules such as nucleosides released by indirect laser-induced thermal desorption. Furthermore, the experiments presented in this thesis provide new evidence for the excited state dynamics and photostability of specific biomolecules being sensitive to isomeric form. This highlights the importance of building experiments which can produce targets that are pure

not only in terms of thermal decomposition, but also in terms of structure. In addition to our experiments on RNA/DNA constituents, we have adapted an existing concept in reflectron time-of-flight mass spectrometry to analyse complex metastable fragmentation patterns and identify sequential fragmentation pathways of photo-excited molecular ions and applied it to the biomolecule 3-aminophenol. This chapter introduces the motivations for the research presented in the thesis.

1.2 Informational building blocks of life

From the standpoint of biological function, we can distinguish between two classes of *informational biopolymers*: nucleic acids and proteins. Nucleic acids are responsible for the storage and transmission of genetic information as well as the synthesis of proteins (discussed in the next paragraph). There are two types of nucleic acids: ribonucleic acid (RNA) formed by a single polynucleotide strand and deoxyribonucleic acid (DNA) formed by two strands as indicated in Fig. 1.1. Their nucleotide subunits are composed of a nucleoside and a phosphate group. RNA/DNA nucleosides comprise one of five nucleobase units and a sugar unit (*ribose minus OH* in RNA and $2'$*-deoxyribose minus OH* in DNA). There are four types of nucleobases in DNA: adenine and guanine (classed as *purine* bases as they share its double-ring structure), and cytosine and thymine (pyrimidine bases). In single-stranded RNA, thymine is replaced by uracil (also a pyrimidine base). DNA has coding regions, exons, that determine the order of amino acids in proteins as well as non-coding regions, introns, that perform checking and regulatory functions in the transcription and translation of genes. RNA also plays a crucial role in the coding, regulation and expression of genes. Messenger RNA (mRNA) conveys genetic information from DNA to a ribosome. The genetic information is encoded in the nucleotide sequence of mRNA which is complementary to the DNA strand template. This genetic information specifies the amino acid sequence of the protein products of gene expression. Transfer RNA (tRNA) transfers amino acids to the ribosome and ribosomal RNA (rRNA) links the amino acids to form proteins [10].

Whereas nucleic acids determine the genotype (genetic constitution), proteins determine the phenotype (observable characteristics) of cells and consequently the whole organism. They consist of polypeptide chains, i.e. amino acids bound together by peptide bonds. The sequence of amino acids in proteins is dictated by the sequence of nucleotides in DNA coded in triplets. Polypeptide chains *fold* into complex three-dimensional structures, which then determine their function. Proteins are not only fundamental structural biopolymers, but are also responsible for transmission of information, regulation of the body's tissues and

organs, intracellular and extracellular transport, growth and many other vitally important processes. Therefore, any disruption of RNA/DNA induces a risk of disturbing the normal process of cell cycle which can then result in cell death. Alternatively, introducing mistakes in the transcription and translation of genes can lead to mutations, genomic instability and eventually carcinogenesis. DNA is particularly radiosensitive during its replication phase, when it splits into two separate strands, inviting analogies with single-stranded RNA. This is when the nucleosides themselves are most exposed to reactive species. By this rationale, RNA is expected to be more radiosensitive than DNA and hence its damage may be more important than generally assumed in determining the long-term effect of radiation on living systems. Cells have evolved repair mechanisms to maintain RNA and DNA integrity, however, these become markedly less effective as damage sites become more complex and concentrated (often referred to as a *clustered lesion*) or if the disruptive agent acts repeatedly for a longer period of time [10]. Mutations can cause uncontrolled cell division and hence lead to formation of tumours. Martincorena et al. [11] estimated the average number of driver mutations needed to develop tumours in different parts of human body to be in the range $1 - 10$. On the other hand, mutations can have positive effects as they are responsible for driving evolution.

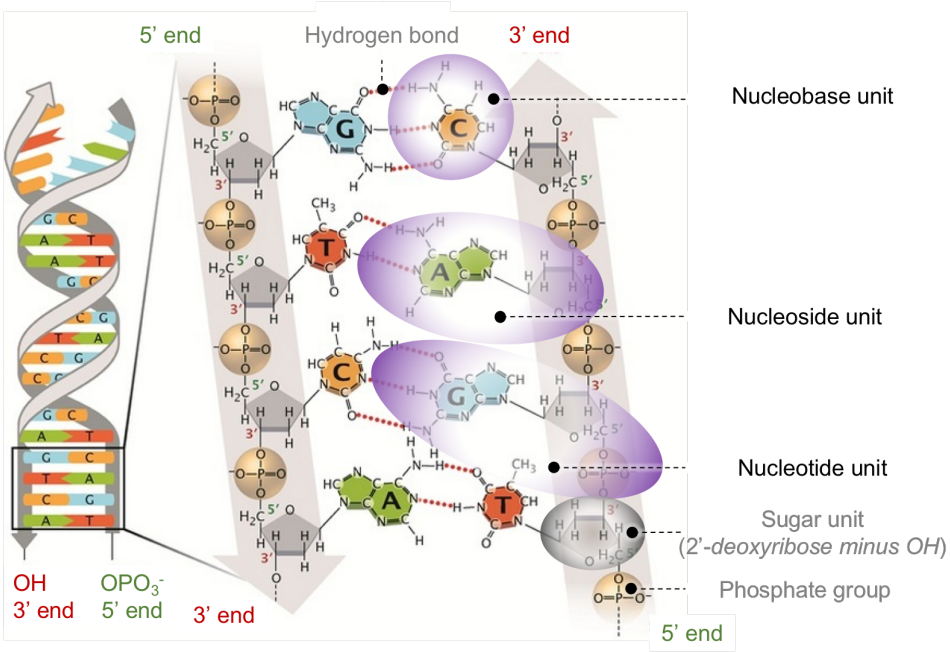

Fig. 1.1: Schematic diagram showing a double helix of DNA (left-hand side) with a detailed view of a part of the helix (right-hand side). Nucleobase units (A - adenine, G - guanine, C - cytosine and T - thymine) are bound to sugar units ($2' - deoxyribose\,minus\,OH$) via *N*-glycosidic bonds to form nucleoside units. These have phosphate groups bound at $3'$-*C* atoms of sugar units to form nucleotide units. Within the same strand of DNA, nucleotide units are bound via phosphodiester bonds, while hydrogen bonds between nucleotide units bind the two strands together (two hydrogen bonds between A and T, three hydrogen bonds between G and C). Adapted from [12].

One of the most common causes of RNA/DNA damage is radiation [10]. Radiation-induced damage to nucleic acids, but also other important biomolecules such as proteins, has therefore attracted considerable attention in different scientific communities in the past years. Huge efforts have been made in the field of physical chemistry/chemical physics with the central aim to understand the underlying mechanisms responsible for radiation-induced damage on the molecular level [7, 13–15, and references therein]. However, biomolecules such as nucleic acids are very complex species on their own, while furthermore they interact with a number of other molecules (e.g. histones and water). This complexity creates a barrier for pinning down the exact mechanisms responsible for a particular radiation-induced action. In addition, treating such a big molecular system theoretically at a high level becomes unattainable within the current practical limits of computational power. To tackle this complexity issue, many research groups apply a *bottom-up* approach [8, 16–18]. The essential idea is to first focus on isolated fundamental building blocks in the gas-phase and then systematically develop insights into radiation-induced processes with increasing complexity. This PhD thesis focuses on the application of the *bottom-up* approach for the study of radiation-induced processes in nucleic acids and addresses some of its problems. The next section provides a brief overview of the processes initiated when radiation interacts with biomolecular systems, notably nucleic acids and proteins, which will help the reader understand the importance of the experiments presented later in the thesis as well as to appreciate the contribution of this thesis within the broader field.

1.3 Radiation interactions with biomolecular systems

1.3.1 Radiation-induced damage of RNA/DNA

The nanoscale processes responsible for radiation damage in cellular material are often divided into two classes of effect upon DNA and other critical biomolecules. *Primary processes* are those initiated by direct interactions with incident energetic particles. *Secondary processes* are those initiated by low-energy radicals, ions, or electrons released by the dissociation and/or ionisation of neighbouring molecules. Water molecules represent the major source of these secondary reactive species in cells. Both the production of local OH radicals [19] and low-energy electrons ($< 20\,eV$) [20] have been demonstrated to increase the occurrence of single and double strand breaks in DNA. The schematic in Fig. 1.2 shows examples that illustrate the difference between the *primary* and *secondary* radiation-induced damage of DNA [13].

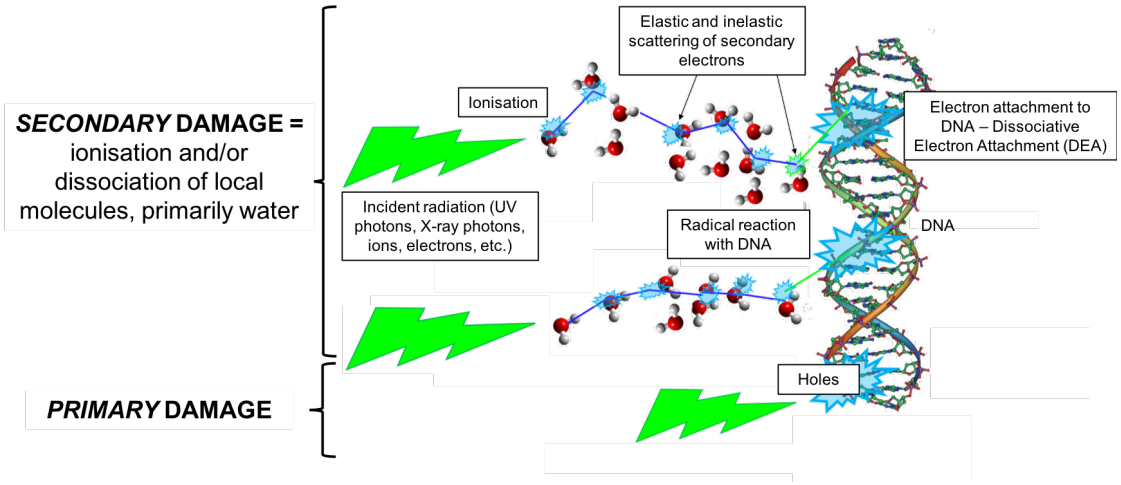

Fig. 1.2: Schematic diagram illustrating examples of *primary* and *secondary* radiation-induced damage of DNA (adapted from [13]).

It has been estimated that approximately $2/3$ of all radiation-induced damage to DNA is due to *secondary* processes [13]. Note that DNA comprises only a negligible part of the cell, and that ionisation of the surrounding medium has to happen in a close proximity to DNA (1 to $10\,nm$ is an estimate based on the mean free path of electrons in water) in order to induce damage through the production of low-energy secondary electrons [13]. However, some radiation damage mechanisms do not fall easily within this classification of *primary* or *secondary* actions. In particular, multiscale modelling of ion beam cancer therapy has revealed a new damage mechanism: thermochemical DNA damage which arises from shock waves produced on the nanometer scale around the swift ion path [21].

1.3.1.1 *Primary* radiation-induced damage of RNA/DNA

In the case of *primary* damage, radiation (e.g. energetic electrons, ions, or photons) directly hits the RNA/DNA molecule causing ionisation and hence creation of electron holes which weaken the backbone and disrupt the molecular structure [13, 22]. It has been shown that electron holes can migrate from the locus of formation to trapping sites [23]. The energetics of hole trapping is determined in the first place by the ionisation energy of the base. As the ionisation energy of guanine is lowest amongst all nucleobases, it is considered to be the preferential site for such trapping [24]. Yun et al.'s study of oxidatively generated damage to DNA in aerated solutions [25] revealed clear evidence that single- and double-strand breaks occur in DNA containing holes [13, 22]. In addition to ionisation, a neutral electronic excitation initiating unimolecular or intermolecular reactivity and bond breaking represents another important potential radiation damage pathway in RNA and DNA [18, 26].

1.3.1.1.1 Photodamage of RNA/DNA induced by UV radiation

As the majority of the experiments presented in this thesis are multi-photon ionisation experiments in the ultraviolet (UV) range of the electromagnetic spectrum ($265 - 220\,nm$), we will devote special attention to explaining the motivation and applied context behind these experiments. We normally categorise UV radiation as follows: UVA ($400 - 315\,nm$, corresponding to $3.10 - 3.94\,eV$), UVB ($315 - 280\,nm$, corresponding to $3.94 - 4.43\,eV$) and UVC ($280 - 200\,nm$, corresponding to $4.43 - 6.20\,eV$). It is well known that UV radiation acts as a mutagen, with UVC naturally being the most damaging of these three classes due to its high energy. The first experiments indicating the destructive effect of UV radiation on living organisms were conducted in 1929 by Gates [27], who studied its bactericidal effect. He related the lethal action of UV radiation on living cells to the absorption of UV energy by the molecules responsible for reproduction and growth, and later on it was discovered that nucleic acids are critically important in these processes. Since then, numerous experimental and theoretical studies have been carried out to investigate the photophysical properties of nucleic acids and their constituents to better understand the cell killing and mutagenic effects of UV radiation [28]. The most important ones with respect to this thesis are discussed below.

Nucleobases are the key UV chromophores in nucleic acids. They absorb radiation in the UVC region of the electromagnetic spectrum (see Fig. 1.3), most notably via transitions from the electronic ground state (S_0) to the molecules' second-lowest singlet excited states (S_2) with $\pi\pi^*$ character, i.e. $S_2 \leftarrow S_0$ transitions with oscillator strengths that are several orders of magnitude greater than $S_1 \leftarrow S_0$ transitions [29]. Electronically excited nucleobases can then initiate damaging photochemical reactions, which may result in photolesions, e.g. the formation of thymine dimers [6]. The second strong absorption band of nucleobases (S_0 to S_3) also peaks at about $200 - 180\,nm$, just within the vacuum-ultraviolet (VUV) range of the electromagnetic radiation ($200 - 10\,nm$). The sugar-phosphate backbone absorbs radiation only at wavelengths below $\sim 220\,nm$ [28]. The laser system used for multi-photon ionisation in this thesis can access the UV wavelength range $277 - 220\,nm$, coinciding with the lowest-energy singlet transitions of RNA/DNA nucleobases (see the red bands in Fig. 1.3, note the resultant colour is purple due to overlap with the blue bands).

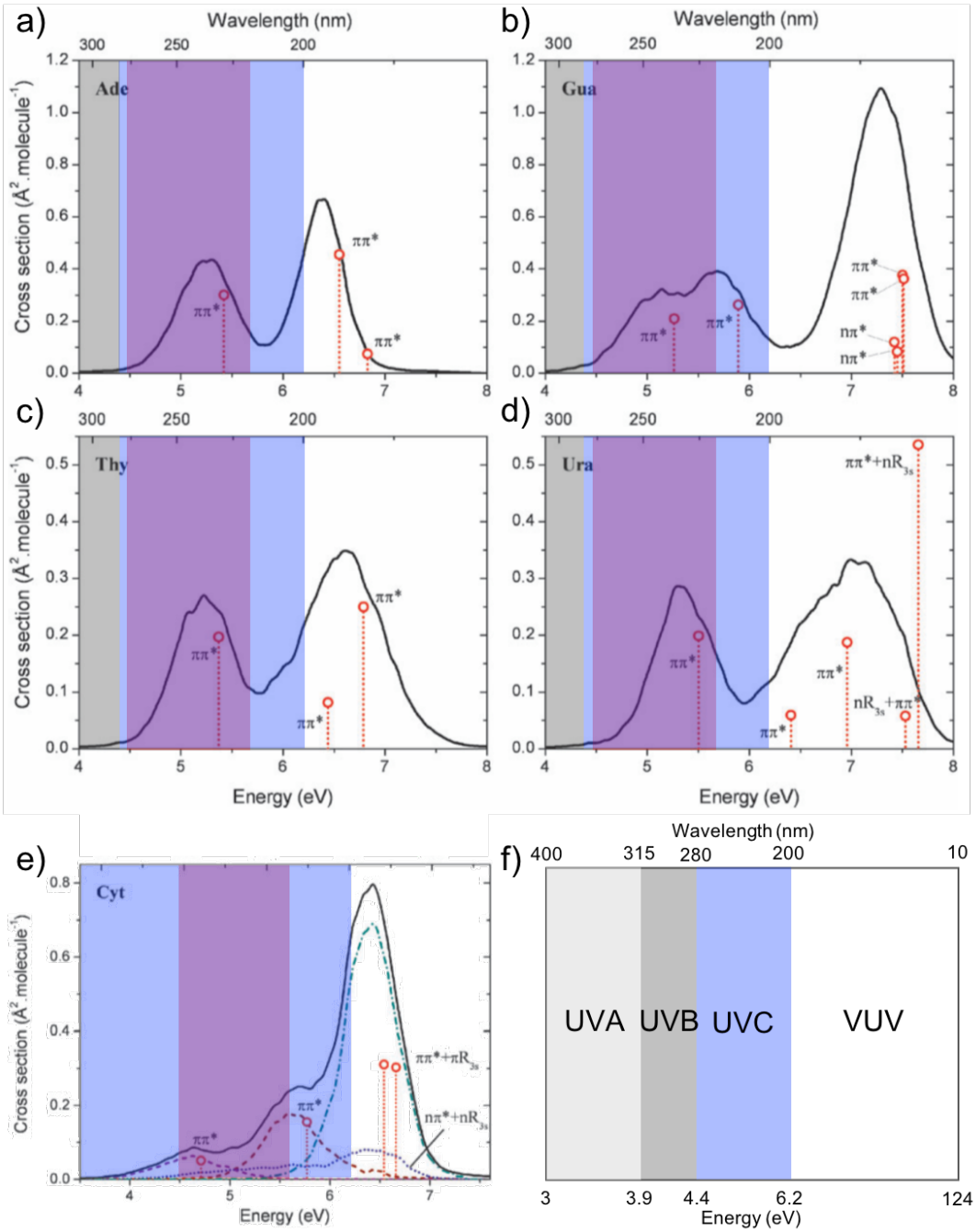

Fig. 1.3: Absorption spectra of isolated nucleobases: a) adenine; b) guanine; c) thymine; d) uracil and e) cytosine. f) Ultraviolet (UV) part of the electromagnetic spectrum. Solid lines represent simulated spectra, the circles transition energies and oscillator strengths (height) of the vertical excitations at ground state minima. Broken lines in e) represent individual state contributions to the final absorption spectrum (note that wavelength scale is not shown here for panel e) because it was presented incorrectly in the original source [29]). The red band (note the resultant colour is purple due to overlap with the blue bands) shows UV laser wavelength/energy range ($277 - 220\,nm$, corresponds to $4.48 - 5.64\,eV$) in the multi-photon ionisation experiments at the Open University (adapted from [29]). The light grey, grey and blue bands indicate different ranges of UV part of the electromagnetic spectrum and white band indicates VUV part of the electromagnetic spectrum (as shown in f)).

VUV radiation is strongly absorbed by atmospheric gasses (mainly oxygen and nitrogen) and therefore solar VUV does not harm biological systems on the present-day Earth [30]. UVC radiation is absorbed by oxygen and ozone in the stratospheric layer of Earth's atmosphere. Solar UVC radiation therefore reaches the biosphere with negligible flux. Although solar UVB radiation is also to a great extent absorbed by the ozone layer, a not negligible part of it reaches Earth's surface. UVB represents about 5 % of the total terrestrial (at the Earth's surface) UV radiation [31]. The long-wavelength band of nucleobases has an overlap with the UVB wavelength range and therefore its absorption can cause direct excitation of nucleobases and subsequently their damage. On the contrary, UVA is not absorbed by the ozone layer and most of it reaches ground level. Solar UVA therefore represents around 95 % of the total terrestrial UV radiation [31]. As UVA is extremely weakly absorbed by RNA/DNA, its contribution to *primary* RNA/DNA damage is zero to any reasonable approximation [28, 32–34].

As discussed above, the ozone layer in the stratosphere acts as a barrier which protects all living organisms on Earth from destructive UV radiation. However, the early Earth did not have an ozone layer and thus was exposed to roughly 100-times higher flux of UV radiation compared with the surface of the present-day Earth [35]. This suggests that UV radiation presented a challenge to life on the early Earth and its actions as a mutagen and a selective agent might have played critical roles in the evolution of the molecular basis for life as we see it today [35–37].

Considerably more attention has been paid to the investigation of radiation-induced processes in DNA and its constituents than to RNA. This is clearly due to the essential role of DNA in coding genetic information. However, when it comes to the molecular origins of life, the importance of RNA escalates. In 1986 Gilbert [38] proposed a hypothesis that RNA initially acted as the only informational biopolymer, being responsible for storing the genetic information as well as performing basic cellular operations, including RNA replication. The main arguments in support of the *RNA world* hypothesis are that present-day life appears to have originated from heavily RNA-based organisms. Furthermore, it has been shown that RNA catalysts can perform many of the functions which are nowadays carried out by proteins [39–42]. According to this model, the diversification and evolution of RNA led to the RNA organisms developing the ability to synthesise polypeptides which then replaced RNA in most catalytic tasks. The role of RNA in storing genetic information was subsequently replaced by DNA, the more chemically stable nucleic acid [10, 39–42].

RNA and DNA feature effective mechanisms to convert absorbed energy from electronic

modes to vibrational modes on short timescales (*ps*-order or less), helping to minimise the generation of photolesions due to UV exposure. This property may have been one of the evolutionary drivers that led to the selection of DNA and RNA to perform their current biological functions. This rapid dissipation (or *thermalisation*) of absorbed energy happens via conical intersections of the potential energy surfaces of different electronic excited states of the nucleobase sub-units of DNA and RNA with the molecules' electronic ground states [43]. The electronic excited state dynamics of nucleobases have been extensively studied both experimentally and using theoretical methods [18, 44–46], however this work is far from complete. For example, the great majority of ultrafast time-resolved pump-probe experiments on gas-phase nucleobases have been carried out by pumping at $267\,nm$, close to the origin of the S_2 band [47]. Very few experiments have been carried out to investigate the relaxation pathways from high vibrational levels of the S_2 excited state and/or from S_3 [9].

One of the main approaches applied by the Molecular Clusters Group at the Open University (OU) for investigating processes happening in neutral electronic excited states of biomolecules involves comparing ion production by multi-photon ionisation (MPI, step-wise ionisation via one or more electronic excited states in the present laser fluence regime) and electron impact ionisation (EII, direct access to ionic states). Observations of differences in fragment ion production by MPI and EII can provide experimental evidence of structural changes (isomeric transitions) or dissociation processes in neutral electronic excited states. In particular, the group has carried out an extensive set of MPI ($270 - 220\,nm$) and EII ($200\,eV$) experiments to investigate neutral excited state dynamics and fragmentation pathways of RNA base uracil, the only nucleobase in RNA which is distinct from the ones present in DNA [18, 26]. Investigating the response of RNA constituents and their derivatives at different levels of complexity might help to understand the selection criteria which determined the molecular architecture of life at the early stages of life evolution. Uridine, the RNA nucleoside that features a dehydrogenated uracil unit, has been much less studied compared with the isolated base. It should be noted that the replacement of thymidine in DNA with uridine or its fluorinated derivatives is exploited in chemotherapy. Chemotherapy is often combined with radiotherapy so this provides an extra motivation for understanding the radiation response of uridine and its derivatives. To shed more light on the response of uridine upon interaction with UV radiation, a new MPI ($265 - 220\,nm$) study of this molecule and a selection of closely-related nucleosides is presented in Chapter 6 of this PhD thesis.

1.3.1.2 *Secondary* radiation damage of RNA/DNA

The reader should keep in mind that there are a great number of different secondary DNA/RNA damage processes and this short summary section only highlights a few which are particularly relevant to the studies in this thesis. To find out more, we recommend [48, 49]. In their natural environment within cells, RNA and DNA are surrounded by other molecules, mainly water and proteins. Therefore, any incident radiation is likely to interact with these molecules before reaching the nucleic acids. Such interactions can result in their ionisation and hence in the generation of secondary species, notably secondary electrons and radical neutrals and ions (mainly hydroxyl $HO^{\bullet}$ and alkoxy $RO_2{}^{\bullet}$ radicals). As noted above, RNA/DNA reactions with these species can be called *secondary* processes and the importance of secondary radicals in biological radiation damage has been recognised for many years. Free radicals are very reactive and therefore attack RNA/DNA, disrupting their molecular structure. Secondary electrons undergo inelastic collisions with biological medium causing further excitation and ionisation. The overall result is a radiation cascade in which most electrons have energies $< 30\,eV$, with the mean electron energy at around $9 - 10\,eV$ [13, 50, 51]. These electrons are called low energy electrons (LEEs) and they can cause damage to RNA/DNA as described below [13, 22].

LEEs propagate through the medium interacting elastically and, more importantly, inelastically with molecules, losing their energy by transferring it to electronic and vibrational excitations and hence creating numerous potentially damaging species (radicals) before becoming thermalised. Moreover, in 2000 Sanche and co-workers [20] demonstrated for the first time that LEEs with energies below the ionisation threshold can induce single- and double-strand breaks by resonantly attaching at particular sites of DNA, forming transient negative ions (TNIs) which can subsequently dissociate via the process of *dissociative electron attachment* (DEA) [13, 17, 50]. As a large proportion of any cell (about $70 - 80\,\%$) comprises water, LEEs with energies close to $7\,eV$ [52] can also resonantly attach to water molecules and cause dissociation which results in the formation of a hydroxyl radical $HO^{\bullet}$ and a hydride anion H^{-}. However, it should be noted that radicals are also produced in metabolic processes and therefore radical-driven damage is very likely to be more readily repaired by the cell than structural damage induced by LEEs attaching directly to RNA/DNA [13]. In addition, secondary electron scattering can be an efficient mechanism for neutral electronic excitation of DNA and RNA. This provides a mechanism for direct access to long-lived triplet states and other optically-forbidden transitions that may be important from a radiation damage standpoint.

LEEs-induced damage to DNA can be enhanced by covalently binding radiosensitisers

and chemotherapeutic agents to the molecule. The higher propensity for dissociation can be either a result of the appearance of new TNIs near the binding sites or due to the enhancement of already existing DEA channels. Weakening of the bonds within the molecule can also contribute to higher dissociation rate. Understanding these processes in depth has great potential to inspire the development of new techniques in cancer treatment radiotherapy [50].

Despite the great interest in DEA, the current understanding of low-energy electron driven processes in biologically relevant targets is limited by the scarcity of DEA experiments on gas-phase molecules larger than nucleobases or simple sugars. This is related to increased propensity of biomolecules for thermal degradation with their increasing size and therefore difficulties for bringing them intact into the gas-phase. Whereas it can be highly relevant to study various radiation-induced processes in large intact biomolecular ions produced by electrospray ionisation (ESI, discussed further in Chapter 5), DEA can only be studied meaningfully using neutral targets. To tackle this problem, we have developed a new experimental system for studying DEA processes to neutral nucleosides. The design, the principles of operation, and the preliminary optimisation of this set-up are described in Chapter 7.

1.3.2 Radiation-induced damage of proteins

We have already discussed ways in which radiation can induce damage to nucleic acids and this, in turn, can cause problems in the synthesis of new proteins. Analogously to nucleic acids, proteins can be subject to both *primary* and *secondary* radiation-induced damage. Due to their diverse roles in the biological systems (see Section 1.2), proteins are highly abundant. In addition, they carry UV chromophores (aromatic amino acids) and therefore they are major cellular targets for photooxidation [48]. In addition to neutral electronic excitation, ionisation plays a crucial role in radiation damage induced by *primary* interactions of UV photons with proteins. The break up of an excited amino acid ion within a complex protein structure represents a damage site and the fragments (neutral and ionic) can then react with adjacent molecules and hence escalate the destructive effect.

Although the ionisation and fragmentation pathways of amino acids and their derivatives have been extensively studied [53–55], a number of details remains unresolved, including the identification of specific fragmentation pathways. This provided part of the motivation for our reflectron time-of-flight mass spectrometry experiments probing the metastable fragmentation of excited 3-aminophenol (3-AP) ions (see Chapter 4). The main strength

of the experiment is that it enables the identification of sequential fragmentation routes. Studying fragmentation of 3-AP upon multi-photon ionisation is not only interesting due to its biological relevance; the molecule has also proved to be valuable for testing the capability of the metastable dissociation experiment at the OU as it reveals a very rich metastable fragmentation pattern. The principles of operation of this experiment and the new Matlab simulation which has been developed to analyse metastable dissociation pathways are discussed in detail in Chapter 3.

1.4 *The bottom-up* approach in the study of radiation-induced damage of biomolecules

In the previous sections we have summarised a selection of key radiation interactions with biomolecules that can lead to damage to biological systems. The study of individual radiation-induced processes on the molecular level often starts with relatively simple isolated species with the central aim of developing detailed insights which can then help to explain processes in more complex targets, i.e. by applying the *bottom-up* approach. The starting points in the *bottom-up* approach in the study of radiation response of nucleic acids are often nucleobases or sometimes even their subunits (e.g. pyrimidine or imidazole). In addition to the studies of progressively more complex biomolecules, the OU Molecular Clusters Group tries to link the insights from experiments on gas-phase molecules to realistic biological systems by studying clustering effects, i.e. exploring how the chemical environment affects the radiation response of isolated species (see, for example, references [56–58]). This is, however, not addressed in this thesis and therefore we will not pay special attention to it here.

Excitation, ionisation, dissociative ionisation, and DEA pathways have been investigated extensively for most of the nucleobases isolated in the gas-phase [26, 47, 59–63]. Experimental studies on guanine are, however, much more rare mainly due to its poor stability with respect to thermal decomposition, when bringing a solid-state sample into the gas-phase [64, 65]. This problem escalates quickly with increasing size of biomolecules and even a single step in complexity to nucleosides has presented a significant experimental challenge for the *bottom-up* approach. While the production of intact charged species of complex biological molecules in the gas-phase has been successfully achieved thanks to the development of electrospray ionisation, the production of analogous neutral targets has not been fully resolved yet. In addition, despite the high thermal lability of nucleosides and larger RNA/DNA constituents, an in-depth study of thermal decomposition of these species is often absent in the literature. In this thesis indirect laser-induced thermal

desorption (ILTD) has been chosen for bringing the nucleosides uridine, thymidine and their derivatives 2′-deoxyuridine and 5-methyluridine into the gas-phase. Although ILTD has been previously applied for vaporising DNA nucleosides [8, 43, 66], to the best of our knowledge no direct evidence of the lack of thermal decomposition has been presented. Our experiments to address this gap in the literature are presented in Chapter 5.

Another important aspect to consider in the *bottom-up* approach is the biological relevance of the isomeric forms of the molecules produced in the gas-phase. In general, with increasing size of the molecules, the number of different isomeric forms increases rapidly. Our MPI experiments on *ILT*-desorbed uridine in Chapter 6 provide, to the best of our knowledge, the first experimental evidence supporting changes in the isomer population of uridine as a function of desorption conditions. Moreover, these experiments provide the first experimental evidence that supports theoretically-predicted isomer-specific neutral excited state dynamics [67]. This suggests that in addition to developing methods for the production of intact neutral gas-phase targets of increasingly large biomolecules, it is important to develop methods which will enable experiments to probe only selected isomers out of all of the structures produced in the gas-phase.

Irrespective of the above-mentioned difficulties associated with applying the *bottom-up* approach in the study of radiation-induced processes in complex biomolecules such as nucleic acids, an important question to ask is the true relevance of the approach. Can the insights from experiments and theoretical calculations on simple building blocks provide relevant information which can be linked to processes happening in real biological environments or are the perturbations due to bonding with other molecules and the surrounding environment so big that the effects observed in simple building blocks become untraceable? Chapter 6 includes an investigation of how previous studies of fragment ion production from uracil and ribose (both closely related to the base and sugar units of uridine) help to interpret fragment ion production from uridine. In order to provide more insights with respect to answering the question above, we will briefly review a selection of pivotal findings from the literature.

Starting with a step from nucleobases to nucleosides, both theoretical [68] as well as experimental [43] studies comparing excited state dynamics of nucleobases and nucleosides have shown a certain level of similarities, i.e. the lowest lying singlet excited states ($n\pi^*$ and $\pi\pi^*$ with respective lifetimes of *ps*-order or $<$ approximately $100\,fs$ [9]) were in both cases localised on the aromatic ring of nucleobases. However, binding to the sugar units has turned out to significantly affect the nature of the upper two excited states

(also when binding phosphate to form nucleotides [68]) as well as their decay rates which were reduced by a factor of 2 in the experiments on adenosine, thymidine, and cytidine [43]. The decay rates were unchanged in the case of guanine/guanosine, which could be potentially linked to the presence of different isomers in the gas-phase, highlighting the need to develop methods for the production of structurally pure targets.

Flosadóttir et al.'s studies [69] of the metastable decay of dehydrogenated anions produced by matrix assisted laser desorption/ionisation mass spectrometry (MALDI) yielded insights into how the radiation response of DNA constituents evolves across the extended range of nucleobases up to oligonucleotides (short strands of DNA or RNA). They concluded that the dominant metastable fragmentation channels of isolated components continue to be observed when progressing one step in complexity, i.e. from isolated sugars and nucleobases to nucleosides. However, the new dominant fragmentation channel often becomes the rupture of the new bonds, which is then very likely to be the only one persisting when one further component is added. It should be noted that MALDI sources produce a wide range of different gas-phase cations, neutral, and anions. It was essential for Flosadóttir et al. to focus on metastable dissociation channels in order to trace specific fragment ions to specific precursor ions.

Kopyra [17] successfully applied the *bottom-up* approach in the analysis of ion yield curves from DEA experiments on the nucleotide 2′-deoxycytidine 5′-monophosphate (*dCMP*). She was able to link some of the features observed in the energy profile of the ion yields observed for *dCMP* to processes previously observed in DEA to isolated phosphate and sugar units. Kočišek et al. [70] subsequently carried out DEA experiments on microhydrated *dCMP* which revealed that hydrogenation of the transient negative ion in the water environment can significantly change the fragmentation and final charge localisation over the molecule. To our knowledge, these experiments by Kopyra, Kočišek, and their co-workers are the only examples in the literature of bringing intact nucleotides into the gas-phase successfully by conventional heating in an effusive oven (discussed further in Chapter 5).

Stavros and Verlet's 2016 review [7] looked into how the excited state dynamics of imidazole (the isolated chromophore of adenine) evolves by increasing the complexity of its molecular environment. They showed that site-specific chemical modification can be used to mimic the way adenine binds to sugar and phosphate units, which can provide insights into the excited state dynamics of nucleotides. After excitation at $260\,nm$, nucleotide deoxyadenine monophosphate anions decayed on similar timescales in the gas-phase and

in solution, i.e. a fast initial decay followed by a channel with a time constant of 340 fs. Although the dynamics of di- and trinucleotides in the gas-phase appeared to be similar to those of mononucleotide, this was not the case for aqueous solutions, where a dramatic increase in lifetimes was observed due to the formation of excimers. In light of these similarities and differences in the excited state dynamics as a function of molecular complexity and solvation, the review highlights the importance of the *bottom-up* approach and suggests new routes for its development.

In a closely related field, the *bottom-up* approach has been successfully applied in the study of ultrafast photodynamics of sunscreen molecules with the aim of uncovering an ideal molecule, which will strongly absorb UVA and UVB radiation (see Section 1.3.1.1.1) and quickly dissipate the excess energy in the form of heat without causing permanent change to its original structure [32]. First, the sunscreen molecules were studied in isolation in the gas-phase and the effect of changing their structure was examined. The key *bottom-up* step was the transfer from the gas-phase to the liquid-phase, where the effect of the surrounding environment (solvent polarity, pH, viscosity) on the photodynamics of isolated species was also investigated. Interestingly, the change from the gas-phase to the solution does not always affect the photodynamics of the molecules significantly [71]. An analogous approach in the study of nucleic acids evolution on the early Earth has been employed with aim to uncover which pathways have led to their evolution in their current form and why those specific ones were favoured compared to the others. However, so far the experiments on neutral gas-phase molecules and clusters have primarily been limited to the complexity level of nucleobases and, much more rarely, nucleosides [72, and references therein].

In summary, the above-mentioned studies have clearly shown some very promising results with respect to the value of the *bottom-up* approach for the study of radiation-induced processes in biomolecular systems. It should be noted though that we are still at the beginning of the long journey towards getting a complete picture of the nanoscale processes initiated by radiation interacting with living tissue. Several experimental challenges have to be tackled to enable further progress in the gas-phase experiments, notably the production of high-density neutral targets which are pure firstly in terms of the absence of any thermal decomposition and secondly in terms of molecular structure. The former challenge is partially addressed in this thesis. A substantial research effort is still required to fully understand how the radiation responses of key macromolecules are modified by the aqueous environment, the specific sequencing of subunits, and secondary and tertiary molecular structure.

1.5 Summary

UV- and electron-induced processes play significant roles in radiation damage to nucleic acids. Although they have been of great interest from astrobiological and radiation biology standpoints for many years, understanding of the specific pathways remains incomplete. Gas-phase experiments on relatively small components of RNA/DNA enable the most direct comparisons with high-level calculations, while comparing the radiation response of sequentially more complex biomolecules can provide a basis for linking insights from gas-phase experiments to effects in real biological environments. This thesis tackles a major experimental challenge of the so-called *bottom-up* approach, which is bringing progressively more complex neutral biomolecules intact into the gas-phase. This challenge is particularly pertinent for the study of DEA processes to RNA/DNA components of increasing complexity in the gas-phase because pure DEA experiments (observing dissociation following the attachment of a free electron as opposed to the complementary technique of analysing electron photodetachment from anions) rely on neutral targets. Accordingly, this thesis reports on the development of a novel experiment to study DEA to nucleosides, building on the extensive literature of DEA studies of nucleobases and simple sugars. In addition, the thesis also provides insights into the excited state dynamics of RNA nucleoside uridine and metastable fragmentation routes of excited 3-AP ions.

1.6 Layout of the thesis

Chapter 2 introduces the fundamental concepts that govern radiation interactions with isolated molecules. Chapter 3 provides a description of the experimental set-up which has been used for the multi-photon ionisation experiments presented in this thesis. An emphasis is placed on the experimental approach supported by a new Matlab simulation for studying metastable dissociation of excited ions. These have been applied in the experiments on 3-aminophenol, which is the main topic of Chapter 4. Chapter 5 provides an in-depth literature review of the approaches applied for bringing thermally labile biomolecules into the gas-phase and tests the suitability of *indirect laser-induced thermal desorption* for the production of intact neutral gas-phase targets of nucleosides uridine, thymidine and their derivatives 2′-deoxyuridine and 5-methyluridine. The MPI experiments in Chapter 6 bring new insights into the fragmentation pathways, electronic excited state dynamics and photostability of uridine. A newly built experimental apparatus for studying dissociative electron attachment processes to targets produced by indirect laser-induced thermal desorption is introduced in Chapter 7. Finally, Chapter 8 summarises the main outcomes of this thesis and proposes ideas for future research.

Chapter 2

Theoretical background

This PhD thesis is aimed at enhancing our understanding of the nanoscale processes by which radiation, notably UV photons and electrons, initiates chemical and structural changes in RNA/DNA. The central aim of this chapter is therefore to introduce the general theoretical basis for understanding photon and electron interactions with molecules. It begins with Molecular orbital theory, then summarises different types of molecular isomerisation before giving a brief overview of the interactions which lead to the aggregation of molecules into molecular clusters. After this, it addresses the excitation and relaxation of molecules drawing on key concepts such as potential energy surfaces, the Franck-Condon principle, the Born-Oppenheimer approximation and non-adiabatic processes. These provide the basic framework for understanding photon-induced phenomena in molecules, notably radiative and non-radiative decay mechanisms, photodissociation and multi-photon ionisation, the key experimental tool applied in Chapters 4, 5 and 6. Furthermore, we discuss two collision-induced processes that play critical roles in biological radiation damage: electron impact ionisation and dissociative electron attachment. Understanding of the former process is important to interpret the results presented in Chapter 6, while studying the latter is the main motivation behind building the new experimental system presented in Chapter 7. This chapter also introduces the concept of metastable dissociation which is the central topic of Chapter 4.

2.1 Molecular orbital theory

Molecular orbital theory describes the distribution of electrons in a molecule in terms of molecular orbitals (MOs), mathematical descriptions of single electron quantum states. Thence electrons in molecules are distributed among a set of MOs of discrete (quantised) energies. They are not solely assigned to individual atoms, but can extend over the entire molecule and their quantum states are determined by taking into account all nuclei as well

as all other electrons. Molecular orbitals are typically represented pictorially as regions of space with high probability of finding the electrons at any given time. Examples of molecular orbitals of uridine, the molecule studied in Chapter 6, are illustrated in Fig. 2.1. Molecular orbital theory is based on quantum-mechanical principles, i.e. on the Schrödinger equation:

$$H\Psi = E\Psi \tag{2.1}$$

where H is the Hamiltonian operator, Ψ is a wave function of a MO describing the interaction of the electron with all the nuclei and other electrons in the molecule and E is the energy of an electron in a particular orbital.

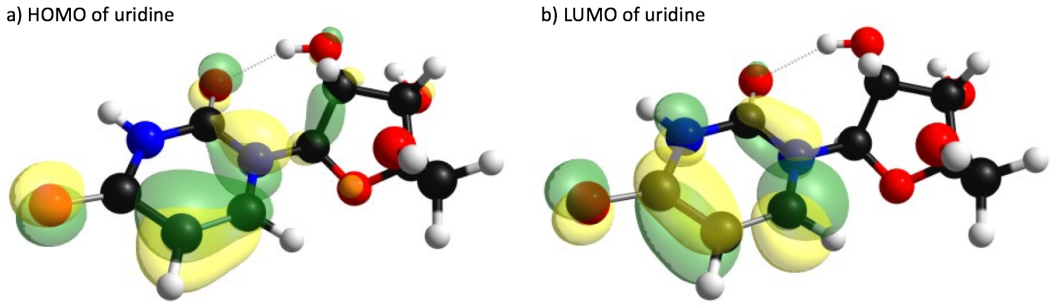

Fig. 2.1: Electron density of a) highest occupied (π) and b) lowest unoccupied (π^*) molecular orbitals of uridine (calculated by A. Rebelo, PhD student in the Molecular Clusters Laboratory at the OU). The green and yellow colours are used to indicate opposite phases of molecular orbital wave functions.

Full analytical solutions to the Schrödinger equation for molecular orbitals are beyond the practical limits of current computing power for all the simplest molecules, notably simple homo-nuclear diatomics. Therefore, molecular orbital wavefunctions are often treated as a linear combination of atomic orbitals (LCAO)

$$\Psi = c_1\phi_1 + c_2\phi_2 + ... + c_n\phi_n \tag{2.2}$$

where c_i is a weighting factor (atomic coefficient) for i-th atomic orbital wavefunction, ϕ_i is a corresponding atomic orbital. A specific chosen combination of atomic orbital wavefunctions ϕ_i chosen is called a basis set [73].

As noted above, some molecular orbitals are delocalised over more than one atom or even the entire molecule. Formation of delocalised molecular orbitals in the so-called valence shells of molecules leads to lowering of the total energy of the system and therefore its stabilisation. As a result of delocalisation, these molecular orbitals result in much more complex shapes than atomic orbitals. The highest occupied molecular orbital is normally referred to as HOMO, while the lowest unoccupied molecular orbital is referred to as

LUMO. The HOMO and LUMO orbitals of uridine are depicted in Fig. 2.1. It should be noted that experiments presented in this thesis probe only valence shell orbitals and that valence orbital occupation is responsible for covalent bonding.

In general, valence molecular orbitals can be classified in the following ways:

1. According to their energy:

    - A bonding molecular orbital

      Electrons occupying bonding MOs lowers the energy of a system of two or more atoms compared with those atoms being free. This favours the formation of bonds and hence a stable molecule.

    - An antibonding molecular orbital

      Electrons occupying antibonding MOs raises the energy of a system of two or more atoms compared with those atoms being free. This opposes formation of bonds. These are typically denoted by * next to the symbol describing orbital, e.g. the σ^*.

    - A non-bonding molecular orbital

      Electrons occupying non-bonding molecular orbitals does not change the energy of a system of two or more atoms compared with those atoms being free, therefore occupation of non-bonding MO by electrons neither favours nor opposes the formation of bonds in the molecule. These are typically denoted by n.

2. According to their shape (symmetry):

    - Sigma (σ) - their electron probability is perfectly centred about the internuclear axis, i.e. the line passing through two nuclei.
    - Pi (π) - their electron probability is concentrated above and below the internuclear axis. They are formed by sideways overlap of two adjacent p orbitals [74, 75].

Although this is a well-established classification, some molecular orbitals are of a more complex character. They can be described by two letters, e.g. dark $n\pi^*$ and bright $\pi\pi^*$ orbitals in nucleobases. Furthermore, some delocalised orbitals have mixed valence and Rydberg character. A Rydberg orbital is one which is sufficiently large and diffuse that it bares analogy to the atomic orbitals of hydrogen. In this case, all the other electrons as well as the nuclei in the molecule are encompassed within the Rydberg orbital and can be considered to analogise a hydrogen nucleus.

2.2 Molecular isomers

Polyatomic molecules (comprising more than two atoms) can have linear, planar or non-planar, i.e. three-dimensional structures. As molecules get larger, so the possibilities increase for isomerisation, i.e. the transformation of a molecule from one structure to another. Isomers are molecules with the same type and number of atoms but the arrangement of the atoms differs and therefore they have different properties. Thermally-driven isomerisation of uridine is discussed in Chapter 6. There are several classes of isomers and they are schematically listed in Fig. 2.2. It should be noted that the geometry of a molecule depends on its electronic structure. Therefore, the geometry in neutral electronic excited states and in ionic states can differ significantly from that in the neutral electronic ground state [76].

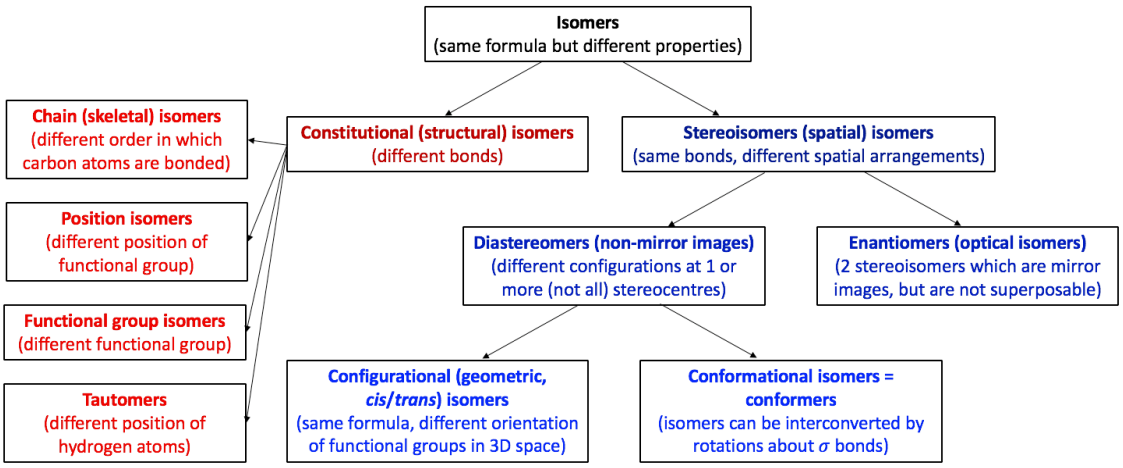

Fig. 2.2: Schematic diagram of classification of molecular isomers (adapted from [74]).

2.3 Intermolecular forces - clusters

When two or more molecules form bonds, we describe this aggregation as a *molecular cluster*. Although *molecular clusters* are not a central topic in this thesis, they represent an important intermediate step between isolated gas-phase biomolecules and real biological environments. As mentioned in Chapter 1, the OU Molecular Clusters Group studies clustering effects (i.e. effects of chemical environment) as well as progressively more complex biomolecules as an integrated strategy to elucidate fundamental radiation-induced process in biomolecular systems. In addition, some of the optimisation work on the new experimental set-up presented in Chapter 7 was done by doing electron impact ionisation experiments on methanol clusters. Therefore, we briefly summarise intermolecular forces that are responsible for the formation of clusters. In general, intermolecular forces are

weaker compared to intramolecular forces and they can be attractive or repulsive. We can categorise them as follows:

1. Van der Waals forces - distance-dependent polar interactions between uncharged molecules. We differentiate between two kinds of Van der Waals forces:

    - London dispersion forces - the weakest intermolecular forces. An instantaneous dipole caused by electron motion in a molecule without a permanent dipole moment induces an instantaneous dipole in a nearby molecule that also has no permanent dipole moment. The interaction of these instantaneous dipoles results in an intermolecular attraction.
    - Dipole-dipole forces - interactions between polar molecules possessing permanent electric dipole moments. These interactions tend to align molecules to increase the attraction and hence reduce potential energy of the system. In addition to dipole-dipole interactions, higher multipole interactions can play a significant role in determining the structure of clusters.

2. Hydrogen bonding - a dipole-dipole interaction between a covalently-bonded partially positive H atom in one molecule (the covalent bond leaves part of the hydrogen atom positive) and a highly electronegative atom (e.g. N, O or F) in the second molecule.

3. Other non-covalent forces:

    - Ion interactions with permanent dipoles, ion interactions with induced dipoles, and permanent dipole interactions with induced dipoles.
    - Cation-π - a weak attraction between a cation of one molecule and an electron rich π orbital of the aromatic ring of an adjacent molecule [77].
    - π-stacking - attractive interaction resulting from the distortion of π electron clouds of two adjacent molecules [78, 79].

Hydrogen-bonding and π-stacking are particularly relevant in this thesis because:

- The base-pairs within RNA and DNA are hydrogen-bonded.
- π-stacking is also prevalent in nucleobase clustering and plays an important role in determining the structure of RNA and DNA.
- Methanol clusters are primarily hydrogen-bonded [80].

- Hydrogen bonds provide ”bridges” for intermolecular hydrogen or proton transfer in excited or ionised molecular clusters and the observation of protonated species is a key piece of evidence for clustering in our experiments.
- Hydrogen bonds within molecules can also provide bridges for hydrogen or proton transfer between different parts of excited or ionised molecules. This is highly relevant to Chapters 5 and 6, which focus on the products of nucleoside dissociation via base/sugar cleavage with or without hydrogen transfer.

2.4 Excitation of molecules

Excited states of molecules (also atoms and ions) are those quantum states which have more energy than the ground state. Molecules can express their internal energy in the form of electronic, vibrational and rotational excitation. The energies of electronic excited states are of the order of a few eV above the ground state, vibrational states tens to hundreds of meV and rotational states of a few meV. The properties and reactivity of molecules in excited states and their relaxation to lower energy states play important roles in the photochemistry of biomolecular systems and, more generally, in the radiation response of living material. This section summarises the key concepts which we use to rationalise molecular excitation and relaxation processes in this thesis.

2.4.1 Multiplicity of electronic states of molecules

The *spin multiplicity* (generally just called the *multiplicity*) of a molecular electronic state is the number of possible orientations of spin angular momentum that it can have. It is given by:

$$Spin\,multiplicity = 2S + 1 \tag{2.3}$$

where S is the sum of spin quantum numbers of all the electrons in the molecule. An electronic state can be classified according to its spin multiplicity as:

1. a singlet - all the electron spins are paired, hence $S = 0$ (see Fig. 2.3 a) and b)),
2. a triplet - unpaired orientations of spins, hence $S = 1$ (see Fig. 2.3 c)). Such states are triply degenerate as they have three possible orientations of the spin vector.

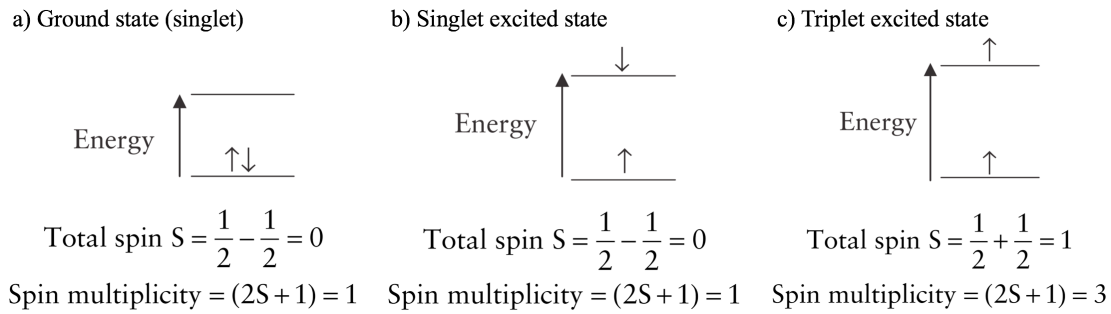

Fig. 2.3: Schematic illustration of the difference between the combination of electron spins in a) the ground state (singlet) of a molecule; b) a singlet excited state and c) a triplet excited state [81].

The concept of spin multiplicity in this thesis relates to spin selection rules of photo-excitation, discussed in Section 2.5.1.

2.4.2 Potential energy surfaces

A potential energy surface (PES) represents a relationship between the energy of a molecule and its geometry in a particular electronic state [82]. PES can be generated as a function of internuclear distances in a molecule or, more typically, for a smaller selection of key degrees of freedom. If potential energy is plotted as a function of only one coordinate, we use term potential energy curve. Imagined potential energy curves of the ground state and an excited state of a molecule are presented in Fig. 2.4 to illustrate several key features, notably avoided crossing, local minima, the Franck-Condon region and conical intersections. These are discussed in the sections below.

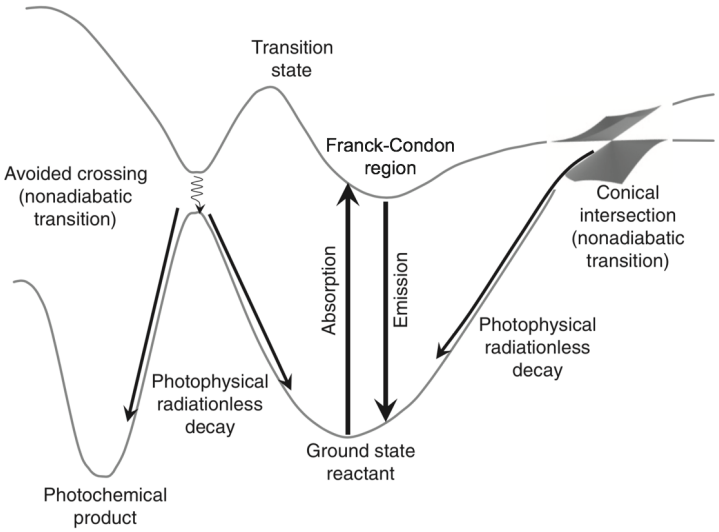

Fig. 2.4: Schematic diagram showing imagined potential energy curves of the ground state and an excited state of a molecule [81].

2.4.3 The Franck-Condon principle

The intensity distributions of vibronic transitions were qualitatively explained by Franck in 1925 and then further elucidated by Condon in 1926 [83, 84]. A vibronic transition is a change in the electronic state of a molecule (including ionisation) accompanied by a simultaneous change in vibrational energy. Fig. 2.5 shows several examples of vibronic transitions, specifically excitations from the lowest vibrational level of the neutral electronic ground state to higher vibrational levels of the lowest-energy ionic state. The Franck-Condon principle states that electronic transitions occur on much faster timescales than nuclear motion, so that in a vibronic transition the nuclei will have very nearly the same position and velocity immediately before and immediately after the transition. Franck-Condon factors f_{FC} describe the probability of a particular transition. The probability for a transition is highest where the vibrational wave functions of the initial and final electronic states have maximum overlap. The most probable transition occurs from a point where vibrational motion is about to reverse and the kinetic energy associated with the vibration is at its minimum.

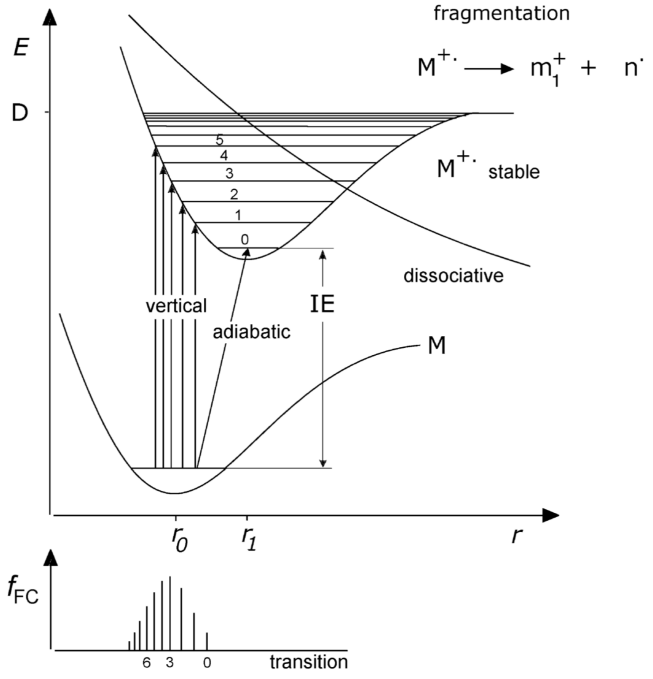

Fig. 2.5: Schematic illustration of the Franck-Condon principle (E is energy, r is internuclear distance, r_0 and r_1 are the equilibrium internuclear distances for the neutral electronic ground state and the lowest-energy ionic state of molecule M, respectively, D is the dissociation energy of the $M^{+\cdot}$ state and IE is the adiabatic ionisation energy). The lower part shows a distribution of Franck-Condon factors (f_{FC}) for various vibronic transitions between the M and $M^{+\cdot}$ states. A dissociative state is also shown. This could be accessed via a direct photo-excitation (transitions and FC factors not shown) or it may be accessible from the $M^{+\cdot}$ state via one or more conical intersections (often referred to as *predissociation*) [85].

The lower graph in Fig. 2.5 shows the distribution of the Franck-Condon factors for the transitions between the neutral electronic ground state and the lowest-energy ionic state of a molecule. The requirement that the position of the nuclei does not change during the electronic transitions means that the transition is between points which lie on a vertical line on the main graph. The probability distribution of the internuclear distance (r) values within the lowest vibrational level of the electronic ground state of the molecule dictates where the most probable vertical transition should start, i.e. at equilibrium position r_0 (see Fig. 2.5). The most probable transition is referred to as the *vertical transition* and it has an associated *vertical energy*. In Fig. 2.5, this is the energy difference between the lowest vibrational level ($v'' = 0$) of the electronic ground state to the $v' = 3$ level of the lowest-energy ionic state. The counterpart of the vertical transition is a process where the transition happens between lowest vibrational levels of the initial and final electronic states of a molecule. Such a transition is referred to as an *adiabatic transition* (also $0 \leftarrow 0$) and the corresponding energy is called *adiabatic energy* (see diagonal line in Fig. 2.5) [75, 76, 85].

2.4.4 The Born-Oppenheimer approximation

In 1927, Born and Oppenheimer [86] proposed that although molecules can be simultaneously excited electronically, vibrationally and rotationally, these three degrees of freedom can be treated separately. This separation can be partially rationalised by the large difference in the mass of nuclei and electrons and hence large differences in timescales for the nuclear and electronic motion (see Section 2.4.3). The Born-Oppenheimer approximation can be expressed in quantum mechanical terms as follows.

The Hamiltonian for a molecule can be written as a sum of the kinetic energy T (or its quantum mechanical equivalent) and the potential energy V

$$H = T + V \tag{2.4}$$

The kinetic energy has two components T_e and T_n corresponding to the motion of electrons and nuclei, respectively. Therefore, the total kinetic energy can be written as

$$T = T_e + T_n \tag{2.5}$$

The potential energy comprises three components:

$$V = V_{ee} + V_{nn} + V_{en} \tag{2.6}$$

where V_{ee} and V_{nn} are the components corresponding to Coulombic repulsions between electrons and nuclei, respectively, while V_{en} is due to attractive forces between electrons and nuclei.

For fixed nuclei $T_n = 0$ and V_{nn} is constant. The electronic wave functions Ψ_e then satisfy the Schrödinger equation:

$$H_e \Psi_e = E_e \Psi_e \tag{2.7}$$

where E_e is the electronic energy and the Hamiltonian is

$$H_e = T_e + V_{en} + V_{ee} \tag{2.8}$$

Because of the term V_{en} in Eq. 2.8, H_e and consequently Ψ_e and E_e (see Eq. 2.7) depend on nuclear coordinates. However, as nuclei move much slower than electrons due to their much larger mass we can approximate that Ψ_e and E_e involve nuclear coordinates only as fixed parameters. As electrons adjust *almost instantaneously* (on timescales of tens to hundreds of attoseconds [87, 88]) to any nuclear motion, E_e can be considered as a part of the potential field in which the nuclei move and hence

$$H_n = T_n + V_{nn} + E_e \tag{2.9}$$

The corresponding Schrödinger equation will then be

$$H_n \Psi_n = E_n \Psi_n \tag{2.10}$$

where Ψ_n represents nuclear wave function and E_n nuclear energy. Based on the Born-Oppenheimer approximation, the total wave function Ψ can be written as the product of the electronic wave function describing the molecule with clamped nuclei and the nuclear wave function describing the vibration of the nuclei and the rotation of the total molecule

$$\Psi = \Psi_e(q, Q)\, \Psi_n(Q) \tag{2.11}$$

where q and Q are electron and nuclear coordinates, respectively. Consequently, based on Eq. 2.11, the total internal energy of the molecule is

$$E = E_e + E_n \tag{2.12}$$

Nuclear wave function Ψ_n can be also factorised into two components:

$$\Psi_n = \Psi_v\, \Psi_r \tag{2.13}$$

where Ψ_v represents the vibrational part and Ψ_r the rotational part of the nuclear wave function. It follows that

$$E_n = E_v + E_r \tag{2.14}$$

By substituting Ψ_n from Eq. 2.13 in Eq. 2.11, we get the following equation for the total wave function Ψ

$$\Psi = \Psi_e \, \Psi_v \, \Psi_r \tag{2.15}$$

and hence

$$E = E_e + E_v + E_r \tag{2.16}$$

The physical meaning of the Born-Oppenheimer approximation is therefore that the vibration of the nuclei does not change the electronic state of the molecule. As discussed in the next section, this approximation breaks down near degeneracies, i.e. where potential energy surfaces cross and even a small change in nuclear coordinates may result in a large change in the electronic part of the wave function [75, 76].

2.4.5 Non-adiabatic processes

Within the Born-Oppenheimer approximation, the behaviour of molecules is described by the dynamics of the nuclei moving along a single potential energy surface generated by the electrons. Non-adiabatic processes are facilitated by a close proximity of PESs. When at least two potential energy surfaces approach each other, the coupling between them becomes important and the Born-Oppenheimer approximation breaks down. The energy separation between the PESs determines the rate of the non-adiabatic process. Traditionally, non-adiabatic transitions were understood in terms of tunneling across an avoided crossing. However, ultrafast experimental techniques revealed non-adiabatic processes of femtosecond timescales which could not be described by traditional theories. These were explained by conical intersections, which are actual crossings between potential energy surfaces [15]. Examples of the non-adiabatic transitions (an avoided crossing and a conical intersection) are shown in Fig. 2.4. For more information on non-adiabatic processes, the reader is referred to [89].

2.4.5.1 Conical intersections

It has been previously shown that non-adiabatic dynamics and conical intersections actively participate in photobiology [45, 90–92]. Therefore, we will illustrate the concept of a conical intersection in more detail with reference to Fig. 2.6.

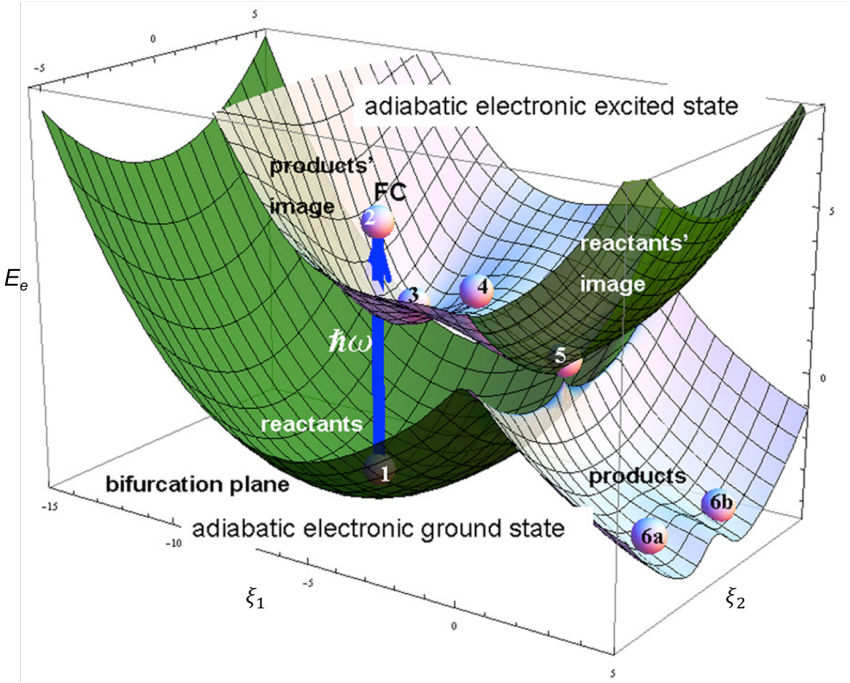

Fig. 2.6: Schematic representation of a system passing through a conical intersection between the electronic ground state and an electronic excited state of a molecule (1 - optimal position of the nuclei in the electronic ground state, 2 - Franck-Condon region, 3 - local minimum of the potential energy surface of the electronic excited state, 4 - potential energy barrier, 5 - conical intersection). The figure shows the electronic energy E_e as a function of the spatial coordinates ξ_1 and ξ_2. The blue arrow represents a photoexcitation by absorption of a photon with energy $\hbar\omega$ (adapted from [89]).

Fig. 2.6 shows two adiabatic potential energy surfaces: the lower one corresponding to the electronic ground state of a molecule and the top one corresponding to an electronic excited state. The optimal positions of the nuclei in the electronic ground state are represented by point 1 in the configurational space (the nuclei vibrate around this point, however we will now neglect the quantum nature of these vibrations). The absorption of a photon with energy $\hbar\omega$ (where $\hbar$ is reduced Planck constant and ω is angular frequency), vibronically excites the molecule in the Franck-Condon region, (i.e. vertically) to point 2 in Fig. 2.6. The PES near the FC region has the shape of a well. Within a few femtoseconds, the system slides down from point 2 to the vicinity of point 3 (the local minimum of the PES near the FC region). Point 3 is separated from the conical intersection at point 5 by a barrier with the corresponding potential energy saddle point 4 (corresponding to a *transition state*). If the system has enough kinetic (i.e. vibrational) energy, it can reach the top of the saddle point and overcome the barrier. Alternatively, the system can get through the barrier by tunnelling. Behind the saddle point, there is normally an energy valley with a deep *funnel* which leads to the conical intersection (point 5) with probability approaching 1. After passing through the conical intersection, the system will get back to the electronic ground state, where it can either relax towards the products at points 6*a* or

b or it can return to point 1. As the total energy of the system has to be conserved, the non-radiative path will take place if the system has a way to dissipate the excess energy, i.e. to transfer the excess of electronic energy into vibrational, rotational and translational degrees of freedom and/or those of surrounding molecules [89].

2.5 Photon- and electron-induced processes in molecules

In the Molecular Clusters Laboratory at the OU, reflectron time-of-flight (TOF) mass spectrometry is used to probe photon- and electron-induced processes in biomolecules. To date, we have used the system to perform multi-photon ionisation (MPI) and electron impact ionisation (EII) experiments. However, a new experimental set-up for probing dissociative electron attachment (DEA) to biomolecules has been built and is currently in the process of optimisation and testing. Consequently, this section provides more insights into MPI, EII and DEA processes. Although the results presented in this thesis are mainly from MPI experiments (Chapters 4, 5 and 6), understanding the basis of EII is valuable for following the arguments presented in Chapter 6. All three of these processes will be studied using the new experimental set-up described in Chapter 7.

2.5.1 Photon-induced processes

The interactions of photons with molecules can be classified into absorption, scattering and pair production [93]. With respect to the experiments presented in this thesis (Chapters 4, 5 and 6), we will consider only the first one of the above-mentioned phenomena as the latter two happen at much higher energies than the energy of photons which can be generated by the Nd:YAG/dye laser system in the Molecular Clusters Laboratory at the OU ($4.48 - 5.64\,eV$). Photon absorption processes can be further distinguished as single or multi-photon absorption. Significant multi-photon absorption by the molecules in this thesis occurs in our UV laser irradiation conditions (typically averaging $10^6 - 10^7\,W cm^{-2}$ during partially-focused $7\,ns$ pulses). The first photon absorption causes neutral electronic excitation (generally vibronic). After this, the excited molecule can remain in the same state for long enough for a subsequent photon to be absorbed. Alternatively, it may decay before this, either radiatively (with photon emission), non-radiatively (without photon emission), or by a combination of both. Radiative and non-radiative transitions are discussed in the two sections below with reference to the energy-level (or *Jablonski*) diagram in Fig. 2.7. Multi-photon ionisation and photo-dissociation are addressed in the subsequent sections.

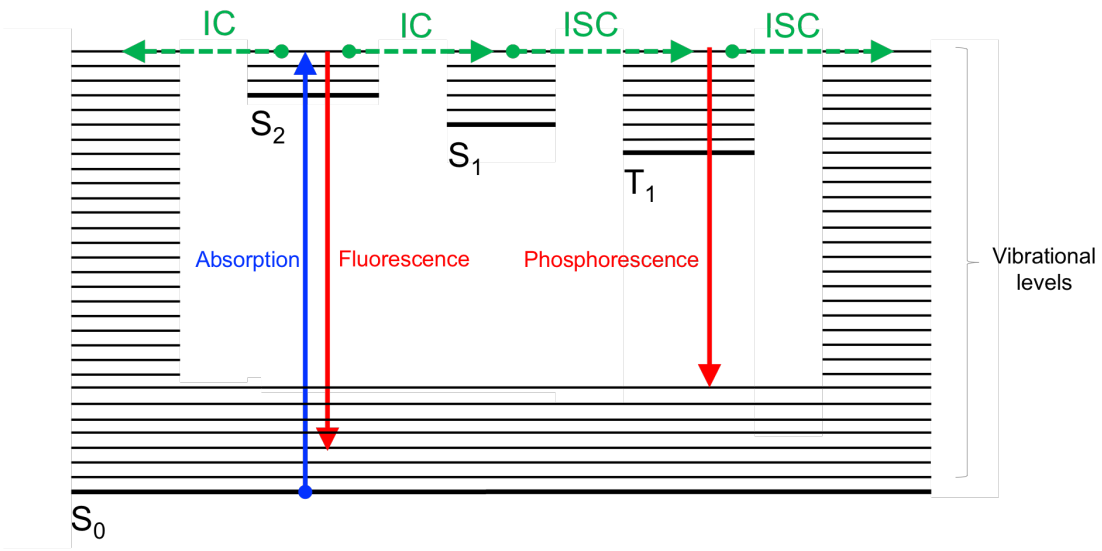

Fig. 2.7: A Jablonski-type diagram illustrating possible relaxation processes following single-photon absorption to an electronically excited state. Radiative (fluorescence and phosphorescence) and non-radiative (*IC* - internal conversion and *ISC* - intersystem crossing) decay mechanisms are depicted by solid and dashed lines, respectively [57, 58, 94].

2.5.1.1 Spin selection rule for radiative transitions

The spin selection rule for radiative electronic transitions (photon absorption or emission) states that *spin-allowed* transitions are those where spin multiplicity of the initial and final electronic states is the same. Radiative transitions where a change of multiplicity is involved are called *"spin-forbidden"* and have zero spin-overlap integral as defined below:

$$M_S = \langle S_i \,|\, S_j \rangle \tag{2.17}$$

where S_i and S_j are the spin functions of the initial and final electronic states, respectively, and r_S represents the spin coordinates of electrons. The electronic ground state of a stable molecule is always a singlet. The probability of a *"spin-forbidden"* transition becomes more probable when spin-orbit coupling is significant. Spin-orbit coupling represents the interaction between spin angular momentum and orbital angular momentum. For a given atom, the coupling strength scales approximately with the fourth power of the nuclear charge z. In the case of molecules, the interaction becomes more significant in the presence of a heavy atom, however, the z^4 dependence has to be scaled to include the probability that an electron is near the atom [94, 95]. As a result of the transitions involving a change in the multiplicity being only very weakly allowed, triplet states generally have very low photoabsorption cross sections and also have long lifetimes with respect to radiative decay. In view of the low cross section for singlet to triplet photo-excitation, access to triplet excited states generally requires initial photo-excitation to a singlet state

followed by a radiationless decay process (discussed in the next sub-section).

In addition to the spin selection rule, radiative transitions can be forbidden based on the lack of orbital overlap or symmetry mismatch. The latter optical selection rules can be also relaxed due to vibronic coupling when molecular geometry gets distorted due to vibrational motion. The interaction between electronic and nuclear vibrational motion is known as vibronic coupling [96]. Note that collision-induced transitions between electronic states of molecules are not subject to optical selection rules. For example, direct singlet to triplet excitations become significant in electron scattering at relatively low electron collision energies and relatively high scattering angles [97].

We differentiate between two radiative decay mechanisms which are also shown in Fig. 2.7:

1. Fluorescence – emission of light associated with a radiative transition between electronic states with the same spin multiplicity (e.g. $S_2 \rightarrow S_0$ in Fig. 2.7). It is a *spin-allowed* transition and the average lifetime of electronic excited states with respect to fluorescence is typically $< 10^{-6}\,s$ (but still several orders of magnitude longer than the lifetime with respect to radiationless transitions of electronically excited nucleobases and many other biomolecules).

2. Phosphorescence – emission of light associated with a radiative transition between electronic excited states with different spin multiplicity (e.g. $T_1 \rightarrow S_0$ in Fig. 2.7). It is a *spin-forbidden* transition and therefore occurs even more slowly than fluorescence. The average lifetime of electronic excited states from which phosphorescence occurs ranges from $10^{-6}\,s$ to several s.

2.5.1.2 Non-radiative decay mechanisms

Non-radiative decay mechanisms play crucial roles in the photochemistry of biological systems. For example, ultrafast non-radiative decay via conical intersections (for more details see Section 2.4.5.1) is responsible for the exceptional stability of nucleobases and nucleosides [43, 98] with respect to UV irradiation. With reference to Fig. 2.7, we can differentiate between the following non-radiative decay mechanisms:

1. Internal conversion
   Any radiationless transition between two states with the same multiplicity is called internal conversion (timescales typically of the order of $10^{-12}\,s$). For example, $S_2 \rightarrow S_0$ and $S_2 \rightarrow S_1$ internal conversions are indicated in Fig. 2.7.

2. Intersystem crossing

   Non-radiative decay mechanisms are not limited to states with the same spin multiplicity. The non-radiative relaxation between states with different spin multiplicity is called intersystem crossing (typical timescales $\sim 10^{-8}\,s$). For example, $S_1 \rightarrow T_1$ and $T_1 \rightarrow S_0$ intersystem crossings are indicated in Fig. 2.7 [94].

2.5.1.3 Multi-photon ionisation

While in single-photon ionisation (SPI, see Fig. 2.8 b)) absorption of one photon with energy above the ionisation threshold is sufficient to ionise a molecule, multi-photon ionisation (MPI) is a process in which the absorption of several photons of energies below the ionisation threshold can bring a molecule from a neutral excited state into an ionic state. Several examples of MPI processes are shown schematically in Fig. 2.8 c) to f). The number of photons required to produce an observed ion is referred to as the photon order. In the absence of saturation effects, it can be estimated using the perturbation theory expression:

$$I = c.E^{\alpha} \tag{2.18}$$

where α is the photon order, c is a constant (notably depending on target density, photoabsorption cross sections, excited state lifetimes, and ion detection efficiency), I is the ion yield and E stands for the laser pulse energy [99, 100].

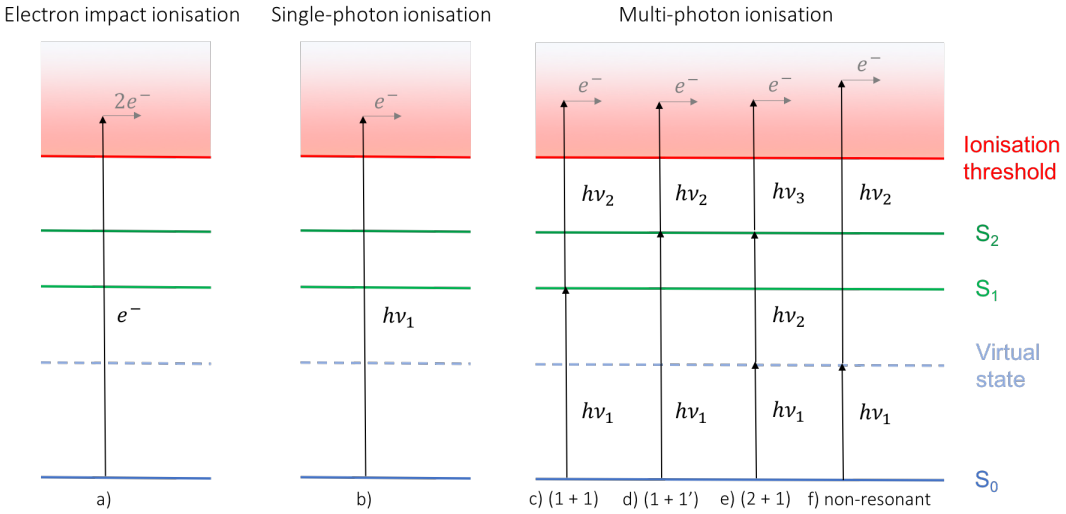

Fig. 2.8: Scheme of a) electron impact ionisation; b) single-photon ionisation and c) to f) multi-photon ionisation processes (partially adapted from [101]).

MPI processes are usually described in terms of $(n+m)$, where n stands for the number of photons needed to pump a molecule from its ground state into a neutral electronic excited state and m refers to the number of photons needed to remove an electron from this

bound excited state, and thus ionise the molecule. We can distinguish between one colour MPI processes, where the wavelength of n and m photons is the same, and two colour processes, where the wavelength differs. The latter ones are marked with prime next to the m number, e.g. $(1+1')$ in Fig. 2.8 d) [101]. All of the MPI experiments presented in this thesis apply one colour processes.

An MPI process can be described as resonant when the energy of n photons corresponds to the energy difference between the ground state and an excited state of the molecule (see Fig. 2.8 c) to e)). The technique studying resonant MPI processes is often called Resonance-Enhanced Multi-Photon Ionisation (REMPI). However, as the neutral electronic excited states accessed in the present experiments are energetically broad, we prefer to use the more general term of MPI here. If the absorption of the n photons does not reach any eigenstate of the molecule, the MPI process is referred to as non-resonant (see Fig. 2.8 f)). The efficiency of MPI is determined by laser parameters (e.g. wavelength, fluence, etc.) as well as by the excited state lifetimes and cross sections of individual absorption processes. Because virtual excited states are very short-lived, the probability of MPI via virtual states is much lower compared to the resonant processes [101]. Non-resonant MPI signals of xenon were previously observed by Schechter et al. [102] at $266\,nm$ with a laser fluence of $7.49\times10^{9}\,W\,cm^{-2}$. This is more than one order of magnitude higher than achievable laser fluence using our current UV nanosecond laser system (see Chapters 3 to 7), but still well below the threshold where photon stimulated field ionisation becomes noticeable ($\sim10^{13}\,W\,cm^{-2}$) [103]. For more information on MPI we recommend [101].

2.5.1.4 Photodissociation

Photodissociation is the breakage of one or several bonds in a molecule induced by the absorption of a single photon (single-photon dissociation) or several/many photons (multi-photon dissociation) [104]. Most of the fragment ion production in the present MPI experiments occurs via what we might call multi-photon dissociative ionisation, whereby the absorption of several photons gives access to a dissociative ionic state. However, single-photon dissociation in a neutral excited state followed by multi-photon ionisation of one of the neutral fragments is also possible and the group has observed this previously in MPI experiments on uracil [18]. In either case, the dissociation can happen via several different processes:

- Direct photodissociation in an electronic excited state – absorption of photons excites a molecule or an ion into an electronic excited state that is repulsive with respect to the nuclear coordinates. Because the timescales for spontaneous emission are relatively long compared with the dissociation timescales, this leads to the dissociation. In

our experimental conditions fast radiationless decay dominates the deactivation of the neutral electronic excited states (e.g. the bright S_2 ($\pi\pi^*$) states of nucleobases). The deactivation is fast enough to compete efficiently with dissociation, however, so is the absorption of a subsequent photon in the present UV laser conditions. Hence, the rate of dissociation in neutral electronic excited states depends on the competition with relaxation processes and with subsequent photon absorption.

- Predissociation – absorption of photons excites a molecule into a bound excited state which then relaxes non-radiatively into repulsive state (via a conical intersection).
- Spontaneous radiative dissociation – absorption of photons excites a molecule into a bound electronic excited state. The molecule can then emit photons and get into a lower-lying repulsive state or vibrationally the hot ground state where it dissociates [105].

2.5.2 Electron-induced processes

All physical phenomena observed when incident electrons interact with molecules can be generally referred to as electron-induced processes. This section introduces the two most important electron-induced processes in the context of this PhD thesis: electron impact ionisation (EII) and dissociative electron attachment (DEA). For an extensive explanation and discussion of EII and DEA pathways we recommend [85, 106] and [107], respectively.

2.5.2.1 Electron impact ionisation

When an electron collides with a neutral molecule, part of the kinetic energy of the electron is transferred to the neutral molecule. This transferred energy can exceed the ionisation energy of the molecule [85]. The ionising interaction of an energetic electron e^- with a ground state molecule M can be described as follows (see Fig. 2.8 a)):

$$M + e^- \rightarrow M^{+\bullet} + 2e^- \tag{2.19}$$

where $M^{+\bullet}$ is a molecular radical cation. Depending on the type of the molecule and the energy of the electrons, doubly and triply charged ions can be also observed, however, this is much more rare compared to singly charged ion production [85].

It should be noted that we do not observe an electron-beam equivalent of multi-photon ionisation, i.e. multi-electron-collision ionisation in our experimental conditions. The reason is that electron fluence in our electron beams (maximum fluence of about 10^{17} *electrons* $s^{-1}cm^{-2}$ in previous EII experiments by the Molecular Clusters Group) is many

orders of magnitude lower than photon fluence in laser pulses (usually $\geq 10^{23}$ *photons* $s^{-1}cm^{-2}$). Therefore there is far more time for excited species to relax before encountering another electron in our crossed beam experiments and hence multiple excitation can reasonably be neglected. Thence, contrasting results in MPI and EII experiments can provide evidence for processes happening in neutral electronic excited state of molecules (e.g. see Chapter 6) [18]. The same rationale applies to contrasting results in MPI and SPI experiments where the energy of a single photon exceeds the ionisation threshold.

2.5.2.1.1 Ionisation and appearance energies

The ionisation energy (IE) of a molecule is defined as the minimum energy that has to be absorbed by the molecule in its electronic ground state in order to eject an electron and hence form an ion that is also in its electronic and vibrational ground state. Such a transition is called an *adiabatic transition*, hence we can refer to the corresponding energy as the *adiabatic ionisation energy* [85]. Conversely, the vertical energy difference between the neutral ground state PES and the PES of the lowest-lying ionic state is called the *vertical ionisation energy* and a vertical transition of this kind will typically produce a vibrationally-excited ion. The lowest-energy ionisation involves electron removal from the HOMO, i.e. a valence orbital with lone pair (n), π, or σ character. Ionisation energies of most molecules are in the range $7 - 15\,eV$. Normally the difference between the *vertical* and *adiabatic ionisation energies* is of the order of $0.1 - 0.7\,eV$.

Removing an electron from a molecule normally leads to weakening of the bonding and therefore increases the probability of dissociation. The lifetime of the ion will depend on its potential energy surface, i.e. if it is trapped in a local minimum and its vibrational energy is significantly lower than the energy barrier for dissociation, the ion will have a long lifetime. If the level of excitation is significantly above the dissociation barrier, the ion will dissociate on a fast timescale and we can observe its charged fragment in the mass spectrum. If there is no minimum on the potential energy surface, the dissociation happens even more rapidly (spontaneous dissociation). The dissociation of the radical parent ion (an ion with the same mass as the neutral target) $M^{+\bullet}$ (see Eq. 2.19) results in the formation of a fragment ion and a neutral as follows:

$$M^{+\bullet} \rightarrow {m_1}^{+} + n^{\bullet} \tag{2.20}$$

or

$$M^{+\bullet} \rightarrow {m_1}^{+\bullet} + n \tag{2.21}$$

It should be noted that ionisation always produces reactive species, which highlights its

importance for radiation chemistry, in addition to releasing electrons that can themselves cause damage.

The *appearance energy* of the fragment ion $m_1{}^+$ is then defined as the minimum that needs to be transferred to the neutral ground-state molecule M in order to detect the $m_1{}^+$ ion. *Adiabatic* and *vertical appearance energies* for fragment ions are defined in exact analogy with *adiabatic* and *vertical ionisation energies*. In general, charge tends to remain on the larger fragment following dissociation, so smaller fragment ions tend to have higher appearance energies than larger ones. Double ionisation processes occur at even higher energies.

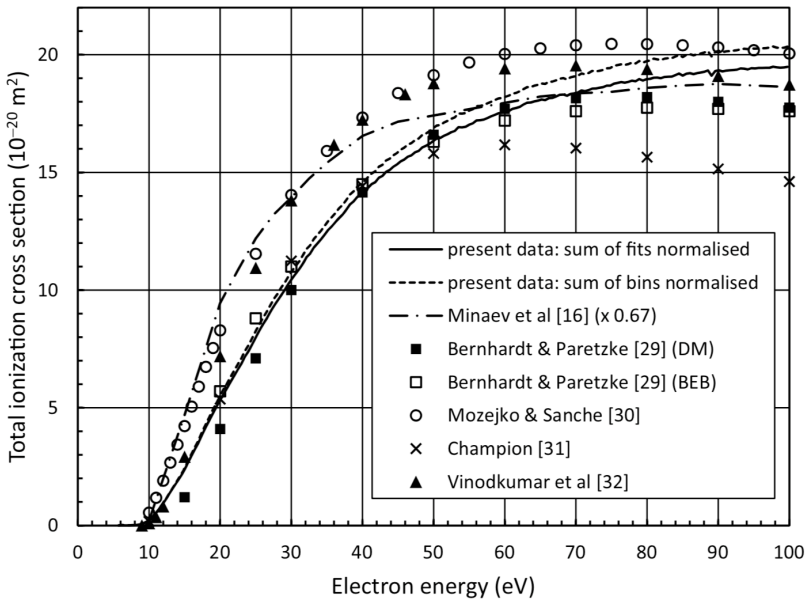

Fig. 2.9: Example of the total ionisation cross sections for electron impact on adenine (the lines indicate normalised experimental and the symbols indicate theoretical results) [108]. Note that the references in the figure are as they appear in [108].

If the energy of the incoming electron is only just equal to the ionisation energy (or the appearance energy if our interest is in a fragment ion), the probability of ionisation will be very low. Even a slight increase in the electron energy will bring a steady increase in the ionisation efficiency. The ionisation cross section graphs of all molecules show similar characteristics, exhibiting a maximum at electron energies at around $70\,eV$ as shown in Fig. 2.9. It is therefore unsurprising that 70 eV is the standard electron impact ionisation energy in mass spectrometry databases, allowing comparison between different molecules and facilities [85]. In addition to the high ionisation cross section, working at $70\,eV$ brings the following advantages:

1. $70\,eV$ is well above the ionisation energy of all molecules (also atoms).

2. There is a plateau region around $70\,eV$ in the ionisation efficiency curves (see Fig. 2.9), which means that small variations in the electron energy will have negligible effects.

3. The relatively high kinetic energy (KE) of $70\,eV$ electrons makes the beams relatively easy to manage with respect to divergence due to space charge and stray fields [85].

2.5.2.2 Dissociative electron attachment

Dissociative electron attachment (DEA) is a resonant process with electron energies below $20\,eV$. Collision of a low-energy electron (LEE) with a molecule (AB in Eqs. 2.22 and 2.23, and Fig. 2.10) results in the resonant capture of the electron in a virtual orbital of the molecule, which leads to the formation of a transient negative ion (AB^{-*} in Eqs. 2.22 and 2.23, and Fig. 2.10). The transient negative ion is energetically unstable and can either result in the *autodetachment* of the electron and hence formation of the neutral molecule AB

$$e^- + AB \rightarrow AB^{-*} \rightarrow AB + e^- \tag{2.22}$$

or in a dissociation that produces a neutral fragment A and a stable negative ion B^- . This latter process is DEA and can be summarised in the general reaction formula below:

$$e^- + AB \rightarrow AB^{-*} \rightarrow A + B^- \tag{2.23}$$

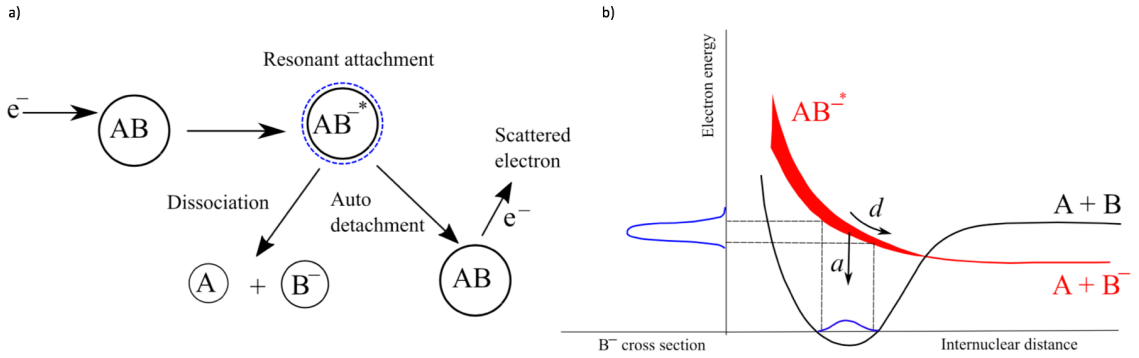

Fig. 2.10: a) Schematic showing processes induced by low-energy electron interaction with molecule AB and b) potential energy surfaces of the parent neutral and transient negative ionic states [109].

We can distinguish four transient negative ion (TNI) resonances:

- Shape resonances – the electron is temporarily trapped in a shallow potential well created by an attractive polarisation of the molecule in its electronic ground state and a repulsive component due to the angular momentum of the trapped electron.

Most shape resonances have short lifetimes of the order of $10^{-15} - 10^{-10} s$. For example see Fig. 2.11.

- Core-excited shape resonances – similar to shape resonances, however a higher energy of the incident electron results in inelastic scattering prior to the resonant capture, which leaves the molecule in an electronically excited state.

- Nuclear-excited (vibrational) Feshbach resonances – involves coupling of the kinetic energy of the incident electron with vibration in the target molecule. The potential energy surface of the TNI lies below the potential energy surface of the ground state molecule, which stabilises the resonant state and thus leads to longer lifetimes of the order of $10^{-6} s$. For example see Fig. 2.11.

- Electron-excited Feshbach resonances – the incident electron first uses part of its energy for electronic excitation of the molecule and then is trapped in the field of electronically excited molecule. The remainder of the electron's energy is coupled to the vibration of the excited molecule. Because in this case the vibrational levels of the excited state of the TNI can be energetically lower than the vibrational ground state of electronically excited molecule, this type of resonance can have a relatively long lifetime [107].

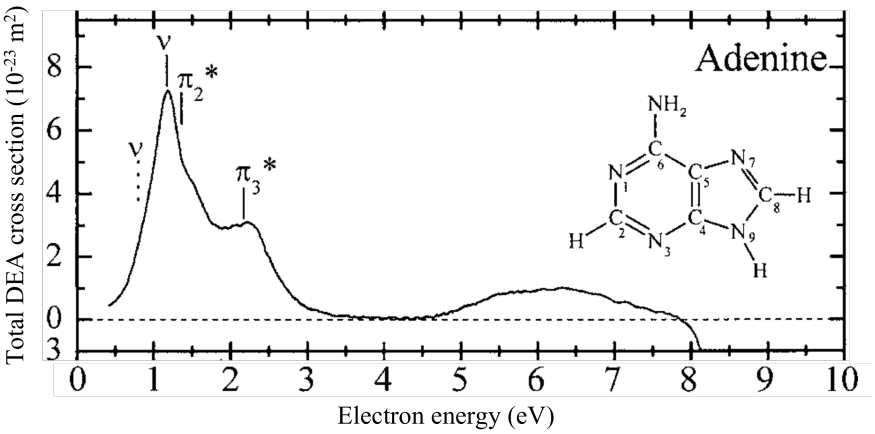

Fig. 2.11: Example of the total DEA cross section for DEA to adenine (adapted from [110]). The solid vertical lines labelled π^* and *"ν"* indicate π^* shape resonances and vibrational Feshbach resonances determined by Aftalooni et al. [111] and the dotted vertical line labelled *"ν"* indicates vibrational Feshbach resonance located by Gohlke et al. [112].

Fig. 2.11 shows an example of how DEA cross section varies as a function of electron energy. Compared with EII (see Fig. 2.9), DEA to RNA/DNA constituents generally exhibits significantly lower cross sections (see Fig. 2.11), which makes its experimental

detection more challenging. The new experimental set-up developed in the Molecular Clusters Laboratory at the OU, which is described in Chapter 7, has been built to enable measurements of DEA cross sections of thermally labile RNA/DNA constituents.

2.6 Metastable dissociation

Metastable dissociation of excited 3-aminophenol ions is the main topic discussed in Chapter 4. Metastable (delayed, μs-timescale) dissociation of ions during their journey through a mass spectrometer was observed for the first time by Hipple and Condon in 1946. The term metastable refers only to ions which fragment en route throughout the mass spectrometer due to the internal energy acquired in the interaction region, i.e. not by collisions with a target gas or radiative excitation as they traverse the mass spectrometer (for more information on the functioning of the reflectron mass spectrometer see Section 3.2.2 and for more details on the metastable dissociation measurements in the Molecular Clusters Laboratory at the OU see Section 3.3). In order to explain the basis of metastable dissociation in our experiments, we will first set out the key principles that determine the timeframe of any unimolecular dissociation [94].

2.6.1 Unimolecular dissociation

Quasi-equilibrium theory (QET) is a theoretical approach to describe unimolecular dissociations. Based on QET, ions isolated in the gas-phase can redistribute energy only internally and undergo only unimolecular reactions such as isomerisation and dissociation. For more information on QET see [85, and references therein].

2.6.1.1 Transition states and activation energy

A transition state of a chemical reaction is a short-lived configuration at a local energy maximum along the reaction coordinate. The reaction diagram in Fig. 2.12 shows the dissociation of an ion, $ABC^{+\bullet}$, which can result in three possible products with corresponding transition states (TS_1, TS_2 and TS_3). The energies E_{01}, E_{02} and E_{03} in the diagram represent activation energies corresponding to TS_1, TS_2 and TS_3, respectively. An activation energy is the energy which has to be provided to a system to result in a particular chemical reaction, i.e. in this case to access a particular transition state.

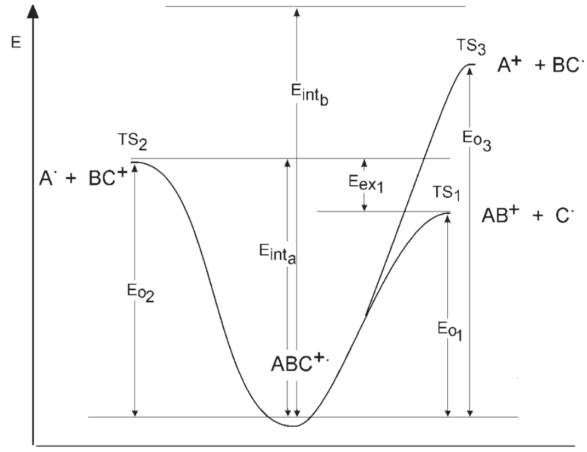

Fig. 2.12: Schematic diagram showing competing fragmentation pathways. TS_1, TS_2 and TS_3 represent three different transition states with respective activation energies E_{0_1}, E_{0_2} and E_{0_3}. E_{int_a} and E_{int_b} are two examples of potential internal energies of the $ABC^{+\bullet}$ ion. E_{ex_1} represents the excess energy for the transition state $TS1$ when the internal energy of $ABC^{+\bullet}$ is E_{int_a} (adapted from [85]).

The relation between the internal energy of the precursor ion and the activation energy of the transition states will affect the presence of the fragmentation products in a mass spectrum. Based on the relation of internal energy E_{int} of the $ABC^{+\bullet}$ ion with respect to the activation energies E_{0_1}, E_{0_2} and E_{0_3} in Fig. 2.12, the following scenarios are possible:

a) Internal energy E_{int_a} of $ABC^{+\bullet}$ ion is slightly above the activation energy E_{0_2} of the TS_2 transition state, but well above the activation energy E_{0_1} of TS_1. The energy difference between the internal energy and the activation energy is called the *excess energy*. Both TS_1 and TS_2 can be overcome, but TS_3 can not be accessed at all. Therefore the mass spectrum will only contain product ions of the first two fragmentation pathways, while $BC^{+\bullet}$ will be of very low abundance due to negligible *excess energy* (for more information see Section 2.6.1.2).

b) Internal energy E_{int_b} of $ABC^{+\bullet}$ ion is well above the activation energies of the three transition states and therefore we will see product ions of all three dissociations in the mass spectra. Their abundance will be determined by their corresponding rate constants as discussed below [85].

2.6.1.2 Rate constants

The rate of a chemical reaction is defined by a rate constant k. QET defines the unimolecular rate constant (as required to treat unimolecular dissociation) as follows:

$$k = \int_0^{E-E_0} \frac{1}{h} \frac{\rho^*_{(E_{int},E_0,E_t)}}{\rho_{(E_{int})}} dE_t \tag{2.24}$$

where h is Planck's constant, $\rho_{(E_int)}$ represents the density of energy levels with internal energy E_{int} and $\rho^*_{(E_{int},E_0,E_t)}$ is the density of energy levels of the transition state with activation energy E_0 and translational energy E_t in the reaction co-ordinate, i.e. the bond which is being broken. By approximating the system by as many harmonic oscillators as there are vibrational degrees of freedom s we obtain

$$k = \left(\frac{E_{int} - E_0}{E_{int}}\right)^{s-1} \frac{\prod_{j=1}^{s} \nu_j}{\prod_{i=1}^{s} \nu_i^*} \tag{2.25}$$

where ν_j ($j = 1, ..., s$) and ν_i ($i = 1, ..., s$) are the vibration frequencies associated with the precursor ion and the transition state, respectively. This expression can be further simplified by replacing the complex expression of probability functions by ν which is a frequency factor determined by the number and the density of vibrational states, i.e.

$$k = \nu \left(\frac{E_{int} - E_0}{E_{int}}\right)^{s-1} \tag{2.26}$$

This equation can be further simplified as follows:

$$k = \nu \left(\frac{E_{ex}}{E_{int}}\right)^{s-1} \tag{2.27}$$

where E_{ex} is the excess energy for a particular combination of transition state and internal energy. This expression is valid only when the internal energy is considerably above the dissociation threshold, i.e. $(E_{int} - E_0)/E_{int} \approx 1$ and can be written in the exponential form as follows:

$$k = \nu e^{-(s-1)\frac{E_o}{E_{int}}} \tag{2.28}$$

If the internal energy of an ion is close to the dissociation threshold, the number of degrees of freedom has to be replaced by an effective number of oscillators which can be obtained by using an arbitrary correction factor [85, 113].

Based on QET, the rate constant of a unimolecular reaction therefore depends on the *excess energy* of the reactants with respect to the transition state and hence on the distribution of the internal energies of the precursor ions. The curve in Fig. 2.13 represents the general shape of a rate constant as a function of energy (E). If the *excess energy* is close to $0\,eV$ (e.g. for TS_2 in Fig. 2.12, where $E_{int_a} \approx E_{0_2}$), the rate constant is very low (close to $0\,s^{-1}$), while it rises sharply with a small increase in the *excess energy*. The maximum of the rate constant is defined by the vibrational frequency of the bond which dissociates, i.e.

the fragments can not fly apart at higher velocities than determined by their vibrational motion [85].

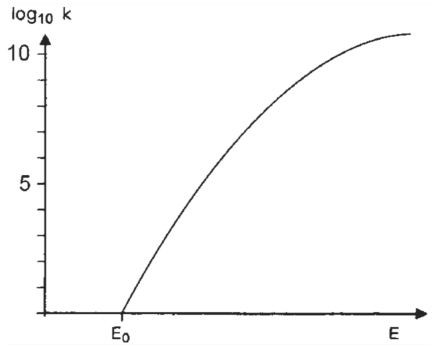

Fig. 2.13: General shape of the $log_{10}(k)$ (k is the rate constant) versus energy E plot (adapted from [85]).

2.6.1.3 Timescales of dissociations

Timescales of ion dissociation are defined with respect to their passage through a mass spectrometer as follows:

1. *Stable ions* - dissociate with rate constants $k < 10^5\,s^{-1}$, hence they will reach the detector without fragmentation and we will observe them in the mass spectrum with the same mass as they had prior to ionisation. We generally refer to these as *parent ions* in Chapters 3 to 7.

2. *Metastable ions* - dissociate with rate constants $10^5\,s^{-1} < k < 10^6\,s^{-1}$, hence many of these ions will dissociate on their journey through the mass spectrometer. We refer to these as *metastable precursor ions* in Chapter 4.

3. *Unstable ions* - dissociate with rate constants $k > 10^6\,s^{-1}$, hence they will not reach detector and we will not observe them in the mass spectrum. However, we can observe their fragment ions, and these are referred to as *prompt fragment ions* later on in the thesis.

The rate constants above relate to flight times in our mass spectrometry experiments, and are also typical of studies of molecular ions on this scale. The correlation between the rate constants of ion dissociation and their stability during their journey through a typical mass spectrometer is shown in Fig. 2.14. It should be noted that this classification is only meaningful when considering isolated ions in the gas-phase as outside vacuum, nearly all ions would spontaneously react with surrounding molecules in the atmosphere/solution [85].

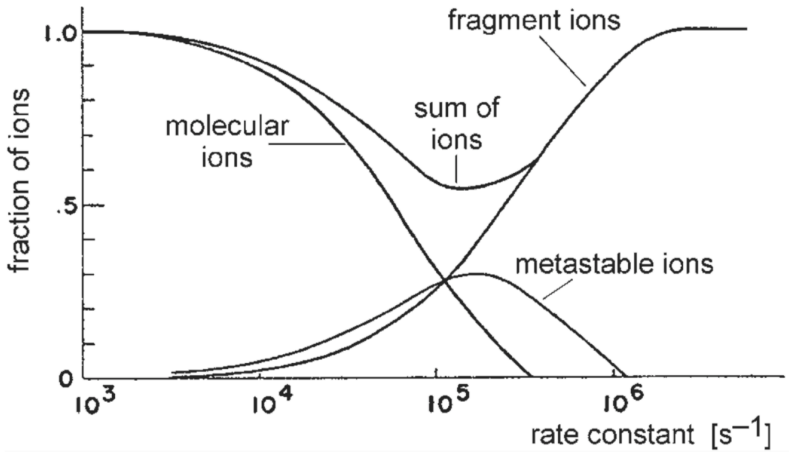

Fig. 2.14: Classification of ions based on their stability within the mass spectrometer with respect to rate constants (adapted from [85]).

2.6.1.3.1 Unstable and metastable ions

In the case of unstable excited ions, fragmentation happens either during the first vibration, or predissociation which involves a transition from one potential energy surface to another one. In such cases, the dissociation happens very rapidly in the interaction region of a mass spectrometer, resulting in what we have referred to as *prompt dissociation*.

The existence of metastable ions and hence *metastable* (also delayed) *dissociation* can be explained by different mechanisms. We can distinguish between the following scenarios:

1. Electronic (forbidden) predissociation via repulsive states:

   If the crossing of potential energy surfaces is spin-forbidden, some of the ions will undergo electronic predissociation, but at a reduced rate.

2. Dissociation by tunnelling:

   If the excess energy of an excited molecular ion is just below the dissociation threshold for this state then dissociation can take place on a *metastable timescale*.

3. Vibrational predissociation (in the case of large metastable ions):

   Ionisation followed by a radiationless transition to high vibrational levels of the electronic ionic ground-state results in a distribution of internal energies, some of which lead to unimolecular decomposition with decay rates on the timescale of metastable dissociation [94].

2.7 Summary and outlook

This chapter provides a short review of the main theoretical concepts which are important for interpreting the experimental work presented in Chapters 4 - 7. Particular emphasis is placed on multi-photon ionisation (the main radiative process applied in this thesis) and electron impact ionisation phenomena. Differences in fragment ion production by these two processes can provide indirect evidence for processes (structural changes or even dissociations) taking place in neutral electronic excited states (see Chapter 6). Here experiments are of particular importance as the complexity of reactive processes in electronic excited states make a pure theoretical treatment extremely difficult. In addition, electron impact ionisation is used to optimise the new experimental system which is presented in Chapter 7. The new system was built with the main motivation of studying dissociative electron attachment to relatively large biomolecules such as nucleosides. Therefore, dissociative electron attachment is also introduced here. Finally, the fundamentals of metastable dissociation of excited molecular ions are described in this chapter in the context of our reflectron time-of-flight mass spectrometry experiments to characterise sequential fragmentation pathways. The method is explained thoroughly in Chapter 3 and applied to the study of metastable dissociation of excited 3-aminophenol ions in Chapter 4. As indicated several times in this chapter, describing molecular systems by theory often requires numerous approximations. This highlights the importance of experiments for revealing radiation-induced processes on the molecular level.

Chapter 3

Experimental

This chapter describes the *Compact MPI/EII experimental set-up* in the Molecular Clusters Laboratory at the Open University (OU) which I used to carry out multi-photon ionisation time-of-flight (MPI-TOF) experiments on gas-phase biomolecules presented in Chapters 4, 5 and 6. The chapter also presents my contributions to the enhancement of this experimental system as well as describing the method that I have applied to study *metastable* (delayed) dissociation of excited ions using reflectron time-of-flight mass spectrometry. The Matlab simulation that I developed for the analysis of metastable dissociation completely replaced the Molecular Clusters Group's analysis system and enabled the experiment to provide much more detailed information.

3.1 Introduction

The experimental work in this PhD thesis involves two main research activities. The first one covers multi-photon ionisation experiments on biologically relevant isolated molecules, notably 3-aminophenol, nucleobases (uracil, guanine), nucleosides (uridine, thymidine) and their derivatives (2′-deoxyuridine, 5-methyluridine) using the *Compact MPI/EII experimental set-up*. The second one involves designing, building and optimising a new experimental set-up for multi-photon ionisation (MPI), electron impact ionisation (EII) and dissociative electron attachment (DEA) studies of molecules produced either by indirect laser-induced thermal desorption or Stark selected molecules produced in a molecular beam (the system is attached to a *Stark deflection experiment* which was previously built mainly by M. Ryszka, former PhD student at the OU). As designing, building and optimising the new experimental system represents a substantial piece of work, a separate chapter is dedicated to this (Chapter 7).

The *Compact MPI/EII experimental set-up* uses reflectron time-of-flight mass spectrome-

try to study isolated molecules and clusters upon irradiation with UV laser pulses (MPI) or electrons (EII). The set-up can currently be operated in two modes: *molecular beam mode* (for more details see Section 3.2.2) and *indirect laser-induced thermal desorption mode* (*ILTD mode*, for more details see Section 3.2.3). The system in its *molecular beam mode* was mainly built by B. Barć (former PhD student in the Molecular Clusters Laboratory), and it was further modified by E. al Maalouf (former MSc project student), M. Ryszka and R. Pandey (both former PhD students in the Molecular Clusters Laboratory). First steps towards building an ILTD source at the OU based on the technique devised by Greenwood and co-workers at Queens University Belfast [43] were carried out by M. Ryszka and R. Pandey. I have refined the design of the OU system and optimised its performance, notably by rebuilding the *ion source* to improve stability and repeatability between successive sample preparations and by redesigning the desorption laser alignment system (see Section 3.2.3.3). I have also investigated the UV laser stability which enabled me to gain better control of the UV laser pulse energy fluctuations than the Group had previously achieved. This was valuable because multi-photon ionisation signals are affected by the fluctuation of laser pulse energies during a measurement, as well as by more obvious parameters such as the average fluence and the wavelength (see Section 3.2.4.1). Finally, I have extended the Molecular Clusters Group's technique to analyse metastable fragmentation pathways of excited isolated and cluster ions by developing a Matlab simulation, which has enabled us to study more complex metastable dissociation patterns and make more precise assignments than the Group could do using the old approach (see Section 3.3).

3.2 *Compact MPI/EII experimental set-up*

3.2.1 Overview

The *Compact MPI/EII experimental set-up* probes ion production when a UV laser beam or an electron beam interacts with isolated molecules and/or clusters. Depending on how the neutral target of molecules and/or clusters is produced, we differentiate between *molecular beam mode* and *indirect laser-induced thermal desorption mode* of this set-up (see Sections 3.2.2 and 3.2.3, respectively). The radiation response of molecular clusters is not investigated in this thesis, however the reader should keep in mind that the system in its *molecular beam mode* can be exploited for the experiments on clusters as well as isolated molecules and this will be briefly mentioned in Section 3.2.2.

3.2.2 *Molecular beam mode*

A detailed description of the set-up in *molecular beam mode* has been reported in B. Barć's [56] and M. Ryszka's [57] PhD theses. Shorter descriptions were also published in R. Pandey's PhD thesis [58] as well as in several papers by the Molecular Clusters Group [18, 26, 114–116]. The scheme of the set-up in this *mode* is shown in Fig. 3.1.

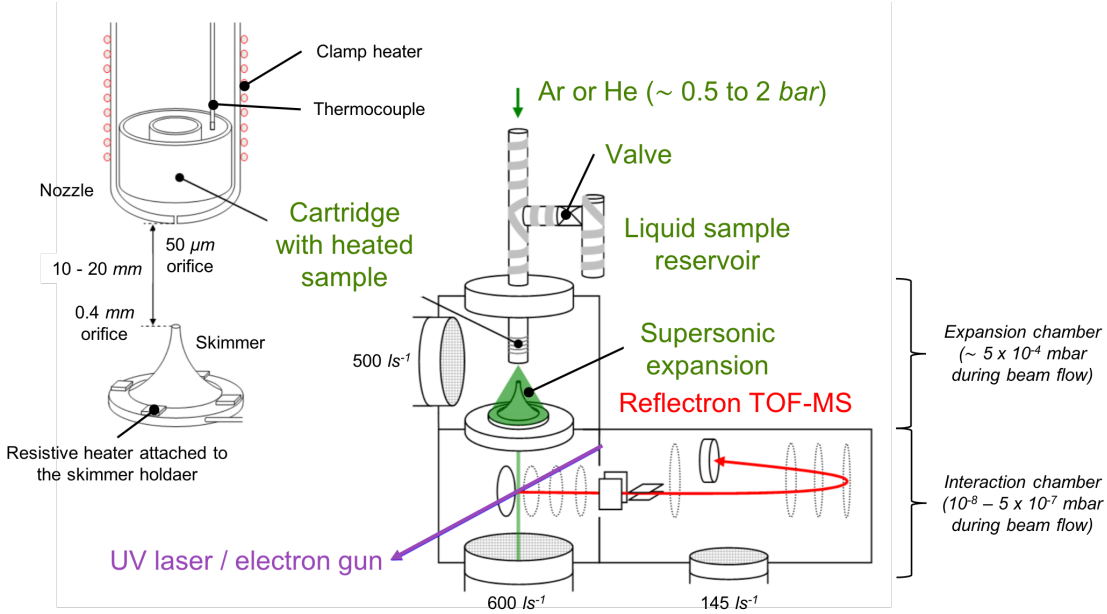

Fig. 3.1: Scheme of the *Compact MPI/EII experimental set-up* in *molecular beam mode* (adapted from [57]). A detailed description of individual parts of the reflectron TOF-MS is provided in Fig. 3.3.

Briefly, a molecular beam is formed by supersonic expansion of *Ar* or *He* carrier gas seeded with vaporised sample molecules through a $50\,\mu m$ diameter pinhole nozzle (laser-drilled into the closed end of a stainless steel tube by Lenox Laser) into a pumped chamber ($500\,ls^{-1}$). In the case of supersonic molecular beams, a gas expands from a high-pressure zone ($\sim$0.5 to $2\,bar$ in our experimental conditions) to a low pressure zone ($\sim 5\times10^{-4}\,mbar$ in our experimental conditions) through an orifice which is significantly larger than the mean free path of the gas particles. This results in numerous collisions of the gas particles during the expansion. The internal degrees of freedom are cooled (rotational and vibrational cooling), as are the relative translational degrees of freedom (the velocities of the gas particles with respect to each other). The beam is supersonic if the *Mach number*, i.e. the ratio of the average flow velocity of the gas to its speed of sound, is greater than unity [117]. For an example of a typical thermal (Maxwell-Boltzmann curve) distribution of a static gas and two supersonic jets with different *Mach numbers* see Fig.3.2. The reader is referred to [56–58, 117, 118] for more information on the supersonic expansion of a gas.

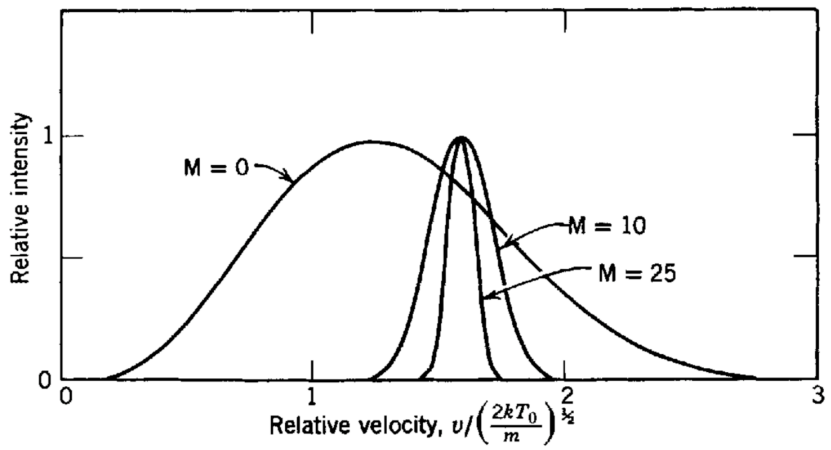

Fig. 3.2: Theoretical axial velocity distributions for two *Mach numbers* ($M = 10$ and 25) in a supersonic jet and the Maxwell-Boltzmann distribution of the reservoir gas marked as $M = 0$ (reproduced from [118]).

A clamp heater is used to heat the nozzle to vaporise a powder sample, which is loaded into a stainless steel cartridge near the nozzle orifice (see the detailed view in Fig. 3.1). The clamp heater also prevents condensation of the molecules in the nozzle orifice. A thermocouple is inserted into the powder cartridge, in order to directly monitor the temperature of the sample. This provides a very reliable temperature measurement of the sample compared with, for example, monitoring the temperature of the wall of the stainless steel nozzle [56]. Precise and repeatable temperature measurements are particularly important when working with thermally labile biomolecules. A stainless steel liquid sample reservoir can be used to produce various alternative targets such as hydrated biomolecular clusters. A small central portion of the supersonic expansion is then transmitted through a skimmer into another pumped chamber ($600 ls^{-1}$), resulting in a narrow *molecular beam*. The skimmer (Beam Dynamics model 2, orifice diameter $0.4 mm$) is heated to prevent molecular deposition. This is achieved by heating the aluminium holder of the skimmer to $125\,^{\circ}C$. The nozzle-skimmer separation is between 10 and $20 mm$ in the present experiments. The molecular beam is crossed at 90° by a pulsed UV laser beam (for more details see Section 3.2.4). The spot diameter of the UV laser pulses ($3 mm$ without lens) at the interaction with the molecular beam can be adjusted by moving a convex lens on a slider. A commercial electron gun (Kimball ELG-2) can be used instead of the UV laser beam to perform electron impact ionisation experiments, but no measurements of this kind are presented in the thesis so this aspect of the system is not described here.

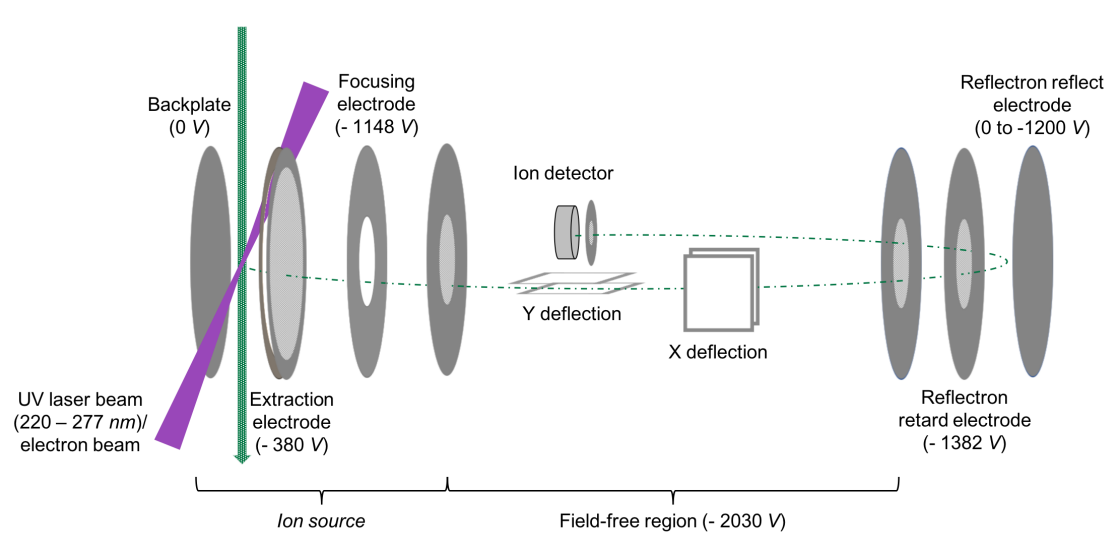

Fig. 3.3: Scheme of the reflectron TOF mass spectrometer with typical voltages.

Ion production is probed using a reflectron time-of-flight (TOF) mass spectrometer shown schematically in Fig. 3.3. Cations formed by the interaction of the molecular beam with UV laser pulses are extracted in a pulsed electric field ($-380\,V\,/\,1.26\,cm = -302\,V\,cm^{-1}$), then accelerated to about $-2\,kV$ and deflected to compensate for the molecular beam velocity (see X and Y deflectors in Fig. 3.3). Ions then pass through the mass spectrometer's field-free region (FFR), are decelerated in the retarding field and reflected to pass through the FFR for the second time before reaching a discrete dynode electron multiplier detector or alternatively a micro-channel plate (MCP) detector. The voltage on the reflectron reflect electrode (further referred to as *reflection voltage*) can be adjusted to discriminate ions according to their kinetic energies in the FFR and thus test for metastable (delayed) dissociation (for a detailed explanation of this method see Section 3.3). The second advantage of using a reflectron TOF mass spectrometer is higher mass resolution compared to typical linear TOF systems or quadrupole filters. This is achieved by doubling the ions' path in the FFR as well as by partially compensating for the differences in the velocities of ions of same mass produced at different places in the ion extraction volume by their interaction with retarding field [119]. The pre-amplified ion signals are timed using a Fast ComTec *P*7887 time-to-digital conversion (TDC) card with a $250\,ps$ minimum bin width. The *"sync out"* pulse from the Nd:YAG laser provides the *"start"* trigger for the TDC card. Data are collected using a LabVIEW acquisition system, developed by M. Ryszka. This interfaces with the TDC card and a laser pulse energy meter (Spectrum Detector $SPJ-D-8$), which terminates the UV laser beam path after its interaction with the molecular beam.

3.2.2.1 The *ion source* of the time-of-flight mass spectrometer

The original mass spectrometer was built by KORE Technology and the voltage divider unit which supplies voltages for individual electrodes was built by the Intra-Faculty Electronics and Computing Facility at the Open University. The backplate supplied by KORE Technology was modified to accommodate the foil required for indirect laser-induced thermal desorption (ILTD) and a new viewport to transmit a CW laser beam to heat the foil (see Section 3.2.3.3). Furthermore, I applied a new design and construction of all the components of the *ion source* of the TOF system. The *ion source* is the first part of the reflectron mass spectrometer (see Fig. 3.3) and consists of 5 electrodes mounted to a *DN*100*CF* flange. There were two major changes applied to the design of the old *ion source*:

1. In the original ion source, three of its component electrodes (the extraction electrode, the focusing electrode, and the first FFR electrode) were supported by only 2 pillars (see Fig. 3.6). This caused uneven separation between the adjacent electrodes around their circumference. More seriously, this uneven separation would be slightly different each time the ion source was removed from the experiment and then re-installed. This required a re-optimisation of the deflector voltages of the mass spectrometer, costing time and complicating comparisons between previous experiments. To solve this problem, an extra pillar was added (the idea behind this is that three non-collinear points uniquely define a plane).

2. A *sandwich system* was applied to attach grids onto the extraction electrode, focusing and FFR electrodes. The grids in the original *ion source* were spot welded onto these electrodes and were slightly distorted in places due to a few small accidents as the *ion source* was removed and re-installed many times over the years, which disrupted the homogenity of the electric fields within the *ion source*. This is particularly undesirable when carrying out metastable dissociation measurements (for more details on metastable dissociation measurements see Section 3.3). To resolve this issue, a so-called *sandwich* system was applied. It is based on stretching a grid between two rings of the same electrode which sit one on top of the other as schematically shown in Fig. 3.4.

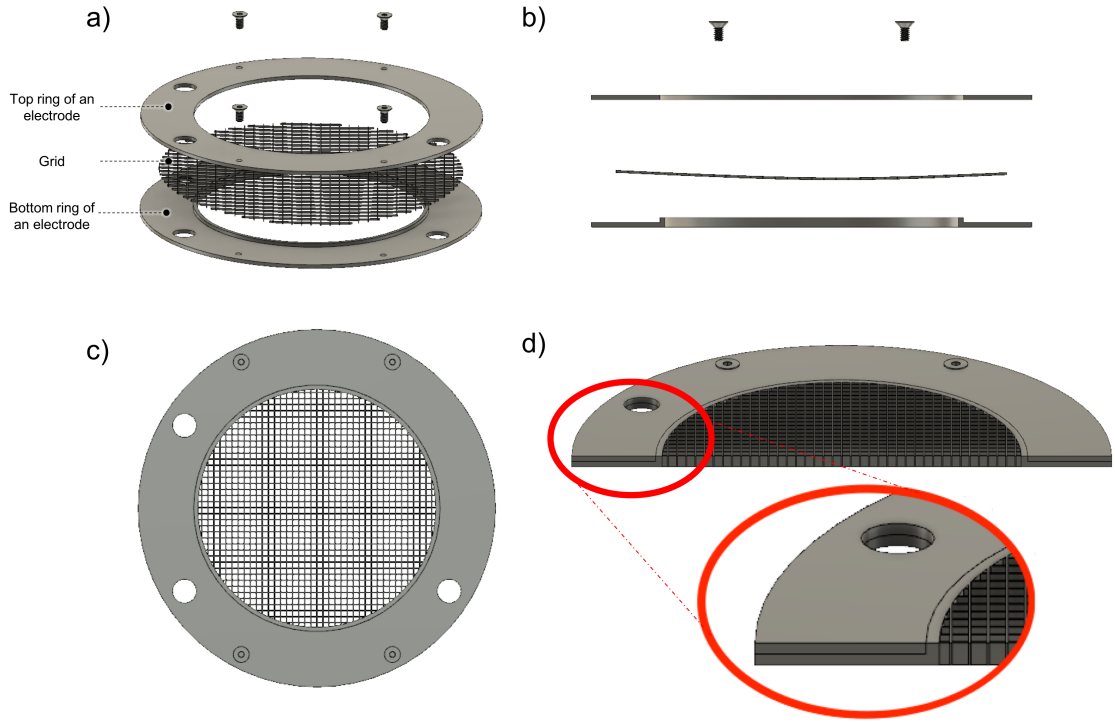

Fig. 3.4: Schematic view of the *sandwich system* of electrodes: a) and b) in the process of assembling; and c) and d) after being assembled. b) and d) show cross-sectional views.

3.2.3 *Indirect laser-induced thermal desorption mode*

The indirect laser-induced thermal desorption system of the *Compact MPI/EII experimental set-up* at the OU underwent three stages of development which are schematically depicted in Fig. 3.5 and described in detail in Sections 3.2.3.1 to 3.2.3.3. The *first generation* preceded the CW laser installation but is noted in this section for completeness.

3.2.3.1 *First generation* – thermal desorption system from a resistively-heated backplate

The first system for the thermal desorption of molecules from the backplate of the TOF system was established in the Molecular Clusters Laboratory at the OU by M. Ryszka. The aim was to produce uracil targets with rovibrational temperature similar to targets produced in the indirect laser-induced thermal desorption system at Heriot-Watt University (for details see [57]). The thermal desorption system is shown schematically in Fig. 3.5 a). A resistive heater attached to the back of the aluminium backplate (aluminium chosen for its high thermal conductivity) was used to enhance sublimation of the molecules from the holes drilled on the front side of the backplate. A thermocouple was used to measure the temperature of the backplate. The system produced strong signals of uracil$^+$ in MPI experiments, however it also produced strong signals due to impurities.

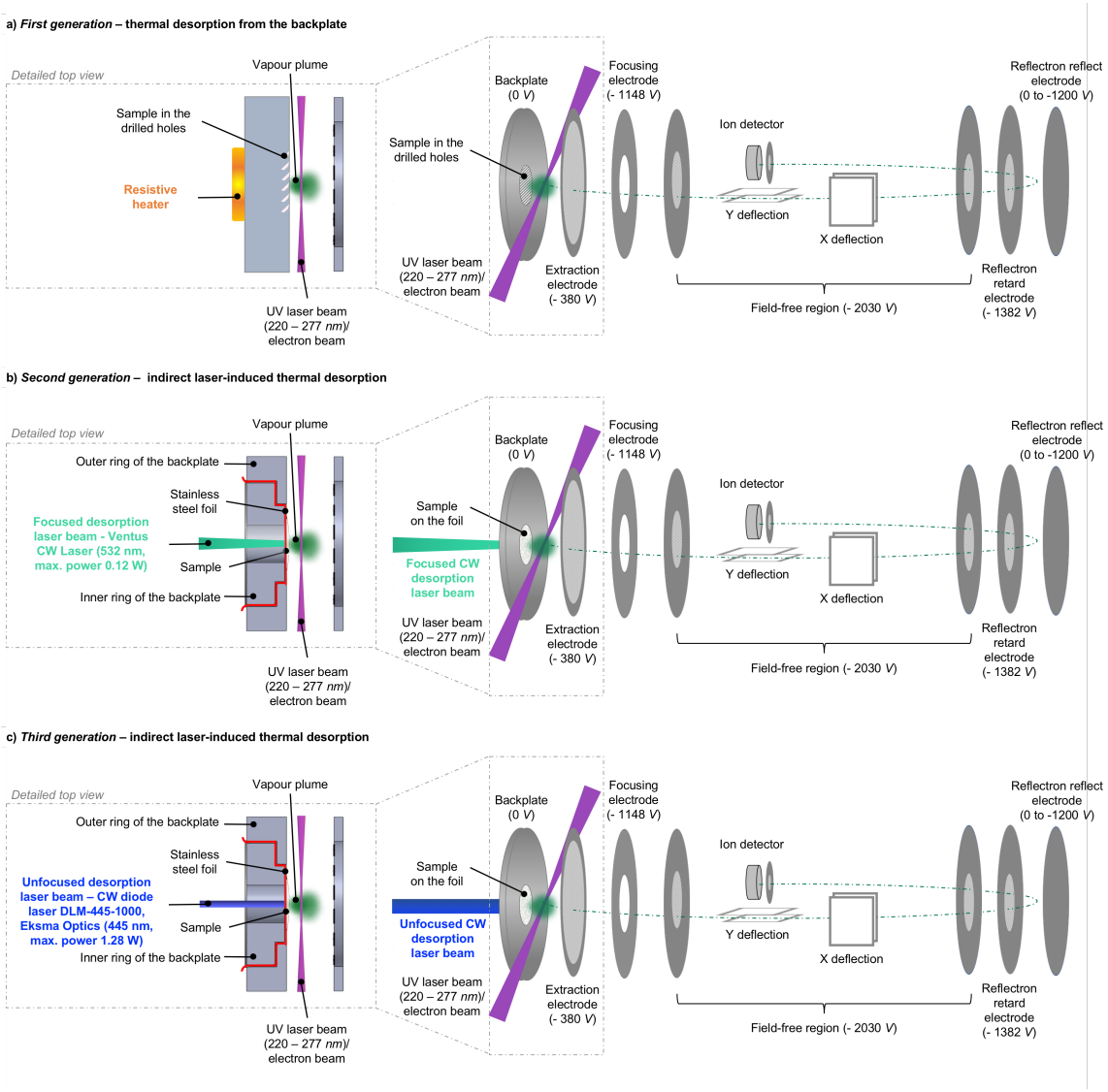

Fig. 3.5: Schematic representation of the development of indirect laser-induced thermal desorption system in the Molecular Clusters Laboratory at the Open University.

3.2.3.2 *Second generation* – indirect laser-induced thermal desorption

The next generation of the ILTD system at the OU was designed and built by R. Pandey and T. da Fonseca Cunha (an exchange PhD student from the Universidade NOVA de Lisboa that worked in the Molecular Clusters Laboratory at the OU for six months). The system was based on replacing the resistive heater by a CW laser (hence indirect laser-induced thermal desorption, see Fig. 3.5 b)) in order to reduce impurity signals via more localised heating and achieve a close analogy to the sample introduction system used in the experiments at Heriot-Watt University (Townsend and co-workers [43]). In turn, the Heriot-Watt ILTD system was a close adaptation of the original ILTD set-up developed at Queen's University Belfast (Greenwood and co-workers [120]).

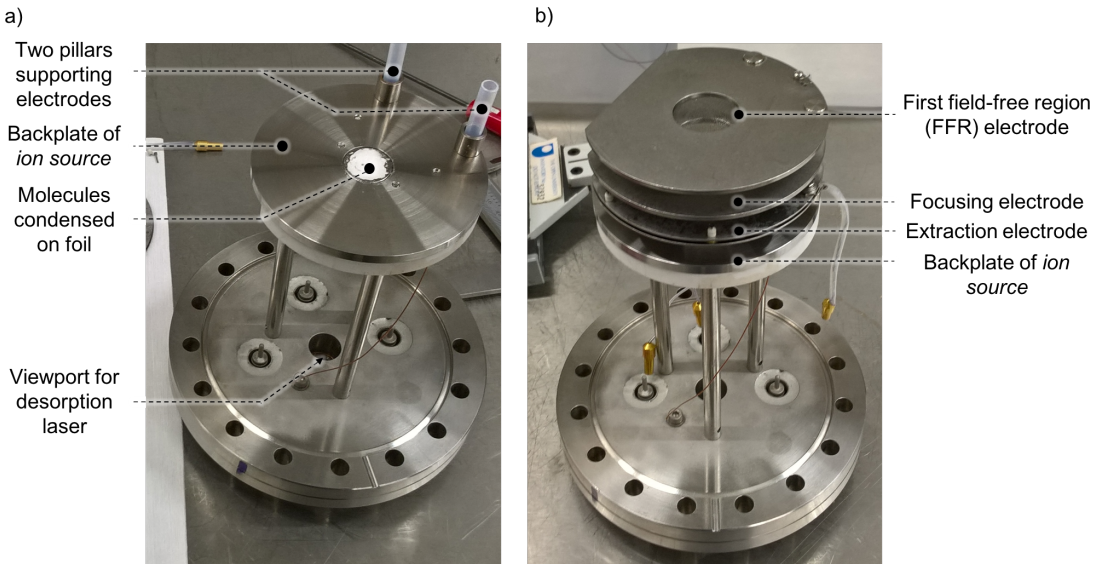

Fig. 3.6: Photographs of the *ion source* used for the ILTD experiments at the OU. a) The *ion source* at the stage of partial construction and b) assembled *ion source* with the exception of electrical connections (adapted from [58]).

In the ILTD system in the Molecular Clusters Laboratory at the OU, a Ventus CW laser beam ($532\,nm$, maximum power $0.12\,W$) passed through a $DN16CF$ viewport connected to a $DN100CF - to - DN16CF$ zero-length adapter inside of a vacuum chamber. *Ion source* electrodes were mounted to this adapter as shown in Fig. 3.6. The backplate of the *ion source* was specially modified by C. Hall and co-workers from Research Design and Engineering Facility at the OU to allow for ILTD experiments. The schematic picture of the customised backplate where a *sandwich system* was used to install a piece of foil is shown in the detail of Fig. 3.5 b). A convex lens with $20\,cm$ focal distance was used to focus the desorption laser beam onto the foil, while the sample was desorbed from the opposite side of the foil. In R. Pandey's and T. da Fonseca Cunha's experiments using this ILTD system, the maximum power of Ventus CW laser ($532\,nm$) of about $0.12\,W$ was high enough to desorb 3-aminophenol molecules. It was, however, not high enough to efficiently desorb uracil molecules, which resulted in MPI measurements with low signal-to-noise ratios (S/Ns).

3.2.3.3 *Third generation* – indirect laser-induced thermal desorption

I extended the development of the indirect laser-induced thermal desorption system at the OU. To tackle the problem of low desorption laser power of the Ventus CW laser ($0.12\,W$) I set up a new desorption laser (CW diode laser $DLM - 445 - 1000$, Eksma Optics, $445\,nm$, the maximum power $1.28\,W$ measured here using a Gentec-EO power meter, whereas the maximum power given in the manufacturers' technical summary is $1\,W$). The Gentec-EO power meter was checked in November 2018 against a recently-calibrated laser power

meter by a visiting laser engineer and the two meters agreed to within 10 %. Setting up the new desorption laser involved building a new system to mount the laser and move it in a controlled way for alignment as well as installing an interlock system for safety which was done with the support from D. Pound from Intra-Faculty Electronics and Computing Facility at the OU. I also optimised the experiment to attain better signal-to-noise ratios (S/Ns). This was achieved by adjusting the position of the focused UV spot with respect to the foil ($1-3\,mm$ from the foil) as well as by adjusting the desorption laser power and the position of the spot of the desorption laser on the back of the stainless steel foil. A schematic view of the *third generation* of the ILTD system at the OU is shown in Fig. 3.5 c). It has been exploited in previous published work about uracil [9] and 5-fluorouracil [121] but its specifics are described here for the first time.

The backplate is removed from the vacuum chamber and mounted horizontally for sample preparation. This involves placing $30-40\,mg$ of sample powder onto the stainless steel foil ($10\,\mu m$ thick) and then adding a few drops of methanol (Fisher Scientific UK Ltd, $99.8+\%$ (GLC) for HPLC), spreading using a spatula, leaving to allow the methanol to evaporate in air ($1\,bar$, $296\,K$). The resulting layer of adhered nucleoside has a thickness of several μm. The backplate is then re-installed in the chamber and pumped down.

We tested for the possible effect of the focusing lens between the desorption laser and the viewport by carrying out MPI experiments on uridine with and without the lens. No significant changes were observed in the mass spectra taken with and without the lens (see Fig. 3.7). Therefore, the experiments using ILTD presented in this thesis were done without using the focusing lens, which significantly simplified the installation (the lens had to be removed for sample replacement and then re-aligned). The unfocused laser beam is of approximately elliptical shape with the major axis (vertical direction) of about $4.5\,mm$ and the minor axis (horizontal direction) of about $1\,mm$. When using the ILTD system, it is periodically necessary to compensate for changes in the gas-phase target density as there is slow depletion of the sample with time and consequently the amount of desorbed molecules. When the signal gets too low, the desorption laser is moved using a $3D$ movement system so that a new portion of the condensed sample can be heated. The absolute intensity of the mass spectrum signal is thus not stable over time, and rate at which it drops naturally increases when working with high desorption laser powers and higher experimental target densities. This can be tackled by normalising of the signal either by the total ion yield or by the yield of a specific parent/fragment ion. It should be noted that each separate preparation of the foil and sample leads to a slightly different desorption laser power threshold for ion detection. Therefore, we consider that the *desorption laser*

power above the ion detection threshold is generally a more useful parameter than absolute values of the desorption laser power if we want to compare experiments in this thesis that were carried out with different ILTD samples. The desorption laser power is determined based on a calibration curve of the laser power supply current against the output power measured using a UNO laser power meter (Gentec-EO).

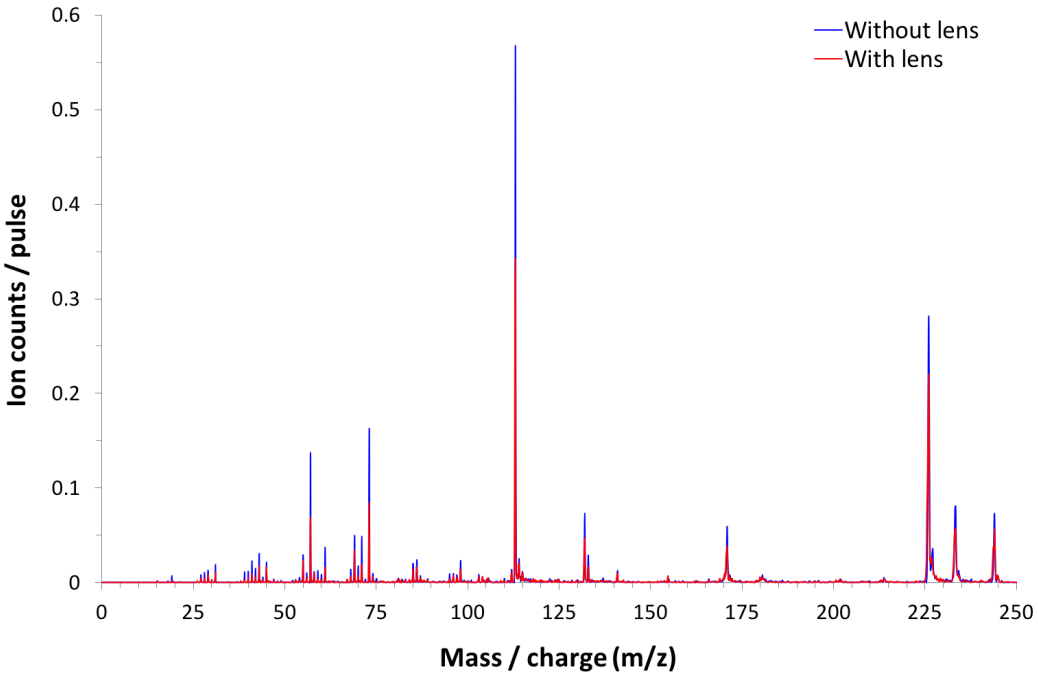

Fig. 3.7: $265\,nm$ (average UV laser fluence $6 \times 10^6\,W\,cm^{-2}$) MPI spectrum of uridine with and without lens between the desorption laser and the viewport ($445\,nm$ desorption laser power $0.03\,W$ above the ion detection threshold of $0.46\,W$).

3.2.4 The UV laser in the Molecular Clusters Laboratory at the OU

In the *Compact MPI/EII experimental set-up*, UV laser beam pulses (width $7\,ns$, repetition rate $10\,Hz$) are generated by a Sirah Cobra-Stretch dye laser which is pumped by the third harmonic output ($355\,nm$) of an Nd:YAG laser (Continuum Powerlight *II* 8000). A schematic diagram of the Nd:YAG/dye laser system in the Molecular Clusters Laboratory at the OU is shown in Fig. 3.8. Higher efficiency of the dye laser is achieved by distributing the incoming pump energy of the Nd:YAG laser between resonator, pre-amplifier and amplifier modules. A difraction grating with a groove density of $1800\,lines/mm$ allows us to select wavelengths with resolution better than $10^{-3}\,nm$. The fundamental dye laser radiation (see orange line in Fig. 3.8) is frequency-doubled using a Frequency Conversion Unit (FCU) consisting of a non-linear crystal (second harmonic generation – SHG, barium borate – BBO), a compensator and four Pellin-Broca prisms. The SHG crystal doubles the frequency of the fundamental dye laser beam pulses and the compensator

compensates for refraction by the SHG crystal. The arrangement of the four Pellin-Broca prisms separates the generated frequency-doubled (UV) beam pulses (see blue line in Fig. 3.8) from the fundamental dye laser beam pulses and changes the direction of their propagation so that it matches the initial direction of the fundamental dye laser beam pulses. The wavelength selection is achieved by positioning the first prism such that the fundamental dye laser beam pulses are guided onto a ceramic dump and the frequency-doubled beam pulses pass close to the dump. The three remaining Pellin-Broca prisms compensate the angle and the linear shift of the frequency-doubled beam pulses as indicated in Fig. 3.8.

Coumarin laser dyes, i.e. Coumarin 450, 480, 503 and 540*A*, allow us to effectively operate in the $220 - 277\,nm$ frequency-doubled wavelength range. After being pumped by the $355\,nm$ Nd:YAG laser pulses, each dye produces fundamental dye laser pulses across a specific wavelength range and then a single wavelength is selected by tuning the angle of the grating. After changing the wavelength, the SHG crystal's angle has to be also tuned in order to maintain phase matching inside of the SHG crystal and enable frequency-doubling. It should be noted that turning of the SHG crystal and compensator is synchronised by the same control system. For brevity, we will further refer to the SHG crystal-compensator system's angle as SHG crystal's angle [122].

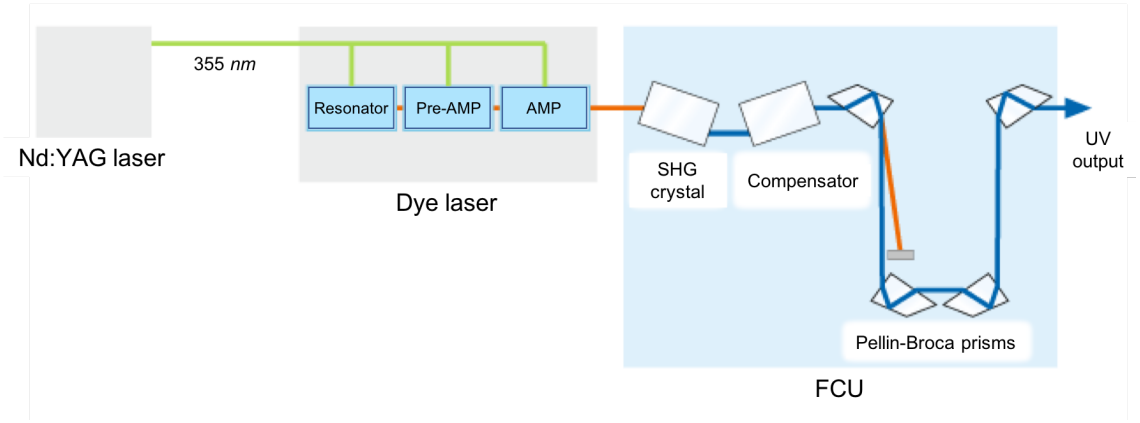

Fig. 3.8: Schematic of the Nd:YAG/dye laser system in the Molecular Clusters Laboratory at the OU (adapted from [123]).

Adjustment of the output laser pulse energy can be achieved in one of the two following ways:

1. by changing the delay between the pulses triggering xenon flashlamps and Q-switch of the Nd:YAG laser,

2. by adjusting SHG crystal's angle (see Fig. 3.11 a)).

A shield for the Nd:YAG and UV laser beam path was designed, built and installed with the help from A. Jones from the Research Design and Engineering Facility at the OU.

3.2.4.1 Characterisation of UV laser performance in the Molecular Clusters Laboratory at the OU

Systematic study of changes in fragment ion production as a function of the MPI wavelength is an important tool of the Molecular Clusters Group as it can provide evidence for critical processes happening in electronically excited biomolecules [18, 115]. UV laser performance was carefully studied due to an initial observation of an increase of UV laser pulse energy fluctuations with increasing wavelength (relative standard deviation of UV laser pulse energy increasing from around $15-20\%$ at $225\,nm$ to about $40-50\%$ at $265\,nm$). In addition, higher laser energy fluctuations were observed at wavelengths closer to the edge of the wavelength range of a particular Coumarin laser dye compared to the middle of the range. An example for the frequency-doubled wavelength range $252-262\,nm$ of Coumarin 503 laser dye is shown in Fig. 3.9.

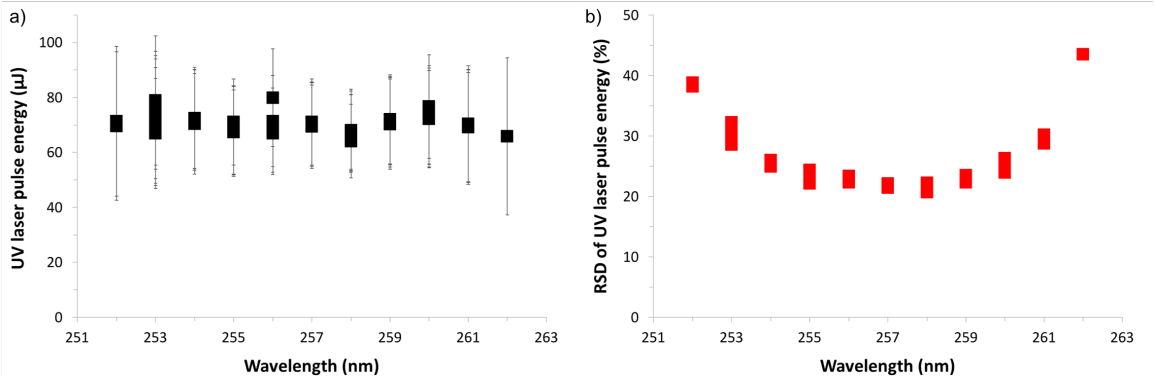

Fig. 3.9: a) Average UV laser pulse energies with standard deviations (SD) and b) relative standard deviations (RSD) of UV laser pulse energy as a function of wavelength in the $252-262\,nm$ wavelength range of the Coumarin 503 laser dye after frequency-doubling.

The effect of laser energy fluctuations on signal intensity was tested in MPI experiments on 3-aminophenol (3-AP, $m/z\,109$) at $225\,nm$. The laser pulse energy fluctuations were manipulated by varying the delay between the pulses triggering xenon flashlamps and Q-switch of the Nd:YAG laser in the range between 511 and $526\,\mu s$ (for more details on the effect of the delay between the pulses triggering xenon flashlamps and Q-switch of the Nd:YAG laser on laser energy fluctuations see Fig. 3.13). The ion yield of the 3-AP^+ isotope ($m/z\,110$) is plotted as a function of *RSD* of UV laser pulse energy in Fig. 3.10. The isotope ion peak was used instead of the parent ion peak ($m/z\,109$) in order to avoid saturation effects due to exceptionally strong MPI signals from 3-AP. The plot shows a substantial increase in the signal intensity with increasing fluctuations of the UV laser pulse energies around their average value during a measurement (see Fig. 3.10). This is due to the fact that the dependence of ion production on pulse energy is non-linear in most multi-photon ionisation conditions (see Eq. 2.18). This indicates that

improving the UV laser pulse energy stability is important for MPI experiments. The following steps were taken to isolate which part of the Nd:YAG/dye laser system is the main source of instabilities and hence to find a method to control the level of laser pulse energy fluctuations.

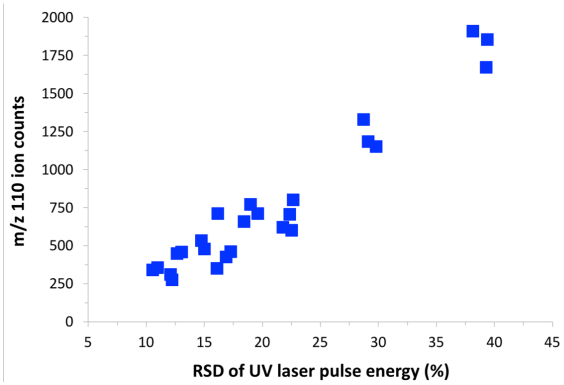

Fig. 3.10: a) Increase in the intensity of isotope peak of 3-aminophenol ($m/z\,110$) with increasing relative standard deviation (RSD) of UV laser pulse energy in the MPI molecular beam experiments on 3-aminophenol ($237\,nm$, average UV laser fluence $4 \times 10^6\,W\,cm^{-2}$, average sample temperature $112\,°C$, pressure of He $0.5\,bar$).

First, the stability of laser pulse energy was investigated at several different positions of the laser beam path:

1. output of Nd:YAG laser beam before entering the dye laser ($355\,nm$) – RSD of laser pulse energy about 7%,
2. dye laser beam before reaching the FCU ($450\,nm$) – RSD of laser pulse energy about 26%,
3. dye laser beam after passing through the FCU ($225\,nm$) – RSD of laser pulse energy about 32%.

These results could be viewed as implying that the main source of the laser instability is within the dye laser. Thus, the next steps were aimed at identifying possible reasons of laser pulse energy fluctuations related to the dye laser:

- change of the filters in dye reservoirs,
- tweaking of the dye concentrations in the dye circulator systems,
- cleaning of Pellin-Broca prisms of the FCU,
- testing the effect of the SHG crystal's angle on laser pulse energy fluctuations.

None of these improved the stability of the UV laser pulse energy. In particular, Fig. 3.11 shows that the laser pulse energy fluctuations were independent of the SHG crystal's angle.

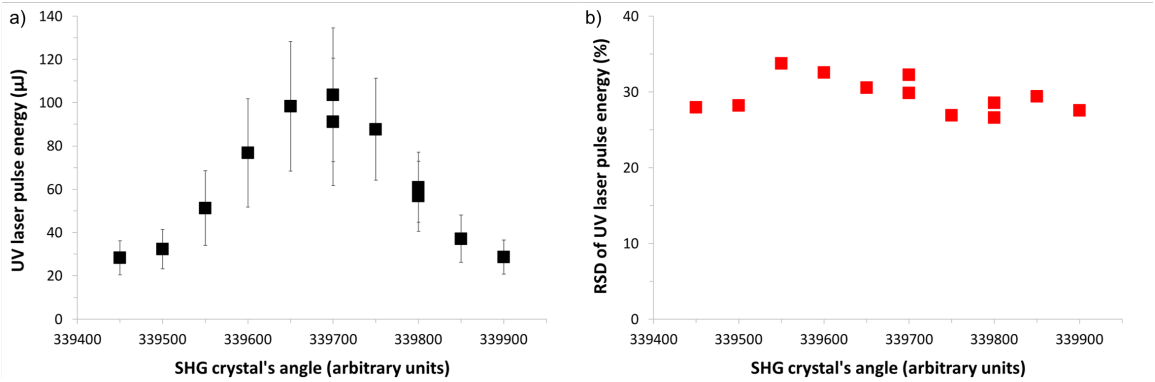

Fig. 3.11: a) UV ($225\,nm$) laser pulse energy dependence as a function of FCU crystal angle and b) relative standard deviation (*RSD*) of laser pulse energy as a function of SHG crystal's angle (arbitrary units quoted directly from the laser control software interface).

As laser pulse energy fluctuations seemed to be unaffected by the changes that we made in the dye laser, we investigated whether changing some of the settings of the Nd:YAG laser will have any effect on the stability of the UV pulse energy. The following tests were carried out:

1. Laser pulse energy fluctuations were tested as a function of time taken between the adjustment of the delay between the pulses triggering xenon flashlamps and Q-switch of the Nd:YAG laser (see Fig. 3.12) and start of a measurement. An approximate 5% decrease in the *RSD* of laser pulse energy was observed $20\,min$ after the adjustment of the delay between the pulses triggering xenon flashlamps and Q-switch of the Nd:YAG laser.

2. The effect of the delay between the pulses triggering xenon flashlamps and Q-switch of the Nd:YAG laser on UV laser pulse energy fluctuations was assessed (see Fig. 3.13). The biggest improvement of laser beam pulse stability was observed between 510 to $516\,\mu s$. The *RSD* of laser pulse energy was about 6-times lower at $516\,\mu s$ compared to $510\,\mu s$. Further increase of the delay time did not result in another significant improvement.

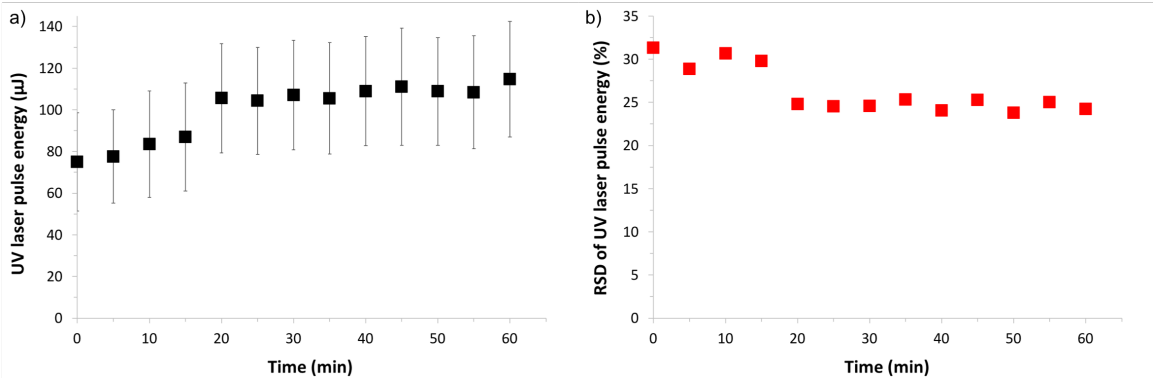

Fig. 3.12: a) Average UV (225 *nm*) laser pulse energies with standard deviations (SD) and b) relative standard deviation (RSD) of UV laser pulse energy as a function of time between the adjustment of the delay between the pulses triggering xenon flashlamps and Q-switch of the Nd:YAG laser and start of a measurement.

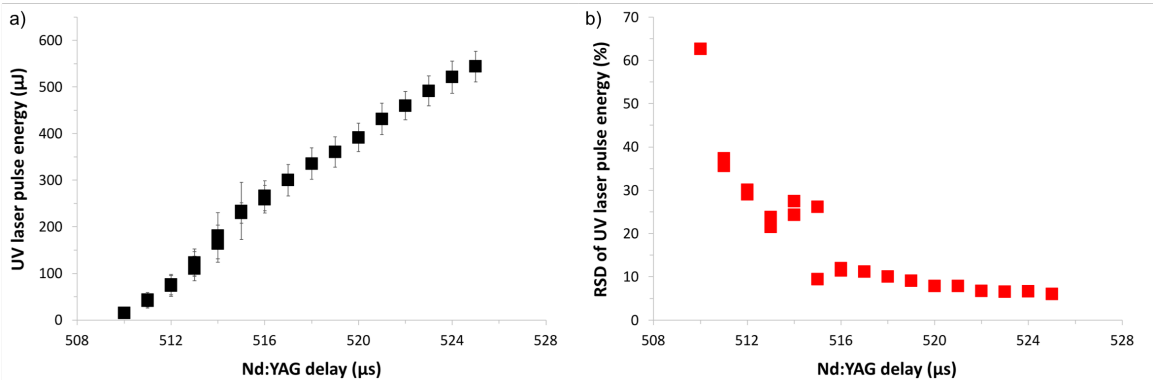

Fig. 3.13: a) Average UV (225 *nm*) laser pulse energies with standard deviations (SD) and b) relative standard deviation (RSD) of UV laser pulse energy as a function Nd:YAG delay (delay between the pulses triggering xenon flashlamps and Q-switch of the Nd:YAG laser).

The above-mentioned tests on laser pulse energy stability helped to optimise the Nd:YAG/dye laser system for the MPI experiments presented later in this PhD thesis. The new way of operating the Nd:YAG/dye laser system in the Molecular Clusters Laboratory is based on tuning the laser pulse energy fluctuations by varying the delay between the pulses triggering xenon flashlamps and Q-switch of the Nd:YAG laser and then adjusting the laser power to the desired level using the SHG crystal's angle.

3.3 Identification of metastable dissociations using reflectron TOF-MS in combination with a Matlab simulation

Various techniques are available to study the metastable dissociation of excited ions, including the post-source decay mode of matrix-assisted laser desorption/ionisation (MALDI) mass spectrometry [124], double-focusing sector-field mass spectrometry [125, 126], and modified linear time-of-flight (TOF) mass spectrometry [126, 127]. Reflectron TOF mass spectrometry is also a long-established tool for analysing metastable dissociation channels [128, 129]. This section describes the specific method that I have applied to study the metastable dissociation of excited molecular ions using the OU MPI-TOF system. Ion detection using the reflectron mass spectrometer is *mapped* against flight-time and reflection voltage (see Fig. 3.14 b)). Microsecond-timescale dissociations are recognisable on the resultant image as a series of extended curves, which are then identified using a simulation developed in Matlab (see Section 3.3.2).

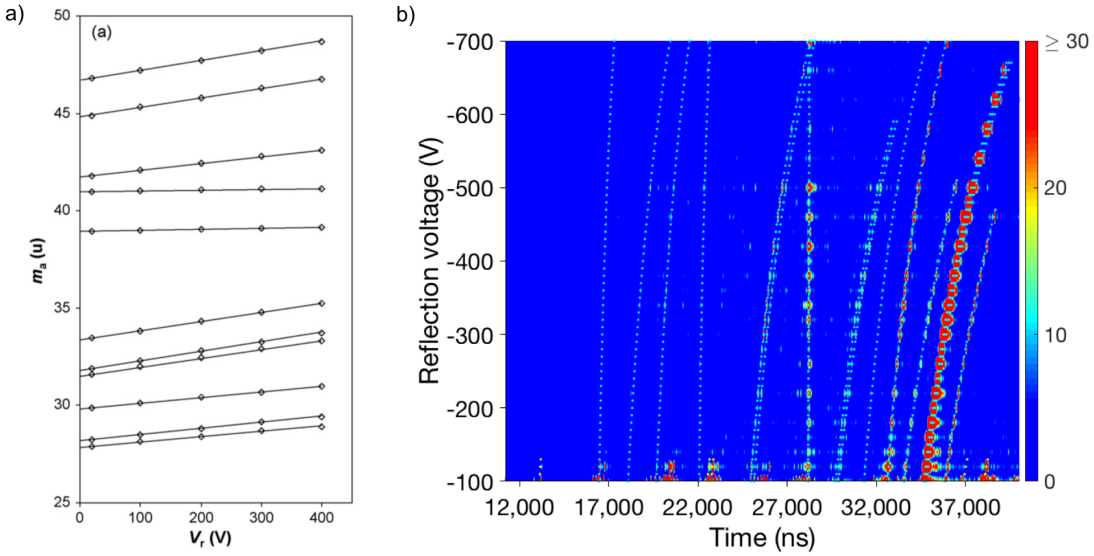

Fig. 3.14: a) To the best of our knowledge, the most complex *metastable dissociation map* presented in the literature (the apparent masses of the *metastable peaks* in calibrated mass spectra from ionised polyethylene oxide plotted against the reflector potential) [128] and b) a superposition of a *metastable dissociation map* of multi-photon ionised ($225\,nm$, average UV laser fluence $7\times10^{6}\,W\,cm^{-2}$, $445\,nm$ desorption laser power up to $0.24\,W$ above the ion detection threshold of $0.40\,W$) guanine recorded in the Molecular Clusters Laboratory at the OU and a *map* produced using the new Matlab simulation (cyan dots for fragment ions resulting from metastable dissociation and yellow dots for some of the *prompt* fragment ions i.e. those produced less than $100\,ns$ after ionisation).

To our knowledge, the earliest paper presenting plots of ion flight-time (or a related

parameter such as the *apparent mass* of a *metastable peak* in a conventional calibrated mass spectrum) against reflection voltage to aid assignments was Gilmore and Seah's [130] study of the metastable decay of polytetrafluoroethylene (PTFE) by static secondary-ion mass spectrometry (SIMS). Their *2D decay maps* were constructed by plotting the reciprocal of the time difference between postulated *precursor* and product flight-times against five different reflection voltages. Shard and Gilmore [128] subsequently applied the method to identify metastable dissociations of three further ionised polymers. L'Hermite and co-workers' version [131] of the approach (evidently developed independently and then published a short time after Gilmore and Seah's paper [130]) involved plotting the flight-time against the reciprocal of the reflection voltage and was used in their studies of the fragmentation of clusters containing Ag, H_2O, and SF_6 [131], and silver bromide clusters [132]. A variant of the concept was also applied by Ponciano et al. [133] to produce *2D ion dynamics plots* of $(LiF)_nLi^{+*}$ clusters produced by ^{252}Cf-plasma desorption. Former PhD students in the Molecular Clusters Group at the Open University, M. Ryszka and R. Pandey, studied metastable dissociation of multi-photon ionised uracil and thymine by constructing *maps* of ion flight-time against reflection voltage. Each molecule revealed a single strong metastable dissociation channel [115]. In Fig. 3.14 we can see a comparison between, to the best of our knowledge, the most complex *map* of metastable dissociations presented previously in the literature (11 metastable channels) and a *map* recorded in our laboratory (14 metastable channels, while the most complex *map* in this thesis features 18 (see Fig. 4.5)). One advantage of the present variant of the approach is that the plot communicates to the reader the intensities of different metastable bands compared with each other and with the background noise levels.

3.3.1 Principles of measurements of metastable dissociation using reflectron TOF-MS

Figs. 3.15 and 3.16 show a scheme of our reflectron time-of-flight mass spectrometer (TOF-MS). Most of the fragment ions are produced shortly (less than $100\,ns$) after ionisation, in which case we talk about *prompt* dissociations. Prompt dissociations happen in the extraction region (between the backplate and the extraction electrode) of the reflectron MS (see Fig. 3.15). Any given prompt dissociation product ion produces signals within a single peak in the time-of-flight spectrum and the fragment ion mass can be determined from a simple calibration of the TOF spectrum based on $\sqrt{m} = a \times t + b$, where m is the mass of the fragment ion, t is its time-of-flight, and a and b are constants. In addition to prompt dissociations, the reflectron TOF-MS enables us to study metastable dissociations (delayed dissociations introduced in Section 2.6) by varying the voltage on the reflectron

reflect electrode (reflection voltage, see Fig. 3.16).

If the delayed dissociation happens between the extraction electrode and the first FFR electrode, it will result in a broad distribution of flight-times around the flight-time of the prompt fragment ion with the same mass as the ion produced by the delayed fragmentation. This will be manifested in the calibrated mass spectrum as a tail feature associated with the corresponding prompt fragment ion peak. If the delayed metastable dissociation happens at any point during the first journey in the FFR, it will result in a single flight-time, and thus can normally be spotted in a calibrated mass spectrum as a peak at non-integer m/z value. This is because flight-time-to-mass calibration relies on ions having the same mass throughout their journeys through the MS, which is not the case for metastable dissociation. However, some of the peaks resulting from metastable dissociation can coincidentally appear in the mass spectrum at or very close to integer or half-integer *mass / charge* (m/z) values, and thus could be falsely assigned to prompt peaks or doubly-charged ions, respectively. This can be resolved by varying reflection voltage of the reflectron MS, which will cause a *metastable peak* to shift to a different (but still not meaningful) m/z value in the calibrated mass spectrum.

Maps constructed by a systematic study of time-of-flight spectra as a function of reflection voltage contain a lot of information about ion dynamics in the reflectron time-of-flight mass spectrometer. For an example of such a *map* see Fig. 3.14 b). The schematic in Fig. 3.15 shows how the *parent ion's* flight path (and consequently flight-time) changes with the reflection voltage. Here, we define the parent ion as an ion with the same mass as the neutral target (e.g. guanine$^+$ in the example in Fig. 3.14 b)) prior to multi-photon ionisation. The parent ion is abbreviated here as *Pa*. The experimental concept behind the metastable dissociation measurements can be explained with reference to this figure as follows:

- Consider V_{Pa} to be the voltage at the point in the extraction region where ionisation happens. The ion is accelerated to the field-free region (FFR) where it travels at constant velocity (v_{Pa}) and then is decelerated in the reflectron part of the mass spectrometer (between the second FFR electrode and reflectron reflect electrode). The difference between the absolute values of the FFR voltage (V_4 in Fig. 3.15) and the voltage at the point in space where the ionisation takes place (V_{Pa} in Fig. 3.15), determines the parent ion's kinetic energy immediately prior to entering the reflectron optics (at the second FFR electrode). The parent ion's kinetic energy (and thus velocity) drops to $0\,eV$ ($0\,ms^{-1}$) at the point in space after the second FFR electrode which has voltage V_{Pa}. A fragment ion which is a result of prompt

fragmentation of the parent ion will have slightly different kinetic energy than the parent ion due to dissociative kinetic energy release (typically up to several eV for single ion production by MPI [134]). Depending on the relation between the reflection voltage V_6 and the voltage V_{Pa}, we can differentiate between the following scenarios:

a) If $\mid V_6 \mid < \mid V_{Pa} \mid$: the position where the parent ions' velocity drops to $0 ms^{-1}$ will be inside of the reflectron region of the MS (see Fig. 3.15 a)), which means the ion will accelerate back to the FFR and reach the detector, i.e. we will see the corresponding peak in the mass spectrum.

b) If $\mid V_6 \mid = \mid V_{Pa} \mid$: the position where the parent ion's velocity drops to $0 ms^{-1}$ will be at the reflectron reflect electrode (see Fig. 3.15 b)), which means the parent ion will hit the electrode and will not reach the detector, i.e. we will not observe the parent ion peak in the mass spectrum. The reflection voltage at which the parent ion signal cuts-off can be determined by varying the reflection voltage from $0 V$ to more negative values until the parent ion signal disappears. The cut-off voltage of a parent ion (V_{Pa}) enables us to determine the distance z_i from the backplate (always grounded, $V_1 = 0 V$) where the laser beam crosses the molecular beam using the following equation:

$$z_i = d_1(V_{Pa}/V_2) \tag{3.1}$$

where d_1 is the distance between the backplate and the extraction electrode and V_2 is the extraction electrode voltage. This equation assumes uniform field between the backplate and the extraction electrode along the central axis of the mass spectrometer, which was confirmed by QuickField simulations reported in the PhD thesis of former student in the Molecular Clusters Group, R. Pandey [58]. The cut-off voltage of the fragment ions resulting from prompt fragmentation is slightly more negative than the parent ion's cut-off voltage as kinetic energy release during the dissociation process results in some of the prompt fragment ions being reflected back to the detector. By varying the reflection voltage to more negative values than the cut-off voltage of parent ions V_{Pa}, we will reach the voltage V_{FrP} where the signal of the fragment FrP resulting from a prompt fragmentation of the parent ion cuts-off. The difference between V_{FrP} and V_{Pa} then gives us information about the kinetic energy release in the direction of extraction field. However, our experimental conditions with the mass spectrometer voltages fluctuating by $\pm 1 V$, do not enable us to use this direct route for determination of kinetic energy release

[58].

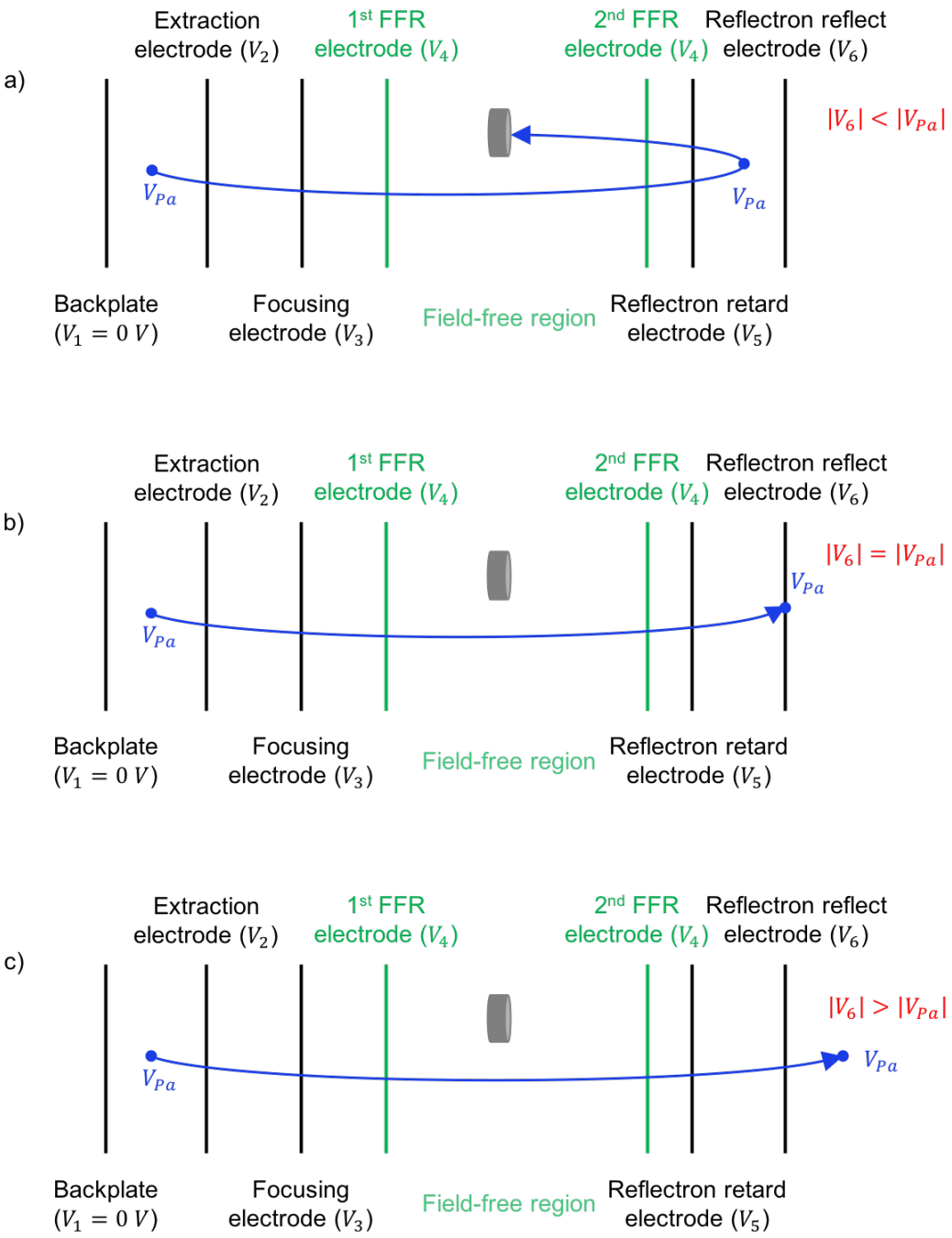

Fig. 3.15: Scheme of the reflectron TOF-MS with different settings of reflection voltage V_6 with respect to the cut-off voltage V_{Pa} of parent ion *Pa*. a) Parent ion *Pa* is reflected back to the detector; b) V_6 corresponds to the parent ion's cut-off voltage V_{Pa}, i.e. the *Pa* signal cuts-off; c) V_6 is even more negative than in b) so again no *Pa* signal is detected.

c) If $|V_6| > |V_{Pa}|$: the position where the parent ion's velocity drops to $0\,ms^{-1}$ will be outside of the reflectron region of the MS (see Fig. 3.15 c)). This means the ion will not be reflected back to the detector, i.e. we will not observe the parent ion peak in the mass spectrum.

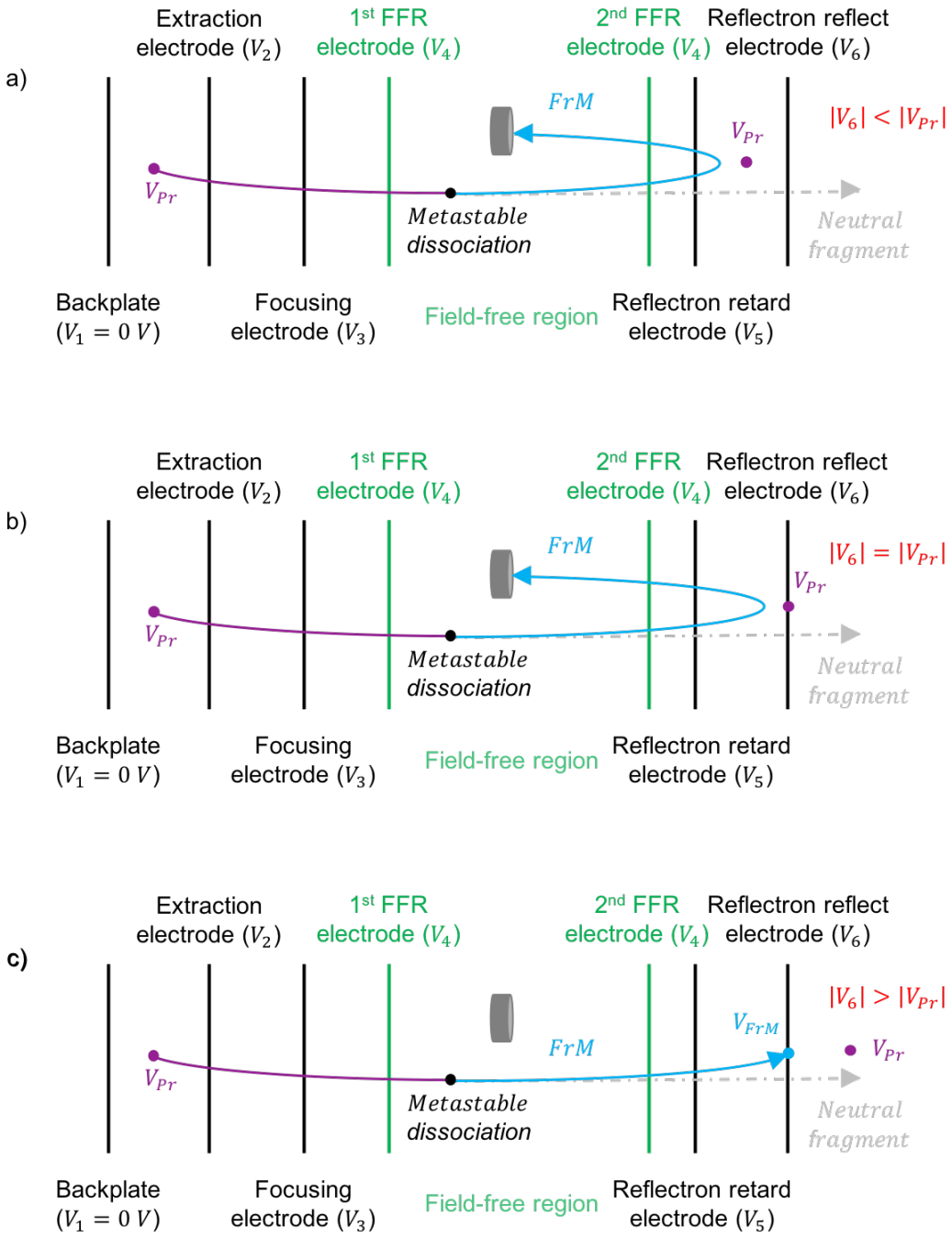

Fig. 3.16: Scheme of the reflectron TOF-MS with different settings of reflection voltage V_6 with respect to the cut-off voltage V_{Pr} of the precursor ion Pr. a) Fragment ion FrM resulting from metastable dissociation of the precursor ion Pr is reflected back to the detector at a more negative voltage than V_{Pr} (the voltage corresponding to the voltage in space where Pr is formed); b) V_6 corresponds to the precursor ion's cut-off voltage V_{Pr}, FrM is still detected; c) V_6 is more negative than V_{Pr} and corresponds to the FrM's cut-off voltage V_{FrM} and the FrM signal cuts-off.

- Now consider FrM to be a fragment ion produced by metastable dissociation of its precursor ion Pr (this could possibly the parent ion but it could alternatively be a fragment ion produced in the extraction region) during its first journey through the

FFR. The FrM will have the same velocity during the first journey in the FFR as its precursor ion Pr ($v_{FrM} = v_{Pr}$), but will have lower kinetic energy KE due to its lower mass ($m_{FrM} < m_{Pr}$, and thus $KE_{FrM} < KE_{Pr}$). To within the sensitivity limit placed on the experiment by the $\pm 1V$ fluctuations of MS voltages, the KE of the precursor ion (Pr) in the FFR is the same as that of the parent ion (Pa) or a prompt fragment ion (FrP). Hence the respective cut-off voltages are also equal: $V_{Pr} = V_{Pa} = V_{FrP}$. The flight-time and path length of the fragment ion produced by metastable dissociation FrM will vary with the reflection voltage as follows:

a) If $\mid V_6 \mid < \mid V_{Pr} \mid$: as the kinetic energy of the FrM in the FFR is lower than that of its precursor ion Pr, the FrM can be reflected by a weaker field and thus will spend shorter time in the reflectron part of the MS (see Fig. 3.16 a)), i.e. its flight-time will be shorter than the precursor ion's flight-time would have been if the metastable fragmentation had not taken place. In contrast, the flight-time of the fragment ion produced by metastable dissociation FrM will be longer than the flight-time of the equivalent fragment ion resulting from prompt fragmentation, FrP. To a rough approximation, the *metastable peak* appears half way between the precursor ion mass (m_{Pr}) and the fragment ion mass (m_{FrM}) in a calibrated mass spectrum.

b) If $\mid V_6 \mid = \mid V_{Pr} \mid$: as the kinetic energy of the fragment ion resulting from metastable dissociation FrM in the FFR is lower than the kinetic energy of its precursor ion, the FrM can be reflected by a weaker field and will reach the detector (see Fig. 3.16 b)). Parent ions and prompt fragment ions will be cut-off in this case (see Figs. 3.15 b) and 3.16 b)). The FrM will penetrate deeper in the reflectron than in a) and thus will have a longer flight-time than in a).

c) If $\mid V_6 \mid > \mid V_{Pr} \mid$: if we keep increasing the magnitude of the reflection voltage $\mid V_6 \mid$, we will eventually reach V_{FrM} where the FrM signal cuts-off (see Fig. 3.16 c)). We can measure V_{Pa} (which is equal to V_{Pr}) and we know the FFR voltage (V_4) so we can determine the kinetic energy KE_{Pr} of the precursor ion in eV in the FFR as $\mid V_4 \mid - \mid V_{Pa} \mid$. Analogously, the kinetic energy KE_{FrM} in eV in the FFR can be determined as $\mid V_4 \mid - \mid V_{FrM} \mid$. As the velocities of the precursor ion Pr and the fragment ion produced by metastable dissociation in the FFR FrM are the same, we can work out the ratio of their masses as follows:

$$\frac{E_{K_{FrM}}}{E_{K_{Pr}}} = \frac{m_{FrM}}{m_{Pr}} = \frac{\mid V_4 \mid - \mid V_{FrM} \mid}{\mid V_4 \mid - \mid V_{Pa} \mid} \tag{3.2}$$

Equation 3.2 enables us to work out m_{FrM}/m_{Pr} using parameters that we know

(V_4) or can directly measure (V_{FrM} and V_{Pa}). However, of course this ratio on its own is not enough to work out m_{FrM} and m_{Pr}. We can narrow down the candidate masses using the rough approximation that the *metastable peak* will appear half way between m_{FrM} and m_{Pr} in a calibrated mass spectrum but this is not sufficient for precise identification of a metastable dissociation channel.

3.3.2 Analysis of metastable dissociation data using the new Matlab simulation

Previously, the Molecular Clusters Group based the assignments of metastable dissociation channels on measuring cut-off reflection voltages (linked to kinetic energy in the field-free region) and flight-times with the reflection voltage close to ground [57, 58, 115]. Based on the voltages and dimensions of the mass spectrometer electrodes, a TOF calculator (in Microsoft Excel) developed by M. Ryszka calculates the expected difference between arrival time of the investigated ion and a reference ion (usually a parent ion) and compares it with the equivalent value obtained experimentally [57]. As the calculator worked out time differences, it only worked at reflection voltages close to ground (when the prompt ions are also visible). However, comparing the time difference at only one reflection voltage (or possibly at few voltages) close to ground, might not be sufficient to precisely determine the metastable dissociation pathways as several candidate dissociations can give close fits. This is a major problem especially when we can not use the cut-off voltage analysis as a complementary tool because of the cut-off voltage of fragment resulting from metastable dissociation being more negative than $-1200\,V$, which is the maximum voltage we can apply to the reflectron reflect electrode using our voltage divider unit. In addition, a very rich metastable dissociation pattern can cause overlaps of peaks of some of the fragments resulting from metastable and prompt dissociations, which would make it difficult to precisely pin down the experimental flight-times. In order to eliminate the above-mentioned drawbacks, a Matlab simulation for identification of metastable dissociations in the field-free region of reflectron time-of-flight mass spectrometer was developed. The programme is comprised of three main parts:

1. Visualisation of experimental data
   The programme constructs a contour plot by plotting mass spectra as a function of reflection voltage ($0\,V$ to $-1200\,V$).

2. Simulation of metastable dissociations
   The programme calculates the flight-times of candidate dissociations of ions iteratively at different reflection voltages (for more details see Figs. A.3 and A.4,

Appendix A.2) and generates a *map* of the calculated flight-times against reflection voltage.

3. Superposition of experimental and simulated *maps*
   This is key for the user to recognise the metastable dissociation that matches the experiment.

3.3.2.1 Visualisation of experimental data

Visualisation of the experimental data is a two-step process. The first step involves importing measured data into a matrix which is done by running Matlab script *"import_data.m"* shown in Fig. A.1, Appendix A.1. The input data have to be saved in a Microsoft Excel worksheet, where each row in the worksheet represents a non-calibrated time-of-flight mass spectrum (with the time-of-flight axis in time bins) at a different reflection voltage. The mass spectra have to be ordered with increasing magnitude of reflection voltage (i.e. from $0V$ to $-1200V$). The resultant matrix is then used as the input for the second script (*"contour_plot.m"*), which creates a contour plot of ion signals against flight-time and reflection voltage. The detailed description of individual commands of the second script is shown in Fig. A.2, Appendix A.2.

3.3.2.2 Simulation of metastable dissociations

The Matlab simulation of metastable dissociations calculates absolute values of flight-times for plausible candidate dissociations (precursor and fragment ions masses). These are estimated beforehand based on the cut-off reflection voltage analysis (see Eq. 3.2) and the position of the *metastable peak* in a calibrated mass spectrum. The script *"results.m"* shown in Figs. A.3 and A.4, Appendix A.2, creates a scatter plot of calculated flight-times at different reflection voltages for candidate dissociations. For each candidate dissociation, estimated mass of the precursor (*mass*2) and the fragment ion (*mass*3) needs to be specified as well as the reflection voltage range of the corresponding metastable band, which is defined by its cut-off voltage. If the cut-off voltage for a specific metastable dissociation exceeds the maximum voltage that we applied in the metastable dissociation measurements to the reflectron reflect electrode, we calculate and plot ion flight-times for such dissociation in the whole range of measured reflection voltages. The time-of-flight is calculated for each candidate dissociation at progressively more negative values of reflection voltage by calling Matlab script *"in_ffr_for_loop.m"* shown in Figs. A.5 to A.14, Appendix A.2.

The *"in_ffr_for_loop.m"* script contains a *"for loop"* for calculation of ions flight-times

at k different reflection voltages. k varies for each individual metastable channel and it is defined by its cut-off voltage/maximum voltage applied to the reflectron reflect electrode in the metastable dissociation measurements in the case the cut-off voltage exceeds the maximum voltage applied (for more details see the script in Figs. A.5 to A.14, Appendix A.2). The inputs for the flight-time calculations are distances within the mass spectrometer, the mass spectrometer electrodes voltages, and the crossing point of the laser beam with the neutral molecular target. The latter input is determined using the measured V_{Pa} and Eq. 3.1. The distances within the MS and the MS voltages define the electric field strengths between individual electrodes of the MS as follows:

$$E_j = (|V_{j+1}| - |V_j|)/d_j \tag{3.3}$$

where E_j is the magnitude of the electric field strength between j-th and $(j+1)$-th electrode in the direction of ion propagation, d_j is the distance between j-th and $(j+1)$-th electrode, and V_j and V_{j+1} are the voltages applied to j-th and $(j+1)$-th electrodes, respectively. $(j+1)$ defines the next electrode after the j-th one in the direction of ion propagation. The distances between the MS electrodes were obtained from Kore Technology and as they are a trade secret of the company we do not have a permission to publish their exact values (the total flight distance of the ions in the mass spectrometer is around $2\,m$). In our UV laser fluence conditions we have never observed any evidence of doubly or multiply charged ions and thus the charge of all investigated ions is set to 1 by default.

The *"in_ffr_for_loop.m"* script calculates the time ions spend between each pair of adjacent electrodes of the mass spectrometer (see Fig. 3.15) separately and the total flight-time is then obtained by summing the partial contributions. In the reflectron MS an ion is first accelerated from the position where it is formed towards the extraction electrode (corresponding time t_1), then between the extraction electrode and the focusing electrode (corresponding time t_2) and afterwards between the focusing electrode and the first FFR electrode (corresponding time t_3). The flight-time in each of these three sections is calculated as follows:

$$t_j = \frac{-v_{0j} + \sqrt{{v_{0j}}^2 + 2a_j d_j}}{a_j} \tag{3.4}$$

where t_j is the time an ion spends in the j-th section of the MS (i.e. between j-th and $(j+1)$-th electrode), v_{0j} and a_j are the initial velocity and the acceleration of the ion in the direction of ion propagation in the j-th section of the MS, respectively. The initial velocity in the j-th section (v_{0j}) is equal to the velocity after acceleration in the $(j-1)$-th

section (v_{j-1}) which can be calculated as follows:

$$v_{0j} = v_{j-1} = \sqrt{{v_{0(j-1)}}^2 + 2a_{j-1}d_{j-1}} \tag{3.5}$$

In the calculations, we neglect any contribution of velocities resulting from the initial kinetic energy of neutrals and from kinetic energy release during dissociation processes as they are much smaller than the kinetic energy that ions obtain when accelerating in the MS. The acceleration a_j can be calculated as follows:

$$a_j = \frac{E_j q}{m} \tag{3.6}$$

where q and m are the charge and the mass of the investigated ion.

In the FFR, the ion travels at constant velocity which is equal to the velocity v_3 just before passing through the first FFR electrode. The time the ion spends in the FFR will be then calculated as:

$$t_4 = \frac{d_4}{v_3} \tag{3.7}$$

where d_4 is the distance the ion travels during the first journey in the FFR. After leaving the FFR, the ion will decelerate in the reflectron part of the MS (i.e. a_5 and a_6 are negative). Time t_5 that it spends between the second FFR electrode and the reflectron retard electrode will be calculated analogously to Eq. 3.4. The ion will then stop between the reflectron retard electrode and reflectron reflect electrode at distance d_{PPR} from the reflectron retard electrode, where

$$d_{PPR} = -\frac{{v_5}^2}{2a_6} \tag{3.8}$$

v_5 is the velocity just before passing through the reflectron retard electrode and a_6 is the acceleration in the last part of the reflectron before the ion stops. The time the ion spends in the last part of the reflectron until it stops is then calculated as:

$$t_6 = -\frac{v_5}{a_6} \tag{3.9}$$

Afterwards, the ion is accelerated back towards the detector and the time it spends to accelerate between the position where it stopped and the second FFR electrode is equal to the time it took the ion to decelerate from the second FFR electrode until it stopped. When passing the FFR for the second time, the ion travels again at constant velocity until it reaches the FFR electrode in front of the detector (the corresponding time t_7 is calculated analogously to Eq. 3.7). The ion is then accelerated to the detector (the corresponding time t_8 is calculated analogously to Eq. 3.4) where it travels the additional distance inside

of the detector before it hits the active surface. The corresponding time t_{add} is calculated analogously to Eq. 3.7). Details of the calculations of ions flight-times in individual parts of the reflectron mass spectrometer along with the explanations are shown in Figs. A.5 to A.14, Appendix A.2.

If an ion has the same mass throughout its journey through the mass spectrometer (e.g. a prompt fragment ion or a parent ion) the time it spends in the reflectron MS is then calculated as follows (using the example of a parent ion, *Pa*):

$$\begin{aligned} t_{total}(Pa) = & t_1(Pa) + t_2(Pa) + t_3(Pa) + t_4(Pa) + 2t_5(Pa) + 2t_6(Pa) + t_7(Pa) + \\ & + t_8(Pa) + t_{add}(Pa) + t_{const} \end{aligned} \tag{3.10}$$

where t_{const} is the time constant that accounts for the time difference between the start pulse for the TDC card counting and the precise time of the laser pulse interaction with the molecular beam. If the precursor ion *Pr* dissociates during its first journey through the FFR forming the *FrM* (see Fig. 3.16 a) and b)) the corresponding time will be calculated as follows:

$$\begin{aligned} t_{total}(FrM) = & t_1(Pr) + t_2(Pr) + t_3(Pr) + t_4(FrM) + 2t_5(FrM) + 2t_6(FrM) + \\ & + t_7(FrM) + t_8(FrM) + t_{add}(FrM) + t_{const} \end{aligned} \tag{3.11}$$

3.3.2.3 Superposition of experimental and simulated *maps*

The experimental contour plot created by *"contour_plot.m"* (see Appendix A.1) and the simulated scatter plot created by *"results.m"* and *"in_ffr_for_loop.m"* (see Appendix A.2) are combined in a common plot using the script in Fig. A.15, Appendix A.3. Simulated candidate metastable dissociation bands are overlaid onto the experimental ones, and precursor and fragment ions masses are varied iteratively until a good match is achieved. The accuracy of the simulation is checked by calculating the flight-times of ions traced to prompt dissociations that can be identified unambiguously using a calibrated mass spectrum. For an example of such a superposition of experimental and simulated *maps* see Fig. 3.14 b), where yellow dots represent calculated flight-times for some of the prompt dissociations and cyan dots for metastable dissociations. A more thorough analysis of metastable dissociation data using the above-mentioned experimental approach in combination with the Matlab simulation is presented in the following chapter, where the metastable dissociation of excited 3-aminophenol ions is investigated.

3.4 Summary and outlook

This chapter provides a description of the *Compact MPI/EII experimental set-up* in the Molecular Clusters Laboratory at the Open University which allows multi-photon ionisation and electron impact ionisation experiments on gas-phase targets. The targets can be produced by either heating samples in a supersonic expansion nozzle which are then seeded in a supersonic beam of He or Ar carrier gas, or by desorbing them adjacent to the interaction region using an *indirect laser-induced thermal desorption* system. The results obtained using this experimental set-up are presented in Chapters 4, 5 and 6. The chapter also provides the description of the Molecular Clusters Group's technique for probing metastable dissociation of excited molecular ions and explains the newly developed Matlab simulation for the analysis of experimental metastable dissociation results.

3.5 Contributions by co-workers

The *Compact MPI/EII experimental set-up* in the Molecular Clusters Laboratory at the Open University was mainly built by B. Barć. The first indirect laser-induced thermal desorption systems were built by M. Ryszka, R. Pandey and T. da Fonseca Cunha. Metastable dissociation of excited molecular ions in the Molecular Clusters Laboratory was first employed by M. Ryzska and R. Pandey. I worked on the enhancement of the *third-generation* indirect laser-induced thermal desorption system, investigated and optimised the performance of the Nd:YAG/dye laser system and developed a Matlab simulation for the analysis of metastable dissociation data supported by Dr. S. Eden.

Chapter 4

Fragmentation pathways of excited 3-aminophenol ions

This chapter reports on multi-photon ionisation experiments on the biologically relevant molecule 3-aminophenol (3-AP, C_6H_7NO). Unusually high signal intensities revealed normally weak metastable dissociation channels. The existing reflectron mass spectrometry concept of *mapping* ion detection against flight-time and reflection voltage was applied to analyse these channels in detail. Comparisons with simulated ion flight-times using a program that I developed in Matlab led to the assignment of 18 different μs-timescale dissociations. This represents the most complex metastable dissociation pattern revealed to date using the reflectron *mapping* approach. The results included the rare observation of a double hydrogen loss channel from a fragment ion. Comparisons with Density Functional Theory (DFT) calculations by my collaborator provided further insights into the most prominent apparent fragmentation sequence: 3-AP$^+$ $(m/z\,109) \rightarrow HCO + C_5H_6N^+\,(m/z\,80) \rightarrow CNH + C_4H_5{}^+\,(m/z\,53) \rightarrow C_2H_2 + C_2H_3{}^+\,(m/z\,27)$.

4.1 Introduction

The dissociation processes of biomolecules, notably the subunits of DNA and proteins, have attracted considerable attention in recent years with the motivation of better understanding the nanoscale mechanisms by which ionising radiation can initiate damage in biological material [46, 109, 135, 136]. As discussed in Chapter 3, mass spectrometry studies of metastable ions are valuable to identify sequential fragmentation pathways because they simultaneously define ion mass before and after dissociation. Furthermore, metastable dissociation experiments have previously revealed distinct fragmentation patterns of different molecular isomers [137]. This is of considerable interest because biological function is often highly sensitive to molecular conformation. Metastable dis-

sociation experiments can also provide information on fragment ion energetics, as the microsecond-order time delay implies that the vibrational energy of the precursor ion was very close to the relevant dissociation barrier [116]. Such studies are particularly prevalent in research into the structure and stabilities of molecular clusters [138–143]. This chapter demonstrates the capability of a reflectron mass spectrometry experiment at the Open University (OU) to probe complex metastable fragmentation patterns. The *mapping* technique for analysing metastable dissociation channels is described in Section 3.3 and the Matlab program to assign the specific metastable dissociations is provided in Appendix A. The subject of this study is multiphoton ionised 3-aminophenol (3-AP) and the data interpretations are enhanced by comparisons with DFT calculations by Dr. J.-C. Poully. Comparing complementary metastable dissociation experiments on 3-AP at $225\,nm$ and at $270\,nm$ enabled the identification of an extra fragmentation channel. In addition, the comparison revealed a dramatic change in relative intensities of the metastable dissociations, suggesting that further studies of the wavelength dependence of metastable channels in MPI experiments on 3-AP may offer insights into the molecule's excited state dynamics.

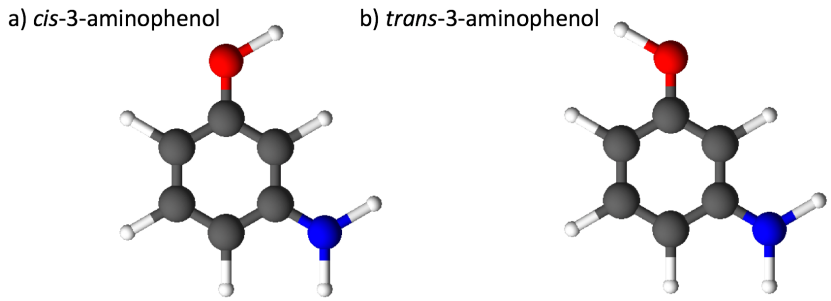

Fig. 4.1: Chemical structure of a) *cis*- and b) *trans*- conformers of 3-aminophenol (C atoms are coloured in grey, O in red, N in blue and H in white). The structure was drawn using ACD/Labs software.

Although aminophenol (C_6H_7NO, $m/z\,109$) shares the same phenol group as the amino acid tyrosine and it is also closely related to the neurotransmitter dopamine [144], the experimental and theoretical work in the literature on the electronic states, ionic states, and fragmentation of 3-aminophenol is extremely sparse. Shinozaki et al. [144] performed resonance-enhanced multi-photon ionisation (REMPI) experiments on 3-AP in the photon energy range $4.2 - 4.6\,eV$, as well as laser-induced fluorescence (LIF) measurements and quantum chemical calculations to support their assignments of vibronic structure. More recently, Yatsyna et al. [145] have performed infrared action spectroscopy measurements on the full set of aminophenol isomers: 2-AP (*cis*- and *trans*-), 3-AP (*cis*- and *trans*-), and 4-AP.

To our knowledge, only two mass spectrometry studies of 3-AP have been reported before the present work. The first is an electron impact ionisation (EII) measurement reported by the Japanese National Institute of Advanced Industrial Science and Technology (AIST) in the Spectral Database for Organic Compounds (SDBS) [146] (later reproduced by the National Institute of Standards and Technology - NIST [147]). The second was a set of $220\,nm$ MPI experiments that I performed in the Molecular Clusters Laboratory at the OU working with PhD student R. Pandey and T. da Fonseca Cunha. These preliminary measurements were included in R. Pandey's PhD thesis [58] and their main purpose was to test the *second generation of thermal desorption system at the OU* - indirect laser-induced thermal desorption (see Section 3.2.3.2). A single metastable dissociation channel was observed and assigned to a dissociation of $m/z\,80$ fragment ions ($C_5H_6N^+$ or $C_5H_4O^+$) to form $m/z\,52$ ions ($C_4H_4{}^+$). To our knowledge, no other assignments have been proposed for 3-AP's fragment ions (whether produced promptly or some time after ionisation) prior to the present work.

3-AP exists in approximately equal populations of $cis-$ and $trans-$ conformers (see Fig. 4.1) in the gas-phase [144] and Shinozaki et al.'s REMPI assignments enabled Küpper, Meijer and co-workers to demonstrate the complete separation of these conformers in Stark-deflected pulsed supersonic beams [148]. Such beams are suitable for diverse action spectroscopy experiments but are much less applicable to studies of collision-induced processes with relatively low cross sections. We are currently investigating electron impact and UV-induced processes in Stark-deflected continuous (CW) beams at the OU and 3-AP has proved to be quite readily manipulated [58]. Hence, the present study of 3-AP in a beam without any deflection provides a valuable starting point for our efforts to explore conformer-dependence in the dissociative ionisation pathways of biomolecules.

4.2 Experimental details

The *Compact MPI/EII experimental set-up* has been described in Chapter 3 as well as in previous publications [18, 26, 114–116]. The experiments probing metastable dissociation involved measuring MPI-TOF spectra of 3-AP at more than one hundred different reflection voltages. *Maps* comprising all the TOF spectra against reflection voltage (with ion flight-time on the x-axis, reflection voltage on the y-axis, and signal intensity colour-coded – see section 3.3) were then compared with simulated flight-times (see section 3.3.2), enabling specific metastable dissociations to be identified. In the experiments in this chapter, helium carrier gas ($0.5\,bar$) was seeded with sublimated 3-AP (Sigma-Aldrich with stated purity 98 %) within the supersonic expansion nozzle. The 3-AP sublimation temperature in the

experiments presented in this chapter (with the exception of Fig. 4.2 and 4.4 a)) was $112 \pm 1\,^{\circ}C$. This is lower than $150\,^{\circ}C$ used in the EII measurement in the AIST database [146] but higher than $80 - 100\,^{\circ}C$ used in the previous action spectroscopy experiments [144, 145]. MPI mass spectra were compared in the sublimation temperature range $60 - 113\,^{\circ}C$. No changes in the relative peak heights were observed that could indicate thermally-driven decomposition, changes in tautomeric populations, or reactivity. Fig. 4.2 shows a comparison of two MPI mass spectra of 3-AP at temperatures $102\,^{\circ}C$ and $111\,^{\circ}C$. A large number of mass spectra at these temperatures enabled a comparison with good statistics despite the relatively weak detection of fragment ions. Similarly, any clustering in the expansion would be expected to depend strongly on the vapour pressure of 3-AP in the nozzle so the fact that the relative peak heights did not change as a function of sublimation temperature suggests that the detected ions did not come from clusters. Background ion signals due to residual gas in the chamber were negligible.

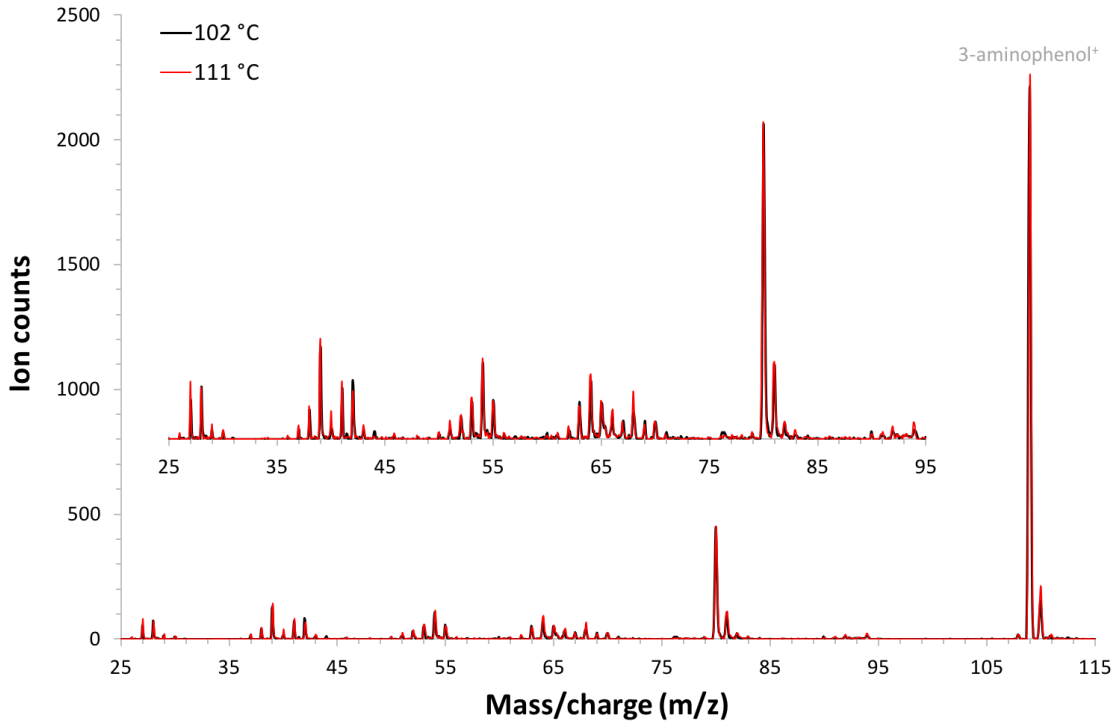

Fig. 4.2: Comparison of MPI mass spectra of 3-AP at $102\,^{\circ}C$ and $111\,^{\circ}C$ ($225\,nm$, average UV laser fluence $2 \times 10^7\,W\,cm^{-2}$, pressure of He $0.5\,bar$, reflection voltage $0\,V$) indicating lack of thermal decomposition, changes in tautomeric population, or reactivity. The inset shows a detailed view of $m/z25$ to $m/z95$ range of the mass spectrum.

Most of the MPI measurements in this chapter were carried out at $225\,nm$, whereas our earlier experiments on 3-AP were performed at $220\,nm$ [58]. $225\,nm$ is in the middle of the Coumarin 450 dye range after frequency doubling and, therefore, the UV laser energy is more stable (analogous to Fig. 3.9), Moreover, the Nd:YAG laser power can be kept at

reasonably low values because it is not necessary to compensate for energy fluctuations by increasing the Nd:YAG laser power (see Fig. 3.13), which helps to preserve the lifetime of the dye.

4.3 Experiments probing prompt fragmentation of 3-aminophenol upon multi-photon ionisation at 225 *nm*

Fig. 4.3 shows an MPI mass spectrum of 3-AP with a reflection voltage ($-200V$) that is closer to ground than the cut-off ($-254V$) for signals traced to the parent ion and prompt fragment ions (*prompt* fragment ions are defined here as those originating from dissociation in the extraction region of reflectron TOF-MS - see Section 3.3.1 for more details). It is dominated by the 3-AP$^+$ signal (with detector saturation), while the strongest fragment ions have m/z80, 39 and 27. This is broadly consistent with the mass spectra in the literature [58, 146, 147], but we recommend against detailed comparisons of peak heights because the present data have not been corrected for kinetic energy release effects on the transmission of different product ions to the detector.

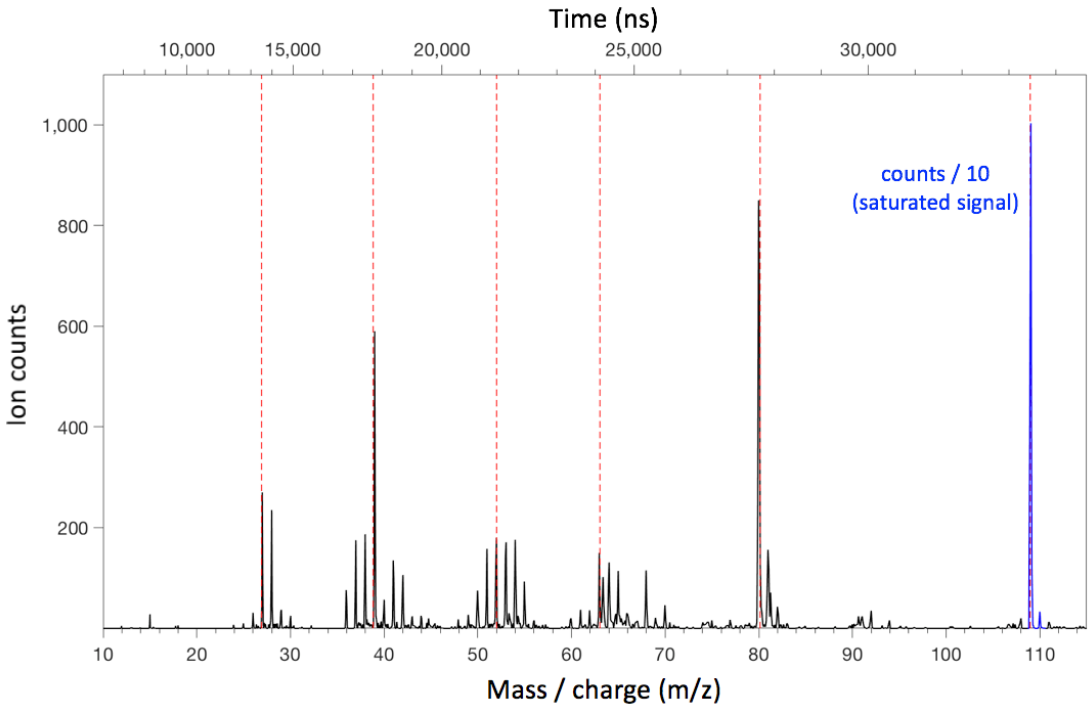

Fig. 4.3: MPI mass spectrum of 3-AP (average UV laser fluence $3 \times 10^7 Wcm^{-2}$, average sample temperature $112\,^{\circ}C$, pressure of He $0.5\,bar$, reflection voltage $-200V$). The red dashed lines represent calculated flight-times of prompt fragment ions of m/z27, 39, 52, 63, 80 and 109 using the Matlab simulation (described in detail in Section 3.3.2.2) to demonstrate the agreement of the simulation with the measured TOF mass spectrum. The simulated flight-times agree with the experimental TOF spectrum to within 0.5 %.

Tab. 4.1 lists the main prompt fragment ions in Fig. 4.3; only the peak at m/z36 ($C_3{}^+$) is new and may possibly provide indirect evidence for a structural change or dissociation in a neutral excited state [18]. Several features due to metastable dissociation are visible at non-integer m/z values in the mass spectrum in Fig. 4.3, but only one (labelled *F* and assigned on the basis of the *maps* in Fig. 4.5 in Section 4.5.1) has intensity comparable with the prompt fragment ion peaks. Metastable dissociation of excited 3-aminophenol ions is discussed in detail in Section 4.5, where the Matlab simulation described in Section 3.3.2 was used for analysis of experimental data. The agreement between the simulated flight-times and the experimental mass spectrum is within 0.5 % and is illustrated in Fig. 4.3, where red dashed lines correspond to calculated flight-times of selected prompt ions.

Tab. 4.1: Summary of the prompt fragment ion signals in Fig. 4.3.

m/z[a]	**Plausible product ions**[b]
109[c]	3-AP$^+$ ($C_6H_7NO^+$)
80[cd]	$\boldsymbol{C_5H_6N^+}$
68[c]	$C_3H_2NO^+/C_4H_6N^+/C_4H_4O^+$
66[cd]	$C_4H_4N^+/C_4H_2O^+/C_5H_6{}^+/C_3NO^+$
65[d]	$C_4H_3N^+/C_5H_5{}^+$
64[d]	$C_4H_2N^+/C_5H_4{}^+$
63	$C_4HN^+/C_5H_3{}^+$
55[c]	$C_2HNO^+/C_3H_5N^+/C_4H_7{}^+/C_3H_3O^+$
54[ccdd]	$C_3H_4N^+/C_3H_2O^+/C_4H_6{}^+/C_2NO^+$
53[ccd]	$\boldsymbol{C_4H_5{}^+}$
52	$C_3H_2N^+/C_4H_4{}^+$
51[d]	$C_3HN^+/C_4H_3{}^+$
50	$C_4H_2{}^+/C_3N^+$
42	$C_2H_4N^+/C_2H_2O^+/C_3H_6^+/CNO^+$
41[cdd]	$C_2H_3N^+/C_2HO^+/C_3H_5^+$
40[d]	$C_2H_2N^+/C_3H_4^+$
39[dd]	$C_2HN^+/C_3H_3^+$
38	$C_3H_2^+/C_2N^+$
37	C_3H^+
36	$C_3{}^+$
28[dd]	$CH_2N^+/C_2H_4{}^+/CO^+$
27[d]	$\boldsymbol{C_2H_3{}^+}$

[a] Only peaks which have intensity ≥ 5 % of the m/z 80 peak intensity are listed.
[b] The fragmentation sequence identified in DFT calculations is highlighted in bold (Fig. 4.8). For the other channels, all possible product ions are listed apart from those which are strongly counterintuitive.
[c] Also present as the precursor ion of one or two (^{cc}) metastable dissociation bands (see Tab. 4.2).
[d] Also present as the product ion of one or two (^{dd}) metastable dissociation bands (see Tab. 4.2).

One of the most striking aspects of the present MPI measurements on 3-AP is the high signal intensity compared with the molecules previously studied using the same experimental set-up such as uracil, thymine, adenine, cytosine, 5-fluorouracil, hypoxanthine and alanine [18, 26, 56–58, 115, 116]. Signal saturation has never occurred before in our MPI experiments on the above-mentioned sublimated molecules using the molecular beam [56–58]. The strong MPI signals of 3-AP at 225 *nm* (see Fig. 4.3) can be attributed

to one or more of the following:

1. High target densities.

2. High absorption cross section for the first photon absorption, which brings the molecule into a neutral electronic excited state.

3. Efficient ionisation - linked to the relatively low ionisation energy of 3-AP (previously reported theoretical values: $7.78\,eV$ and $7.71\,eV$, experimental values: $7.62\,eV$ and $7.65\,eV$ [149] for *cis*- and *trans*- conformers, respectively) compared with the energy delivered by two photons at $225\,nm$ ($11.02eV$).

4. Relatively long lifetimes of the neutral electronic excited states of the molecule accessed prior to the absorption of the ionising photon. This may be possibly linked to efficient access to triplet states compared with the molecules previously studied using the present MPI system.

As mentioned in Chapter 1, one of the major research interests of the Molecular Clusters Laboratory at the OU is the neutral electronic excited state dynamics of biomolecules. We were therefore intrigued by the exceptionally strong MPI signals of 3-AP at $225\,nm$ as these could be linked to processes happening in neutral excited 3-aminophenol (see points 2 and 4 above). As discussed in Section 4.1, the neutral excited state dynamics of 3-aminophenol have not been investigated extensively. To the best of our knowledge, Shinozaki et al. [144] were the only ones to report studies of excited states of 3-aminophenol in the literature. They determined adiabatic energies of the S_1 state of *cis*- and *trans*-conformers of 3-AP to be 4.23 and $4.27\,eV$, respectively. These are well below the $5.51\,eV$ and $4.59\,eV$, which is the energy of UV photons in our MPI experiments at 225 and $270\,nm$.

The following experiments could help to elucidate which of the points 1 to 4 (or combinations thereof) play a critical role in the above-mentioned phenomenon. We investigated point 1 by comparing the MPI signal intensity from 3-AP with that from a reference molecule, thymine, at nozzle temperatures corresponding to approximately equivalent vapour pressure (see section 4.4 below). Point 2 and 4 could be investigated in vacuum-ultraviolet (VUV) photoabsorption measurements, while point 3 and 4 could be addressed in time-resolved pump-probe experiments. To investigate point 2, we planned to carry out VUV photoabsorption studies in the Centre for Storage Ring Facilities (ISA), Aarhus, Denmark. Preparatory experiments for this work are presented in Section 4.4, below.

4.4 Experiments to estimate the vapour pressure of 3-aminnophenol and hence assess the feasibility of VUV photoabsorption experiments on 3-aminophenol at ISA, Centre for Storage Ring Facilities, Aarhus

In this section we describe experiments for the estimation of the vapour pressure of 3-AP, which were carried out in the Molecular Clusters Laboratory at the OU in order to assess the feasibility of performing VUV photoabsorption experiments on ASTRID2 apparatus at ISA. A detailed description of the ASTRID2 apparatus can be found in [150]. The entrance LiF and exit MgF_2 windows of the gas cell are sensitive to high temperature and can be heated only up to $75\,^{\circ}C$. In order to protect the windows and prevent condensation of molecules on the walls of the gas cell, samples can be heated to a maximum temperature of $60\,^{\circ}C$, so we designed an experiment to estimate the vapour pressure of 3-AP at this temperature. Beamline scientist Dr. N. Jones reported that a sample vapour pressure of at least $0.1\,Torr$, corresponding to $0.13\,mbar$, is typically required to obtain good VUV photoabsorption results using the ASTRID2 apparatus. In addition, we carried out analogous experiments on thymine because comparisons of MPI signal intensities of 3-AP at approximately equal vapour pressures could provide more insight into whether point 1 in the list in Section 4.3 is significantly involved in high MPI signals of 3-AP at $225\,nm$.

To the best of our knowledge, the only information on the vapour pressure of 3-AP in the literature is a calculated estimate of $1.86\times10^{-3}\,Torr$ ($2.48\times10^{-3}\,mbar$) at $25\,^{\circ}C$ ($298.15\,K$) [151]. We used this value as our reference for the estimation of the vapour pressure at $60\,^{\circ}C$ ($333.15\,K$) using the method described below. We first measured the temperature dependence of the 3-AP MPI signal in the temperature range of $60-113\,^{\circ}C$ ($333.15-386.15\,K$) using the *Compact MPI/EII experimental set-up* in the *molecular beam mode* (see Section 3.2.2). $60\,^{\circ}C$ is the lowest temperature at which we could obtain an MPI signal in a reasonable acquisition time. The results are shown in Fig. 4.4 a). We then fitted the experimental data based on the Clausius-Clapeyron-type equation. The Clausius-Clapeyron equation can be expressed in the form:

$$log(P) = A - B\times(1/T) \tag{4.1}$$

where P is the vapour pressure in $mbar$, T is temperature in K, and A and B are constants that are specific to the molecule. Thomson [152] as well as Rodgers and Hill [153] argued that empirically, Eq. 4.1 has been shown to be valid only over *"small"* temperature ranges

(with *"small"* undefined) and a modified version, the so-called Antoine equation,

$$log(P) = a - b \times [1/(c+T)] \tag{4.2}$$

where a, b and c are constants specific to the molecule, should be used to fit vapour pressure against temperature across larger ranges [152, 153]. Ferro et al. [154] used a *torsion-effusion* technique to measure the vapour pressure of cytosine and thymine in the $480-553\,K$ and $420-503\,K$ temperature ranges, respectively, and derived the pressure-temperature equations for the two molecules in the form of Eq. 4.1. In addition, Tabet et al. [155] used the Clausius-Clapeyron equation to determine the molar enthalpy of sublimation of uracil in the temperature range $400-493\,K$. Following these studies, we use Eq. 4.1 to fit and extrapolate pressure-temperature dependence for 3-AP between 298 and $386\,K$, i.e. $88\,K$ temperature range which is comparable with Ferro et al's $73\,K$ temperature range for cytosine and $83\,K$ range for thymine [154] as well as Tabet et al.'s $93\,K$ temperature range [155] in the case of uracil. Nonetheless, considering the empirical nature of the Clausius-Clapeyron equation and the necessity of an extrapolation here, it is important to stress that the present vapour pressure estimation should be treated as a guide for experimental planning instead of as a precise determination of vapour pressure.

Assuming direct proportionality of the signal intensity S (in ion counts) of 3-AP$^+$ in our MPI experiments to the vapour pressure P of the molecule in the nozzle gives:

$$S = d \times P \tag{4.3}$$

and hence

$$log(S) = log(P) + log(d) \tag{4.4}$$

where d is a constant that is specific to the molecule, the MPI conditions, and the ion detection efficiency. Therefore, we can write (using Eq. 4.1):

$$log(S) = A' - B \times (1/T) \tag{4.5}$$

where $A' = A + log(d)$. A weighted fit of our experimental data in Fig. 4.4 a) using Eq. 4.5 enabled us to determine A' and B as expressed in the equation below:

$$log(S) = (13.55 \pm 0.13) - (3990.97 \pm 48.87) \times (1/T) \tag{4.6}$$

To determine $log(d)$ in the following relation for vapour pressure (based on Eq. 4.4 and

4.5):

$$log(P) = A' - B \times (1/T) - log(d) \tag{4.7}$$

we extrapolated the linear fit of $log(S)$ from Eq. 4.6 to $25\,^{\circ}C$ ($log(S_{25\,^{\circ}C})$) as indicated in Fig. 4.4 a). $log(d)$ can be then calculated from Eq. 4.4 using $log(S_{25\,^{\circ}C})$ (see black square in Fig. 4.4 a)) value and the 3-AP vapour pressure value from the literature [151] at $25\,^{\circ}C$ (see red triangle in Fig. 4.4 a)). The derived pressure-temperature equation is then

$$log(P) = (10.78 \pm 0.16) - (3990.97 \pm 48.87) \times (1/T) \tag{4.8}$$

It should be noted that the above-described experimental procedure based on measuring the MPI signals with increasing temperature of the sample is not a conventional technique for estimating vapour pressure and therefore we carried out additional experiments to verify this approach. Examples of standard methods for vapour pressure measurement are Knudsen-effusion [156, 157] and torsion-effusion techniques [154, 158], static methods [159, 160], etc. The reader is referred to [154, 156–160] for more information. The reliability of our approach applied to 3-AP was investigated by carrying out experiments on thymine with all experimental conditions the same except for the sublimation temperature range ($223 - 264\,^{\circ}C$, i.e. $496.15 - 537.15\,K$) and the UV laser power, which was higher in the experiments on thymine in order to obtain sufficient statistics. Thymine was chosen as a reference as it has been one of the more thoroughly studied molecules in the Molecular Clusters Laboratory at the OU as well as in the literature [60, 161–164]. Although the MPI signals at $225\,nm$ from thymine are weaker than those from 3-AP, thymine showed strong MPI signals in our experiments using the *Compact MPI/EII experimental set-up* [58, 115] compared to other previously studied molecules by our group such as uracil, adenine, cytosine, 5-fluorouracil, hypoxanthine and alanine [18, 26, 56–58, 115, 116]. More importantly, the pressure-temperature dependence of thymine was previously determined by Ferro et al. [154] in $420 - 503\,K$ temperature range as follows:

$$log(P) = (13.79 \pm 0.11) - (7016 \pm 51) \times (1/T) \tag{4.9}$$

where P is the vapour pressure of thymine in *mbar* and T is temperature in K.

The grey squares in Fig. 4.4 b) show the dependence of thymine^{+} signal as a function of temperature in the MPI experiments at the OU and the black line is a weighted linear fit of the experimental data (analogous to Fig. 4.4 a) and Eq. 4.6), where

$$log(S) = (16.19 \pm 0.39) - (6976.70 \pm 204.61) \times (1/T) \tag{4.10}$$

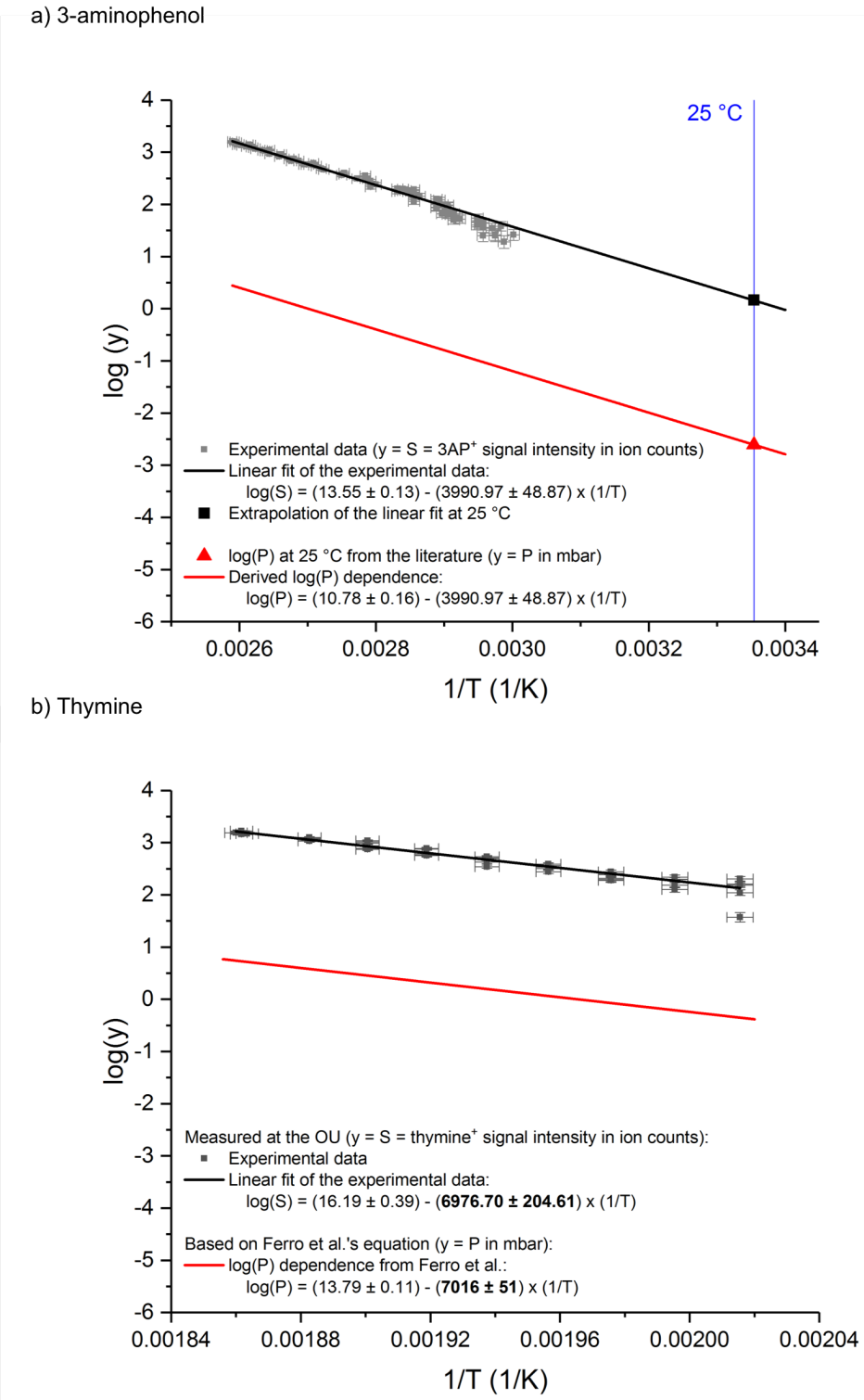

Fig. 4.4: a) Experimental procedure for determination of vapour pressure of 3-AP in MPI experiments at $225\,nm$ (average UV laser fluence $2 \times 10^7\,W\,cm^{-2}$, average sample temperature $60 - 113\,°C$, pressure of He $0.5\,bar$) and b) comparison of thymine$^+$ signal dependence on temperature measured in MPI experiments at $225\,nm$ (average UV laser fluence $3 \times 10^7\,W\,cm^{-2}$, average sample temperature $223 - 264\,°C$, pressure of He $0.5\,bar$) and pressure-temperature dependence from Ferro et al. [154] shows that our experiment provides a reliable direct measure of the B constant in the Clausius-Clapeyron equation and hence supports our approach of normalising to obtain the A constant (see Eq. 4.1).

The gradient of the signal intensity (and thus vapour pressure) dependence on temperature obtained in the MPI experiments on thymine (see 4.10 and black line in Fig. 4.4 b)) agrees with the gradient of pressure dependence on temperature obtained by Ferro et al. [154] (see Eq. 4.9 as well as red line in Fig. 4.4 b)). This suggests that our experimental approach of measuring signal intensity as a function of temperature enables us to directly determine the B constant in the Clausius-Clapeyron equation and hence supports our approach of normalising to obtain the A constant (see Eq. 4.1).

A weak point of our approach for estimating the vapour pressure of 3-AP is that in order to estimate absolute values, we have to rely on a single vapour pressure value reported in literature. We do not have any information about the theoretical method that was used to obtain the vapour pressure of 3-AP ($2.48 \times 10^{-3}\,mbar$) at $25\,^{\circ}C$ ($298.15\,K$) from the literature [151] or about the accuracy of this value. In addition, Eq. 4.1 is known to apply only across limited temperature ranges [152, 153] and we do not know how accurately Eq. 4.8 describes the vapour pressure of 3-AP at $25\,^{\circ}C$. Because we cannot determine the uncertainty on the vapour pressure caused by the specifics of the data fitting and the extrapolation applied here, we can consider the values calculated from Eq. 4.8 only as the first-order estimates. Based on Eq. 4.8, we can estimate the vapour pressure at $60\,^{\circ}C$ ($333.15\,K$) to be just below $10^{-1}\,mbar$, which is at the low limit for the Aarhus experiment. Therefore, we attempted the VUV photoabsorption experiments at ISA, Aarhus. However, high water contamination of the sample in combination with the low vapour pressure of 3-AP at this temperature resulted in the photoabsorption spectra being dominated by water absorption (a VUV photoabsorption spectrum can be found in [165]), which prevented us from successfully carrying out the photoabsorption experiments on this molecule.

Provided Eq. 4.8 gives reasonably close approximation of vapour pressure dependence on temperature, then Eq. 4.8, and 4.9 indicate that comparable vapour pressures are achieved at $111\,^{\circ}C$ for 3-AP and $258\,^{\circ}C$ for thymine in our experiments. It should be noted that the UV laser power in the MPI experiments on thymine in Fig. 4.4 b) was higher than in the MPI experiments on 3-AP in Fig. 4.4 a) in order to obtain sufficient statistics in the experiments on thymine. Therefore, to compare signal intensity of the two molecules at equivalent vapour pressures in the same experimental conditions (including UV laser power), we carried out additional experiments on 3-AP at $111\,^{\circ}C$. The higher UV laser power resulted in detector saturation for 3-AP$^+$ signal. Despite this saturation, 3-AP$^+$ signals were 11-times greater than the corresponding thymine$^+$ signals. This suggests that the exceptionally strong MPI signals of 3-AP are unlikely to be solely due to high target densities. This increases the plausibility of electronic excited state spectroscopy (i.e.

strong absorption) and/or dynamics (i.e. long excited state lifetime) of the molecule playing a role in the very efficient multi-photon ionisation of 3-aminophenol in the present laser conditions. In future, we are planning to repeat the VUV photoabsorption experiments at higher temperatures using a high-temperature system at ISA, Aarhus, which has been built for circular dichroism experiments. We are also investigating the possibility of performing time-resolved pump-probe experiments externally to the OU in order to test the excited state lifetimes.

4.5 Metastable dissociation of excited 3-aminophenol ions

The high MPI signals of 3-aminophenol at 225 *nm* enabled us to spot even relatively minor dissociation channels such as fragment ions resulting from metastable dissociation (i.e. a dissociation several microseconds after ionisation). To identify metastable dissociation channels, ion signals were *mapped* against flight-time and reflection voltage, as explained in Section 3.3.1, prior to comparisons with a simulation developed in Matlab (see Section 3.3.2). Briefly, the initial inputs of the simulation are the distances within the mass spectrometer, the electrode voltages (except for the reflection voltage), and the crossing position of the laser beam with the molecular beam. The latter is determined by measuring the cut-off reflection voltage at which the intact parent ion signal is extinguished, following the method described by Ryszka et al. [26]. The next step is to input one or more candidate dissociations (specific combinations of precursor and product ion masses) that might take place in the field-free region (FFR) of the mass spectrometer (see Fig. 3.3). The program then generates a *map* of flight-time against reflection voltage that can be overlaid onto an experimental *map*. Different candidate dissociations are tested iteratively until a good match is achieved between the simulated and experimental *maps*.

18 metastable dissociation channels (extended curves in *metastable dissociation maps*) were detected and identified despite four band overlaps. To the best of our knowledge, this represents the most complex dissociation pattern analysed using the *mapping* approach to date. All the previous *metastable dissociation maps* [128, 130–132] have in common that they show a relatively small number of metastable dissociation channels (maximum 11 [128]) and only one includes a band overlap that can complicate the analysis [131]. The *mapping* approach was critical to the outcome of this study; without it we would not have been able to recognise many of the observed metastable dissociation channels above the detector noise and our assignments would have been less precise.

4.5.1 Experiments probing metastable fragmentation pathways of 3-aminophenol following MPI at 225 *nm* and involving the loss of at least one *heavy* atom (*C*, *N*, or *O*)

Fig. 4.5 a) shows an experimental *map* of ion counts from multi-photon ionised ($225\,nm$) 3-AP plotted against flight-time and reflection voltage. The intense bands visible at reflection voltages between -190 and $-254\,V$ are due to the detection of prompt fragment ions and 3-AP$^+$ (consistent with the conventional TOF spectrum in Fig. 4.3). The curved bands at reflection voltages between -254 and $-1200\,V$ are due to metastable dissociations in the FFR and/or, conceivably, ions dissociating as they scatter off the FFR grids (see Fig. 3.3). To test the latter possible effect, a set of measurements was repeated with two extra grids at the FFR entrance. This doubled the scattering surface but did not change the ratio of metastable band signals/prompt ion signals. Therefore, ion interactions with grids had negligible effects on the present data.

TOF measurements carried out at reflection voltage intervals of $10\,V$ are shown in Fig. 4.5 a) so the reader can follow individual metastable bands easily. Fig. 4.5 b) shows an equivalent series of measurements with larger voltage intervals ($100\,V$) to enable convenient comparison with the simulations. Tab. 4.2 lists the 18 metastable dissociations (labelled $A-R$) that could be identified on the basis of the agreement between the experimental and simulated *maps*. Band A ($m/z\,109 \rightarrow 80$) has a very broad profile and thus we suspect additional weak contributions of ($m/z\,109 \rightarrow 79$) and/or ($m/z\,109 \rightarrow 81$) channels.

Aside from showing the agreement of the experimental bands with the simulations that determine their assignments, it is worth commenting on how the band shapes in the *maps* such as Figs. 4.5 and 4.6 can be read in more general terms. To a first approximation, the flight-time at a reflection voltage close to ground (e.g. $-200\,V$) is proportional to $\frac{1}{2}(\sqrt{m_{Pr}} + \sqrt{m_{FrM}})$, where m_{Pr} is the precursor ion mass and m_{FrM} is the product ion mass. Then the ratio of $\frac{m_{FrM}}{m_{Pr}}$ determines how far the band extends in reflection voltage (see [115] for the precise relation). A high ratio corresponds to a high kinetic energy of the product ion when it exits the FFR (held at $-2027\,V$) so a strong electric field is required to reflect it onto the detector. Hence, the metastable band cuts-off at a reflection voltage that is relatively close to ground. The $\frac{m_{FrM}}{m_{Pr}}$ ratio also affects the slope of the band on a *map* in a given reflection voltage range because the dependence of flight-time on reflection voltage becomes stronger when the ion travels closer to the reflection electrode (thus spending a longer time in the reflecting field).

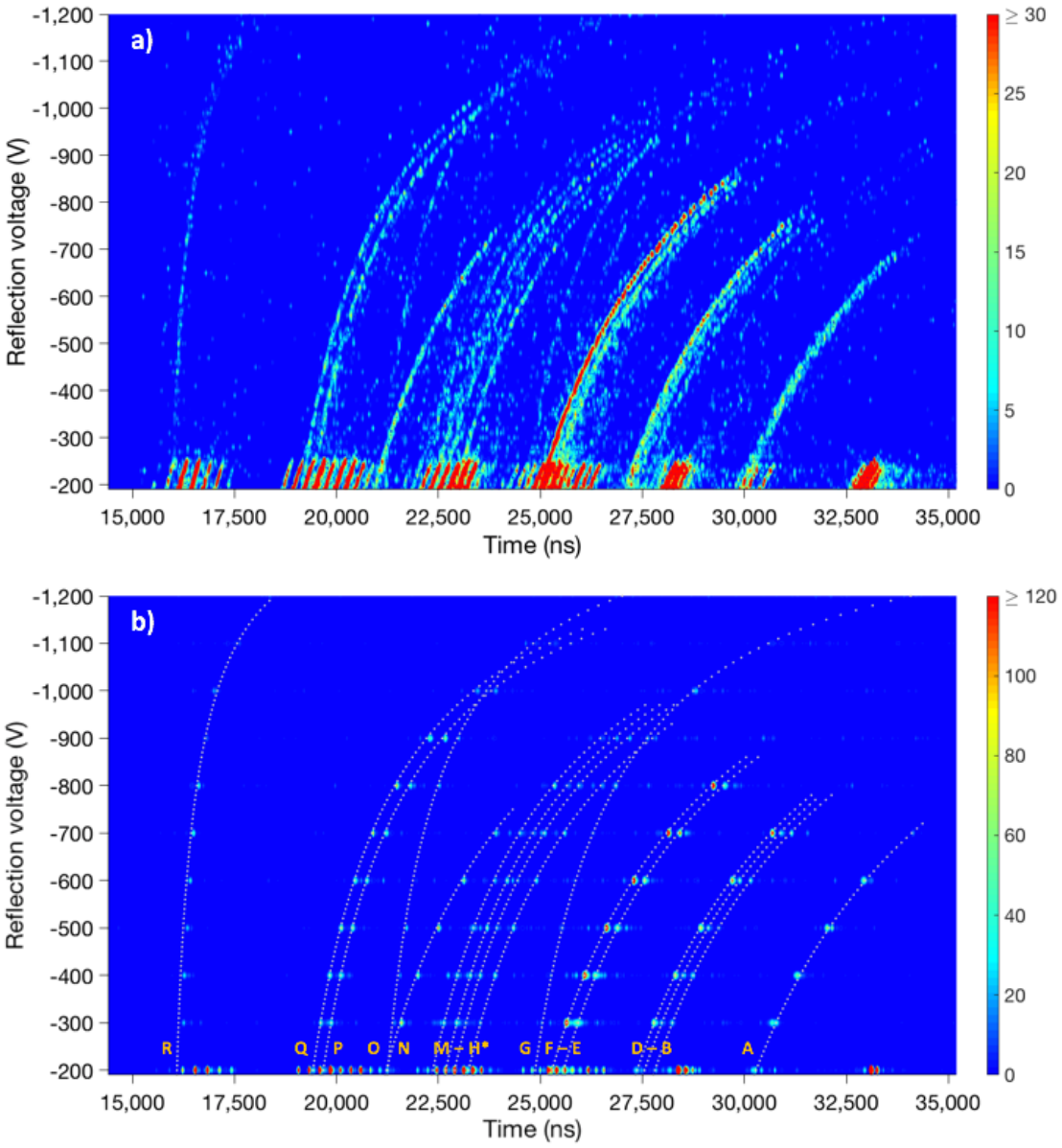

Fig. 4.5: a) Experimental *map* of MPI signal ($225\,nm$, average UV laser fluence $3 \times 10^7\,W\,cm^{-2}$, average sample temperature $113\,^{\circ}C$, pressure of He $0.5\,bar$) against flight-time and reflection voltage and b) superposition of experimental and simulated *maps* with the simulated bands shown as dotted white lines. The scales on the right hand side of the *maps* are in ion counts per $32\,ns$ time bin. Bands H and J are shown in detail in Fig. 4.6.

A family of metastable dissociations is suggested by the steady evolution of the shapes of 13 bands in Fig. 4.5 ($A-F$, I, $K-M$, Q, and R). Tab. 4.2 shows that these dissociations involve the loss of a neutral comprising two heavy atoms (C, N, or O, as well as up to three H atoms). Only two relatively weak bands (G and O) involve the loss of neutrals with three or more heavy atoms and only one band (N) involves the loss of a neutral with a single heavy atom. The remaining two observed bands (H and J) involve double and single H loss. Further experiments and/or calculations are required to explain why metastable channels involving the loss of neutrals comprising two heavy atoms dominate the present

results. As a precedent, it is worth noting that the only metastable dissociations observed in EII experiments on the imino tautomer of 2-aminopyrimidine ($C_4H_5N_3$, with a C_4N_2 central ring instead of the C_6 ring in 3-AP) were five *HCN* loss channels and two *H* loss channels [125].

Tab. 4.2: Summary of the metastable band assignments from Fig. 4.5 and 4.6.

Band label[a] in Fig. 4.5 b) and Fig. 4.6	**m/z of precursor and product ion**	**Neutral fragment mass in a.u.**	**Plausible product ions[b]**
A	**109 → 80**	**29 *(HCO)***	***$C_6H_7NO^+$* (3-AP$^+$) → *$C_5H_6N^+$***
B	94 → 66	28	$C_5H_4NO^+ \rightarrow C_4H_4N^+/C_4H_2O^+/C_3NO^+$ $C_6H_6O^+ \rightarrow C_5H_6{}^+/C_4H_2O^+$
C	92 → 65	27	$C_6H_4O^+ \rightarrow C_4HO^+$ $C_6H_6N^+ \rightarrow C_5H_5{}^+/C_4H_3N^+$
D	91 → 64	27	$C_6H_5N^+ \rightarrow C_5H_4{}^+/C_4H_2N^+$
E	82 → 54	28	$C_5H_6O^+ \rightarrow C_4H_6{}^+/C_3H_2O^+$ $C_4H_4NO^+ \rightarrow C_3H_4N^+/C_3H_2O^+/C_2NO^+$
F	**80 → 53**	**27 *(CNH)***	***$C_5H_6N^+ \rightarrow C_4H_5{}^+$***
G	91 → 41	50	$C_5H_6O^+ \rightarrow C_6H_3O^+/C_2HO^+$ $C_6H_5N^+ \rightarrow C_2H_3N^+$
H	55 → 54	1	$C_3H_3O^+ \rightarrow C_3H_2O^+$ $C_3H_5N^+ \rightarrow C_3H_4N^+$ $C_4H_7{}^+ \rightarrow C_4H_6{}^+$ $C_2HNO^+ \rightarrow C_2NO^+$
I	70 → 43	27	$C_4H_6O^+ \rightarrow C_2H_3O^+$ $C_3H_4NO^+ \rightarrow C_2H_3O^+/CHNO^+$
J	53 → 51	2	$C_3H_3N^+ \rightarrow C_3HN^+$ $C_4H_5{}^+ \rightarrow C_4H_3{}^+$
K	69 → 41	28	$C_4H_5O^+ \rightarrow C_3H_5{}^+/C_2HO^+$ $C_4H_7N^+ \rightarrow C_3H_5{}^+/C_2H_3N^+$ $C_3H_3NO^+ \rightarrow C_2H_3N^+/C_2HO^+$
L	68 → 40	28	$C_4H_4O^+ \rightarrow C_3H_4{}^+/C_2O^+$ $C_3H_2NO^+ \rightarrow C_2H_2N^+/C_2O^+$ $C_4H_6N^+ \rightarrow C_3H_4{}^+/C_2H_2N^+$
M	66 → 39	27	$C_4H_4N^+ \rightarrow C_3H_3{}^+/C_2HN^+$ $C_5H_6{}^+ \rightarrow C_3H_3{}^+$
N	54 → 39	15	$C_3H_4N^+ \rightarrow C_2HN^+/C_3H_3{}^+$ $C_4H_6{}^+ \rightarrow C_3H_3{}^+$
O	69 → 28	41	$C_4H_5O^+ \rightarrow CO^+/C_2H_4{}^+$ $C_4H_7N^+ \rightarrow CH_2N^+/C_2H_4{}^+$ $C_3H_3NO^+ \rightarrow CH_2N^+/CO^+$
P	54 → 28	26	$C_3H_4N^+ \rightarrow CH_2N^+/C_2H_4{}^+$ $C_3H_2O^+ \rightarrow CO^+$ $C_4H_6{}^+ \rightarrow C_2H_4{}^+$ $C_2NO^+ \rightarrow CO^+$
Q	**53 → 27**	**26 *(C_2H_2)***	***$C_4H_5{}^+ \rightarrow C_2H_3{}^+$***
R	41 → 15	26	$C_2H_3N^+ \rightarrow CH_3{}^+/NH^+$ $C_3H_5{}^+ \rightarrow CH_3{}^+$

[a] The fragmentation sequence identified in DFT calculations is highlighted in bold.
[b] In the absence of calculations or any channels that are strongly counterintuitive, all possible ions are listed.

4.5.2 Metastable single- and double-hydrogen loss from excited fragment ions of multi-photon ionised 3-aminophenol

TOF measurements recorded at reflection voltage intervals of $5V$ between -235 and $-375V$ are presented in Fig. 4.6 in order to demonstrate metastable single- and double-hydrogen loss from fragment ions. Observations of metastable single-hydrogen loss are quite prevalent in the literature (e.g. from toluene [127] and several derivatives of pyrimidine and purine [125, 166]) even though the similar kinetic energies and flight-times of the precursor and product ions in a TOF mass spectrometer necessitate sensitive measurements and analysis. However, experimental observations of metastable double-hydrogen loss (H_2 or two separate hydrogens) are relatively rare. These channels typically require complex atomic rearrangements, most obviously in the form of *hydrogen scrambling*, and hence pose a challenge to theoretical models of dissociation dynamics. Band J in the Fig. 4.6 corresponds to metastable double hydrogen loss from a fragment ion ($C_3H_3N^+$ or $C_4H_5{}^+$).

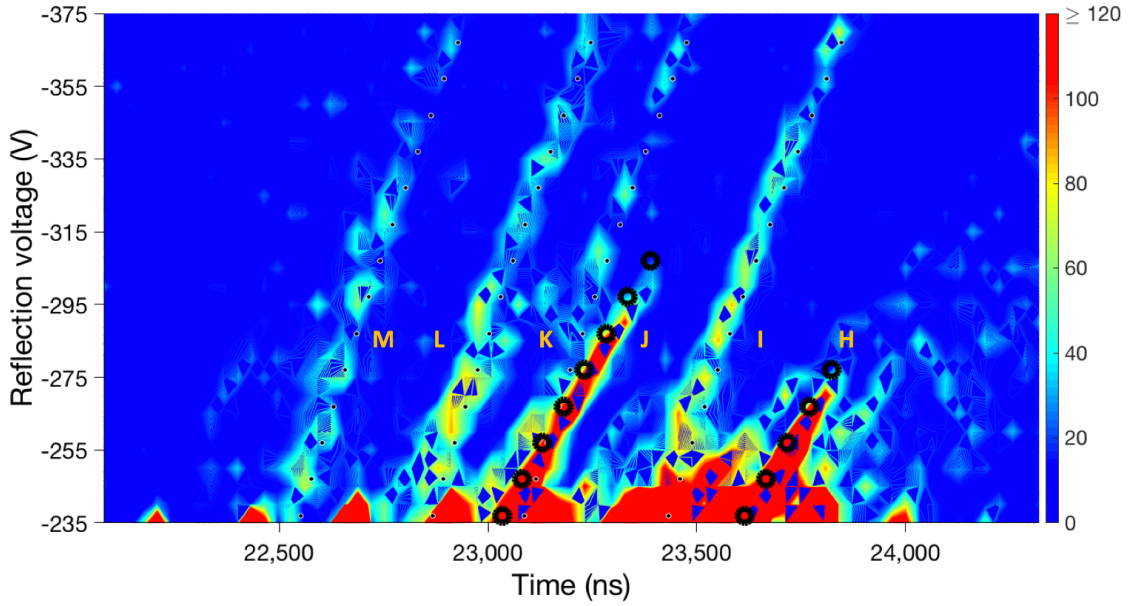

Fig. 4.6: Detail of the experimental *map* of MPI signal ($225\,nm$, average UV laser fluence $3\times10^7\,W\,cm^{-2}$) against flight-time and reflection voltage. The simulated bands for $m/z\,55\rightarrow54$ and $53\rightarrow51$ metastable dissociations (involving single- and double-hydrogen loss) are indicated by open black circles and agree closely with the experimental H and J bands, respectively. The scale on the right-hand side of the *map* is in ion counts per $32\,ns$ time bin.

To our knowledge, channels of this kind have only been observed previously from a small selection of pure hydrocarbons with numerous hydrogens [167, and references therein] and from electron impact ionised acrylonitrile (C_3H_3N) [168]. Gluch et al. [168] showed that the time dependence of double hydrogen loss from $C_2H_2{}^+$ fragments of acrylonitrile

can be fitted best using a combination of two separate decay functions and argued that this suggests H_2 production in stable and unstable states with respect to subsequent dissociation. Other metastable dissociative ionisation experiments that provide evidence to distinguish between the production of H_2 or of two separate hydrogens include Feil et al's [169] and Roithová et al.'s [170] observations of H_2 loss from doubly-charged toluene. The present experiment does not provide this capability, notably due to the absence of kinetic energy release information.

4.5.3 Comparison of metastable dissociation of 3-aminophenol following MPI at 225 *nm* and 270 *nm*

Our understanding of metastable dissociation is centred on the production of vibrationally hot ions. If the total vibrational energy of an ion matches (or is very close to) the threshold required for a specific dissociation, then a suitable redistribution of the activated modes can lead to delayed dissociation. The delay can be due to tunnelling through a low potential barrier or a low rate constant for unimolecular fragmentation when the excess internal energy is small [139].

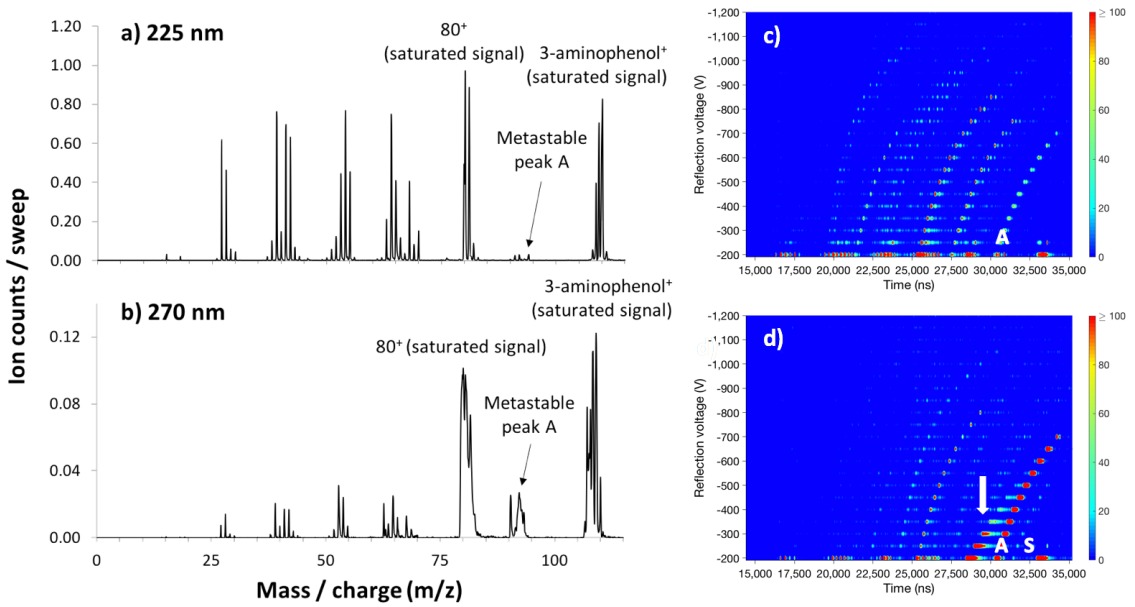

Fig. 4.7: Comparison of MPI mass spectra of 3-AP at a) 225 *nm* and b) 270 *nm*; and experimental *maps* of MPI signal against flight-time and reflection voltage at c) 225 *nm* and d) 270 *nm* (average UV laser fluence $3 \times 10^6 W cm^{-2}$, average sample temperature 112 °*C*, pressure of *He* 0.5 *bar*). The scales on the right hand side of the *maps* in c) and d) are in ion counts per 32 *ns* time bin.

In contrast with our recent experiments on nucleobases [115], the strongest metastable channels in Fig. 4.5 and 4.7 c) involve the delayed dissociation of fragment ions instead of

the excited parent ion. This suggests that our MPI experiments at 225 *nm* produced relatively small populations of 3-AP$^+$ ions in vibrational levels close to a critical dissociation barrier. By contrast, the strongest metastable dissociation channel in our MPI experiments at 270 *nm* (see Fig. 4.7 d)) was $m/z\,109 \rightarrow 80$ (3-AP$^+$ $\rightarrow C_5H_6N^+$, band *A*). This channel is even stronger than most of the prompt fragment ions with m/z lower than 80 in the MPI spectrum at 270 *nm* (reflection voltage $0\,V$) in Fig. 4.7 b). It should be noted that MPI measurements presented in Fig. 4.7 were carried out roughly at an order of magnitude lower UV laser power than the ones presented in Figs. 4.5 and 4.6. This is because the dye laser conditions did not allow us to obtain the same high UV laser powers at 270 *nm*.

Such strong wavelength effects on the metastable dissociation of the excited parent ion may be linked to the level of vibrational excitation in the electronically-excited neutral prior to the absorption of the ionising photon [115]. In this case we would expect the difference in the fragmentation pattern at different wavelengths to be more pronounced in the metastable dissociation *maps* rather than in the prompt mass spectra. Unfortunately, the saturation of the parent ion ($m/z\,109$) as well as $m/z\,80$ fragment ion in the MPI measurements at both wavelengths, 225 and 270 *nm* (see Fig. 4.7 a) and b)), do not allow us to further support this hypothesis with the present data set. It should be noted that the level of saturation is higher in the mass spectrum at 270 *nm* than at 225 *nm*, which agrees well with the corresponding metastable fragmentation channel *A* being much more pronounced in Fig. 4.7 b) and d) rather than a) and c), respectively. Analogously to the metastable dissociation measurements at 225 *nm*, due to the very broad profile of band *A* in Fig. 4.7 d) we expect additional weak contributions of ($m/z\,109 \rightarrow 79$) and/or ($m/z\,109 \rightarrow 81$) channels.

The very strong signals for $m/z\,80$ fragment ion production (both prompt and metastable) at 270 *nm* enabled us to detect for the first time a *bridge* feature in a *metastable dissociation map*, which is marked with a white arrow in Fig. 4.7 d). We assign this feature to the dissociation of 3-AP$^+$ ($m/z\,109$) into 80$^+$ in between the interaction of the molecular beam with the laser beam and the first field-free region (FFR) grid (see Fig. 3.3). If the dissociation takes place after 3-AP$^+$ has only travelled a short distance from the interaction point then the flight-time and the cut-off will be similar to the prompt 80$^+$ ion. If the dissociation takes place when 3-AP$^+$ is close to the FFR grid, then the flight-time and the cut-off will be similar to that of a dissociation in the FFR (i.e. our *"normal"* metastable channel). Accordingly, the new band forms what might be described as *"bridge"* in between the strongly saturated prompt $m/z\,80$ peak and the metastable $m/z\,109 \rightarrow 80$ band.

In general, the metastable dissociation at $270\,nm$ results in the similar fragment ion production as the metastable dissociation at $225\,nm$, however with different intensities. The dissociations resulting in smaller fragments are more pronounced at $225\,nm$ rather than at $270\,nm$. Although metastable dissociation measurements presented in Fig. 4.7 c) and d) are hampered by lower signal intensities due to limited UV laser power at $270\,nm$, an extra metastable dissociation channel was identified in the *map* at $270\,nm$ which is absent at $225\,nm$. The channel is marked as *S* in Fig. 4.7 d) and we assign it as $m/z\,105/106 \rightarrow 92/93$. Precise identification is limited by the relatively low resolution of the experimental *map* in Fig. 4.7 d). Acquiring more data could help to increase the resolution of the *map*. Nevertheless, this result indicates that investigating metastable dissociation at different wavelengths can provide further insights into the fragmentation pattern of studied molecules.

4.6 DFT calculations to assign an apparent sequential fragmentation pathway revealed in the metastable dissociation experiments at 225 *nm*

In order to gain insight into the fragmentation pathways and energetics of the 3-AP radical cation in the gas-phase, Dr. J.-C. Poully carried out a series of quantum-chemical calculations with Density Functional Theory (DFT) on the ionisation of the molecule from its neutral electronic ground state at $0\,K$. All calculations were performed using the Gaussian 09 package [171] with the $B3LYP$ functional (unrestricted spin for radical species in their lowest doublet state) and the $aug-cc-pVDZ$ basis set. This level of theory has been applied widely and successfully for radical cations of organic molecules [172–174] and in particular for the 3-AP radical cation [149]. Geometry optimisation was carried out with the default Berny algorithm for both stable species and transition states. Contamination by higher spin states was found to be negligible for all species considered, since the spin operator value was lower than 0.7510 after annihilation. Vibrational frequencies were calculated to confirm the absence of negative frequencies for minima of the potential energy surface, and the presence of a single negative frequency for first-order saddle points. This also allowed the potential energy to be corrected by the vibrational zero-point energy (ZPE).

Only the *cis*- and *trans*- conformers of a single tautomer of 3-AP$^+$ have been observed previously [149] based on the analysis of vibrational structure up to $0.14\,eV$ above the respective ionisation thresholds ($7.6205\,eV$ and $7.6544\,eV$ [175]). However, as dissocia-

tion clearly necessitates higher internal energies than $0.14\,eV$, we investigated alternative 3-AP$^+$ tautomers that could be used as starting points for our fragmentation pathway calculations. All were at least $0.65\,eV$ higher than the tautomer observed by Unterberg et al. [149], with barriers of $2-3\,eV$ between them. Therefore, the calculated pathways start from the lowest-energy tautomer of the radical cation.

The strongest metastable dissociation channel in the present MPI conditions is $m/z\,80 \rightarrow 53$ (band F in Fig. 4.5 b)). This appears to be consistent with $m/z\,80$ being the strongest fragment ion in the prompt mass spectrum (Fig. 4.3). Conversely, several quite strong prompt fragment ions (e.g. at $m/z\,52$) are completely absent from the metastable dissociation results, either as precursors or as products. Evidently, some dissociations that take place efficiently on timescales of $\leq 100\,ns$ in the present MPI conditions occur too weakly on microsecond timescales to produce discernible metastable dissociation bands. Beyond being the strongest metastable band, the $m/z\,80 \rightarrow 53$ channel is interesting because we have also observed metastable dissociations of $m/z\,109 \rightarrow 80$ and $53 \rightarrow 27$. This suggests an unbroken sequential fragmentation route from the excited 3-AP radical cation to one of the smallest fragment ions visible in Figs. 4.3 and 4.5. To account for this apparent sequence, we have calculated possible pathways for each channel.

Fig. 4.8 a) shows the lowest-energy pathway that we have found for the removal of a $29\,a.u.$ neutral from the lowest-energy tautomer of 3-AP$^+$. $C_5H_6N^+$ and HCO are produced by overcoming a barrier of $4.69\,eV$. Extensive H atom scrambling is observed, which seems to be consistent with the numerous peaks separated by $m/z\,1$ in Fig. 4.3. Starting from the final $C_5H_6N^+$ configuration identified in Fig. 4.8 a), Fig. 4.8 b) shows the lowest-energy pathway that we have found for the loss of a $27\,a.u.$ neutral. This identifies the fragments as $C_4H_5{}^+$ and CNH with a critical barrier of $3.49\,eV$. In Fig. 4.8 c), we show the lowest energy pathway that we have found for the last step of the apparent fragmentation sequence: the loss of a $26\,a.u.$ neutral from $C_4H_5{}^+$. This results in $C_2H_3{}^+$ and C_2H_2 production, overcoming a key barrier of $5.10\,eV$. Two findings are noticeable: first, the final location of the positive charge corresponds, for each pathway, to the fragment detected experimentally, despite the absence of constraint in the calculation. Second, the relative signals for these three metastable dissociations ($m/z\,80 \rightarrow 53$ most intense, then $109 \rightarrow 80$, then $53 \rightarrow 27$) correlates with the respective highest energy barriers (3.49, 4.69, and $5.10\,eV$). Indeed, metastable dissociation is expected to be influenced by rate constants, which depend on potential energy barriers between reactants and products. Future experiments on isotopically-labelled 3-AP and measurements of fragment ion appearance energies would be valuable to test the calculated sequential fragmentation pathway.

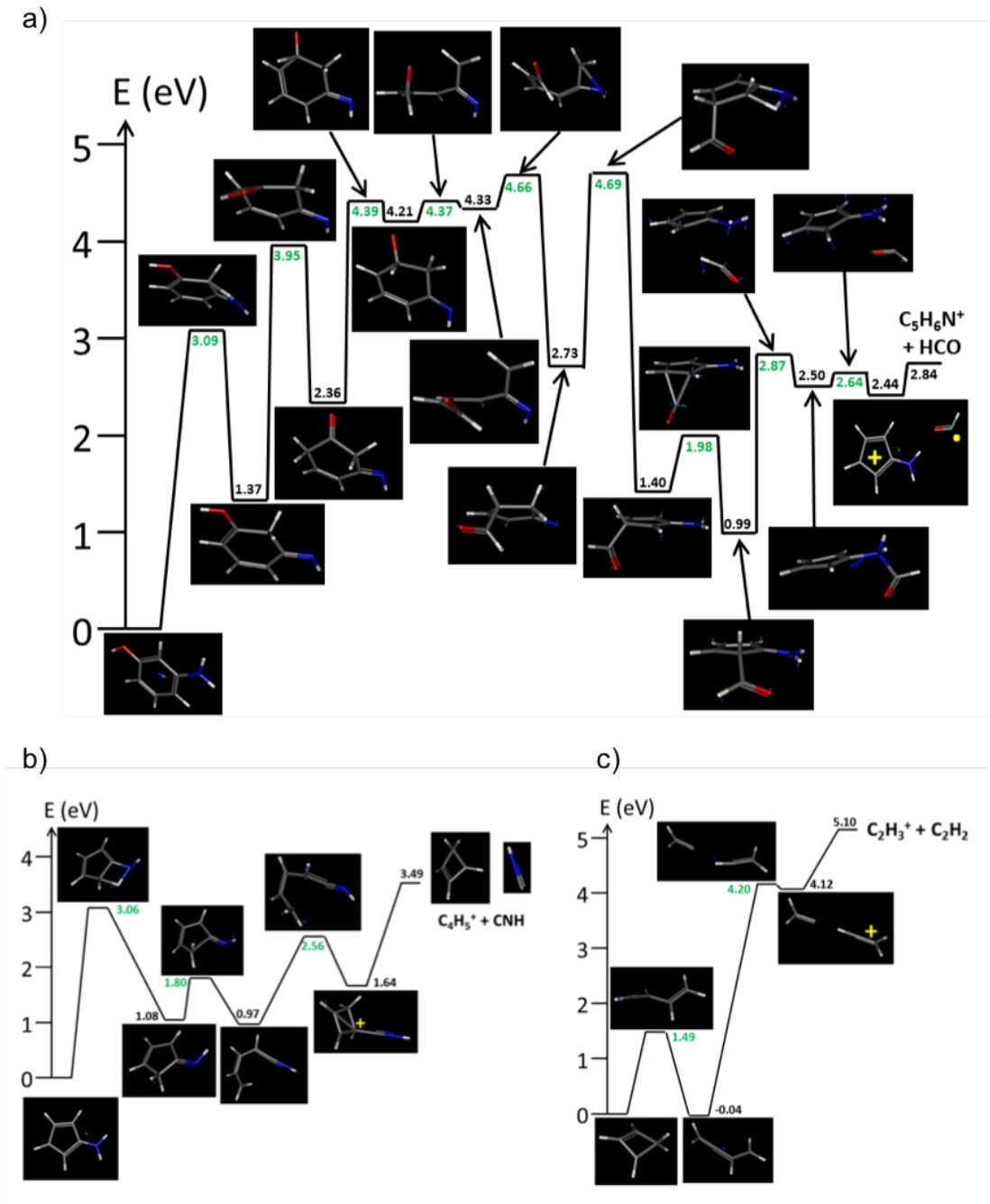

Fig. 4.8: Potential energy surface along a) HCO loss from 3-AP$^+$ ($m/z\,109 \rightarrow 80$, band A in Fig. 4.5); b) CNH loss from $C_5H_6N^+$ ($m/z\,80 \rightarrow 53$, band F) and c) C_2H_2 loss from $C_4H_5{}^+$ ($m/z\,53 \rightarrow 27$, band Q). The zero-point corrected energy of the doublet ground-state of each species (in black for minima and green for transition states) is given in eV, relative to that of the lowest-energy tautomer. The structure of each species is also shown: H atoms are coloured in white, C in grey, O in red and N in blue. The locations of the positive charge and the radical are indicated in yellow for the last minimum before fragmentation.

4.7 Summary and outlook

The work outlined in this chapter reveals a rich array of metastable dissociation channels of a multi-photon ionised molecule of biological interest: 3-aminophenol. 18 metastable dissociation channels have been detected and identified in the metastable dissociation experiments on 3-AP at 225 *nm*. One of the most striking experimental results is the suggestion of a fragmentation sequence which we have assigned to 3-$AP^+ \rightarrow C_5H_6N^+ \rightarrow C_4H_5{}^+ \rightarrow C_2H_3{}^+$ on the basis of comparisons with DFT calculations. Each dissociation in the calculated pathway is preceded by extensive atomic rearrangements, notably *hydrogen scrambling*. Further evidence supporting *hydrogen scrambling* is provided by the rare experimental observation of metastable double hydrogen loss (H_2 or two separate atoms) from an excited fragment ion.

Comparison of the metastable dissociation experiments on 3-AP at 225 and 270 *nm* reveals an extra dissociation channel which is absent in the measurements at 225 *nm*. This highlights the importance of studying metastable dissociation of molecules at different wavelengths as it can bring additional insights into their fragmentation pattern. The most prominent difference between the *metastable dissociation maps* recorded at 225 and 270 *nm* was much stronger signal of the metastable dissociation of the parent ion into $m/z80$ fragment ion at 270 *nm* compared to 225 *nm*. Strong wavelength effects on the metastable dissociation of the excited parent ion are likely to be related to the level of vibrational excitation in the electronically-excited neutral prior to the absorption of the ionising photon. This is particularly intriguing for us because the level of vibrational excitation in multi-photon ionised 3-AP can reasonably be expected to be sensitive to the molecule's conformational state prior to the first photon absorption. Therefore, wavelength-dependent metastable dissociation experiments on Stark deflected 3-AP using the OU experiment described briefly in Section 7.3 would appear to have good potential for observing conformer-dependent unimolecular reactivity.

We explain the rich metastable dissociation pattern of 3-aminophenol observed in our experiments to be partially due to unusually high MPI signals from the molecule in the present experimental conditions. Our measurements of MPI signal as a function of 3-AP temperature have enabled us to get the first order estimation of the dependence of the molecule's vapour pressure on temperature and hence, by comparisons with thymine MPI results, indicate that the strong signals from 3-AP are unlikely to be solely ascribed to high target density. This suggests that neutral electronic excited state absorption and/dynamics are likely to be at least partially responsible for the strong signals in the present MPI

conditions. Accordingly, we are planning (further attempts at) VUV photoabsorption experiments on 3-AP in the future.

4.8 Contributions by co-workers

I carried out metastable dissociation experiments on 3-aminophenol at 225 *nm* and analysed the complex *metastable dissociation map* using a Matlab simulation, which is described in detail in Appendix A. I also carried out the experiments for the estimation of vapour pressure of 3-aminophenol and thymine. For the high-resolution experiments that led to the identification of hydrogen loss channels and the metastable dissociation experiments on 3-AP at 270 *nm*, I worked with fellow PhD student A. Rebelo in the Molecular Clusters Laboratory. I analysed the data from the above-mentioned experiments. All experimental and analytical work was supported by Dr. S. Eden and the results presented in Sections 4.3, 4.5 and 4.6 were published in [176]. Dr. J.-C. Poully performed the Density Functional Theory calculations. The co-authors of the paper that have not already been mentioned in this paragraph (N. J. Mason, P. Limão-Vieira and M. Ryszka) contributed to the work by editing the journal manuscript, aiding the development of the experimental facility, and/or co-supervising students that worked in the lab.

Chapter 5

Indirect laser-induced thermal desorption for the production of intact gas-phase nucleobase, nucleoside and nucleotide targets

This chapter begins with a review of the experimental approaches previously applied to produce gas-phase targets of thermally labile biomolecular species of low volatility such as RNA and DNA components. We then present a series of multi-photon ionisation time-of-flight (MPI-TOF) experiments that demonstrate the suitability of indirect laser-induced thermal desorption (ILTD) for the production of intact neutral gas-phase targets of the most fragile nucleobase guanine, and of the nucleosides uridine, 2′-deoxyuridine and 5-methyluridine. By contrast, we saw evidence for some thermal decomposition in *ILT*-desorbed thymidine and we were unable to produce a viable target of the nucleotide uridine 5′-monophosphate. This is the most extensive investigation to date of the efficacy and limits of using ILTD to study progressively more complex neutral biomolecules in the gas-phase.

5.1 Introduction

The *bottom-up* approach can provide valuable insights for unravelling complex processes initiated by radiation interactions with large biological structures, such as nucleic acids (ribonucleic acid - RNA or deoxyribonucleic acid - DNA). Nucleobases are the UV chromophores in RNA and DNA and the absorption of UV photons can result in the photodamage of nucleic acids [10]. In addition, ionisation in RNA/DNA generates an electron *"hole"* which is also most often located on the nucleobases [177]. As a result, nucleobases

are vulnerable parts of nucleic acids. Therefore, a very large number of studies have been dedicated to radiation-induced processes in these molecules. Starting from nucleobases, our understanding of radiation-induced chemistry can be systematically built by probing the radiation response of increasingly large subunits, i.e. nucleosides (nucleobase + sugar), nucleotides (nucleoside + phosphate group), oligonucleotides, RNA/DNA strands, etc. The present chapter tackles a major challenge in the experimental study of progressively more complex RNA/DNA components in the gas-phase: producing neutral targets with adequate number densities of thermally labile molecules without *target decomposition or reactivity*. In this thesis we use *target decomposition or reactivity* as a common term for any damage of sample molecules induced in the process of bringing them from the solid-phase (powders) into the gas-phase. This can be unambiguously thermal decomposition/reactivity or it can be *photo-induced* fragmentation/reactivity in the case of *direct laser-induced desorption* techniques where there is a direct interaction of the laser beam with the sample molecules (for more details see Section 5.2.3.1).

It is well known that increasingly large building blocks of nucleic acids are more susceptible to thermal decomposition. While producing high-density intact gas-phase targets of nucleobases such as adenine, thymine and uracil is relatively straightforward using *conventional* heating methods (for more details see Section 5.2.1), this is not the case for cytosine and guanine. Previous MPI-TOF experiments by the Molecular Clusters Group at the OU have shown that only very weak targets of intact cytosine can be produced by heating the sample in a supersonic expansion nozzle [57] and the same method has never proved to be successful in the case of guanine. Guanine as well as nucleosides and larger RNA/DNA components have been described as thermally labile species with very low volatility in the majority of the literature dedicated to gas-phase experiments on these biomolecules (see e.g. [64, 65]). Their volatilisation requires special attention and several experimental methodologies have been developed to address this issue. These are discussed in detail in Section 5.2.

While the production of ionic gas-phase biomolecular targets of low volatility has been to a great extent resolved thanks to the development of electrospray ionisation (successfully used for volatilising whole proteomes [178], viruses [179] as well as microbes [180]), no equivalently general solution is currently available for producing intact thermally labile neutral biomolecules in the gas-phase. Despite the well-known low volatility and thermal lability of guanine as well as nucleosides and larger RNA/DNA components, there are very few studies of target decomposition or reactivity presented in the literature on gas-phase experiments on these biomolecules. Furthermore, most of the papers which present

such studies show their degradation at some point when varying experimental conditions. This suggests that studying target decomposition or reactivity of the above-mentioned species is crucial for ensuring that only intact neutral target molecules are probed. This becomes particularly important when high target densities are required, for example to study dissociative electron attachment which is typically a low-cross-section process (e.g. for uracil the maximum electron impact ionisation cross section is about $1.6 \times 10^{-19}\,m^2$ and the maximum dissociative electron attachment cross section is about $2.5 \times 10^{-21}\,m^2$ [181]) and requires low electron beam currents (order of μA to nA depending on the energy resolution required).

The most promising techniques for the production of intense gas-phase targets of neutral thermally labile biomolecules have generally been the ones where a laser is used for their desorption. This is largely due to lasers offering opportunities for highly-localised energy deposition as well as very short *heating* times. In our experiments on guanine as well as nucleosides and a nucleotide, indirect laser-induced thermal desorption (ILTD) was chosen as a tool for their volatilisation. We considered that its greater potential to succeed in this intricate task compared to most other laser-based techniques comes from the fact that in ILTD there is no direct laser interaction with sample molecules which removes the risk of unwanted photo-induced fragmentation/reactivity.

Although ILTD has been previously applied in experiments on the nucleobase uracil and the nucleosides adenosine, thymidine, cytidine and guanosine [8, 43, 66], only in the study of uracil [9] has the potential thermal decomposition induced by the desorption laser been investigated (comparing relative fragment ion signals from photo-ionised uracil as a function of desorption laser power). Uracil is one of the nucleobases that can be brought into the gas-phase most readily without thermal decomposition so it is not a very *challenging* test case for the capabilities of ILTD. This chapter provides evidence that guanine as well as the uracil-related nucleosides uridine, 2′-deoxyuridine and 5-methyluridine can be produced in the gas-phase by ILTD without thermal decomposition/reactivity, while in the case of thymidine we observed some evidence for thermal decomposition in all the conditions we tested. Hence, the chapter also illustrates some limits of the technique and our unsuccessful efforts to produce gas-phase uridine 5′-monophosphate suggest that ILTD does not have good potential for experiments on nucleotides.

It is worth noting here that characterising and understanding the thermal stability of different DNA/RNA subunits has relevance beyond the practicalities of producing gas-phase experimental targets. The low-lying singlet electronic excited states of gas-phase nucle-

osides feature efficient and rapid (e.g. $\sim 100\,fs$ for thymidine [43]) internal conversion pathways to the electronic ground state. Therefore, much of the dissociation of isolated nucleosides following electronic excitation can be expected to take place in high vibrational levels of the electronic ground state, enabling analogies to be drawn with thermal decomposition experiments.

5.2 Review of experimental methodologies for the production of intact gas-phase targets of biomolecules with low volatility

Here we provide a review of the experimental techniques that have been developed to tackle the problem of low volatility in combination with high thermal lability of biological molecules for gas-phase experiments. The techniques are critically discussed with respect to their advantages/disadvantages and representative examples within their subgroups are schematically summarised in Fig. 5.1.

5.2.1 *Conventional* heating techniques

The majority of the experimental set-ups for gas-phase experiments on relatively simple volatile solid-phase molecular targets use resistive heaters to sublimate the molecules either directly in vacuum using effusive ovens or in a supersonic expansion nozzle for seeding molecules in a carrier gas to produce molecular beams. These two methods are described in Sections 5.2.1.1 and 5.2.1.2. In their summary of the literature on gas-phase nucleosides, Li and Lubman [182] noted that more polar nucleosides, such as cytidine and guanosine, as well as all nucleotides are not amenable to thermal vaporisation without degradation. Following a chain of similar referenced statements in earlier papers [183, 184] leads to Hecht et al's mass spectrometry study of ribonucleoside components of transfer RNA [185], although it should be noted that this work does not provide details about how thermal decomposition was recognised.

Volatilisation of chemical compounds can be increased by chemically converting a polar group (e.g. carboxyl or hydroxyl group) into a non-polar one. Derivatisation techniques (derivatisation is a chemical reaction where a compound is transformed into a derivative product with improved physicochemical properties) such as silylation, alkylation or acylation are frequently used prior to gas-chromatography analysis to increase stability and volatility of analysed samples [186, 187]. Trimethylsilyl derivatisation was widely used for structural characterisation of nucleosides by electron impact ionisation mass spectrometry

[188, 189]. Despite increased thermal stability of nucleosides upon trimethylsilylation, this method may be accompanied by various chemical artifacts and uncertainties in the mass spectra [182, 190]. It often also results in low molecular ion abundances due to low conversion yields especially for deoxynucleosides containing pyrimidines [182, 189].

5.2.1.1 *Conventional* heating in vacuum

In the case of effusive ovens, the solid samples are heated in vacuum and molecules arrive at the interaction region through an orifice in the oven (see Fig. 5.1 a)). The separation of the sample and interaction region is much smaller than the mean free path of the molecules (so-called effusive beams) and there are negligibly few collisions of the molecules during the process of sublimation/expansion. In most effusive oven designs the sublimated molecules will collide with the hot oven walls and with the remaining hot condensed sample many times before exiting through the small orifice. As a result, the molecules produced in the gas-phase by heating powders in an effusive oven will have similar translational and internal temperatures as the oven temperature [59, 191]. Effusive ovens have been widely used for gas-phase experiments on nucleobases [59–63, 65, 192]. In addition to effusive ovens, samples can be vaporised directly in the ionisation chamber, e.g. by heating them at the bottom of the chamber [193] or by other systems in commercial machines, e.g. so-called *direct insertion probes* or *heated sample probes*. The common signature of these systems is that samples are normally loaded in a small container/cell/capillary which is then heated [183, 194].

Levola et al. [195, 196] were able to produce intact gas-phase targets of the nucleosides uridine, thymidine and 5-methyluridine by heating the powder samples in an effusive oven. However, their experiments showed evidence for thermal decomposition of thymidine and uridine above certain threshold temperatures, which highlights the importance of studying thermal decomposition/reactivity of nucleosides when using *conventional* heating techniques in vacuum. Such tests are, however, often absent in the literature [183, 194, 197–199].

5.2.1.2 *Conventional* heating in a carrier gas

Conventional supersonic beams of carrier gas seeded with molecular targets sublimated in an expansion nozzle have been used extensively over past decades to carry out gas-phase experiments on a variety of biologically relevant isolated molecular targets and clusters [18, 26, 47, 148, 200, 201, and references therein]. Supersonic beams are produced by expansion of a gas at higher pressure through an orifice of a nozzle that is significantly larger than the mean free path of the expanding gas molecules into a chamber at lower

pressure (see Fig. 5.1 b)). Importantly, the expansion allows numerous collisions between the molecules and/or atoms in the gas. Therefore, supersonic beams of noble gases (typically He, Ne and Ar) seeded with small fractions of sublimated molecular species of interest (normally up to 10%) allow experimentalists to cool the internal degrees of freedom of molecules as well as to narrow their range of translational energies dramatically (see Section 3.2.2). Some expansions like this use a *simple* orifice (pinhole or some other shape, e.g. conical) to create a continuous expansion [18], while many other experiments use pulsed nozzles [148] in order to allow a greater pressure difference for a given amount of pumping.

The stable target density, and the level of cooling and control that supersonic molecular beams provide have been exploited in a broad range of gas-phase spectroscopy and dynamics experiments on nucleobases such as uracil [18, 202], thymine [47, 115], adenine [200, 203] and cytosine [61, 204]. Supported by theoretical calculations [45, 205, 206], experiments of this kind have provided valuable information on their intrinsic structural and dynamic properties. The excited-state dynamics of adenine has been most investigated amongst all nucleobases [207]. Adenine is thermally stable and predominantly exists in a single tautomeric form ($NH9$) in cold molecular beams [208], which simplifies the analysis and interpretation of experimental results. In contrast, experimental studies on guanine are much more rare compared to other nucleobases, which is undoubtedly linked to the difficulties of bringing the molecule into the gas-phase without thermal decomposition or reactivity as has been previously discussed in the literature [64, 65] as well as to the presence of several tautomers of guanine in molecular beams [209]. The experiments in the Molecular Clusters Laboratory on guanine and the nucleoside uridine heated in the supersonic expansion nozzle always resulted in thermal decomposition and/or reactivity (for more details see Sections 5.4.1 and 5.4.2, respectively).

It should be noted that not all experiments using carrier gases involve supersonic expansions (e.g. [16, 210]). Ptasińska et al. [16] used a carrier gas to transfer uridine and thymidine vaporised in an effusive oven to the interaction region for electron impact ionisation experiments. Although they were able to find experimental conditions (heating at $< 147\,^{\circ}C$) for thymidine where thermal decomposition was absent (not investigated for uridine), the subsequent dissociative electron attachment experiments on thymidine by the same group [211] showed signatures of thermal decomposition even at $125\,^{\circ}C$, which is well below the threshold in the previous study. The above-mentioned examples suggest that employing *conventional* heating techniques for the production of gas-phase nucleobase guanine, nucleosides and larger RNA/DNA components is not straightforward

and alternative more *"gentle"* volatilisation methods can be more effective (or in some cases essential).

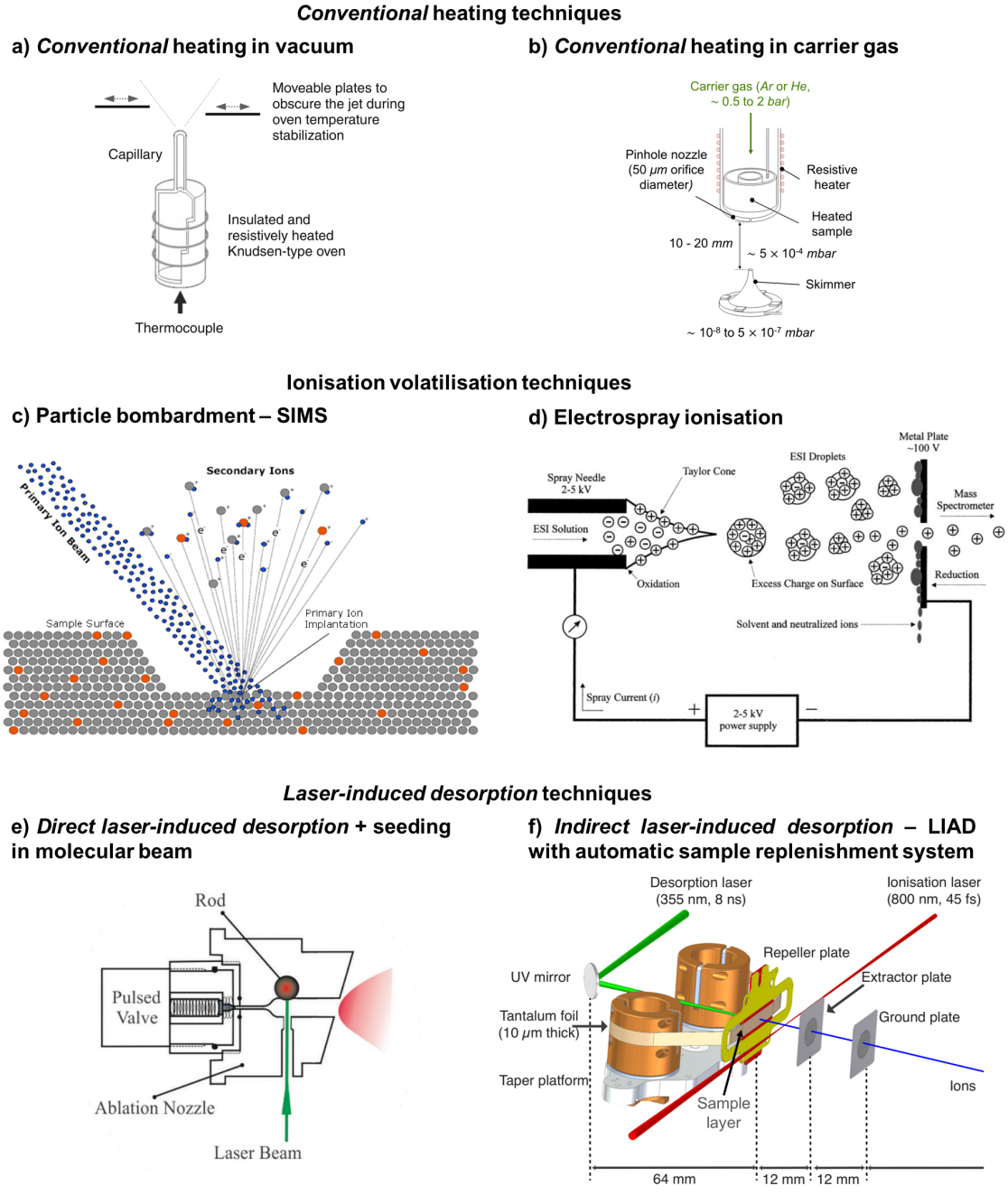

Fig. 5.1: Schematic representations of examples of experimental systems for the production of gas-phase molecular species. a) and b) denote volatilisation of samples by conventional heating in an effusive oven [155] and a supersonic expansion nozzle [57], respectively; c) and d) production of gas-phase molecular ions by secondary ion mass spectrometry (SIMS [212]) and electrospray ionisation [213], respectively; e) and f) represent *direct* [214] and *indirect laser-induced desorption* techniques (in this case laser-induced acoustic desorption - LIAD [215]).

5.2.2 Ionisation volatilisation techniques

The production of charged species (both positive and negative) in the gas-phase can be achieved by particle bombardment techniques (fast atom bombardment [216], secondary ion mass spectrometry [217] and plasma desorption ionisation [218]) as well as by field desorption [219] and electrospray ionisation [220, 221]. Although *direct laser-induced desorption* also belongs to this category, it will be discussed in detail in a separate section which is dedicated to the methods in which a laser is used as a desorption tool (see Section 5.2.3). In fast atom bombardment (FAB) and secondary ion mass spectrometry (SIMS, see Fig. 5.1 c)), the production of ionic species is a result of bombarding a sample surface by high-energy atoms or primary ions, respectively, which leads to the ejection of sample ions. In plasma desorption ionisation (PDI), a sample is deposited on a thin foil and on the opposite side of the foil highly exothermic fission process releases high energy ion pair fission fragments. These induce rapid localised heating of the foil and generation of positive and negative sample ions. It should be noted that neutrals are produced along with the ions in the FAB, SIMS and PDI. In contrast, field desorption produces solely ionic species. This technique is based on using very intense electric fields to ionise molecules deposited on a surface of a specially prepared emitter. The production of intact molecular ions and neutrals in the above-mentioned methods is often accompanied by fragmentation induced in the process of desorption and contamination by matrix species can also be an issue (*matrix-assisted* approaches are mentioned in Section 5.2.3.1 but are also relevant to particle bombardment techniques) [222].

Electrospray ionisation (ESI) has become established as the dominant method for the production of gas-phase ions of thermally labile molecular species such as nucleotides [220] and peptides [221]. The development of ESI was initiated by Dole in 1960s and then subsequently enhanced by Fenn who was awarded a Nobel Prize in Chemistry in 2002 for the invention of electrospray ionisation mass spectrometry [223]. In ESI (see Fig. 5.1 d)), a solution containing analyte molecules is pumped through a capillary at low rates ($10^{-1} - 10 ml/min$). A high voltage (either negative or positive) is applied to the capillary which provides an electric field gradient in space for charge separation at the surface of the liquid. Liquid protrudes through the tip of capillary in a *"Taylor cone"*. At the point where the Coulombic repulsion of surface charge equals the surface tension of the solution, droplets with excess positive or negative charge detach from the tip. As the solvent evaporates, the increased charge density results in Coulombic repulsion releasing ions from droplet surfaces. In addition, a buffer gas may be introduced in the expanding stage of the droplets to allow for collisional cooling of ions as well as to enhance the removal of solvent molecules [207, 224].

As outlined above, the study of ionic species of low volatility in the gas-phase has been greatly advanced thanks to the development of ESI. A big advantage of producing charged targets is that they can be manipulated relatively easily, for example trapped and/or mass-selected, prior to any further interactions with photons/electrons/ions and spectroscopic or mass spectrometric analysis. In addition, studying charged species is relevant from a biological point of view as many molecules are present in ionic forms within cells [207]. However, in many other cases, the neutral molecule is most biologically- or astrochemically- relevant and it should be noted that positively and negatively charged ions can have significantly different characteristics and radiation responses compared to neutrals. Several groups previously built experimental apparatuses for the neutralisation of charged species produced by ESI [225, 226]. However, the weak points of such techniques are extremely low target densities and/or risk of potential damage of biomolecules in the process of neutralisation. Hence, despite the development of ESI, no equivalent *universal* method is available for producing intact thermally labile neutral biomolecules in the gas-phase. Consequently, a significant area of research has developed around the use of lasers for the volatilisation of large fragile biologically relevant molecules.

5.2.3 *Laser-induced desorption* techniques

The term *laser-induced desorption* usually refers to a technique where gas-phase species are formed by irradiating a sample by a pulsed laser beam [227]. In the context of this thesis, however, we will use it as a common term for all of the methods where a laser is used as a tool for initiating desorption of sample molecules. This can happen either by *direct* irradiation of the sample surface with a laser beam, hence *direct laser-induced desorption* techniques, or *indirectly* by irradiating the back of a substrate (normally a thin foil) on which the sample is deposited, hence *indirect laser-induced desorption* techniques.

5.2.3.1 *Direct laser-induced desorption* techniques

As stated above, in the terminology of this thesis, *direct laser-induced desorption* covers all of the techniques where there is a *direct* irradiation of the sample by a desorption laser (e.g. see Fig. 5.1 e)), irrespective of the presence or absence of matrix molecules. It was first introduced for the vaporisation of organic salt ions by laser (pulsed ruby laser, $694.3\,nm$, output $0.1\,J$, pulse length $400-500\,\mu s$) irradiation in 1966 by Vastola et al. [228]. Beavis et al. [229] argued that the use of matrix molecules can prevent thermal decomposition of fragile target molecules in the desorption process. The most commonly used matrix for such experiments has been graphite and focused Nd:YAG laser pulses

(used directly or after harmonic conversion) are normally employed for the desorption, e.g. $532\,nm$, energy density $0.5\,Jcm^{-2}$ per pulse [230]. However, a recent paper by Peña et al. [231] reported significant photo-induced fragmentation of uridine upon direct laser ablation (a small amount of commercial binder was mixed with the sample and pressed in the cylindrical rods, prior to exposure to $355\,nm\ ps$ laser pulses) in all the laser ablation conditions tested by the authors. We expect the photo-induced fragmentation/reactivity in the *direct laser-induced desorption* techniques to be mainly thermal damage, i.e. intense local heating due to vibrational excitation of molecules in the sample by photo-absorption. An important variant of *direct laser induced desorption* is matrix-assisted laser desorption/ionisation (MALDI), invented in the 1980s by M. Karas and F. Hillenkamp [232]. This involves mixing analyte molecules with strategically chosen matrix molecules in the condensed sample prior to laser exposure. The rationale is that matrix molecules absorb laser energy and are evaporated carrying the analyte molecules with them into the gas-phase [233]. However, it is well known that MALDI can cause ionisation as well as photo-induced fragmentation of relatively delicate molecules [234]. Moreover, some experiments are compromised by the presence of vaporised matrix molecules in the target [234, 235].

Another type of sample preparation in *direct laser-induced desorption* experiments involves forming a very thin sample layer on a substrate. This was, for example, employed for the production of polar non-volatile bio-organic molecules such as disaccharide sucrose, digoxin, digitonine, arginine, adenosine and its monophosphate (also disodium salt), etc. by Posthumus et al. [236]. Samples were dissolved in methanol or water and a small amount of the solution was dried on stainless steel probes forming invisible layers. In addition to the sublimation, laser interaction with the sample caused ionisation of the sample molecules (for more information about ionisation volatilisation techniques see Section 5.2.2). Li and Lubman [182] argued that using a rather *low* power CO_2 desorption laser (maximum output $40\,mJ$) prevents ionisation of sample molecules in the desorption process and that using relatively thin sample layers prevents thermal decomposition of the sample as most of the laser energy is absorbed by the substrate. Indeed, the authors mentioned that using the desorption laser in the fluence range of 10^6 to $2\times10^7\,Wcm^{-2}$ did not affect the multi-photon ionisation mass spectra of studied molecules. However, the paper does not show the authors' evidence for the absence of any effect of desorption laser power on the mass spectra and hence for the lack of thermal decomposition of the sample. Examples of targets that have subsequently been produced using *direct laser-induced desorption* include gas-phase neutral tryptophane [237], DNA base pairs [238], and guanosine and its derivatives [239].

In comparison with *conventional* heating techniques, a key advantage of the *direct laser-induced desorption* techniques is that very high target density can be achieved by placing the sample close to the interaction region (typically several *mm*). In addition, the heating process is very rapid (e.g. *ns*-timescale), after which the desorbed molecules cool due to phase-change and expansion. Therefore, the time during which the samples can thermally decompose can be significantly reduced.

5.2.3.2 *Indirect laser-induced desorption* techniques

In order to avoid the ambiguities related to photo-induced fragmentation of sample molecules by desorption laser beams, *indirect laser-induced desorption* techniques were developed, notably laser-induced acoustic desorption (LIAD) in the 1980s [234] later followed by indirect laser-induced thermal desorption (ILTD).

5.2.3.2.1 Laser-induced acoustic desorption (LIAD)

The basic mechanism of LIAD is that a sample is deposited on one side of a thin metal foil (usually 5 to 25 μm thick Ti or Ta) and the back of the foil is irradiated by a pulsed focused laser beam (normally first, second or third harmonic of Nd:YAG laser, pulse duration of several *ns*, typical fluence 10^8 to $10^9 Wcm^{-2}$) in order to achieve molecular desorption. There is no direct interaction between the desorption laser pulses and the sample molecules, which significantly reduces the risk of unwanted changes in the mass spectra. The exact mechanism behind the desorption process in LIAD has been extensively discussed and studied. The first experimental application and observations of LIAD for nonvolatile organic compounds by Lindner and Seydel [240] suggested that laser-generated acoustic waves were responsible for the desorption of the molecules, hence the term *"acoustic desorption"*. There was considerable optimism that LIAD would essentially solve the problem of bringing of intact complex neutral species into the gas-phase as it was assumed there was no thermal contribution in the desorption process. A number of groups have applied it since its invention in the 1980s with varying degrees of success. Further studies have reported LIAD bringing light-sensitive and thermally labile biological species into the gas-phase ranging from amino acids [120, 241] and peptides [242, 243], to whole viruses, bacteria and cells [244]. Within our own network of collaborators, Greenwood and co-workers and Denifl and co-workers attempted LIAD but never obtained evidence that convinced them of significant non-thermal desorption (private communications), whereas Illenberger, Bald and co-workers used the method to

produce satisfactory D-ribose-5-phosphate targets [245].

Later studies by Zinovev et al. [246] showed that direct energy transfer from an acoustic wave to sample molecules adsorbed on the foil is unlikely. They presented evidence indicating that both thermal and acoustic waves generated by laser irradiation are responsible for surface stresses between the substrate and molecular sample which then trigger surface reorganisation. They argued that the desorption itself can be a result of two different mechanisms: (i) the cracking in microscale or nanoscale crystals and consequently the formation of local desorption sites and/or (ii) the formation of non-equilibrium electronic states on the foil surface that are repulsive to the adsorbed sample molecules. This incomplete understanding of the underlying hinders optimising and controlling LIAD and can also lead to uncertainty in the interpretations of experimental results. Furthermore, LIAD brings practical difficulties associated with short measurement times because thin sample deposits are typically required which last only a few hundred pulses of a focused laser beam as well as unstable signal intensity due to gradual sample depletion. Moving foil systems can be used to extend measurement times at the expense of increased design and construction complexity.

To better understand and optimise LIAD, Küpper and co-workers at the Deutsches Elektronen-Synchrotron (DESY) [215] developed a new LIAD source in 2018 for use at central facilities such as free-electron lasers. The new source allows longer measurement times (several hours) with stable signal intensities and a fixed interaction point thanks to the automatic sample replenishment system based on a rotating tape drive (see Fig. 5.1 f)). Their [215, 247] strong-field ionisation experiments on phenylalanine, adenine and glycine supported Zinovev et al.'s desorption model based on surface stress between the substrate and molecular sample [246]. However, the experiments also showed a correlation between high translational temperature of desorbed molecules and increased fragmentation during their journey in the vacuum chamber. This suggests LIAD has limitations with respect to the study of thermally labile molecules. It should be noted that the material properties of the substrate, the sample layer thickness and the sample itself can affect the translational temperature of desorbed molecules and their investigation could help to optimise the use of LIAD for the production of intact thermally unstable molecules in the future. Rapid cooling of the internal and external modes of the molecules after desorption using buffer-gas cells or entrainment in cold molecular beams might prevent additional fragmentation and is currently under investigation in their laboratory. Cooling of desorbed molecules by their entrainment in a supersonic jet expansion has been previously used for *direct laser desorption* methods [182, 231]. A major constraint is a significant reduction

of the target density after the entrainment of desorbed molecules in a gas-jet expansion. Arrowsmith et al. [248] investigated the entrainment of material vaporised with a laser pulse (excimer laser, 248 nm, 20 ns laser pulses, energies $30 - 60\,\mu J$, 1 mm diameter spot on the sample surface) in a jet expansion (pulsed valve, diameter 0.5 mm) from a surface positioned 0.7, 1.7 and 2.7 mm from the jet orifice. He and Ar were used as carrier gases, and perylene was the test substance. They showed that the width of the perylene concentration profile was much narrower than the width of the gas expansion, especially in He, which enabled them to extract about 1 % of the material entrained in the jet expansion through the skimmer.

5.2.3.2.2 Indirect laser-induced thermal desorption (ILTD)

Greenwood and co-workers at Queen's University Belfast modified the existing concept of LIAD by replacing the pulsed desorption laser (third harmonic of Nd:YAG, pulse duration $5 - 6\,ns$, fluence $> 10^8\,W\,cm^{-2}$, focused) for a continuous wave (CW, 100 mW, 532 nm, focused) one [8]. As the desorption process must be purely thermal, the technique can be called *indirect laser-induced thermal desorption* (ILTD), although it has also been referred to as *laser thermal desorption* [8] and *laser-based thermal desorption* [9]). Despite the thermal nature of ILTD, it is considered to be a more *"gentle"* way of bringing molecules into the gas-phase compared to *conventional* oven systems that typically involve either heating the sample in an effusive oven or in a supersonic expansion nozzle. An important difference is that molecules do not repeatedly undergo cycles of evaporation and condensation. The heating time is much shorter than in *conventional* heating sources due to the low thermal mass of the foil and the sample. Our experience is that this is $\leq$ *a few seconds*, i.e. we see ions in multi-photon ionisation experiments as soon as we turn on our desorption laser. Hence the heating time can be viewed as being somewhere in between a typical direct laser desorption system (where intense heating occurs on the timescale of a laser pulse) and a conventional thermal source whose temperature is typically raised gradually over an hour or more. Moreover, gas-phase targets are formed only few mm (1 to 3 mm) from the place where they interact with a laser beam (or possibly electrons/protons/ions etc.), which reduces the effective time in which molecules can thermally decompose [43]. Unlike in *direct laser-induced desorption* techniques and in common with LIAD, the desorption laser in ILTD does not directly interact with sample molecules. In addition to the unambiguous desorption mechanism, ILTD has the advantage over LIAD of allowing a relatively thick sample deposit attached to the foil, which can last for many hours of experiments before depleting. In contrast, LIAD is usually performed using very thin sample layers, which despite using moving foil and/or laser focus systems

(complicated to assemble) still result in limited experimental times and this represents a significant barrier to many types of experiments (private communication with Prof. Dr. I. Bald).

5.2.4 Testing for target decomposition or reactivity in gas-phase guanine, uridine, thymidine, 2'-deoxyuridine and 5-methyluridine

Tests for target decomposition or reactivity (thermal decomposition/reactivity or photo-induced fragmentation/reactivity in the case of *direct laser-induced desorption* techniques) are normally based on searching for differences in the mass spectra (e.g. changes in the relative signals of different ions or the appearance of new peaks) as a function of experimental conditions such as time, temperature (when using *conventional* heating techniques) or desorption laser power (when using *laser-induced desorption* techniques). Complementary techniques can also be applied, e.g. ^1H nuclear magnetic resonance spectroscopy of the remaining solid sample after an experiment [17, 249] or rotational spectroscopy [231].

The experiments presented in this chapter probe the production of neutral gas-phase targets of the nucleobase guanine as well as the nucleosides uridine, thymidine, $2'$-deoxyuridine and 5-methyluridine by indirect laser-induced thermal desorption (ILTD). Several experimental approaches have been applied to bring these molecules into the gas-phase and they are listed in the third column in Tabs. 5.1 to 5.4. It should be noted that we only list those techniques where neutral species were produced. The last column presents comments by the papers' authors with respect to target decomposition/reactivity, while the column *"Evidence shown"* indicates whether authors present direct evidence of the tests of target decomposition/reactivity of their samples. Tabs. 5.1 to 5.4 present also information about the type of experiments which were carried out for each molecule (second column). Each molecule will be discussed in more detail in Section 5.4. In this section we would like to give the reader a general picture of whether target decomposition/reactivity is an issue in experiments on the above-mentioned molecules and what is the state of the literature with respect to providing direct evidence of the presence or absence of target decomposition/reactivity.

We will define here the terminology which is used in this thesis when referring to nucleic acid constituents. We will refer to nucleobases as B, to dehydrogenated nucleobases as $(B-H)$ and to hydrogenated nucleobases as BH. Nucleosides consist of a nucleobase unit (a dehydrogenated nucleobase $(B-H)$) and a sugar unit (*ribose minus OH* or $2'$-

deoxyribose minus OH) bound together by a glycosidic bond. We will refer to the sugar part of a nucleoside as S, to the dehydrogenated sugar part as $(S-H)$ and to the hydrogenated sugar part as SH. This abbreviation scheme is convenient for drawing comparisons between different nucleosides, irrespective of their specific base and sugar components.

Despite the well-known low volatility and lability of the above-mentioned molecules with respect to thermal decomposition (documented by a large proportion of authors commenting on potential thermal decomposition of the sample in their papers), only a limited number of papers provide *direct evidence* of tests for target decomposition or reactivity induced in the process of volatilisation (see the red and green rows in Tabs. 5.2 to 5.4). For example for guanine, most authors highlighted thermal decomposition as an issue and described their strategy for minimising or eliminating this possibility, usually mentioning specific types of test (see the last column in Tab. 5.1). However, it is very rare to actually present these results (see the fourth column in Tabs. 5.1 to 5.4) so the reader can appreciate how conclusive they are. It is remarkable that none of the gas-phase studies of guanine made any evidence of this kind available for scrutiny.

Thermal decomposition of the nucleosides uridine, thymidine, $2'$-deoxyuridine and 5-methyluridine was studied by several authors (see the red and green rows in Tab. 5.2 to 5.4). Only one study by Levola et al. [196] showed that there was no target decomposition/reactivity of 5-methyluridine at any investigated experimental conditions (see the green row in Tab. 5.4). All of the other ones showed decomposition of the sample at certain point (see the red columns in Tabs. 5.2 and 5.3) and two of the studies [211, 231] never managed to completely eliminate target decomposition of their samples at any investigated experimental conditions.

Indirect laser-induced thermal desorption is a relatively young technique (first reported by Poully et al. [8] in 2015) and to the best of our knowledge there have been only three papers presenting experiments on gas-phase nucleosides (thymidine, adenosine, guanosine, and cytidine – not uridine) produced by ILTD (see the light blue rows in Tabs. 5.3 and 5.4). These papers showed that a large proportion of the target comprises intact nucleosides (high yields of parent ions or alternatively high yields of fragment ions which had previously been shown to be due to the fragmentation of intact parent ions), but they did not present evidence to rule out some thermal decomposition induced by the desorption laser.

Tab. 5.1: Literature review on volatilisation techniques and tests of target decomposition or reactivity in experiments on guanine (DLID - *direct laser-induced desorption*, all the acronyms in the second column are defined in the List of acronyms on pages XXXI to XXXIII).

Authors [reference] (year)	Type of experiments	Volatilisation technique	*Evidence shown	Authors' comments with respect to potential target decomposition or reactivity
Guanine				
Rice and Dudek [166] (1966)	EII	Heating using a direct insertion probe (temperature not specified).	X	No comments.
Hush and Cheung [250] (1975)	PeS	Heating using a heated sample probe (temperature not specified).	X	Authors argue that where thermal decomposition was suspected, the remaining material in the sample tubes was examined by mass spectrometry.
Dougherty and McGlynn [251] (1977)	PeS	Heating (method not specified, $300\,^{\circ}C$).	X	No comments.
Dougherty [252] (1978)	PeS	Heating using a heated sample probe (temperature not specified).	X	Authors argue that samples were tested for signs of thermal decomposition such as change of colour, charring or time-dependence of a spectrum.
Lin et al. [253] (1980)	PeS	Heating using a heated sample probe ($340\,^{\circ}C$).	X	Thermal decomposition observed when heated above $340\,^{\circ}C$ for more than $30\,mins$.
AIST: SDBS [146] (1999)	EII	Heating (method not specified, $290\,^{\circ}C$).	X	No comments.
Abdoul-Carime et al. [63] (2005)	DEA	Heating in an effusive oven ($227\,^{\circ}C$).	X	Authors argue that thermal decomposition was absent as the sample temperature was lower than in Lin et al.'s experiments [253] (see above).
Choi and Miller [64] (2006)	IRLS	Heating in an oven ($350\,^{\circ}C$) + seeding in He nanodroplets.	X	Negligible thermal decomposition noted on the basis of the assignments presented in their work. Spectral signatures of potential decomposition products should be possible to spot, however these were absent.
Plekan et al. [254] (2007)	PEPICO	Heating in a home-built furnace ($370\,^{\circ}C$).	X	Authors argue that thermal decomposition was absent as the evaporation temperature was similar ($20\,^{\circ}C$ higher) to the one previously successfully used by Choi et al. [64].
Zaytseva et al. [255] (2009)	PeS	Heating in a home-built furnace ($327\,^{\circ}C$).	X	Absence of thermal decomposition noted on the basis of photoionisation mass spectroscopy measurements.
Zavilopulo et al. [65] (2009)	EII	Heating in an effusive oven ($147-367\,^{\circ}C$).	X	Absence of thermal decomposition noted on the basis of no increase in the intensity of H_2O^+ and $CO_2{}^+$ fragments (referring to a single mass spectrum at $337\,^{\circ}C$) and no change of the colour of guanine powder. Authors ascribe changes in the intensity of ion signals with increasing temperature to the vibrational excitation of molecules.
Minaev et al. [192] (2014)	EII, DEA	Heating in an effusive thermal multichannel source with a system of collimating slits ($\leq 137\,^{\circ}C$).	X	Authors argue that temperatures $\leq 137\,^{\circ}C$ are below thermolysis limit for guanine.
Ostroverkh et al. [256] (2019)	EII	Heating in an effusive thermal multichannel source ($137-357\,^{\circ}C$).	X	No comments on target decomposition or reactivity. Authors ascribe changes in the intensity of ion signals with increasing temperature to the vibrational excitation of molecules.
Zhou et al. [257] (2009)	SPI	Heating in a supersonic expansion nozzle (300, 325 and $395\,^{\circ}C$), DLID (graphite matrix) coupled to supersonic expansion.	X	No comments.
Li and Lubman [182] (1989)	MPI	DLID coupled to supersonic expansion.	X	Authors argue that by adjusting desorption laser parameters, the fragmentation induced by the desorption laser can be controlled.
Nir et al. [258] (1999)	MPI	DLID coupled to supersonic expansion.	X	Authors argue that the wavelength dependence of fragments was essentially identical to parent ions which suggests that fragmentation was not a result of the desorption process.

*Paper *directly* presents results of the study of target decomposition/reactivity: ✓ = *yes*, X = *no*.

Tab. 5.2: Literature review on volatilisation techniques and tests of target decomposition or reactivity in experiments on guanine and uridine (DLID - *direct laser-induced desorption*, all the acronyms in the second column are defined in the List of acronyms on pages XXXI to XXXIII); continued.

Authors [reference] (year)	Type of experiments	Volatilisation technique	*Evidence shown	Authors' comments with respect to potential target decomposition or reactivity
Guanine continued				
Nir et al. [259] (2001)	MPI, SHB	DLID coupled to supersonic expansion.	X	No comments.
Piuzzi et al. [230] (2001)	MPI, LIF, SHB	DLID (graphite matrix) coupled to supersonic expansion.	X	No comments.
Chin et al. [260] (2002)	MPI, LIF	DLID (graphite matrix) coupled to supersonic expansion.	X	No comments.
Mons et al. [261] (2002)	IRS, UVS	DLID coupled to supersonic expansion.	X	No comments.
Nir et al. [209] (2002)	MPI	DLID coupled to supersonic expansion.	X	No comments.
Alonso et al. [262] (2009)	RS	DLID coupled to supersonic expansion.	X	No comments.
Uridine				
Biemann and McCloskey [263] (1962)	EII	Heating using a hot filament system (temperature not specified).	X	No comments.
Rice and Dudek [194] (1969)	EII	Heating using a direct insertion probe (temperature not specified).	X	No comments.
Hecht et al. [185] (1970)	EII	Heating using a direct insertion probe (temperature not specified).	X	No comments.
Wilson and McCloskey [183] (1975)	ChI	Heating using a direct insertion probe ($180 - 290\,^{\circ}C$).	X	No comments.
Smith et al. [264] (1983)	EII, DEA	Heating using a direct insertion probe (temperature not specified).	X	No comments.
Ptasińska et al. [16] (2005)	EII	Heating in an effusive oven and seeding in carrier gas ($117 - 167\,^{\circ}C$).	X	No comments.
Levola et al. [196] (2014)	SPI	Heating in a quartz crucible of an effusion cell ($125 - 170\,^{\circ}C$).	✓	The ratio of B^+/BH^+ was studied as a function of temperature. The increase starting at $140\,^{\circ}C$ indicates thermal decomposition.
NIST [265] (2014)	EII	Not specified.	X	No comments.
Almeida [266] (2014)	PCol	Heating by a lamp in an effusive oven ($\sim 132\,^{\circ}C$).	X	Authors argued that they observed major differences in the relative intensities of fragment anions and appearance of new peaks in TOF mass spectra at $160\,^{\circ}C$ (not presented in the paper) and that temperature of $\sim 132\,^{\circ}C$ was chosen for the experiments presented in the paper to compromise between signal intensity and avoiding thermal decomposition.
Itälä et al. [198] (2015)	PEPIPICO	Heating in an effusion cell with integrated cooling shroud (MBE Komponenten NTEZ40 oven).	X	Authors argue that the evaporation temperature was around $132\,^{\circ}C$, which is below the thermal decomposition temperature in Levola et al.'s experiments [196] (see above).
Peña et al. [231] (2015)	RS	DLID (commercial binder) coupled to supersonic expansion.	✓	Significant photo-induced fragmentation effects: rotational spectra dominated by the presence of the lines belonging to uracil and some common decomposition products of sugars and nitrogen bases such as acetic acid, cyanoacetylene, glyoxylic acid, vinyl cyanide, glyceraldehyde and water complexes.
Muftakhov and Shchukin [267] (2013)	DEA	Heating at the bottom of the ionisation chamber ($\sim 130\,^{\circ}C$).	X	Authors argued that after the experiment the colour of the sample did not change which they considered as a proof of the absence of thermal decomposition.

*Paper *directly* presents results of the study of target decomposition/reactivity: ✓ = *yes*, X = *no*.
•*Red* signifies *presence* of target decomposition/reactivity demonstrated when varying experimental conditions.

Tab. 5.3: Literature review on volatilisation techniques and tests of target decomposition or reactivity in experiments on uridine and thymidine (all the acronyms in the second column are defined in the List of acronyms on pages XXXI to XXXIII); continued.

Authors [reference] (year)	Type of experiments	Volatilisation technique	*Evidence shown	Authors' comments with respect to potential target decomposition or reactivity
Uridine continued				
Muftakhov and Shchukin [268] (2018)	DEA	Heating at the bottom of the ionisation chamber ($130\,^{\circ}C$).	X	Authors commented that m/z132 is a dominant peak in DEA (around $0\,eV$) to ribose [269] and that their DEA experiments on uridine produced insignificant amounts of m/z132 anions (relative intensities $\leq 1\,\%$) which indicates insignificant thermal decomposition of uridine. However, it should be noted that ribose itself has not been observed previously as a thermal decomposition product of uridine (whose sugar unit is *ribose minus OH*).
Muftakhov and Shchukin [193] (2019)	DEA	Heating at the bottom of the ionisation chamber ($\sim 130\,^{\circ}C$).	X	Authors first dried the nucleoside at low temperatures in the chamber to minimise the possibility of reactions with associated water molecules. They also commented that m/z132 anions are produced by DEA to ribose [269] and that their DEA experiments on uridine did not produce m/z132 anions. However, it should be noted that ribose itself has not been observed previously as a thermal decomposition product of uridine (whose sugar unit is *ribose minus OH*). Authors observed temperature dependence of resonance peaks of m/z71 and 58 ions which they ascribed either due to impurities or partial thermal decomposition.
Thymidine				
Wilson and McCloskey [183] (1975)	ChI	Heating using a direct insertion probe ($180-290\,^{\circ}C$).	X	No comments.
AIST: SDBS [146] (1999)	EII	Heating (method not specified, $180\,^{\circ}C$).	X	No comments.
Ptasińska et al. [16] (2005)	EII	Heating in an effusive oven and seeding in carrier gas ($117-153\,^{\circ}C$,).	✓	#The ratio of S^+/B^+ was studied as a function of temperature. The decrease starting at $147\,^{\circ}C$ indicates thermal decomposition.
Ptasińska et al. [211] (2006)	DEA	Heating in a temperature regulated oven ($117-167\,^{\circ}C$).	✓	Changes in the DEA ion yield curves of $(B-H)^-$ and $(S-2H)^-$ anions with increasing temperature indicate thermal decomposition. Even at $125\,^{\circ}C$, signatures of thermal decomposition are present.
Itälä et al. [199] (2013)	PEPIPICO	Heating in an effusion cell with integrated cooling shroud (MBE Komponenten NTEZ40 oven).	X	Authors argue that the evaporation temperature was around $140\,^{\circ}C$, which is below the thermal decomposition temperature reported by Ptasińska et al. [16] (see above).
Levola et al. [195] (2013)	SPI	Heating in a quartz crucible of an effusion cell ($119-148\,^{\circ}C$).	✓	The ratio of B^+/BH^+, B^+/S^+ and $(S-H)^+/S^+$ was studied as a function of temperature. The increase in these ratios starting at $135\,^{\circ}C$ indicates thermal decomposition.
Levola et al. [196] (2014)	SPI	Heating in a quartz crucible of an effusion cell ($125-170\,^{\circ}C$).	✓	The ratio of B^+/BH^+ was studied as a function of temperature. The increase starting at $135\,^{\circ}C$ indicates thermal decomposition.
Maclot et al. [197] (2016)	ICol, PEPICO	Heating in an effusive oven (temperature not specified).	X	The temperature of thymidine in the oven was low enough to avoid thermal decomposition (referring to Levola et al.'s paper [195]).
Poully et al. [8] (2015)	PRI, MPI	ILTD.	X	m/z117 fragment ion was dominating the mass spectrum, m/z98 fragment ion was not abundant, intact parent ion was present. Referring to Levola et al.'s study [195], these suggest negligible thermal decomposition, if any.

*Paper *directly* presents results of the study of target decomposition/reactivity: ✓ = *yes*, X = *no*.
#The subsequent paper by the same group [211] shows thermal decomposition of thymidine already at $125\,^{\circ}C$.
•*Red* signifies *presence* of target decomposition/reactivity demonstrated when varying experimental conditions.
••*Light blue* signifies when indirect laser-induced thermal desorption (ILTD) is used as a volatilisation technique.

Tab. 5.4: Literature review on volatilisation techniques and tests of target decomposition or reactivity in experiments on thymidine, 2′-deoxyuridine and 5-methyluridine (all the acronyms in the second column are defined in the List of acronyms on pages XXXI to XXXIII); continued.

Authors [reference] (year)	Type of experiments	Volatilisation technique	*Evidence shown	Authors' comments with respect to potential target decomposition or reactivity
Thymidine continued				
Camillis et al. [43] (2015)	TRPP-MS	ILTD.	X	Previously reported MPI mass spectra for thymidine [8] show that parent ions make up more than 90 % of the ion yield which provides a lower limit on the proportion of intact molecules in the plume desorbed from a foil.
Mansson et al. [66] (2017)	SPI, MPI	ILTD.	X	The exact temperature of the desorbed molecules is hard to determine accurately, but previous measurements [8, 43] taken under similar desorption conditions have shown that there is no fragmentation induced by desorption laser.
Muftakhov et al. [268] (2018)	DEA	Heating at the bottom of the ionisation chamber ($138\,^{\circ}C$).	X	Authors commented that $m/z98$ is a dominant peak in DEA (around $0\,eV$) to 2′-deoxyribose [269] and that their DEA experiments on thymidine produced insignificant amounts of $m/z98$ anions (relative intensities $\leq 1\,\%$) which indicates insignificant thermal decomposition of thymidine. However, it should be noted that 2′-deoxyribose itself has not been observed previously as a thermal decomposition product of thymidine (whose sugar unit is *2′-deoxyribose minus OH*).
2'-deoxyuridine				
Biemann and McCloskey [263] (1962)	EII	Heating using a hot filament system (temperature not specified).	X	No comments.
AIST: SDBS [146] (1999)	EII	Heating (method not specified, $150\,^{\circ}C$).	X	No comments.
Muftakhov et al. [268] (2018)	DEA	Heating at the bottom of the ionisation chamber ($125\,^{\circ}C$).	X	Authors commented that $m/z98$ is a dominant peak in DEA (around $0\,eV$) to 2′-deoxyribose [269] and that their DEA experiments on 2′-deoxyuridine produced insignificant amounts of $m/z98$ anions (relative intensities $\leq 1\,\%$) which indicates insignificant thermal decomposition of 2′-deoxyuridine. However, it should be noted that 2′-deoxyribose itself has not been observed previously as a thermal decomposition product of 2′-deoxyuridine (whose sugar unit is *2′-deoxyribose minus OH*).
Muftakhov et al. [193] (2019)	DEA	Heating at the bottom of the ionisation chamber ($\sim 125\,^{\circ}C$).	X	Authors first dried the nucleoside at low temperatures in the chamber to minimise the possibility of reactions with associated water molecules. They also commented that $m/z98$ anions are produced by DEA to 2′-deoxyribose [269] and that their DEA experiments on 2′-deoxyuridine did not produce $m/z98$ anions. However, it should be noted that 2′-deoxyribose itself has not been observed previously as a thermal decomposition product of 2′-deoxyuridine (whose sugar unit is *2′-deoxyribose minus OH*). Authors observed temperature dependence of resonance peaks of $m/z71$ and 58 ions which they ascribed either due to impurities or partial thermal decomposition.
5-methyluridine				
AIST: SDBS [146] (1999)	EII	Heating (method not specified, $60\,^{\circ}C$).	X	No comments.
Levola et al. [196] (2014)	SPI	Heating in a quartz crucible of an effusion cell ($125 - 170\,^{\circ}C$).	✓	Authors studied the ratio of B^+/BH^+ as a function of temperature and did not observe any change in the ratio which indicates absence of thermal decomposition.

*Paper *directly* presents results of the study of target decomposition/reactivity: ✓ = *yes*, X = *no*.
••*Light blue* signifies when indirect laser-induced thermal desorption (ILTD) is used as a volatilisation technique.
••*Green* signifies *absence* of target decomposition/reactivity demonstrated when varying experimental conditions.

5.3 Experimental conditions

The multi-photon ionisation experiments presented in this chapter were carried out using the *Compact MPI/EII experimental set-up* (see Section 3.2 as well as [18, 26, 56, 57, 114–116]). The powder samples were provided by Sigma Aldrich with stated purities: uracil $\geq 99\,\%$, guanine $98\,\%$, uridine $\geq 99\,\%$, thymidine $\geq 99\,\%$, $2'$-deoxyuridine $99-100\,\%$, 5-methyluridine $97\,\%$ and uridine $5'$-monophosphate $\geq 98\,\%$. With the exception of three measurements (see Fig. 5.2 a), Fig. 5.4 a) and Fig. 5.9 a)) where the gas-phase targets were produced by heating samples in a supersonic expansion nozzle (for more details see Section 3.2.2), the molecular targets in the present experiments were produced by ILTD under vacuum (for more details see Section 3.2.3.3).

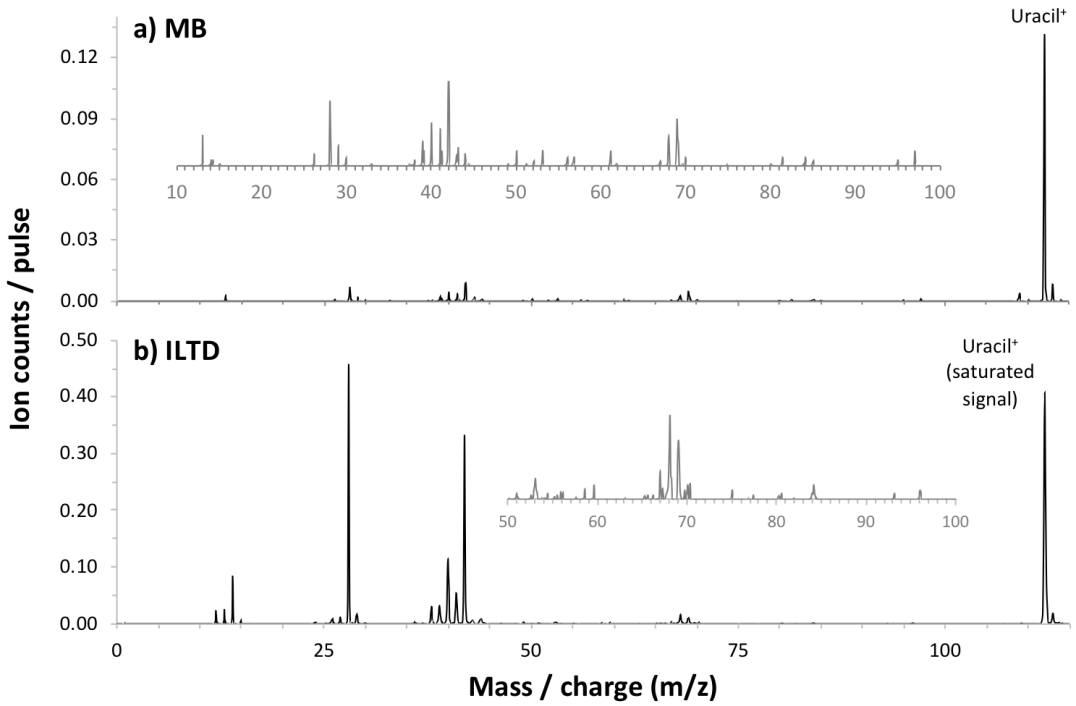

Fig. 5.2: Comparison of MPI ($235\,nm$, average UV laser fluence $2\times10^{7}\,W\,cm^{-2}$) mass spectra of uracil produced by a) heating in supersonic expansion nozzle and seeding in molecular beam (MB, average sample temperature $260.5\,^{\circ}C$, pressure of He $1\,bar$) and b) indirect laser-induced thermal desorption (ILTD, $445\,nm$ desorption laser power $0\,W$ above the ion detection threshold of $0.16\,W$). The insets show a detailed views of a) $m/z\,10$ to $m/z\,100$ and b) $m/z\,45$ to $m/z\,100$ ranges of the mass spectra.

In our experimental system, ILTD generally produces higher ion signals in MPI measurements (indicating higher number densities of neutral targets) than heating samples in the supersonic expansion nozzle for molecular beam (MB) experiments. Fig. 5.2 compares mass spectra of uracil recorded in the same MPI conditions but with the gas-phase target produced by a molecular beam (plot a)) and by ILTD (plot b)). The signal in plot b) is

much higher than in plot a) despite the fact the CW laser power was set at the *ion detection threshold* ($0.16\,W$ in this specific preparation of the system) whereas the supersonic expansion nozzle was heated $11\,^{\circ}C$ higher than we typically use for experiments on uracil using the molecular beam [18, 115]. The *ion detection threshold* is the term we use for the lowest desorption laser power at which we were able to observe MPI signals in a specific set of ILTD experiments. It depends not only on the target molecule, but also on the specific preparation of the sample and alignment of the desorption laser with the irradiated foil. Therefore, we consider that the desorption laser power above the ion detection threshold is generally a more useful parameter than absolute values of the desorption laser power if we want to compare experiments in this thesis that were carried out with different ILTD samples. Note that no new ions from uracil (at lower or higher masses) are produced by ILTD compared with the molecular beam measurements or conventional oven measurements. This is a positive indicator with respect to the lack of thermal decomposition or reactivity. Indeed, the absence of thermal damage in uracil by ILTD has been confirmed by [9]. In the following sections we limit the discussion about *target decomposition/reactivity* induced by ILTD to *thermal decomposition* as we have never observed any peaks with m/z higher than the parent ion which would indicate thermal reactivity.

Investigation of the foil temperature in ILTD experiments can bring new insights into the desorption process and help optimise the method for volatilisation of more complex biomolecules. Estimation of the foil temperature upon CW laser irradiation is, however, not a straightforward process. Camillis et al. [43] estimated the temperature of the $10\,\mu m$ thick stainless steel foil upon the irradiation with a CW desorption laser beam ($445\,nm$) to be $\sim 150 - 250\,^{\circ}C$. No information on the basis for this estimation was provided, but it is consistent with Townsend and co-workers' (Heriot Watt University) *"rudimentary estimations"* of ILTD foil temperatures rising from 135 ± 30 to $167 \pm 30\,^{\circ}C$ when the desorption laser power increased from 0.15 to $0.41\,W$ [9]. The method applied at Heriot Watt involved placing a chromel-alumel K-type thermocouple at the centre of the desorption beam focus (a focused CW laser beam, $445\,nm$, $1\,mm$ spot diameter) with the expectation that the thermal conductivities and reflectivities of chromel and alumel are similar to those of the stainless steel foil in their ILTD system. Clearly, a thermocouple in air represents only a loose analogy for the thermal system of the foil in an ILTD system under vacuum. Furthermore, the state of the foil surface (e.g. polished, cast, oxidised, etc.) will have a big effect on emissivity [270] so the presence and properties of the condensed sample will modify the foil temperature. Considerations such as these led to the large estimated errors ($\pm 30\,^{\circ}C$) on the ILTD temperatures reported in the paper. As the desorption laser beam was unfocused in the present measurements, we consider that

the estimations by the Heriot Watt group should be treated as upper limits of the possible local foil temperatures in our experiments at equivalent laser powers.

5.4 Testing for thermal decomposition in experiments at the OU

5.4.1 ILTD for gas-phase experiments on the nucleobase guanine

Guanine is a building block of both RNA and DNA. It is a purine base (a fused pyrimidine-imidazole ring with conjugated double bonds) which forms three hydrogen bonds with cytosine in DNA. Guanine has the lowest ionisation energy amongst all nucleobases and thus is expected to be the main site for electron loss from RNA/DNA in many ionisation processes [271, 272]. In addition, theoretical work by Sugiyama and Saito [273] showed that guanine-rich regions are not only preferential sites for initial ionisation, but also act as *"sinks"* for *"hole"* migration through RNA/DNA, i.e. electron-loss centres will eventually become localised on guanine units. The experimental work on such an important component of RNA/DNA with respect to radiation interaction has been, however, hampered by the lability of the molecule with respect to thermal decomposition [64, 65]. The list of experimental studies on guanine in the gas-phase is reported in Tabs. 5.1 and 5.2. In all of them either *conventional* heating methods or *direct laser-induced desorption* was used as the volatilisation technique. A number of these papers have stated that there is negligible thermal decomposition in the target but the level of details provided is generally low. None of these papers actually show the results of any of their tests for thermal decomposition (for example mass spectra as a function of desorption conditions), which we consider to be important in the case of such a fragile biological molecule.

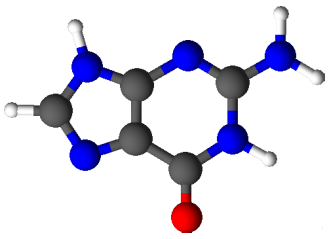

Fig. 5.3: Chemical structure of the nucleobase guanine (*C* atoms are coloured in grey, *O* in red, *N* in blue and *H* in white). The structure was drawn using ACD/Labs software based on the $9H-1H-amino-oxo$ tautomeric form reported by Marian [274] as one of two biologically relevant forms (also as one of the eight most stable tautomeric and rotameric forms) of guanine.

Former PhD students in the Molecular Clusters Laboratory at the OU (B. Barć, M. Ryszka and R. Pandey) exploited the *Compact MPI/EII experimental set-up* in the *molecular beam*

mode (described in detail in Section 3.2.2) for gas-phase experiments on nucleobases adenine, thymine and uracil using nozzle temperatures up to $\sim 280\,^{\circ}C$ [18, 26, 56–58, 115]. Their experiments on cytosine were limited to very weak targets in order to avoid thermal reactivity [57]. We successfully carried out MPI experiments on the nucleobase derivative 5-flourouracil [121], while the experiments by the former group members on 5-chlorouracil and 5-bromouracil were unsuccessful due to thermal reactivity. M. Ryszka also attempted MPI experiments on guanine in a supersonic beam of Ar, but did not obtain any signal even after heating the sample up to $300\,^{\circ}C$. We repeated MPI experiments on guanine seeded in a supersonic expansion of He and only obtained a signal when the powder temperature reached $331 - 334\,^{\circ}C$ (see Fig. 5.4 a)). The ion count rate is approximately 3 orders of magnitude lower than in equivalent experiments on guanine using the ILTD source (see Fig. 5.4 b)). In addition, peaks above the parent ion m/z value (at m/z159, 173 and 175) and numerous small fragments in the mass spectrum in Fig. 5.4 a) strongly suggest thermal reactivity and decomposition of the sample. Furthermore, a subtle change in the colour of guanine powder (see Fig. 5.5 a)) after heating to $300\,^{\circ}C$ (see Fig. 5.5 b)) and a more prominent discolouration after heating to $334\,^{\circ}C$ (see Fig. 5.5 c)) suggest a permanent degradation of the sample during the heating in the supersonic expansion nozzle.

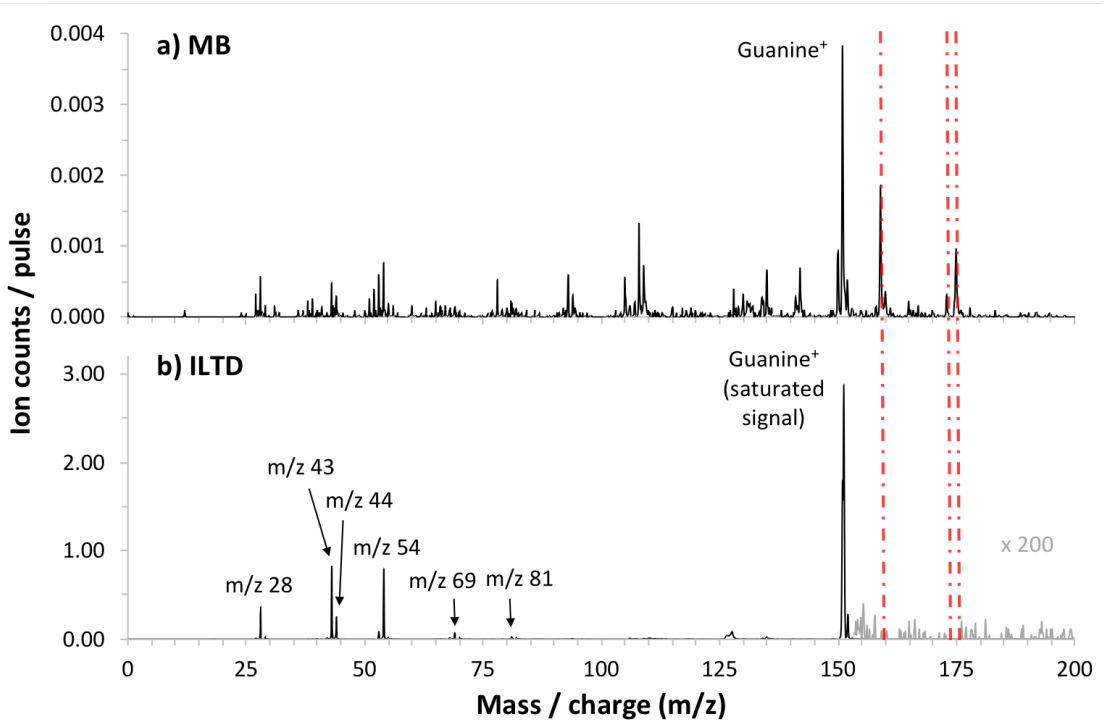

Fig. 5.4: Comparison of $225\,nm$ MPI spectra of guanine produced by a) heating in supersonic expansion nozzle and seeding in molecular beam (MB, average UV laser fluence $5 \times 10^7\,W cm^{-2}$, average sample temperature $332.4\,°C$, pressure of $He\,1\,bar$) and b) indirect laser-induced thermal desorption (ILTD, average UV laser fluence $7 \times 10^6\,W cm^{-2}$, $445\,nm$ desorption laser power $0.03\,W$ above the ion detection threshold of $0.40\,W$). Red dash-dotted lines indicate presence of thermal reactivity products in MB experiments and absence in ILTD experiments. Higher UV laser fluence in MB experiments was used to increase the probability of signal detection at the lowest possible temperatures.

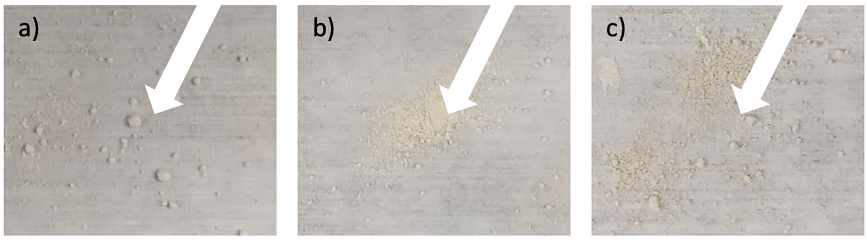

Fig. 5.5: Comparison of guanine sample a) before heating; b) after heating to $300\,°C$ and c) after heating to $334\,°C$ in the supersonic expansion nozzle. White arrows are used to help the reader recognise the discolouration of the sample induced by heating.

We tested for possible thermal decomposition of guanine produced by indirect laser-induced thermal desorption by searching for differences in the production of fragment ions as a function of desorption laser power. MPI mass spectra were compared in the desorption power range of $0 - 0.21\,W$ above the ion detection threshold of $0.40\,W$. Fig. 5.6 shows a comparison of two MPI mass spectra of guanine at desorption laser powers of 0.03 and $0.15\,W$ above the ion detection threshold. It should be noted that guanine$^+$ signals

are saturated and are plotted only to give the reader an idea of the low relative intensities of fragment ions with respect to the parent ion. No significant changes in the relative peak heights of the *prompt* fragment ions (see Section 3.3.1 for the distinction between *prompt* and *metastable* fragment ions) were observed that could indicate thermally-driven decomposition or reactivity. The only noticeable difference between the two mass spectra is in the intensities of the peaks arising from metastable dissociation signals that appear at around $m/z\,125$. Metastable dissociation is strongly dependent on the amount of vibrational energy of the precursor ions (see Section 4.5.3). In addition, it has been previously shown that different isomeric forms can result in the differences in metastable dissociation patterns [137]. Therefore, we expect that the differences in the intensities of metastable peaks in the spectra in Fig. 5.6 are linked to the changes in the amount of vibrational excitation and/or changes in the relative populations of different isomeric forms of the molecules resulting from changes in the desorption laser power.

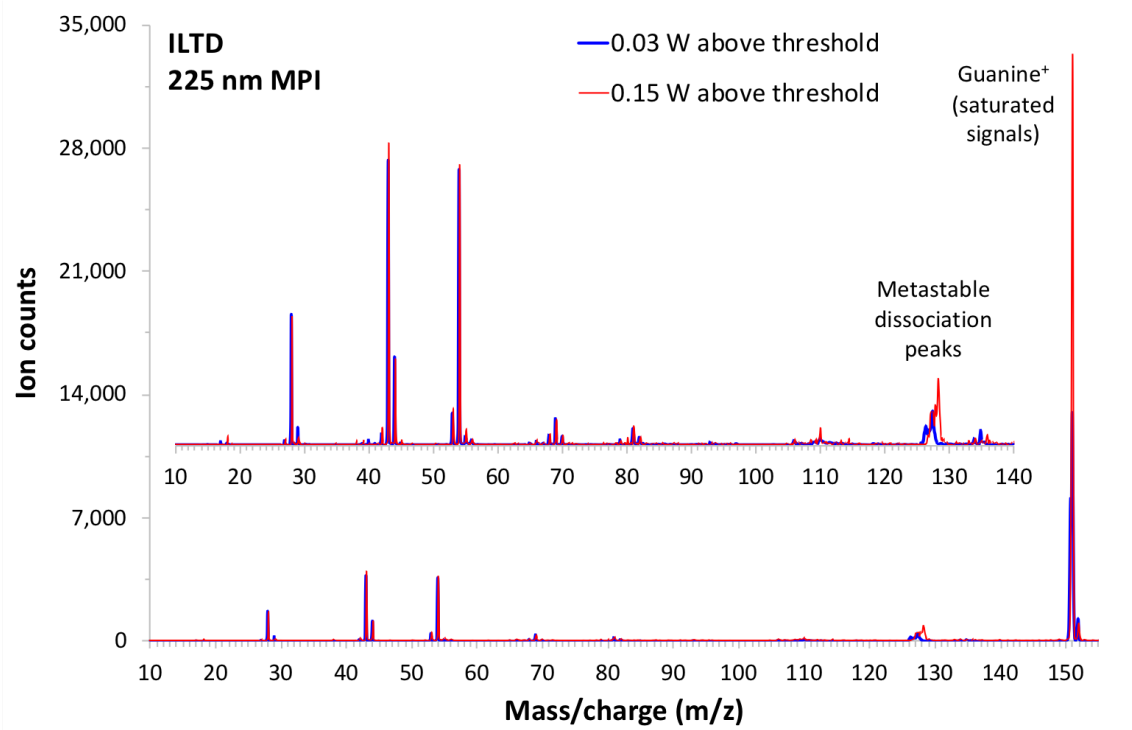

Fig. 5.6: MPI (average UV laser fluence $7 \times 10^6\,W\,cm^{-2}$) mass spectra of guanine at $445\,nm$ desorption laser power 0.03 and $0.15\,W$ above the ion detection threshold of $0.40\,W$. The MPI mass spectrum at $0.15\,W$ above the ion detection threshold was multiplied by 4 in order to ease the comparison of relative peak heights. The inset shows a detailed view of $m/z\,10$ to $m/z\,140$ range of the mass spectrum.

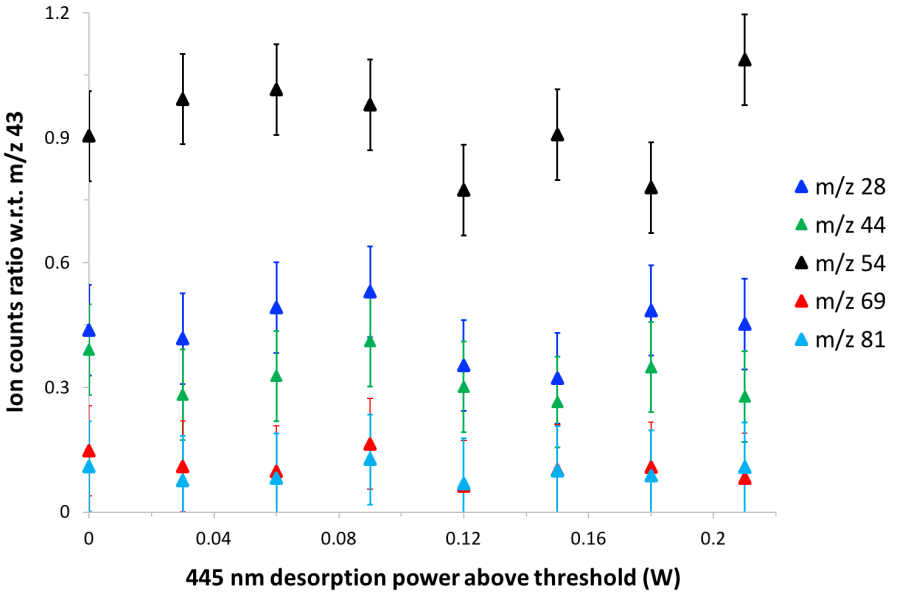

Fig. 5.7: MPI (225 nm, average UV laser fluence $7 \times 10^6 W cm^{-2}$) signal ratios of the most intense guanine fragment ions over the $m/z43$ fragment ion (w.r.t. – with respect to) plotted against the 445 nm desorption laser power above the ion detection threshold (0.40 W).

The signal ratios of the strongest fragment ions (see Fig. 5.4 b) and Fig. 5.6) over the $m/z43$ fragment ion are plotted as a function of desorption power in Fig. 5.7. $m/z43$ is the strongest fragment ion in our MPI measurements at 225 nm and was used as a reference as the parent ion signal could not be considered due to its saturation. The ratios do not show any trend which would suggest thermal decomposition. Taken together, Figs. 5.6 and 5.7 provide strong evidence that ILTD is a suitable method for producing gas-phase guanine targets without thermal decomposition or reactivity. Moreover, the target density was sufficient to also enable us to detect normally weak metastable dissociation channels (see Fig. 3.14 b)).

5.4.2 Thermal decomposition of nucleosides

After nucleobases, nucleosides consisting of a nucleobase unit ($(B-H)$) and a sugar unit (S) bound together by a glycosidic bond represent the second step in the *bottom-up* approach in the study of progressively more complex RNA/DNA component molecules (see Fig. 5.8).

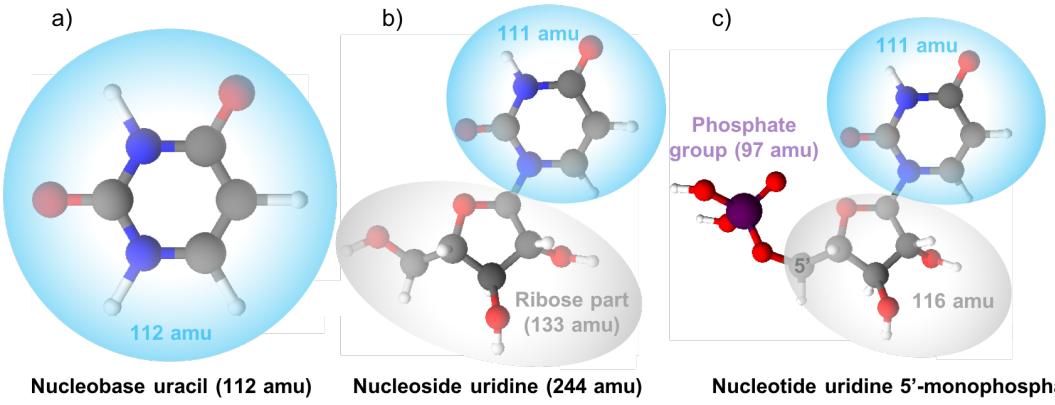

Fig. 5.8: Chemical structures of a) the nucleobase uracil; b) the nucleoside uridine and c) the nucleotide uridine 5′-monophosphate (*C* atoms are coloured in grey, *O* in red, *N* in blue and *H* in white). The structures were drawn using ACD/Labs software. The uracil structure was based on the diketo tautomeric form which was previously reported as the only tautomeric form present in gas-phase experiments [57, 275, 276]. The structure of uridine was based on the $U1$ isomer reported by Delchev [67] and the structure of uridine 5′-monophosphate was based on $gg-2'-endo-anti$ isomer reported by Inagaki et al. [277].

Nucleosides are characterised by even lower volatility than nucleobases due to their large mass and high polarisability [16]. Ts'o [184] ordered nucleosides according to their volatility as follows: guanosine $<$ cytidine $<$ adenosine $<$ uridine. Considering its relatively high volatility and following previous MPI experiments on the nucleobase uracil [18, 26, 115] in the Molecular Clusters Laboratory at the OU, we attempted MPI experiments on its corresponding nucleoside uridine seeded in a supersonic beam. It was necessary to heat the powder sample to $252\,^{\circ}C$ to observe weak ion signals (count rate $1\,count/pulse$). Increasing the temperature to $255\,^{\circ}C$ (lowered to $247\,^{\circ}C$ by the end of the measurement) enabled us to obtain reasonable signals (count rate $3.5\,counts/pulse$), however, this evidently caused thermal decomposition. The corresponding MPI mass spectrum is shown in Fig. 5.9 a) and is dominated by strong signals of small fragment ions and extremely weak production of any ions with higher m/z than 112 (B^+). The powder remaining in the nozzle after the experiment was discoloured. As expected for ionisation measurements on an extensively thermally-decomposed nucleoside [16, 195, 196] (discussed further below), the B^+ signal dominated over the BH^+ signal. Our further attempts to study uridine in the molecular beam (with four separate sample preparations in the nozzle and heating up to $253\,^{\circ}C$) were also unsuccessful; they produced no signals that could be traced unambiguously to multi-photon ionised uridine and they resulted in discoloured samples.

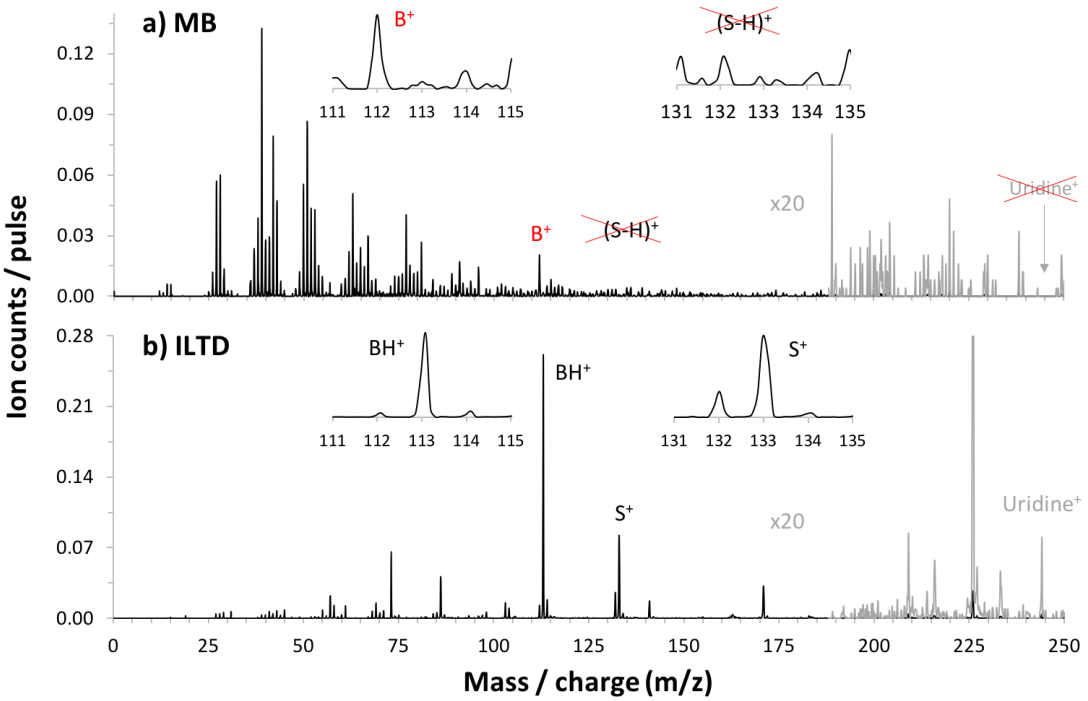

Fig. 5.9: Comparison of 235 nm MPI spectra of uridine produced by a) heating in supersonic expansion nozzle and seeding in molecular beam (MB, average UV laser fluence $3 \times 10^7 W cm^{-2}$, sample temperature $255 - 247°C$, pressure of He 1 bar) and b) indirect laser-induced thermal desorption (ILTD, average UV laser fluence $7 \times 10^6 W cm^{-2}$, 445 nm desorption laser power 0.03 W above the ion detection threshold of 0.46 W). The MPI spectrum in a) indicates strong signs of thermal decomposition: a lot of small fragments, absence of parent ion, higher production of B^+ compared to BH^+ and weak ion production at $m/z > 112$. Higher UV laser fluence was in the MB experiments used to increase the probability of signal detection at lowest possible temperatures.

Due to their high propensity for decomposition upon heating, thermal decomposition of nucleosides has been studied by several authors [16, 184, 195, 196]. Ts'o's experiments [184] on adenosine and cytidine revealed changes in the production of B^+ ions compared to BH^+ ions as a function of sample temperature. Ptasińska et al. [16] studied thermal decomposition of thymidine in their electron impact ionisation (EII, 70 eV) experiments by observing the ratio of S^+ and B^+ ions signal with increasing temperature of the sample in an effusive oven. They reported thermal decomposition of thymidine starting at 147 $°C$. Although EII of uridine was studied as well, its thermal decomposition was not discussed. The DEA mass spectra of thymidine [211] obtained by the same group at 125 $°C$ suggest that the *vast majority* of the molecules were produced intact, however they observed changes in the DEA ion yield curves of $(B - H)^-$ and $(S - 2H)^-$ anions with increasing temperature which indicate thermal decomposition. Levola's VUV photoionisation experiments on thymidine [195, 196], uridine and 5-methyluridine [196] showed thermal decomposition of the sample starting at around 135 $°C$ for thymidine and 140 $°C$

for uridine, while no sign of thermal decomposition of 5-methyluridine was observed within the studied temperature range up to $170\,^{\circ}C$. The common signature of thermal decomposition of nucleosides in the above mentioned studies [16, 184, 195, 196] was an increase in the relative production of B^+ and $(S-H)^+$ ions compared to the total ion signal or some carefully-chosen reference ion. This indicates that the lowest-energy thermal decomposition reactions of nucleosides result in glycosidic bond cleavage accompanied by a hydrogen transfer from the sugar part of the nucleosides to the base part, hence increased formation of B^+ and $(S-H)^+$ fragment ions [196]. No previous studies have reported temperature-dependent effects on the mass spectra of nucleosides at lower temperatures than the threshold for enhanced relative production of nucleobase ions (B^+). The increase in the B^+/BH^+ ratio is normally more pronounced than the increase in the $(S-H)^+/S^+$ ratio as the sugar part of a nucleoside is generally more prone to dissociation [16, 195]. This is also manifested in our MPI mass spectrum of uridine in the molecular beam experiment in Fig. 5.9 a), where no S^+ ($m/z\,133$) or $(S-H)^+$ ($m/z\,132$) fragment ions are present and the spectrum is dominated by numerous small fragments. Moreover, the absence of any protonated base (BH^+, $m/z\,113$) signal in combination with the significant B^+ ($m/z\,112$) signal suggests significant thermal decomposition of the sample.

In contrast to our MPI experiments on uridine produced by heating in the supersonic expansion nozzle, our MPI mass spectrum of uridine produced by ILTD (see Fig. 5.4 b)) does not exhibit obvious signs of thermal decomposition. BH^+ and S^+ signals dominate over B^+ and $(S-H)^+$ signals and we can also see the parent ion signal as well as several fragments of relatively high mass (e.g. $m/z\,141$, 171, 209, 226). This, however, does not provide firm evidence of the lack of any thermal decomposition in the target produced by ILTD and therefore it was further investigated. As noted above, previous mass spectrometry experiments on the present nucleosides and others [16, 195, 196] have led to a general acceptance that enhanced relative production of nucleobase cations (typically referenced to the protonated nucleobase signal or to the total ion signal) can be treated as the first indicator of thermal decomposition. This provided the test for thermal decomposition in the present MPI experiments.

5.4.2.1 Thermal decomposition study of *indirect laser-induced thermally* desorbed nucleosides uridine, thymidine, 2'-deoxyuridine, 5-methyluridine

The RNA nucleoside uridine, its DNA analogue thymidine as well as their derivatives $2'$-deoxyuridine and 5-methyluridine (see Fig. 5.10) were brought into the gas-phase for MPI experiments using indirect laser-induced thermal desorption. Greenwood and co-workers have previously applied ILTD in three studies of gas-phase nucleosides – adenosine,

guanosine, cytidine and thymidine (not uridine) [8, 43, 66]. These studies showed that a large proportion of the target comprises intact nucleosides (high yields of parent ions or alternatively high yields of fragment ions which had previously been shown to be due to the fragmentation of intact parent ions), but they did not present evidence to rule out some thermal decomposition induced by the desorption laser. We investigated potential thermal decomposition by ILTD by studying mass spectra at increasing desorption laser powers.

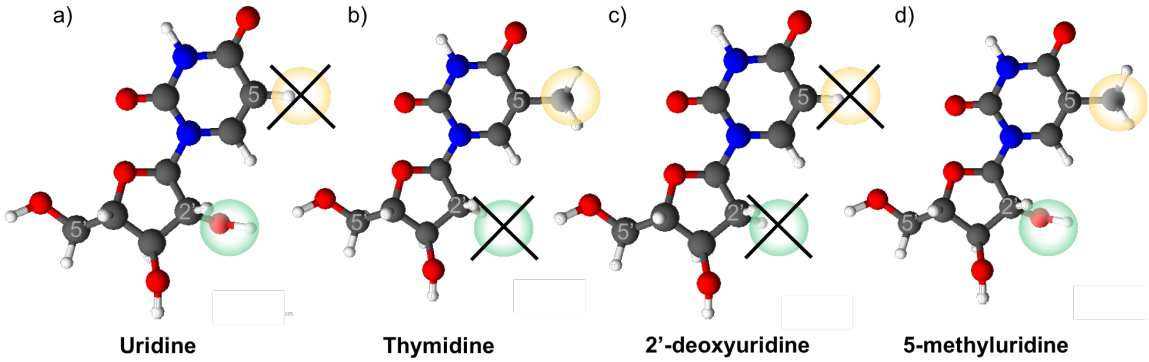

Fig. 5.10: Schematic representation of the chemical structures of a) uridine (244 *amu*); b) thymidine (242 *amu*); c) 2′-deoxyuridine (228 *amu*) and d) 5-methyluridine (258 *amu*). *C* atoms are coloured in grey, *O* in red, *N* in blue and *H* in white. The yellow circles relate to the presence or absence of a CH_3 group on the base part and the green circles relate to the presence or absence of an *OH* group on the sugar part of the nucleosides. The structures were drawn using ACD/Labs software. These structures are schematic to clearly communicate the differences and are not based specifically on any previously reported lowest energy isomers.

Fig. 5.11 shows the ratios of B^+/BH^+ as a function of desorption laser power above the ion detection threshold. The photon energies and fluences used in the present experiments produce strong signals of uracil$^+$ and thymine$^+$ by 2-photon ionisation of gas-phase uracil and thymine [18, 115], respectively, whereas we can only speculate about the possible efficiency of multi-photon ionising $(S-H)$. Therefore, we have followed Levola et al. [196] in monitoring the B^+/BH^+ ratio to look for experimental evidence of thermal decomposition. In the studied desorption power range, no increase in B^+/BH^+ was observed for uridine, 2′-deoxyuridine and 5-methyluridine, which shows these can be produced in the gas-phase by ILTD without any thermal decomposition or reactivity to within the experimental signal-to-noise ratios (S/Ns). Slightly higher error bars in the case of uridine as indicated in Fig. 5.11 a) are due to very weak signals of B^+ (see Fig. 5.9 b)). Notwithstanding the statistical errors, the absence of any systematic increase in the B^+/BH^+ ratio indicates that uridine did not undergo thermal decomposition in the present desorption laser power range.

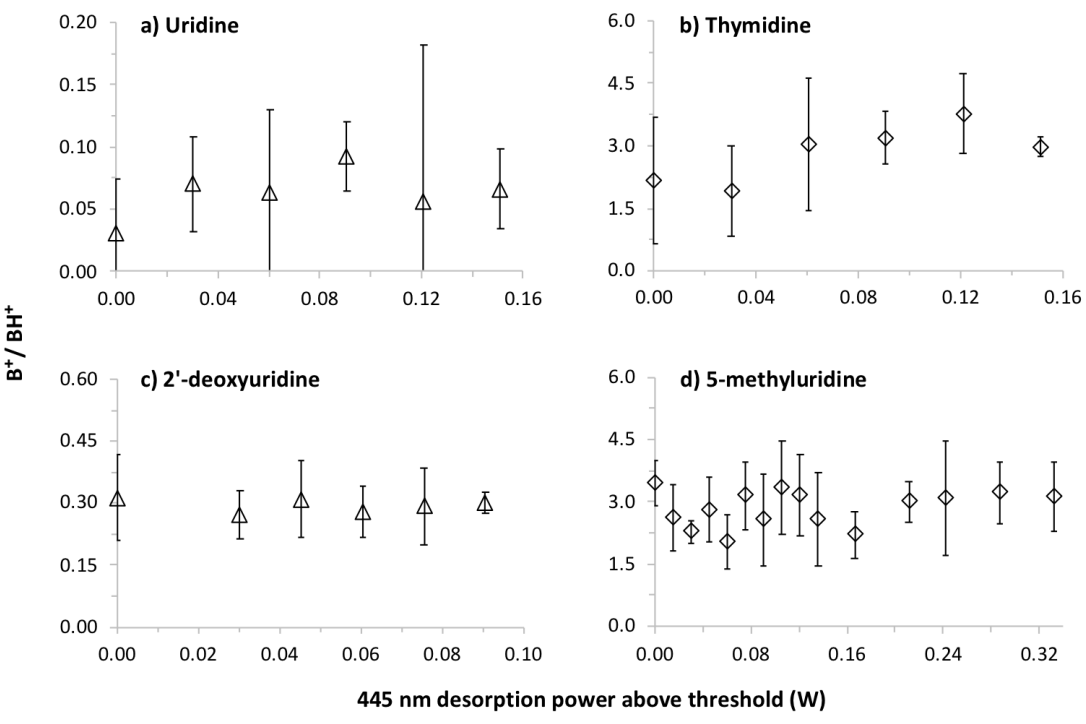

Fig. 5.11: The ratios of B^+/BH^+ in multi-photon ionised ($225\,nm$, average UV laser fluence $7 \times 10^6\,W\,cm^{-2}$) nucleosides a) uridine (ion detection threshold $0.46\,W$); b) thymidine (ion detection threshold $0.37\,W$); c) $2'$-deoxyuridine (ion detection threshold $0.18\,W$) and d) 5-methyluridine (ion detection threshold $0.19\,W$) produced by ILTD. No increase in the ratio of B^+/BH^+ in a); c) and d) indicates a lack of thermal decomposition of uridine, $2'$-deoxyuridine and 5-methyluridine, produced by ILTD ($445\,nm$). A slight increase in the ratio with desorption laser power in b) suggests some thermal decomposition of thymidine induced by ILTD.

Compared to uridine, thymidine has previously been shown to be a more fragile nucleoside with respect to thermal decomposition [16, 196]. Accordingly, a slight increase in the B^+/BH^+ ratio with desorption laser power in Fig. 5.11 b) suggests some thermal decomposition induced by the desorption laser. The mass spectra in Fig. 5.12 were taken in a separate set of measurements from the ones in Fig. 5.11 b). An increase in the desorption laser power by $0.15\,W$ resulted in a major increase in the production of T^+ fragment ions compared to TH^+ ions, which is not the case in the measurements in Fig. 5.11 b). Although our experiments have proved that using indirect laser-induced thermal desorption is not straightforward for thymidine, a systematic investigation of the effect of foil material and its thickness as well as sample layer thickness could help optimise the experimental conditions and enhance the capacity of the method for the production of intact gas-phase thymidine targets. Rapid cooling of thymidine by seeding them in cold molecular beams as suggested by e.g. Huang et al. for LIAD experiments [215, 247] could also result in greater stability of these molecules with respect to thermal decomposition induced by desorption laser. Visiting student T. Hajj built a system to attempt this in the

Molecular Clusters Laboratory using CW supersonic expansions of Ar and He but the pick-up efficiency was too low to produce a viable experimental target [278]. Greater carrier gas flow using a pulsed beam is expected to solve this problem and plans are underway to adapt the system accordingly.

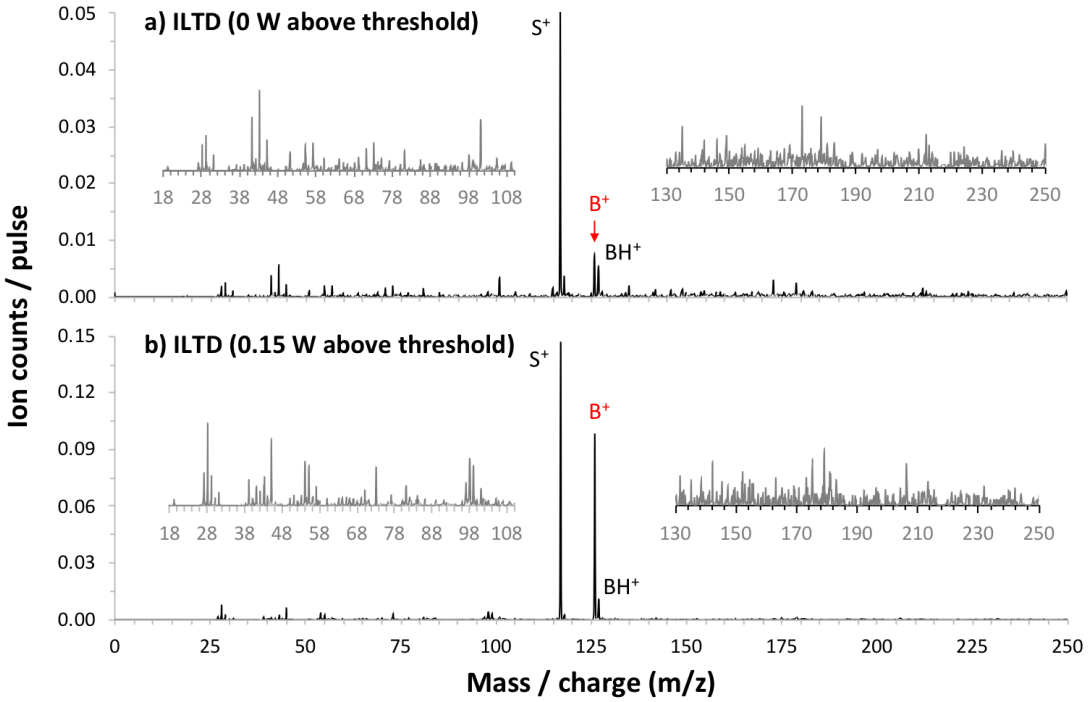

Fig. 5.12: Increased production of B^+ ions compared to BH^+ in $225\,nm$ MPI (average UV laser fluence $7\times10^6\,W\,cm^{-2}$) experiments on thymidine when increasing the $445\,nm$ desorption laser power by $0.15\,W$ above the ion detection threshold of $0.22\,W$. The insets show detailed views of $m/z\,18$ to $m/z\,108$ and $m/z\,30$ to $m/z\,250$ ranges of the mass spectra.

In contrast to thymidine, we have never observed any signature of thermal decomposition of uridine or 5-methyluridine produced by ILTD. These molecules were also tested for potential permanent damage of the sample powder induced by high desorption laser powers ($0.98\,W$). We did this by measuring MPI ($225\,nm$, average UV laser fluence $7\times10^6\,W\,cm^{-2}$) mass spectra at $0.06\,W$ above the ion detection threshold ($0.43\,W$) before and $5\,mins$ after increasing the desorption laser power to $0.98\,W$ for $2.5\,mins$ (this before-and-after approach was adopted because mass spectra measured at $0.98\,W$ desorption laser power were strongly saturated). The B^+/BH^+ ratio was 0.06 ± 0.05 before the $0.98\,W$ laser exposure and it was 0.06 ± 0.02 after. An analogous test was performed for 5-methyluridine where the ratio at the ion detection threshold of $0.30\,W$ was 2.80 ± 0.34 before the $0.98\,W$ laser exposure and 2.66 ± 0.53 after. It should be noted that the latter measurement was carried out at $0.23\,W$ above the ion detection threshold because the powder depletion after increasing the desorption laser power to $0.98\,W$ did not enable us to obtain an MPI mass spectrum at the same ion detection threshold power at the same

spot. As the ratios of B^+/BH^+ did not show any increase after exposure to a $0.98\,W$ desorption laser beam, we exclude the possibility of any permanent damage of the uridine and 5-methyluridine samples.

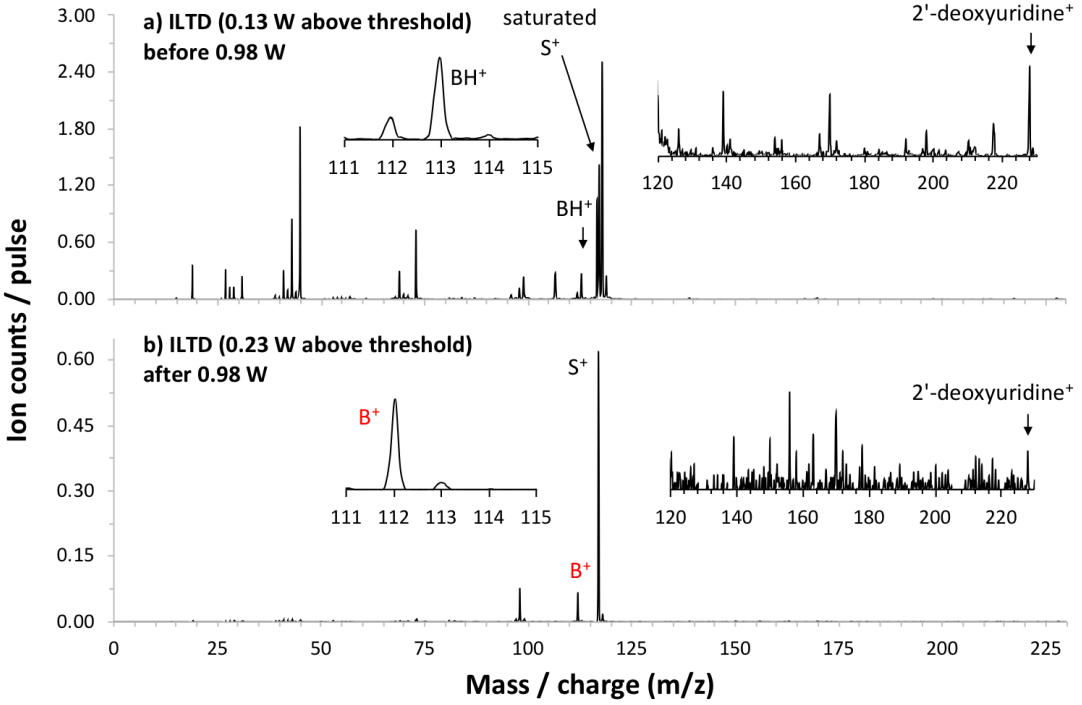

Fig. 5.13: Comparison of $225\,nm$ MPI (average UV laser fluence $7\times10^6\,W cm^{-2}$) mass spectra of $2'$-deoxyuridine produced by ILTD a) before and b) after increasing the $445\,nm$ desorption laser power to $0.98\,W$. Higher production of B^+ ions compared to BH^+ ions after increasing the desorption laser power to $0.98\,W$ indicates permanent damage of the sample at $0.98\,W$. The ion detection threshold power before the $0.98\,W$ laser exposure was $0.14\,W$. The insets show detailed views of $m/z\,111$ to $m/z\,115$ and $m/z\,120$ to $m/z\,225$ ranges.

A similar test for $2'$-deoxyuridine gave clear evidence of a permanent damage of the nucleoside sample as indicated in Fig. 5.13. This suggests that the OH group at $2'-C$ in ribonucleosides (containing *ribose minus OH*) uridine and 5-methyluridine is likely to have a stabilising effect with respect to thermal decomposition compared to their respective $2'$-deoxyribose analogues (containing $2'$-*deoxyribose minus OH*) $2'$-deoxyuridine and thymidine (see Fig. 5.10). In addition, the CH_3 group at $5-C$ in deoxyribonucleosides seems to have destabilising effect with respect to thermal decomposition, i.e. in our ILTD experiments thymidine proved more thermally labile than $2'$-deoxyuridine. Although Levola et al.'s [196] thermal decomposition study using an effusive oven showed greater thermal stability of 5-methyluridine compared to uridine, we cannot draw any conclusion about the effect of CH_3 group on thermal stability in ribonucleosides, as no thermal decomposition of uridine and 5-methyluridine was observed in the studied desorption power range in our experiments.

5.4.3 ILTD for the production of the gas-phase nucleotide uridine 5'-monophosphate

The next step in the *bottom-up* approach in the study of progressively more complex RNA/DNA related biomolecules are nucleotides, which consist of a nucleoside and a phosphate group bound to the $5' - C$ atom of the sugar unit of the nucleoside (see Fig. 5.10). An example of a nucleotide structure is shown for uridine 5′-monophosphate (5′-UMP) in Fig. 5.8. The literature of gas-phase experiments on nucleotides is even more sparse than that of nucleosides and is mainly limited to the studies of charged species produced by electrospray ionisation [279, 280]. To the best of our knowledge, the only experiments on a neutral isolated nucleotide (2′-deoxycytidine 5′-monophosphate, produced by *conventional* heating in an effusive oven) were performed by Kopyra in 2012 [17]. These were followed in 2018 by the experiments on microhydrated 2′-deoxycytidine 5′-monophosphate carried out by Kočišek et al. [70].

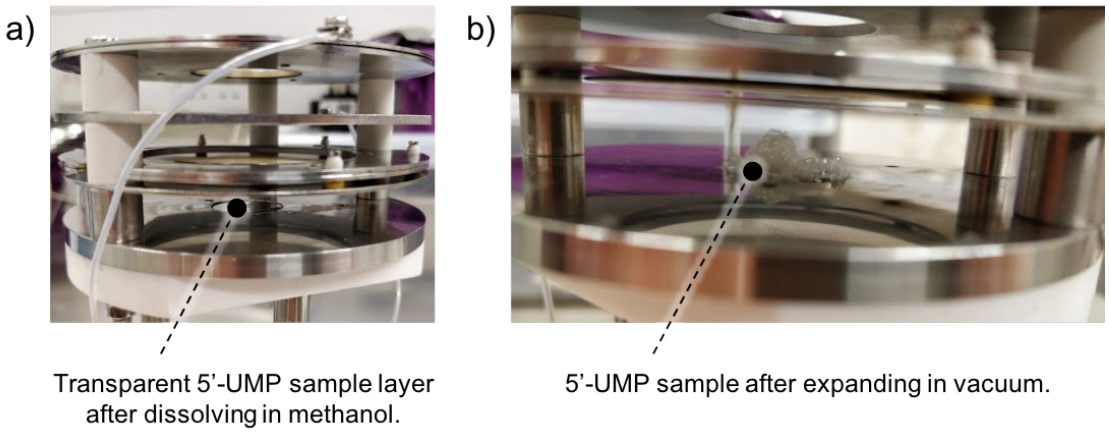

Fig. 5.14: Photographs of the *ion source* with 5′-uridine monophosphate (5′-UMP) sample a) before and b) after placing the system in vacuum.

We attempted using the ILTD source for the production of the nucleotide 5′-UMP in the gas-phase. Applying the same sample preparation method as for nucleobases and nucleosides (described in detail in Section 3.2.3.3) resulted in complete dissolution of the sample molecules in methanol, forming a transparent layer of a gel-like substance on the foil (see Fig. 5.14 a)). Inserting the sample into the experimental chamber and pumping down led to its expansion as shown in Fig. 5.14 b), which prevented us from carrying out any experiments on 5′-UMP. Replacing methanol for a non-polar solvent dichloromethane (DCM) in combination with an unsuccessful attempt to dry the sample for 2.5 *hrs* in a fume hood led to a similar behaviour. We interpret this behaviour in terms of numerous interactions between the molecules of 5′-UMP cause trapping of the solvent molecules. The combination of the ambient temperature $23\,^{\circ}C$ with atmospheric pressure

is not enough to release the trapped solvent molecules, which then subsequently happens under vacuum. The solvent molecules under vacuum form bubbles and escape, disrupting the smooth surface of the sample layer. Possible solutions to this problem might include gently heating the sample in an oven in an inert gas or using a vacuum desiccator to remove the solvent in a more *"gentle"* way before placing the sample inside the high-vacuum chamber (private communication with Dr. K. Nixon). However, as 5′-UMP is thermally very labile and should be stored at $-20\,^{\circ}C$, any unnecessary heating should be avoided in order to minimise the risk of sample degradation. Alternatively, designing a new sample holding arrangement which does not require use of any solvent might offer a convenient solution to this problem in the future. A possible solution could be pressing powder into small grooves or a rough foil surface, analogously to the system described in Section 3.2.3.1. In a such a *"weakly adhered"* sample arrangement, the horizontal foil assembly in the new ILTD system described in Chapter 7 might be advantageous.

5.5 Summary and outlook

The work outlined in this chapter responds to the experimental challenge of producing gas-phase targets of intact complex thermally labile biological molecules. While the production of intact ionic species has been largely resolved using electrospray ionisation, this chapter demonstrates that generating neutral gas-phase targets of species such as nucleosides and larger requires further characterisation and optimisation of existing methodologies. The experimental work presented here focused on potential thermal decomposition induced by indirect laser-induced thermal desorption for the production of the most thermally labile nucleobase guanine as well as the nucleosides uridine, thymidine, 2′-deoxyuridine and 5-methyluridine. Our experiments show that while nucleobases are at the limit of biomolecular lability that we could study using our supersonic beam source, ILTD can be used effectively to generate experimentally-viable targets of the most thermally labile nucleobase guanine without thermal decomposition. We have also demonstrated that ILTD can be successfully used for the production of intact gas-phase uridine, 2′-deoxyuridine and 5-methyluridine targets without any thermal decomposition. However, the experiments on thymidine indicated some thermal decomposition and hence suggest that nucleosides are at the threshold for how far we can go with the studies of progressively more complex species using ILTD. Furthermore, our unsuccessful attempts to produce a uridine 5′-monophosphate target suggest that different samples might require optimisation of the sample preparation procedure for ILTD. Overall, this chapter provides the most extensive study to date of the capabilities and limitations of ILTD for the study of neutral gas-phase biomolecules.

5.6 Contributions by co-workers

I devised the experimental approach to test for thermal decomposition of nucleosides drawing on an extensive review of the literature. I performed the experiments on *indirect laser-induced thermally* desorbed uracil, guanine, uridine (also in MB), thymidine, 2′-deoxyuridine and 5-methyluridine working with PhD student A. Rebelo and internship student R. Ward. I analysed the experimental data on nucleosides and carried out the MPI experiments on guanine in the MB. I analysed the guanine data working with Dr. K. Nixon. I worked on preparing uridine 5′-monophosphate samples for ILTD experiments and revising the sample preparation procedure for indirect laser-induced thermal desorption of nucleotides supported by discussions with P. Landsberg, Dr. M. Batham and Dr. K. Nixon. All experimental and analytical work was supported by Dr. S. Eden. The MPI experiments on 5-fluorouracil mentioned in Section 5.4.1 were published in [121]. We are currently preparing a journal manuscript based on the results in Section 5.4.2. M. Ryszka, R. Pandey, D. Mészáros, P. Limão-Vieira, P. Papp, N. J. Mason, D. Townsend, V. Vizcaino, J.-C. Poully contributed to this work through in-depth discussions, aiding the development of the experimental facility, and/or co-supervising students that worked in the lab.

Chapter 6

Multi-photon ionisation experiments on *indirect laser-induced thermally* desorbed uridine

In Chapter 5 we have demonstrated the efficacy of indirect laser-induced thermal desorption (ILTD) for producing gaseous targets of uridine, 5-methyluridine, and 2′-deoxyuridine without thermal decomposition. Only one multi-photon ionisation (MPI) fragment ion channel from any of these intact nucleosides showed notable dependence on thermal desorption conditions: the relative production of sugar$^+$ ions ($C_5H_9O_4{}^+$, m/z 133) from intact uridine increased with the desorption laser power and this only occurred at wavelengths below 250 *nm* (full range studied $222-265$ *nm*). This effect can only be rationalised plausibly in terms of changing populations of different isomers in the target as a function of the desorption conditions. Furthermore, the wavelength threshold behaviour of this thermally sensitive MPI channel indicates a critical dependence on neutral excited state dynamics in between the absorption of the first and second photons. Further work is required to identify the key dynamics but we suspect the involvement of previously predicted charge transfer states that facilitate isomeric transitions in electronically excited uridine. The experimental results are complemented by Density Functional Theory (DFT) calculations of the optimised geometries of two key isomers of uridine, which were performed by A. Rebelo, PhD student in the Molecular Clusters Laboratory at the OU.

6.1 Introduction

Uridine ($C_9H_{12}N_2O_6$) is one of four nucleosides present in RNA, containing a nucleobase unit and a sugar unit bound together by *N*-glycosidic bond (see Fig. 6.2 a)). The total mass of uridine (244 *amu*) is comprised of 111 *amu* belonging to the dehydrogenated uracil

part ($(B-H)$ in the nomenclature of this thesis) and 133 *amu* belonging to the sugar part (*ribose minus OH*, we refer to this part of uridine in this thesis as *S*). Uracil has a distinct status amongst other nucleobases as it is present only in RNA, while it is replaced by thymine in DNA. There have been numerous discussions about what selection rule led to this substitution in DNA. The two most interesting points with respect to this question are the greater photoresistance of thymine compared to uracil [281] as well as that such replacement prevents DNA mutations induced by deamination of cytosine. Deamination of cytosine leads to the formation of uracil, which can be effectively recognised as a faulty base (unfamiliar to DNA) and excised by enzyme uracil-DNA glycosylase. This would not be possible if uracil was intrinsic to DNA [282]. In addition, uracil is the UV chromophore in RNA. Therefore, the molecule is of great interest and is a natural starting point in the *bottom-up* approach applied to studies of radiation-induced processes in RNA. As a result, there has been a lot of experimental [47, 202, 283, 284] and theoretical [45, 98, 285, 286] work dedicated to this molecule. Electronic excitation and fragmentation of uracil was previously the subject of several studies by the Molecular Clusters Group at the OU too [18, 26, 56, 57]. In addition to the isolated nucleobase, the group also investigated the effect of clustering on its response to UV irradiation in experiments on uracil-water [18] and uracil-adenine [26] clusters.

Compared with uracil, the radiation response of the RNA nucleoside uridine has been much less investigated due to the difficulties with bringing the molecule into the gas-phase without *target degradation*, as discussed in Chapter 5. There have been a few experimental studies investigating the fragmentation pattern of uridine in direct ionisation experiments, i.e. electron impact ionisation (EII) [16, 194, 263, 265] or single-photon ionisation (SPI) [196], but to the best of our knowledge no step-wise ionisation study which could provide evidence for processes happening in electronic excited states. Therefore, we carried out multi-photon ionisation experiments on uridine for the first time. The present chapter discusses thermally-dependent and wavelength-dependent effects in the MPI mass spectra of uridine, which are interpreted in terms of changing populations of isomers with differences in electronic state energies and dynamics.

6.1.1 Experimental conditions

The multi-photon ionisation experiments on uridine (Sigma-Aldrich with stated purity $\geq 99\,\%$) in the $222-265\,nm$ wavelength range and on uracil, 2′-deoxyuridine and 5-methyluridine (Sigma-Aldrich with stated purity $\geq 99\,\%$, $99-100\,\%$ and $97\,\%$, respectively) at $225\,nm$ were carried out using the *Compact MPI/EII experimental set-up* (see Section 3.2 as well as [18, 26, 56, 57, 114–116]) in the *indirect laser-induced thermal*

desorption mode, employing the third generation of thermal desorption systems at the OU (see Section 3.2.3.3). Two different conditions for the UV lens position were examined to identify fragmentation pattern of uridine upon MPI at 225 nm: focused (beam diameter at crossing 0.3 mm, also in the MPI experiment on uracil) and partially defocused (beam diameter at crossing 0.54 mm) UV lens positions. The former one enables us to achieve higher UV laser fluence and thus induce more extensive fragmentation which consequently results in higher signals for smaller fragment ions. In contrast, the latter one enables us to observe larger fragment ions.

Thermal decomposition tests for uridine, 2′-deoxyuridine and 5-methyluridine were reported in Section 5.4.2.1. The experiments on uridine in the present chapter were carried out at desorption laser powers of up to 0.45 W above the threshold for ion detection, which exceeds the desorption power range studied in Fig. 5.11 a), therefore we report a separate thermal decomposition test for uridine in Fig. 6.1. The error bars on the ratios in Fig. 6.1 are purely statistical (analogous to Fig. 5.11 a)) and are quite large due to weak B^+ signals. Notwithstanding the statistical errors, the absence of any systematic increase in the B^+/BH^+ ratio indicates that uridine did not undergo thermal decomposition in the present laser desorption power range.

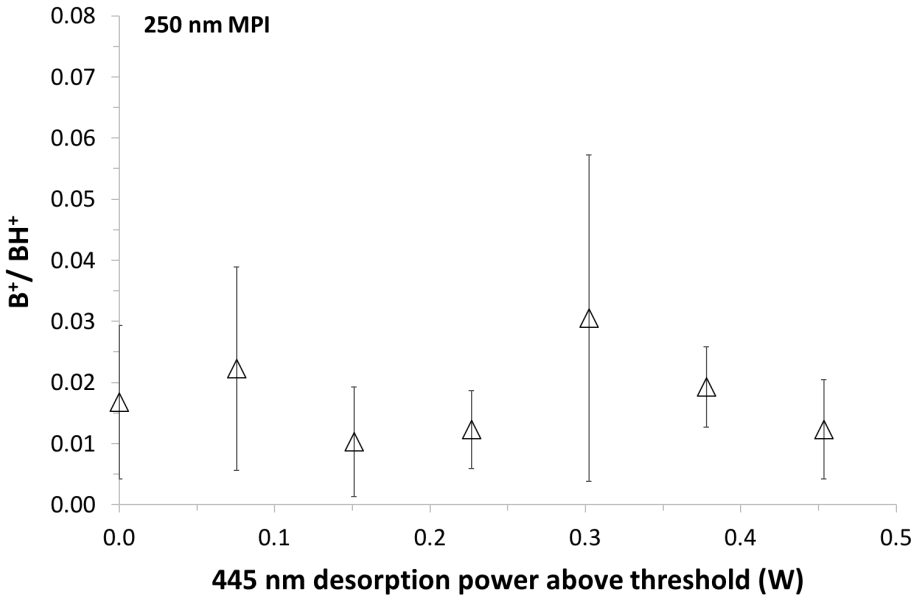

Fig. 6.1: Ratio of uracil$^+$ (B^+, m/z112) over protonated uracil (BH^+, m/z113) MPI production at 250 nm as a function of the 445 nm desorption laser power above the ion detection threshold (0.45 W).

The MPI measurement on uracil was carried out with desorption laser power of 0.64 W (see Fig. 6.3). It should be noted that MPI of uracil was thoroughly investigated by former PhD students in the Molecular Clusters Laboratory B. Barć, M. Ryszka and R. Pandey

[18, 26, 56–58] and we provide here only a complementary measurement for comparison of the fragmentation pattern with uridine in analogous conditions. The present mass spectrum of uracil agrees very well with our earlier MPI mass spectrum presented in [9] where thermal decomposition was investigated and excluded. Therefore, we do not present here an analogous systematic study of thermal decomposition for uracil. The experimental details for each measurement are stated in the caption of the corresponding figure.

6.2 Fragmentation patterns of uridine radical cation

In this section we present, to the best of our knowledge, the first MPI mass spectrum of uridine. By comparing the EII [16, 184, 185, 194, 263–265] and SPI [196] mass spectra of uridine with the ones of uracil [18, 60, 146, 181, 287–293] and ribose [146, 294, 295] we trace the origin of some of the strongest fragmentation products of uridine to its base and sugar constituents. We also discuss the effect of bonding of *ribose minus OH* unit on the previously observed *CO* loss channel in multi-photon ionised uracil [18, 26] and compare the fragmentation pattern of uridine with those of $2'$-deoxyuridine and 5-methyluridine.

6.2.1 Multi-photon ionisation experiments on uridine at 225 *nm*

MPI mass spectra of uridine measured with focused and partially defocused UV lens positions are shown in Fig. 6.2 a) and b), respectively. Tab. 6.1 lists all of the ions in the above-mentioned mass spectra which have ion yields $\geq 5\,\%$ of the strongest fragment ion's yield, i.e. $m/z\,29$ in Fig. 6.2 a) and $m/z\,133$ in Fig. 6.2 b). The assignments of the fragment ions are based on the previous assignments from the literature, where available. For the remaining ions, all possibilities are listed apart from the ones which are strongly counterintuitive. In addition to the listed fragments, we identified weaker peaks above the background level at $m/z\,13$, 53, 54, 58, 68, 70, 71, 87, 95, 96, 103, 104, 132 and 209.

The main fragment ion masses from uridine in our MPI measurements at 225 *nm* are broadly consistent with the EII/SPI literature. Most of the differences in the relative peak heights in mass spectra reported in different papers can be attributed to differences in the energy deposited in the ionisation process (MPI vs. EII/SPI at different electron impact energies or photon energies) as well as to differences in the mass spectrometer configurations. However, it is striking that MPI mass spectra of uridine at 225 *nm* (see Fig. 6.2) feature an exceptionally strong peak at $m/z\,133$ compared with any previous mass spectra. This ion channel is the subject of Section 6.3.

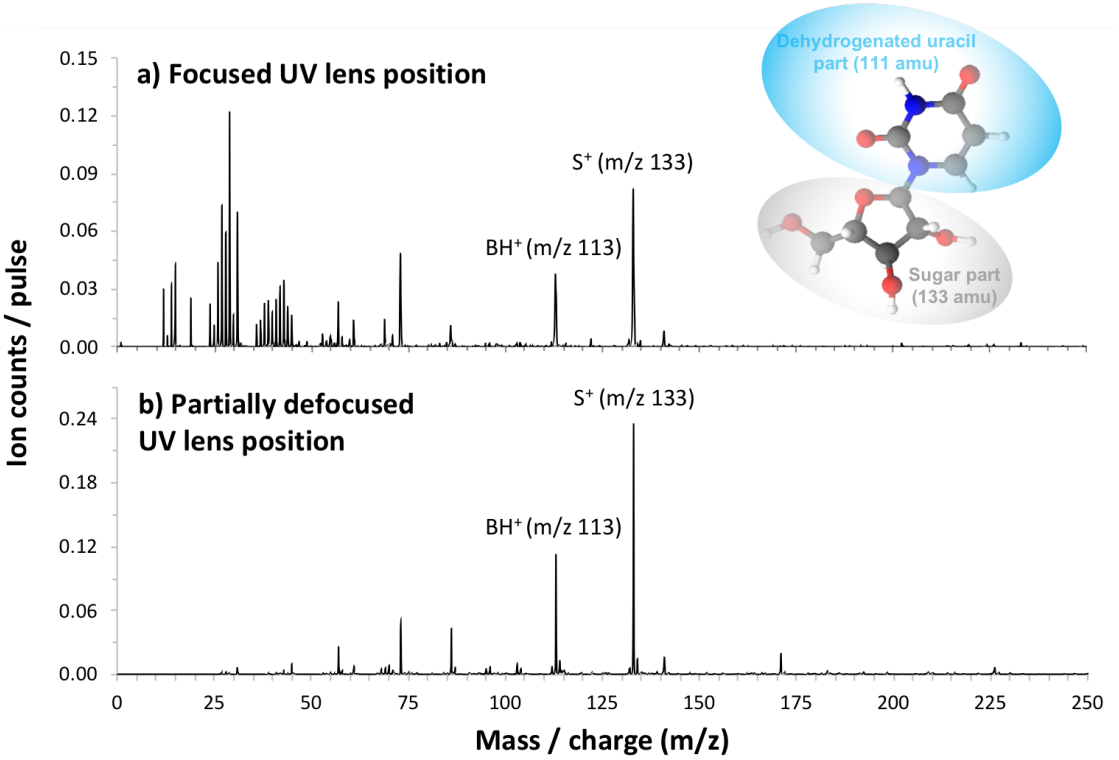

Fig. 6.2: Multi-photon ionisation mass spectra of uridine produced in the gas-phase by indirect laser-induced thermal desorption: a) with a focused UV lens position ($225\,nm$, average UV laser fluence $2\times10^{7}\,W\,cm^{-2}$, $445\,nm$ desorption laser power $0.17\,W$ above the ion detection threshold of $0.16\,W$) and b) with partially defocused UV lens position ($225\,nm$, average UV laser fluence $7\times10^{6}\,W\,cm^{-2}$, $445\,nm$ desorption laser power $0.03\,W$ above the ion detection threshold of $0.46\,W$). a) also depicts the chemical structure of uridine (C atoms are coloured in grey, O in red, N in blue and H in white) which was drawn using ACD/Labs software. The structure was based on the $U1$ isomer reported by Delchev [67].

Tab. 6.1: Fragment ion products of uridine in MPI experiments at 225 *nm* with UV lens at focused and partially defocused positions. Only the ions which have ion yield $\geq 5\,\%$ of the strongest* fragment ion are listed. The assignments are based on the literature, where available, otherwise all possibilities are listed apart from those which are strongly counterintuitive. The intensity of green shading indicates the intensity of an ion's signal with respect to the strongest fragment ion signal in the corresponding mass spectra$^{\#}$.

Uridine fragment ions (*m/z*) - focused UV beam (Fig. 6.2 a))	**Uridine fragment ions (*m/z*) - partially defocused UV beam (Fig. 6.2 b))**	**Assignments**
12		C^+
14		$CH_2{}^+/N^+$
15		$CH_3{}^+/HN^+$
19		H_3O^+
24		$C_2{}^+$
25		C_2H^+
26		$C_2H_2{}^+/CN^+$
27		$C_2H_3{}^+/CHN^+$
28		$C_2H_4{}^+/CH_2N^+/N_2{}^+/CO^+$
29*		CHO^+ [16]
30		$C_2H_6{}^+/CH_4N^+/CH_2O^+/H_2N_2{}^+/NO^+$
31		CH_3O^+ [16]
36		$C_3{}^+/H_6NO^+/H_4O_2{}^+$
37		$C_3H^+/H_7NO^+/H_5O_2{}^+$
38		$C_3H_2{}^+/C_2N^+/H_6O_2{}^+$
39		$C_3H_3{}^+/C_2HN^+/H_7O_2{}^+$
40		$C_3H_4{}^+/C_2H_2N^+/H_8O_2{}^+/CN_2{}^+/C_2O^+$
41		$C_3H_5{}^+/C_2H_3N^+/CHN_2{}^+/C_2HO^+$
42		$C_3H_6{}^+/C_2H_4N^+/CH_2N_2{}^+/C_2H_2O^+/CNO^+$
43		$CHNO^+/C_2H_3O^+$ [16]
44		$C_3H_8{}^+/C_2H_6N^+/CH_4N_2{}^+/C_2H_4O^+/$ $CH_2NO^+/CO_2{}^+/N_2O^+$
45		$C_3H_9{}^+/C_2H_7N^+/CH_5N_2{}^+/CH_3NO^+/$ $C_2H_5O^+/CHO_2{}^+/HN_2O^+$
55		$C_4H_7{}^+/C_3H_5N^+/C_3H_3O^+/C_2H_3N_2{}^+/$ $C_2HNO^+/H_7O_3{}^+$
57	57	$C_3H_5O^+$ [16, 194]
61		$C_3H_{11}N^+/C_2H_9N^+/CH_5N_2O^+/C_3H_9O^+/$ $C_2H_5O_2{}^+/CHO_3{}^+/HN_2O_2{}^+$
69		$C_3H_3NO^+$ [16, 184, 194]/$C_4H_5O^+$ [16]
73	73	$C_3H_5O_2{}^+$ [184, 194]
86	86	$C_2H_2N_2O_2{}^+/C_4H_6O_2{}^+$ [16]
113	113	$C_4H_5N_2O_2{}^+$ [16, 184, 194, 196, 263]
	114	$C_4H_6N_2O_2{}^+/C_5H_6O_3{}^+$ [196] $/C_4H_5N_2O_2{}^+$ with one ^{13}C
133	133*	$C_5H_9O_4{}^+$ [16, 184, 194, 196, 263]
	134	$C_5H_9O_4{}^+$ with one ^{13}C
141	141	$C_5H_5N_2O_3{}^+$ [16, 194, 196, 263]
	171	$C_6H_7N_2O_4{}^+/C_7H_9NO_4{}^+$ [196]

*The strongest ion signal in the corresponding MPI mass spectrum of uridine.

$^{\#}$Intensity colour-coding (based on the percentage of an ion signal with respect to the strongest ion signal):

$5-20\,\%$
$20-40\,\%$
$40-60\,\%$
$>60\,\%$

6.2.2 Tracing fragmentation products of uridine ions to their base or sugar parts based on electron impact ionisation mass spectra in the literature

Previous EII [16, 184, 185, 194, 263–265] and SPI [196] papers on uridine suggested possible origins and assignments of some of the fragment ions, however, none of them presented a detailed comparison of the fragmentation pattern of uridine with uracil and ribose, or theoretical calculations supporting their assignments. It should be noted that it is *uracil minus H* and *ribose minus OH* which are present in uridine rather than *uracil* and *ribose*, respectively. Uracil and ribose are, however, the closest approximations which could be used for such comparisons. As sugars do not generally have chromophores in the wavelength range of our UV laser, we expect the MPI signal of ribose to be extremely weak in our experimental conditions and therefore we could not provide a comparison of MPI experiments for all three above-mentioned molecules. Therefore, we will briefly comment on the origin and assignments of some of the strongest fragment ions in the EII and SPI mass spectra of uridine from the literature [16, 184, 185, 194, 196, 263–265]:

- m/z113 – This ion was previously assigned by several authors as $C_4H_5N_2O_2{}^+$ [16, 184, 194, 196, 263], which is formed by the transfer of two hydrogens from the sugar part to the base part of the ion prior to breakage of the glycosidic bond. We refer to the $C_4H_5N_2O_2{}^+$ fragment ion in this thesis as BH^+. Biemann and McCloskey [263] argued that based on the mass spectra of O,N-perdeuterio derivatives, the two hydrogens have their origin mainly in the hydroxyl groups. They also reported that the absence of the $2'-OH$ group (see Fig. 5.10) results in the suppression of the BH^+ channel, which is not the case when the $5'-OH$ group is absent. This clearly points to $2'-OH$ being critically involved in the transfer of one of the hydrogens.

- m/z73 – This ion is the most prominent fragmentation product in the ribose mass spectrum on NIST [295], AIST [146] and in Zavilopulo et al.'s experiments [294] when heating the molecule to $117\,^{\circ}C$ and is completely absent in the uracil mass spectra [18, 60, 146, 181, 287–293], which strongly points to it having its origin in the sugar part of uridine$^+$. This is in good agreement with the study by Ts'o [184], and Rice and Dudek [194] who previously assigned it as $C_3H_5O_2{}^+$. Rice and Dudek identified it also as a product of the metastable dissociation of m/z133 ion (also [184]), which represents the sugar part of uridine. In addition, Poully et al. [8] observed the same ion in their proton irradiation experiments on ribonucleosides cytidine, adenosine and guanosine and assigned it to originate in the sugar part of these nucleosides.

- $m/z57$ – Analogously to $m/z73$, $m/z57$ ion is very likely to have its origin in the sugar part of the nucleoside ion. The fragment was assigned by Rice and Dudek [194] as well as Ptasińska et al. [16] as $C_3H_5O^+$. Rice and Dudek [194] identified this ion as a product of metastable dissociation of the sugar part of the nucleoside ($m/z133$). Poully et al. [8] also linked $m/z57$ fragment ion produced in their proton irradiation experiments on ribonucleosides cytidine, adenosine and guanosine to the sugar part of these molecules.

- $m/z69$ – This fragment ion is more likely to have its origin in the nucleobase part of uridine$^+$. Rice and Dudek [194] observed this ion in their metastable dissociation measurements and assigned it as $C_3H_3NO^+$ resulting from the metastable dissociation of $C_4H_4N_2O_2{}^+$ ($m/z112$), i.e. uracil part of uridine. Later on, Ptasińska et al. [16] assigned this ion as $C_3H_3NO^+$ (also [184])/$C_4H_5O^+$ in their EII experiments on uridine. In the gas-phase experiments on uracil, $m/z69$ fragment ion was previously identified by several authors [18, 26, 46, 60, 115, 288, 292] as a product of neutral *HNCO* loss from excited uracil radical cation. This suggests that if the $m/z69$ ion from uridine$^+$ has its origin in the base part of the ion, then it is very likely to be $C_3H_3NO^+$ rather than $C_4H_5O^+$. Experiments on isotopically labelled uridine would provide more insights.

In summary, the dominant *small* fragments ($m/z73$ and 57) in the mass spectra of uridine [16, 194, 196, 263–265] are products originating in the sugar part of the ion ($m/z73$ and 57). This is in good agreement with Ptasińska et al. [16] and Levola et al. [195] who reported that the sugar part is more fragile compared to the base part of nucleosides. It should also be noted that even the strongest fragmentation products of protonated uracil in electron collisions experiments by Sadr-Arani et al. [296] ($m/z70$, 85, and 96) and Molina et al. ($m/z44$, 70, 95 and 96) are either relatively weak or completely absent in the EII [16, 184, 185, 194, 263–265] and SPI [196] experiments on uridine in the literature. This indicates that the fragmentation pathways of $m/z113$ ions are not prominent channels. The apparent detection of common ionisation products from *ribose minus OH* in uridine and from isolated ribose suggest that *OH* loss may be the first step in a number of sequential dissociation pathways of excited ribose$^+$. The value of the ribose mass spectrum for peak assignments in the uridine mass spectrum is a good example of the efficacy of the *bottom-up* approach for interpreting the radiation response of biomolecules. Large fragments ($m/z \geq 111$) are dominated by $m/z113$ ions. These comprise intact nucleobase part plus two extra hydrogens which are transferred from the sugar part prior to the glycosidic bond cleavage. It should be noted that $m/z133$ fragment ion is discussed in detail in Section 6.3. The other relatively strong large fragmentation products in the previously reported mass spectra of uridine are:

- m/z141 – previously identified as $C_5H_5N_2O_3{}^+$ [16, 194, 196, 263]. This ion was observed also as a product of metastable dissociation of intact uridine ions in the experiments by Rice and Dudek [125]. The fragment ion consists of CH_2O attached to the intact base part of the uridine radical cation (i.e. $C_4H_3N_2O_2{}^+$).

- m/z171 – Levola et al. [196] previously suggested two potential assignments for this fragment ion, namely $C_6H_7N_2O_4^+$ (i.e. $C_2H_4O_2$ attached to the base part of uridine$^+$ $C_4H_3N_2O_2{}^+$) or $C_7H_9NO_4^+$ (i.e. C_2N attached to the sugar part of uridine$^+$ $C_5H_9O_4{}^+$). The m/z171 fragment ion is due to the loss of 73 *amu* from intact parent ion (m/z244). The m/z73 ion originating from the sugar part of the nucleoside ion is one of the strongest fragmentation products of uridine in the previously reported EII [16, 184, 194, 263–265] and SPI [196] mass spectra. Therefore, it is likely that the same dissociation channel might lead to the production of m/z171 ion, when the charge is localised on the base part of the molecule prior to the glycosidic bond cleavage.

- m/z226 – previously identified by Levola et al. [196] as $C_9H_{10}N_2O_5{}^+$. This fragment ion is the result of the loss of neutral water molecule from intact parent ion. Levola et al. [196] argued that it is more likely that the water loss occurs from the sugar part than from the base part as the sugar part has three hydroxyl groups which can potentially contribute to the production of a neutral water fragment.

Fragment ion production from isolated uridine in the EII experiments shows clear signatures of the fragmentation patterns of ribose$^+$. Applying the *bottom-up* approach has thus proved to be very useful at this stage for the identification of the origin of some of the strongest fragmentation products of uridine upon electron impact ionisation. In general, peaks of $m/z < 111$ mostly have their origin in the dissociated sugar part of the molecule, while the ones with $m/z > 111$ are in principle formed by intact nucleobase unit with a part of the sugar moiety attached to the molecule by a glycosidic bond. This observation is in good agreement with previous papers by Biemann and McCloskey [263], Ptasińska et al. [16] as well as Levola et al. [196]. The low abundance of product ions that can be traced clearly to a breakage of the base part of uridine suggests that the presence of the sugar moiety has a stabilising effect on the base.

6.2.3 Comparing MPI mass spectra of uracil and uridine with particular focus on CO loss

The section above is centred on using the *bottom-up* approach to recognise the origins of fragment ions from uridine that can be produced in various different ionisation processes.

However, multi-photon ionisation mass spectra have the special characteristic that they can yield information about processes in electronic excited states as well as ionic states. Therefore this section compares MPI mass spectra of uracil and uridine (see Fig. 6.3).

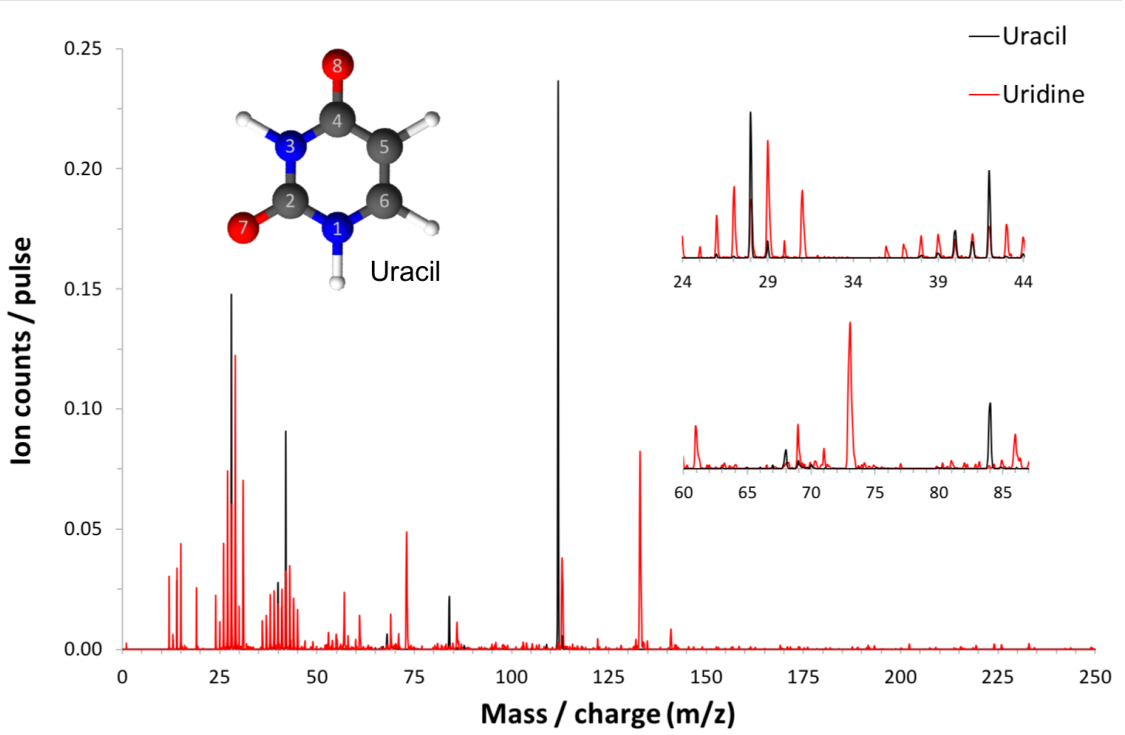

Fig. 6.3: Multi-photon ionisation mass spectra of uracil and uridine produced in the gas-phase by indirect laser-induced thermal desorption (focused UV lens position, $225\,nm$, average UV laser fluence $2\times10^{7}\,W\,cm^{-2}$, $445\,nm$ desorption laser power $0.5\,W$ above the ion detection threshold of $0.14\,W$ and $0.17\,W$ above the ion detection threshold of $0.16\,W$ for uracil and uridine, respectively). The chemical structure of uracil (*C* atoms are coloured in grey, *O* in red, *N* in blue and *H* in white) was drawn using ACD/Labs software and it was based on the diketo tautomeric form which was previously reported as the only tautomeric form present in gas-phase experiments [57, 275, 276]..

The $225\,nm$ MPI measurement on uridine with focused UV lens position is dominated by small fragments with m/z27 to 31, with the exception of m/z30 (see Tab. 6.1 and Fig. 6.3). Ryszka et al. [26] previously assigned the m/z28 ion in their MPI experiments on uracil as CH_2N^+. m/z27, 29 and 30 ions are rather weak or completely absent in the MPI mass spectra of uracil in Fig. 6.3, which gives a strong indication that these peaks in the uridine MPI mass spectra are more likely to have their origin in the sugar part of the molecule. In line with the comparison of the EII mass spectra in the literature, this suggests a greater propensity for the sugar side of the excited ion to fragment despite the fact that MPI is expected to proceed via the removal of an electron from an orbital localised on the base part in the present UV laser conditions. Comparing the relative abundance (see Tab. 6.1 and Fig. 6.3) of uridine parent ion m/z244 ($<5\,\%$ of the strongest ion yield) with the one in uracil (m/z112, strongest ion in the EII mass spectrum), suggests that

uridine is more prone to dissociation rather than uracil due to the presence of glycosidic bond, which makes its structure more fragile.

One of the motivations to carry out MPI experiments on uridine was to investigate the effect of binding of ribose on the CO loss channel previously observed in MPI experiments on uracil between 220 to 232 nm. Barć et al. (a previous PhD student in the Molecular Clusters Laboratory at the OU) carried out wavelength-dependent measurements on uracil with nanosecond UV laser pulses, which showed evidence for a new UV-induced process in uracil [18]. The new process led to m/z84 fragment ion production by MPI at wavelengths $\leq$ 232 nm. This fragment was never observed in direct excitation experiments, e.g. EII [18, 125, 181, 288, 289, 292] or SPI [60], and hence it must depend in some way on a critical process happening in an electronic excited state of uracil. The possibility of the m/z84 ion being produced by the ionisation of a neutral produced by dissociative MPI of uracil could be ruled out because the MPI mechanism was identified as 2-photon absorption. Later on, the MPI experiments by Ryszka et al. [26] on deuterated uracil identified the m/z84 fragment ion as $C_3H_4N_2O^+$, i.e. uracil$^+$ less CO. This channel was interpreted as a potential signature of previously theoretically predicted ultrafast neutral electronic excited state ring-opening. Nachtigallová et al. [45] and Richter et al. [285] reported three different ring-opening conical intersections (CIs) between uracil's S_2 and S_1 states, which all involved ring-opening at the same position of the ring, i.e. $N3-C4$ bond breakage (see the numbering of atoms in uracil structure in Fig. 6.3) which leaves a CO group exposed at one end of the open-ring structure. Depending on the calculation method, all of these three ring-opening CIs were energetically consistent with the wavelength threshold for m/z84 fragment ion production measured in the MPI experiments. In order to provide additional insights for whether sub-picosecond timescale excited state ring-opening mechanisms are involved in the production of m/z84 fragment ions in the MPI experiments at $\leq$ 232 nm, time-resolved ion yield (TRIY) measurements on uracil were carried out [9]. 220 and 200 nm pump excitation wavelengths in combination with 400 nm probe were employed in these measurements. However, even delays extending to 100 ps following the excitation did not lead to the appearance of m/z84 fragment ion. This result suggests that $C_3H_4N_2O^+$ production is not directly linked to the previously theoretically predicted ring-opening channels and another as-yet unidentified excited state process operating at longer timescales (most likely also involving ring-opening) is more likely to be involved.

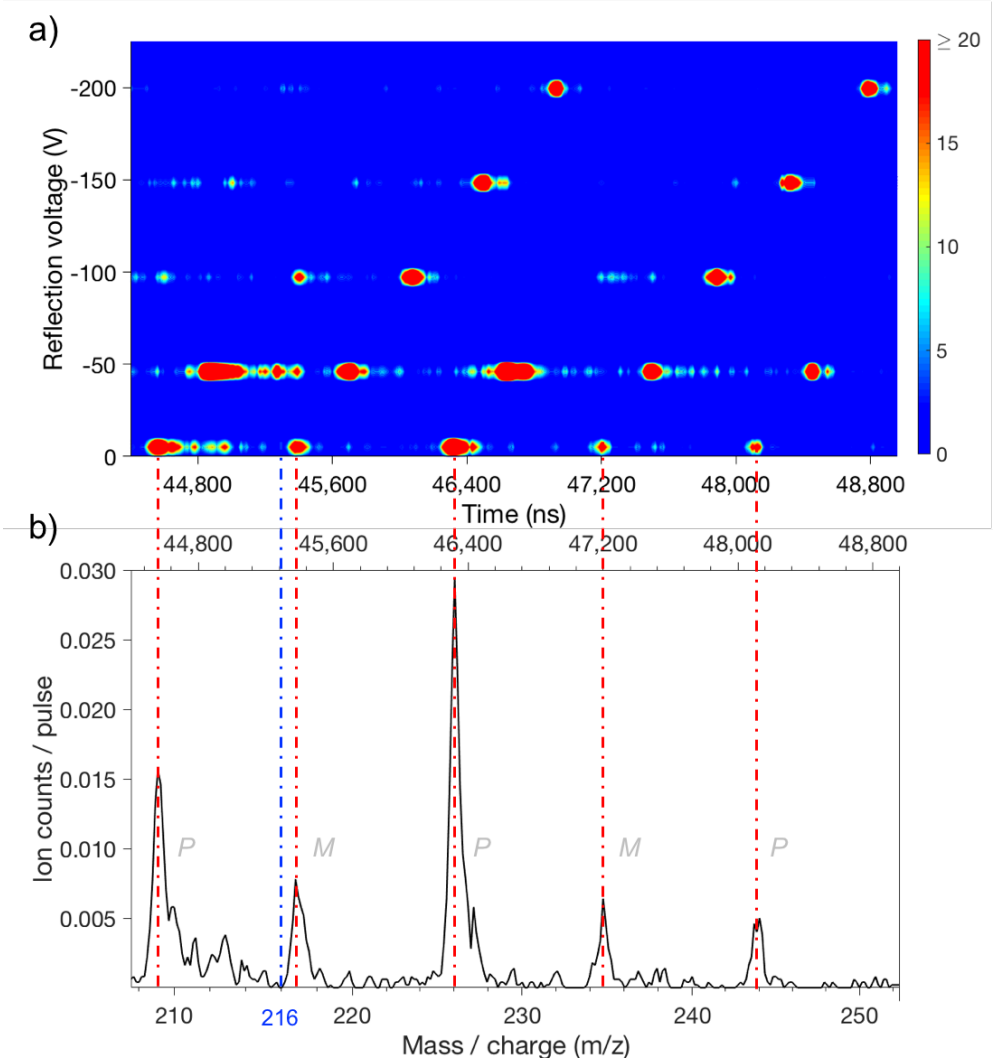

Fig. 6.4: Proof of the absence of *CO* loss channel in the MPI experiments on uridine at $225\,nm$. a) Selected part of MPI time-of-flight map of uridine and b) selected part of MPI mass spectrum of uridine at reflection voltage $-10\,V$ ($225\,nm$, average UV laser fluence $7\times10^{6}\,W\,cm^{-2}$, $445\,nm$ desorption laser power $0\,W$ above the ion detection threshold of $0.30\,W$). Red dash-dotted lines indicate which peak in the mass spectrum in b) corresponds to which red spot in the map in a). The blue dash-dotted line indicates the absence of $m/z216$ peak. *P* and *M* indicate whether peaks are due to prompt or metastable dissociations, respectively.

Notwithstanding the currently unknown nature of the electronic excited state process leading to the production of $C_3H_4N_2O^+$ in multi-photon ionised uracil, this channel is of particular interest as structural changes and bond breaking in electronically excited RNA/DNA components represent potential radiation damage pathways in these vital biopolymers [26]. Therefore, the impact of intermolecular bonding on the *CO* loss MPI channel was further investigated in experiments on uracil-water and uracil-adenine clusters. Barć et al. [18] showed that hydrogen bonding to water stabilises uracil with respect to the *CO* loss MPI channel. In contrast, the channel was enhanced in uracil-adenine clusters compared to pure

uracil clusters [26]. This was tentatively attributed to a significant presence of π-stacked complexes in the neutral beam as the production of hydrogen bonded uracil-adenine pairs was expected to suppress this fragmentation pathway. Any significant modification at $C5$ atom of uracil, i.e. methylation (thymine) [26] or fluorination (5-fluorouracil) [121] led to complete suppression of the CO loss route. The closer proximity of $C5$ atom to $C4O8$ group in uracil rather than to $C2O7$ group (see Fig. 6.3) supports the argument that it is more likely to be the former one that is involved in the loss of neutral CO fragment from uracil. Analogously to hydrogen bonding of uracil in clusters with water and adenine [18, 26] and modification of uracil by methylation or fluorination at $C5$ atom of uracil [26, 121], the MPI experiments on uridine in the range $222-265\,nm$ showed that bonding of ribose stabilises uracil with respect to the CO loss channel. Fig. 6.4 shows evidence that $m/z216$ fragment ions (i.e. uridine$^+$ less CO) are absent in the MPI measurements on uridine at $225\,nm$. The peak in the close proximity (indicated by blue dash-dotted line) is due to metastable dissociation as it cuts-off at more negative voltages than prompt fragment ions (see Fig. 6.4 a)). For more details on metastable dissociation measurements see Section 3.3.

6.2.4 Comparing MPI mass spectra of uridine with its analogues 2'-deoxyuridine and 5-methyluridine

Fig. 6.5 compares $225\,nm$ MPI mass spectra of uridine (a)) with those of 2′-deoxyuridine (b)) and 5-methyluridine (c)). Unlike uridine (see Tab. 6.1), very few fragment ion assignments have been proposed previously for the peaks in 5-methyluridine [196] and 2′-deoxyuridine [263] mass spectra. The agreement of the three strongest peaks aside from B^+, BH^+, or S^+ (i.e. $m/z57$, 73, and 86 – all also prominent peaks from ribose) in the uridine and 5-methyluridine mass spectra is a further indicator that fragment ion production from their common sugar part dominates. By contrast, it is intriguing to note that the mass spectra of 2′-deoxyribose in the literature [297] have relatively little in common with the 2′-deoxyuridine mass spectrum. For example, the strongest fragment ions from 2′-deoxyribose have $m/z44$ and 59, both of which are absent in Fig. 6.5 b).

It is worth noting that the B^+/BH^+ ratio differs significantly for uridine (< 0.1), 2′-deoxyuridine (~ 0.3) and 5-methyluridine (~ 3) in Fig. 6.5. BH^+ formation requires double hydrogen transfer from the sugar part to the base part of a nucleoside ion. Therefore, the low B^+/BH^+ ratio from uridine compared with 2′-deoxyuridine may appear to be broadly consistent with the fact that hydrogen bonding between the sugar and the base parts occurs in the lowest-energy neutral structures of uridine but not in any previously

calculated 2′-deoxyuridine structures [67].

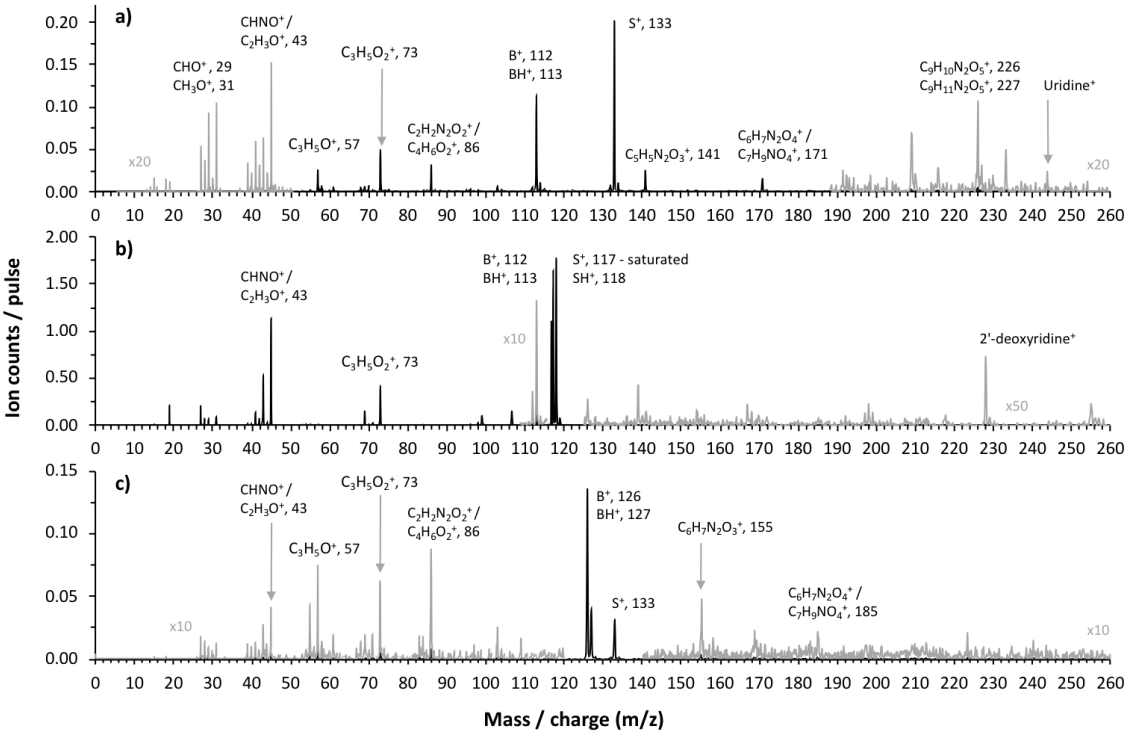

Fig. 6.5: 225 nm MPI mass spectra of a) uridine; b) 2′-deoxyuridine and c) 5-methyluridine. The 445 nm desorption laser powers in these measurements were 0.02 W above the ion detection threshold (0.47 W for uridine, 0.25 W for 2′-deoxyuridine and 0.12 W for 5-methyluridine). The most prominent fragment ion peaks of uridine are labelled with their previous assignments [16, 184, 194, 196, 263], whereas the peak assignments in panels b) and c) are proposed here based largely on an analogy with the uridine results. Note that the peak at about m/z 233 in panel a) is due to delayed (μs-timescale) H_2O loss from excited uridine$^+$.

6.3 Thermal desorption effects on the multi-photon ionisation products of uridine

Thermal lability of nucleosides, including uridine, was discussed in detail in Section 5.4.2. We excluded thermal decomposition of uridine as no systematic changes in the ratio of B^+/BH^+ as a function of desorption laser power were observed. This section focuses on the production of S^+ (m/z 133, $C_5H_9O_4^+$) ions. This stands out because it is the only ion from intact uridine whose relative yield depends on the desorption laser power. Fig. 6.7 a) shows that S^+ production by MPI of uridine at 225 nm increases as a proportion of the total ion signal with increasing desorption laser power. The plot also shows that no equivalent thermal dependence is observed on S^+ production by 225 nm MPI of 5-methyluridine, which shares the same sugar part as uridine. Hence, the base part of uridine appears to

be critically involved in this thermal effect. As the lowest-energy electronic transitions of nucleosides occur between molecular orbitals (MOs) that are localised on the base parts [43, 67], this provides an early hint that neutral electronic excited state dynamics might play a role in the thermal dependence of S^+ production of uridine shown in Fig. 6.7 a). We will develop this idea in this section with reference to the sensitivity of this fragment ion channel on MPI wavelength (drawing on all four panels of Fig. 6.7).

6.3.1 DFT optimisations of selected uridine conformers and dissociation products

This section focuses on the fragments produced by cleavage of the glyosidic bond between $B-H$ and S with or without the transfer of one or two hydrogen atoms. Therefore, the hydrogen atoms that interact with both parts of uridine and those in the immediate vicinity of the glyosidic bond are particularly relevant in the present discussion.

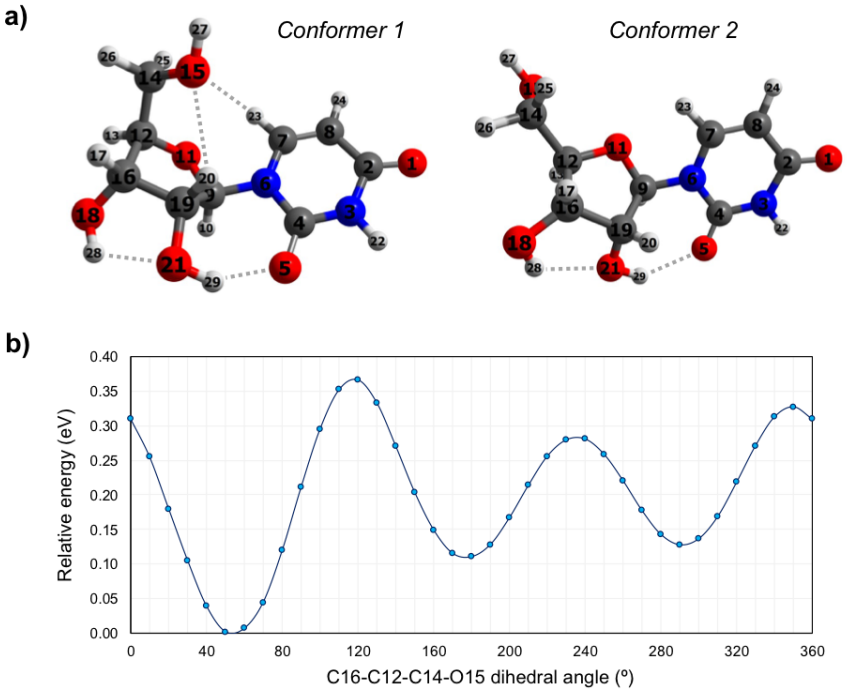

Fig. 6.6: a) Schematic diagrams of DFT optimisations of two key structures of neutral ground state uridine. *Conformer 1* corresponds to the lowest-energy structure identified by Peña et al. [231] on the basis of *ab initio* calculations and rotational spectroscopy experiments. *Conformer 2* corresponds to the lowest-energy structure from DFT calculations by Delchev [67] and by So and Alavi [68]. Hydrogen bonds are indicated by dotted lines and atoms are coloured as follows: blue for nitrogen, dark grey for carbon, red for oxygen, and light grey for hydrogen. b) Energies of the non-optimised structures produced by rotating the hydroxymethyl group of *conformer 1* about the $C12-C14$ bond (i.e. the $C16-C12-C14-O15$ angle). This angle is 55° and 188° in the present optimisations of *conformers 1* and *2*, respectively.

Peña et al. [231] performed an exhaustive conformational search using force field and semi-empirical methods and then carried out *ab initio* optimisations of the five lowest-energy structures. The resultant lowest-energy optimised structure showed excellent agreement with their rotational spectroscopy measurements on a target produced by laser ablation followed by cooling in a supersonic expansion. A. Rebelo, PhD student in the Molecular Clusters Laboratory at the OU, performed a DFT optimisation of Peña et al.'s [231] structure in order to establish the starting point for subsequent calculations. The structure (*conformer 1* in Fig. 6.6 a)) is characterised by four cooperative hydrogen bonds and the similarity of their distances in the present optimisation ($H29\bullet\bullet\bullet O5 = 1.92\mathring{A}$, $H28\bullet\bullet\bullet O21 = 2.05\mathring{A}$, $H20\bullet\bullet\bullet O15 = 2.57\mathring{A}$, $H23\bullet\bullet\bullet O15 = 2.94\mathring{A}$) with Peña et al.'s higher-level optimisation ($H29\bullet\bullet\bullet O5 = 1.93\mathring{A}$, $H28\bullet\bullet\bullet O21 = 2.02\mathring{A}$, $H20\bullet\bullet\bullet O15 = 2.41\mathring{A}$, $H23\bullet\bullet\bullet O15 = 2.97\mathring{A}$) indicates that our level of theory is a suitable choice of framework for describing the structure of isolated neutral uridine ($M05/aug-cc-pVDZ$, see Appendix B for details).

Earlier DFT calculations by Delchev [67] and by So and Alavi [68] identified a different lowest-energy structure of uridine, corresponding to *conformer 2* in Fig. 6.6 a). Delchev [67] presented another five uridine isomers with higher energies but these did not include *conformer 1*. In the present optimisations, *conformer 1* is more stable than *conformer 2* by $0.1\,eV$. The two conformers have very similar structures aside from the orientation of the hydroxymethyl group (CH_2OH) on the sugar. The hydroxymethyl group rotation required for the conformers to approach each other must overcome barriers associated with interactions of the $O15$ atom with the $C7-H23$ and $C19-H20$ bonds. To obtain a first approximation for the barriers between *conformers 1* and *2*, A. Rebelo calculated the energies of the non-optimised structures produced by rotating the hydroxymethyl group of *conformer 1* about the $C12-C14$ bond (see Fig. 6.6 b)). The lowest barrier is thus estimated at $\sim 0.33\,eV$. As an aside, it is worth mentioning that an optimisation starting from the third minimum in Fig. 6.6 b) resulted in a structure that has not been reported previously in the literature. The $C16-C12-C14-O15$ angle in this conformer is 289° and it features an $O15-H27\bullet\bullet\bullet O18$ bond; otherwise its structure is close to that of *conformers 1* and *2*. Its energy is $0.11\,eV$ greater than *conformer 1* (i.e. very similar to *conformer 2*).

Possible thermal decomposition products of uridine were investigated as follows. Starting from *conformer 1*, we split the molecule at the glycosidic bond with the transfer of up to two hydrogens from the base part of the molecule to the sugar part or vice versa, and then optimised the resultant structures at infinite separation. We then compared the

summed energy of each product pair with the energy of *conformer 1*. This was repeated for hydrogen transfer between all of the possible sites on either side of the glycosidic bond and many of the transfers resulted in multiple stable structures. The summed energy of the lowest-energy pair (B and $S-H$) was $0.63\,eV$ higher than *conformer 1* (see Appendix B). The lowest dissociation barrier (not calculable practically with the present computational resources) must be higher than this minimum energy difference, which is almost double our estimated barrier between *conformers 1* and *2*. This confirms that thermally-driven conformational changes in gas-phase uridine can be expected at temperatures which are too low for decomposition to take place.

6.3.2 m/z 133 fragment ion production from *ILT*-desorbed uridine

Fig. 6.7 a) shows that S^+ production by $225\,nm$ MPI of uridine increases as a proportion of the total ion signal with increasing desorption laser power. We observed no equivalent thermal desorption dependence of the relative production of S^+ by $225\,nm$ MPI of 5-methyluridine, which shares the same sugar part as uridine. Hence, the base part of uridine appears to be critically involved in this thermal desorption effect. As the lowest-energy electronic transitions of nucleosides occur between MOs that are localised on the base part [43, 67], this provides an early hint that neutral electronic excited state dynamics might play a role in the thermal desorption dependence of S^+ production from uridine shown in Fig. 6.7 a). We will develop this idea in the next paragraphs with reference to the sensitivity of this fragment ion channel to MPI wavelength (drawing on all four panels of Fig. 6.7).

S^+ ions have been observed and assigned previously in experiments that involved direct ionisation from the electronic ground state [16, 184, 194, 196, 263, 264]. Significantly, however, Levola et al.'s study [196] of thermally-driven effects on the single-photon ionisation mass spectra of uridine did not identify any dependence of the relative signal of S^+ on the sublimation temperature. The thermal desorption dependence seen in Fig. 6.7 a) is new and, furthermore, it depends critically on MPI wavelength. Fig. 6.7 b) shows that the relative production of S^+ by $250\,nm$ MPI of uridine is independent of the desorption laser power.

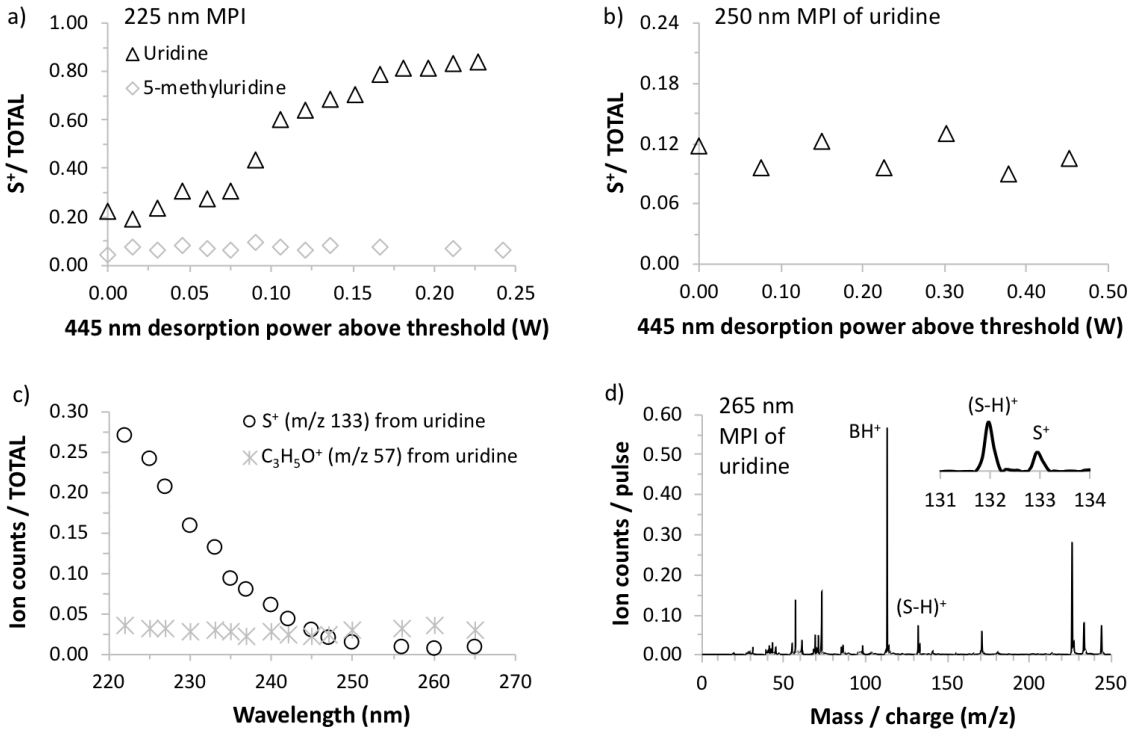

Fig. 6.7: a) $445\,nm$ desorption laser power dependence of S^+/total ion production by $225\,nm$ MPI of uridine (ion detection threshold $0.37\,W$) and 5-methyluridine (ion detection threshold $0.19\,W$); b) $445\,nm$ desorption laser power dependence of S^+/total ion production by $250\,nm$ MPI of uridine (ion detection threshold $0.45\,W$); c) wavelength dependence of MPI production of S^+ and $C_3H_5O^+$ ion signal/total ion production from uridine (average $445\,nm$ desorption laser power $0.02\,W$ above the ion detection threshold of $0.46\,W$); d) $265\,nm$ MPI mass spectrum of uridine ($445\,nm$ desorption laser power $0.03\,W$ above the ion detection threshold of $0.46\,W$). Average UV laser power $5\times10^6\,W\,cm^{-2}$.

Fig. 6.7 c) shows the dependence of the S^+/total ion production from uridine on MPI wavelength from 222 to $265\,nm$. The ratio increases steadily with falling wavelength below a threshold of about $250\,nm$. Wavelength threshold behaviour of this kind in our multi-photon ionisation experiments indicates a critical energy threshold in a neutral electronic excited state. If the threshold corresponds to an isomeric transition or a dissociation then this is likely to modify fragment ion production by MPI [18, 115]. Ionic state thresholds do not manifest themselves as distinct wavelength thresholds in our experiments because any MPI laser fluence that produces reasonably high ion signals involves several different orders of photon absorption within a given measurement (typically 2-photon absorption and 3-photon absorption dominate, while 4-photon absorption contributes relatively weakly [18]). To provide a further indication that the present wavelength threshold behaviour of the S^+ signal is not related to an ionic state threshold, Fig. 6.7 c) also shows the corresponding wavelength dependence for the $C_3H_5O^+$ fragment ion signal. Ptasińska et al.'s EII measurements [16] revealed that $C_3H_5O^+$ has a similar appearance energy ($10.20\pm0.05\,eV$) as S^+ ($10.39\pm0.15\,eV$) but Fig. 6.7 c) shows that its relative signal does

not change significantly with MPI wavelength.

Fig. 6.7 d) shows that S^+ production is small but not negligible at the longest wavelength studied here. Taken together, the results in Fig. 6.7 suggest that two different processes are responsible for producing S^+ ions from uridine in the present experiments: (i) a process activated at MPI wavelengths below $250\,nm$ that is sensitive to desorption laser power and (ii) a process that is insensitive to MPI wavelength and to desorption laser power. It is natural to attribute process (ii) to the same mechanism as S^+ production in electron impact ionisation [16] and single-photon ionisation experiments [196], which have shown no dependence on thermal desorption. Neither the neutral electronic excited states accessed en route to ionisation (which naturally depend on wavelength) nor the thermal desorption conditions have significant effects on this dissociation process. The following discussion considers the possible causes of the MPI wavelength threshold behaviour and the thermal desorption dependence of process (i).

As thermal decomposition can be discounted, the desorption laser power dependence of S^+ production from uridine in Fig. 6.7 a) is most likely to be due to changes in the populations of different isomers in the target. There are numerous examples in the literature of isomeric effects on the relative production of fragment ions in mass spectrometry experiments (e.g. see the contrasting mass spectra produced by single-photon ionisation of α- and β-alanine [298], or by electron impact ionisation of selected isomers of pyrrolobenzodiazepines [299]) so the plausibility of this attribution depends primarily on the idea that the relative populations of different uridine isomers can change significantly as a function of the desorption laser power in the present experiments.

The calculations in Section 6.3.1 confirm that isomeric transitions of uridine can occur at markedly lower temperature than decomposition. Previous experiments to estimate the stainless steel foil temperature in an ILTD system [9] indicated that increasing the desorption laser power by $0.25\,W$ (as in Fig. 6.7 a)) raises the foil temperature by $\sim 50\,K$. The previous experiments used a focused desorption laser whereas we applied an unfocused beam here, so the rise in the local foil temperature in the Fig. 6.7 a) measurements is likely to be significantly lower than this. Furthermore, the foil temperature represents the upper limit for the possible vibrational temperature of the gas-phase uridine molecules. Therefore, we consider it to be unlikely that the 4-fold increase in the relative production of S^+ in Fig. 6.7 a) could be driven solely by the temperature post-desorption. We hypothesise that variations in the molecules' specific structural dynamics during desorption are critical for determining the relative populations of isomers in our gas-phase targets. Fig. 6.6 b)

provides an example of how quite subtle differences in the starting geometry of uridine (the orientation of the hydroxymethyl group) can lead to relaxation into different stable conformers. It is natural to expect a molecule's structural dynamics during desorption to be affected by surface morphology and also by the desorption of neighbouring molecules. The uridine desorption rate in the present experiments rises sharply with the desorption laser power (an increase of $0.02\,W$ approximately triples the total MPI signal), so we consider that resultant changes in the distribution of uridine geometries leaving the surface are entirely plausible. Indeed, there are numerous precedents in the literature for different sublimation temperatures leading to different gas-phase isomer populations [300–302].

The paragraphs above argue that the thermal desorption dependence of S^+ production from multi-photon ionised uridine via what we have called process (i) can be traced to changes in isomeric form prior to MPI. Furthermore, process (i) demonstrates wavelength threshold behaviour and this is indicative of a critical mechanism in an electronic excited state. These two points can be viewed as being inter-related when we consider that vibronic excitation is an excellent tool for changing molecular structure. Delchev's time dependent DFT calculations [67] provide an intriguing clue into how this might account for the present MPI results. His potential energy surface (PES) calculations showed that internal conversion between S_1 ($n\pi^*$) or S_2 ($\pi\pi^*$) states and relatively dark charge transfer (CT) states of $n\pi^*$ character can dramatically reduce the energy required for isomeric transitions in electronically excited uridine. Hence, these CT states can act as bridges for structural changes in uridine following excitation to the bright S_2 ($\pi\pi^*$) state in the present experiments. The calculated vertical excitation energies of the CT states vary significantly ($4.801-5.822\,eV$) in the different uridine isomers considered by Delchev [67]. This variation suggests that the initial isomeric form of the ground state molecule is likely to have a significant effect on the excitation energy required for access to a CT state via a conical intersection (CI). Therefore, we speculate that structural changes in electronically excited uridine via CT states can enhance S^+ production in the present MPI experiments and that the lowest-lying CI for internal conversion from S_2 into a relevant CT state requires $< 250\,nm$ ($> 5.0\,eV$) photoabsorption. In this case, increasing the photon energy beyond this threshold could enable access to CT states from more initial isomeric forms of uridine in the target and/or could access parts of the S_2 PES that relax more readily to a relevant CI. The desorption power dependence could be explained by increasing the relative populations of isomers that give access to CT states at lower photon energies. Further work is required to test this idea and, if it is correct, to identify the specific isomers and CIs involved.

6.4 Summary and outlook

The first part of this chapter discusses the fragment ion channels of uridine that show no clear dependence on desorption conditions. The fact that the dominant *small* fragment ions of uridine in EII and MPI experiments have their origin in the sugar part of the ion suggests that ribose is more prone to dissociation than the uracil part of the molecule. The relatively high instability of ribose was previously discussed with respect to the early evolution of biomolecular building blocks by several authors, e.g. Larralde et al. [303] and Concinero et al. [304]. They concluded that it is unlikely that the primordial genetic material contained ribose or other sugars due to their high instability. Our results are in good agreement with the above-mentioned studies. On the other hand, our MPI experiments on uridine showed that bonding to *ribose minus OH* suppresses the *CO* loss channel previously observed in isolated multi-photon ionised uracil. It is important to mention that previous studies showed that methylation and halogenation of uracil also disrupt this channel and so does intermolecular hydrogen bonding. This suggests that the *CO* loss channel is unlikely to survive within almost any larger molecule or condensed environment. Recognising examples like this where processes are unique to sub-units is an essential part of the *bottom-up* approach.

The second part of the chapter reports MPI experiments showing that desorption laser power dramatically affects the MPI production of sugar-unit ions ($m/z\,133$) from uridine via a critical process with a threshold energy of $5.0\,eV$ in the neutral electronically excited molecule. This dependence on thermal desorption conditions can only be understood plausibly in terms of changing isomeric populations in the target, and my co-worker's DFT calculations indicate that isomeric transitions of uridine can occur at markedly lower temperatures than decomposition. Therefore, although the key dynamics are yet to be identified, this chapter's most significant contribution is the first experimental evidence supporting isomeric effects on the radiation response of uridine. To our knowledge, this is the first experimental result of this kind for any gas-phase nucleoside. It highlights the importance of developing methods to produce neutral gas-phase nucleoside targets that are pure in terms of structure as well as in terms of eliminating thermal decomposition.

6.5 Contributions by co-workers

I carried out metastable dissociation measurements on uridine working with internship student in the Molecular Clusters Laboratory at the OU D. Mészáros. I carried out wavelength dependence measurements on uridine in the range 222 to $265\,nm$. I carried

out thermal decomposition measurements on uridine at 250 *nm* working with PhD student in the Molecular Clusters Laboratory A. Rebelo and Dr. V. Vizcaino. A. Rebelo carried out DFT calculations on uridine presented in Section 6.3.1 and Appendix B with support of Dr. J.-C. Poully. I analysed the experimental data and worked on their interpretation with A. Rebelo and Dr. S. Eden. The time-resolved ion yield measurements on uracil mentioned in Section 6.2.3 were published in [9]. We are currently preparing a journal manuscript based on the results in Sections 6.2.4, 6.3 and Appendix B. M. Ryszka, R. Pandey, P. Limão-Vieira, P. Papp, N. J. Mason, D. Townsend and K. Nixon contributed to this work through in-depth discussions, aiding the development of the experimental facility, and/or co-supervising students that worked in the lab.

Chapter 7

New DEA/EII/MPI experimental set-up for probing *indirect laser-induced thermally* desorbed or *Stark deflected* molecules

This chapter describes the design and principles of operation of a newly built experimental set-up in the Molecular Clusters Laboratory at the Open University. The main objective of this set-up is to carry out dissociative electron attachment (DEA) experiments on biomolecules of low volatility such as nucleosides from an indirect laser-induced thermal desorption (ILTD) source. Adapting ILTD for electron collision experiments has required some significant and original modifications of the design concept. Whereas our ILTD assembly for the *Compact MPI/EII experimental set-up* aimed to replicate Greenwood and co-workers' simplest ILTD system as closely as possible, this chapter presents a truly new desorption system that tackles the specific challenges of DEA. Even the fundamental desorption process will not be exactly same as it will feature some initial *conventional* heating. Besides the DEA experiments, the set-up has been built to also enable multi-photon ionisation (MPI) and electron impact ionisation (EII) experiments in the same conditions. Complementary MPI and EII experiments can provide us with valuable information on electronic excited state dynamics of biomolecules, which can be further exploited to understand DEA processes. In addition to ILTD, the system gives the option to probe Stark-selected isolated molecular targets and clusters produced in molecular beam as the new chamber is attached to the previously built *Stark deflection set-up*. The optimisation of the experimental system is on-going and progress to date is presented here.

7.1 Introduction

The overall aim of this PhD thesis is to enhance our understanding of the processes by which radiation initiates damage to RNA/DNA through studies of progressively more complex RNA/DNA components. *Primary damage* of biomolecules induced by direct interactions with UV photons is addressed in Chapters 4 and 6. The experiments presented in those chapters were performed using the *Compact MPI/EII experimental set-up* in the Molecular Clusters Laboratory at the OU, which is described in Section 3.2. However, it should be noted that direct radiation interactions with biomolecules are not the only cause of the damage and that most of the energy deposited in cells by ionising radiation is directed into the production of low-energy ($1 - 20\,eV$) electrons, radicals and ions through the excitation, dissociation and/or ionisation of surrounding molecules (dominantly water) [20]. As discussed in Chapter 1, the interaction of low-energy electrons (LEEs) with molecules can lead to a resonant process called dissociative electron attachment (DEA) which has been found to play a significant role in radiation damage to DNA [20].

Despite longstanding interest linked to radiation chemistry/biology [20] and astro-chemistry/biology [305], the current understanding of LEE-driven processes in isolated biomolecules has mainly been limited to the complexity of nucleobases [61, 63, 111], simple sugars [110, 306] and amino acids [307, 308]. This stems from the major computational demands of running high-level DEA calculations on larger components of nucleic acids or proteins [109] and also from the difficulties with bringing such species intact into the gas-phase (discussed in detail in Chapter 5). In addition, DEA experiments generally apply low electron beam currents and/or probe channels with low cross sections and thus depend on high target densities of intact molecules. To tackle the complexity problem in the DEA studies on RNA/DNA constituents, we have designed, built and commenced optimisation of a new experimental system for studying low-energy electron interactions with *ILT*-desorbed biomolecules using reflectron time-of-flight mass spectrometry. ILTD not only enables the production of pure intact neutral nucleoside targets of uridine, $2'$-deoxyuridine and 5-methyluridine as proved in our MPI experiments presented in Chapter 5, but also the extremely high signals obtained in MPI experiments in Chapters 5 and 6 indicate high target densities which are key for experiments such as DEA. To date, ILTD has only been used in experiments involving laser interactions [8, 9, 43, 66] and proton collisions [8]. To our knowledge, this is the first attempt to adapt it for electron collision experiments.

When doing photon excitation/ionisation experiments on targets produced in the gas-phase by ILTD, it is easy to avoid interactions with condensed samples. Relatively low velocities

and high masses mean that ion beams are not strongly affected by stray magnetic fields and can be collimated quite readily. By contrast, using ILTD with electron beams brings significant challenges associated with preventing electrons directly hitting the solid-phase sample. This is mainly due to the following reasons:

- Electron beams are hard to focus due to electrons being repelled from each other (sometimes characterised in terms of *"space charge"*). This can be reduced by using low beam currents and adding collimating magnetic fields but it can never be eliminated and some electrons will *"escape"* from the beam's central axis.

- Electrons are extremely sensitive to electric fields (even at the level of those produced by dielectric surfaces in the chamber accumulating charge). This means that mass spectrometry experiments need to be designed very carefully to shield electric fields in MS from the electron beam pulses. Of course, this is not possible during the ion extraction pulse which will also accelerate residual electrons present in between electron pulses (again, inevitable if the experiment applies high pulsing rates to maximise signal).

- Electrons are extremely sensitive to any magnetic fields. This can be harnessed to improve collimation of the electron beam but it can also disrupt the beam if there are any unwanted magnetic fields.

Direct interaction of electrons with solid sample will result in *"processing"* of the sample (and might even lead to desorbing molecules and ions from the surface directly), which will cause ambiguities in the interpretations of measured mass spectra. All of these problems are exacerbated when working with low-energy electron beams. To the best of our knowledge, the only studies of DEA processes on neutral RNA/DNA components or their derivatives produced in the gas-phase by laser desorption where performed by Bald et al. [245, 309] using LIAD. Furthermore, these are - to our knowledge - the only previous electron collision experiments on any molecules produced by an *indirect laser-induced desorption* method (see Chapter 5). However, Bald et al. do not describe any system that had been added to the experiment with the specific aim of preventing any direct interactions of stray electrons from the electron beam with condensed samples.

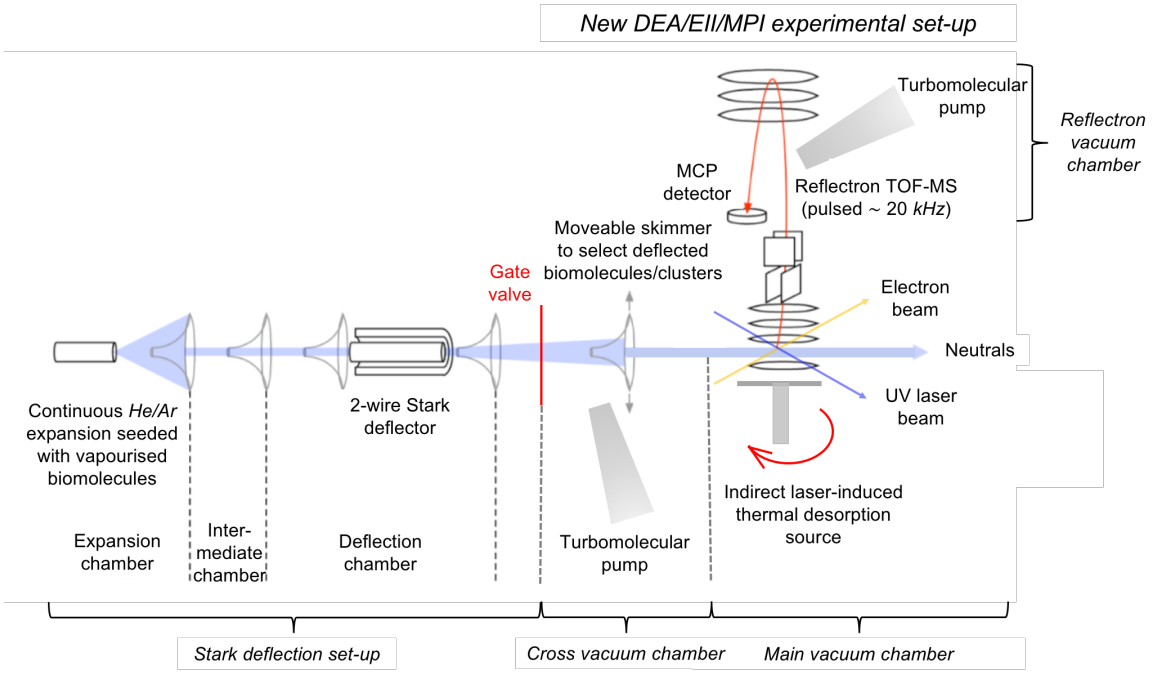

Fig. 7.1: Schematic diagram of the *New DEA/EII/MPI experimental set-up* and the previously built *Stark deflection set-up* (diagram of the *Stark deflection set-up* adapted from [57]).

A great advantage of the new apparatus is that it is designed to enable dissociative electron attachment (DEA), electron impact ionisation (EII) and multi-photon ionisation (MPI) experiments in the same target conditions (see Fig. 7.1) and therefore to draw direct comparisons between them. Complementary MPI and EII experiments can provide us with valuable insights into the electronic excited state dynamics of biomolecules, notably because any fragment ion channels detected by MPI that cannot be accessed by EII can be attributed to dissociations or isomeric transition in neutral electronic excited states [9]. Some critically important DEA processes take place via electronic excited states of temporary negative anions (so-called core-excited shape resonances or Feshbach resonances, see Section 2.5.2.2). Knowledge of the neutral electronic excited states of a molecule, their dynamics, and their dissociation pathways can provide a useful starting point for understanding these DEA resonances, even though the precise fundamental basis for such analogies remains an important open question in the DEA community. In addition, the dissociation and reactivity of excited neutrals compete with DEA as a radiation damage process caused by low-energy secondary electrons. Hence, neutral excited state dynamics and DEA are complementary both from a fundamental and applied perspective. Furthermore, accumulating DEA, EII and MPI data on the same biomolecular target can help to define the isomeric structures present in the target (a major issue for nucleosides and some nucleobases and highly specific to the desorption method applied, as discussed in Chapters 5 and 6). All three processes can exhibit strong and specific dependences on

initial isomeric form so analysing data for all three together enables a more complete characterisation of the target structures than could be achieved with single-process data sets. DEA is particularly sensitive to initial isomeric form as dipole moment plays a critical role in electron attachment (for example, see Haranczyk et al.'s theoretical study of DEA to different guanine structures [310]).

Being able to carry out MPI and EII experiments in the same conditions as DEA experiments is not only interesting from the scientific point of view as discussed above, it also proves to be very useful in the process of optimising the new apparatus. This is because MPI and EII experiments generally yield considerably higher signal rates than DEA experiments. DEA cross sections are generally much lower than EII cross sections and MPI laser fluences are many orders of magnitude greater than typical electron beam fluences. Moreover, mainly MPI but also EII of several biomolecules have been previously investigated in the Molecular Clusters Laboratory at the OU, which provides a useful reference for optimisations of the new system. Therefore, the first tests of the new set-up have been performed using EII and MPI.

As mentioned in Chapter 1, in parallel with experiments on progressively more complex biomolecules, studies of clustering effects represent the second approach of the Molecular Clusters Group at the OU in tackling the problem of how to link insights from the gas-phase experiments on relatively simple biomolecules to effects in biological environments. The *Stark deflection set-up* was built by M. Ryszka, a former PhD student in the Molecular Clusters Laboratory, with the aim of probing neutral clusters of a well-defined size and structure produced in supersonic molecular beams. The Stark deflector applies a strong electric field gradient to deflect isolated molecules and/or clusters in supersonic molecular beams as a function of their *effective dipole moment*-to-mass ratio. M. Ryzka and subsequently R. Pandey and A. Rebelo were able to perform EII and MPI experiments on Stark-manipulated beams [58]. Unfortunately, however, the design of the interaction chamber of the Molecular Clusters Group's original *Stark deflection set-up* has not enabled us to probe DEA processes due to poor transmission of ions from the low-energy electron beam to the extraction region of the mass spectrometer. Therefore, this chamber was replaced by the *main vacuum chamber* of the *New DEA/EII/MPI experimental set-up*, which means that MPI, EII and DEA experiments can be performed on Stark manipulated targets as well as on ILTD targets (see Fig. 7.1).

As this PhD thesis is about studying progressively more complex molecules rather than clustering effects, the *Stark deflection mode* of the *New DEA/EII/MPI experimental set-up*

is described here only briefly and the main focus is on the *indirect laser-induced thermal desorption mode*. It should be noted though that the molecular beam from the *Stark deflection set-up* proved to be useful in the optimisation stage of the new experimental apparatus. The design as well as progress with the testing and optimisation of this set-up is presented below.

7.2 *Indirect laser-induced thermal desorption mode*

Fig. 7.2 shows the *New DEA/EII/MPI experimental set-up* in *indirect laser-induced thermal desorption mode*. The system was designed and developed with the central aim of using reflectron time-of-flight (TOF) mass spectrometry for probing low-energy electron interactions with relatively large biological molecules such as nucleosides, which are difficult to produce in the gas-phase with high target density and without any thermal decomposition by *conventional* heating (see Chapter 5). An additional specific motivation is to carry out electron impact ionisation and multi-photon ionisations experiments on *indirect laser-induced thermally* desorbed uridine in the same experimental conditions to further support our investigation presented in Chapter 6.

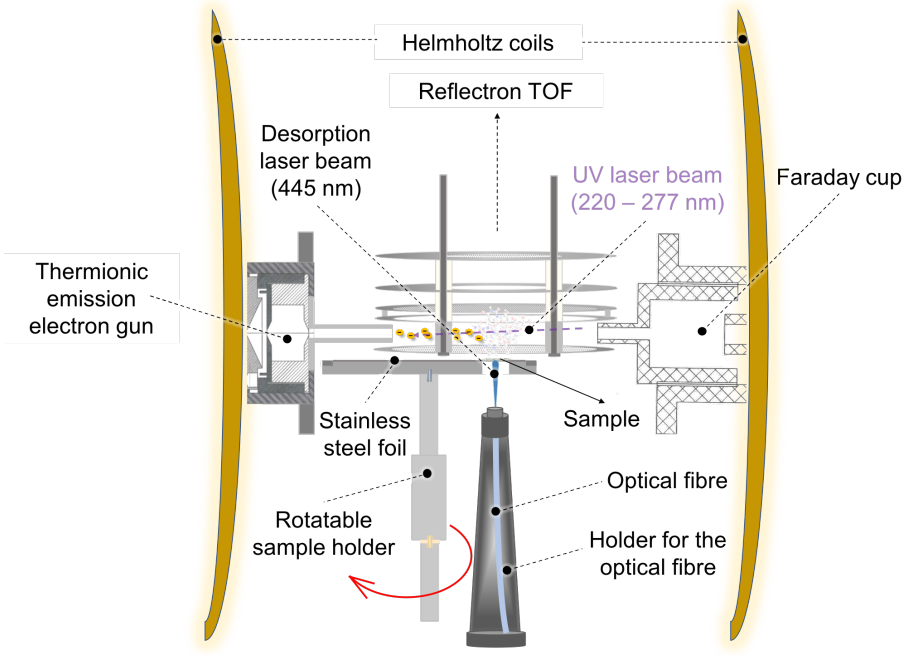

Fig. 7.2: Scheme of the *main vacuum chamber* of the *New DEA/EII/MPI experimental set-up* in *indirect laser-induced thermal desorption mode*. The *main vacuum chamber* is depicted from a front view, i.e. the molecular beam shown in Fig. 7.1 would come out of the page towards the reader in this diagram.

Very briefly, an optical fibre is used to direct the CW desorption laser beam onto the *reverse* side of the stainless steel foil (i.e. the side without the condensed sample). The desorbed

molecules interact with a pulsed electron beam produced by a home-built electron gun (for DEA and EII experiments) and the electron current is measured using a home-built Faraday cup. A current in the Helmholtz coils produces a uniform magnetic field which serves to collimate the electron beam. Alternatively, UV laser pulses can be used instead of electrons for MPI experiments. The resultant ions are detected using a reflectron time-of-flight mass spectrometer (TOF-MS).

7.2.1 General description and the vacuum system

The *New DEA/EII/MPI experimental set-up* consists of three vacuum chambers:

1. *Main vacuum chamber* – contains the *central* components of the experiment: an ILTD source, a calibration gas inlet system, the *ion source* part of the mass spectrometer, an electron gun (EG) and a Faraday cup (Fc). As LEEs are sensitive to any stray magnetic fields, the choice of the materials used for the *main vacuum chamber* as well as individual components inside of the chamber was limited to those with relative permeabilities close to 1, i.e. titanium (relative magnetic permeability ≤ 1.00005 [311]) or stainless steel 316*LN* (relative magnetic permeability ≤ 1.005 [312]) where possible, alternatively stainless steel 316*L* (relative magnetic permeability ≤ 1.1 [312]). The main body of the *main vacuum chamber* is made of stainless steel 316*L*. The tubing is made of stainless steel 316*L* throughout the experiment because rollable stainless steel 316*LN* sheet is not commercially available. The *"open"* flanges of the chamber are the only parts that could have been made of stainless steel 316*LN* but this proved to be impractical in terms of cost and lead time. However, the *"closing"* flanges closest to the electron beam (the ones onto which the EG, the Fc, the *ion source* and the ILTD source are mounted) are all made of stainless steel 316*LN*. The *"closing"* flanges contain far more material than the *"open"* flanges so their magnetic properties are more critical for the experiment. The ion source, EG, Fc and their holders are made of titanium. The electrical feedthroughs for the EG and Fc are made of stainless steel 304 (relative magnetic permeability ≤ 1.3 [312] and therefore two 316*LN* stainless steel *DN*40*CF* full nipples (the tubing is 316*L* and the *DN*40*CF* flange parts are 316*LN*) are used to move the magnetic electrical feedthrough for the EG and a single 316*LN* stainless steel *DN*16*CF* (the tubing is 316*L* and the *DN*16*CF* flange parts are 316*LN*) full nipple is used to move the magnetic electrical feedthrough for the Fc further away from the electron beam. The support frame as well as bolts, nuts and washers used for tightening individual flanges are made of aluminium (relative magnetic permeability ≤ 1.000022 [313]) for the same reason. It should be noted that replacing the

stainless steel (304) bolts, nuts and washers with the aluminium ones dramatically improved collimation of the electron beam.

2. *Reflectron vacuum chamber* – sits on the top of the *main vacuum chamber* and houses the flight tube, the reflectron part of the mass spectrometer and a micro-channel plate (MCP) detector. An important element of the mass spectrometer - the X and Y deflector plate assembly – is mounted on a back-to-back flange in between the *main* and *reflectron chambers* (stainless steel 316*L*).

3. *Cross vacuum chamber* – connects *the main vacuum chamber* to the *Stark deflection set-up* as shown in Fig. 7.1 (stainless steel 304). Most of the experiment's pumping comes through this chamber. A gate valve between the *Stark deflection set-up* and the *cross vacuum chamber* separates the two experiments and it is normally closed when using the system in the *indirect laser-induced thermal desorption mode*.

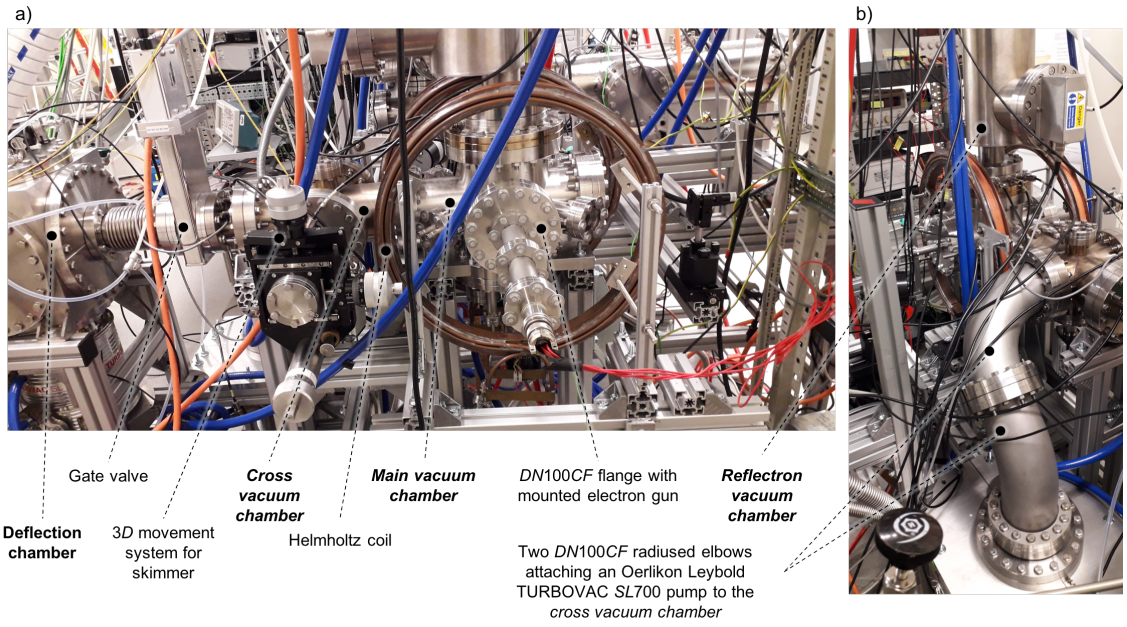

Fig. 7.3: Photographs of the *New DEA/EII/MPI experimental set-up*: a) side view (molecular beam propagating from left to right) and b) the system for attaching a turbomolecular pump to the *cross vacuum chamber*.

A new support frame has been designed and built for the *main vacuum chamber* and the *cross vacuum chamber* (part of it also supporting Helmholtz coils). The experiment is pumped by two turbomolecular pumps. An Oerlikon Leybold TURBOVAC *SL*700 (with N_2 pumping speed of $690\,ls^{-1}$) is attached to the *cross vacuum chamber* via two *DN*100*CF* radiused elbows and a *DN*160*CF*-to-*DN*100*CF* reducing nipple. The pump is supported in the vertical position by a specially designed plate (built with the help of K. Dewar and M. Abbott from Research Design and Engineering Facility at the OU) which is attached

to the *DN*160*CF* ring of the turbomolecular pump. The plate is mounted on a support frame, which is also partially connected to the support frame of the *main vacuum chamber* and the one previously built for the *Stark deflection set-up* in order to increase the stability of the whole apparatus and the turbomolecular pump. The second turbomolecular pump (Oerlikon Leybold TURBOVAC 151 with N_2 pumping speed of $145 ls^{-1}$) is attached to the flight tube of the *reflectron vacuum chamber*. Both turbomolecular pumps are backed by an Edwards *XDS*10 Dry Scroll Vacuum Pump. The pressure in the experimental apparatus is measured using the Leybold IONIVAC ITR 90 pressure gauge attached to the *cross vacuum chamber*. The typical base pressure in the chamber is of the order of $10^{-8} mbar$.

7.2.2 Principles of operation

The *main vacuum chamber* houses the core components of the experimental set-up as shown in Fig. 7.2. The foil of the ILTD source is negatively charged to repel electrons and is placed $3 mm$ underneath the grounded backplate grid of the *ion source* to prevent disrupting the pulsed extraction field. The foil is mounted on a rotating system which allows sample replenishment and consequently longer measurement times, which will be particularly important in DEA experiments and any others with low signals. Heating tapes mounted on the outside of the *main vacuum chamber* will be used during ILTD measurements to heat the whole chamber to moderate temperatures ($80 - 90\,^{\circ}C$) to prevent condensation of the *ILT*-desorbed molecules on the grids of the *ion source*. It should be noted that heating the skimmer base to about $100\,^{\circ}C$ in the *Compact MPI/EII experimental set-up* has been adequate to prevent the condensation of nucleobases at the skimmer orifice (which must be cooler than the base) even though all experiments on nucleobases using *conventional* heating sources heat to much higher temperatures than this. The temperature of the *ion source* will be monitored using a thermocouple (OMEGA Engineering) attached to the *ion source*. The neighbouring chambers (*reflectron vacuum chamber* and the *cross vacuum chamber* with the pump) will not be heated so the desorbed molecules will end up condensed on surfaces inside those chambers. There will be numerous cold surfaces between the heated chamber and the MCP in the reflectron chamber, so we are not particularly concerned about condensation on the detector. Nonetheless, the detector will be baked regularly. Despite baking the detector and the *main vacuum chamber* to temperatures higher than $100\,^{\circ}C$ prior experiments, we are anticipating producing large background signals, particularly in EII experiments where the ion production process is essentially non-selective. If this background does not allow us to perform experiments, more localised heating system will be required, e.g. setting up one or more radiative heating lamps aimed at the *ion source*. The disadvantage is added complexity of construc-

tion (particularly considering the limited space) and less-uniform heating. It should be noted that the EG filament will be several thousand $^{\circ}C$ during operation so an *additional* $\sim 100^{\circ}C$ will make little difference to its operation. The design of the ILTD system is discussed in more detail in Section 7.4.1.

A new *ion source* was designed by A. Rebelo, a PhD student in the Molecular Clusters Laboratory at the OU, and it was built with the help of C. Hall and his colleagues from the Research Design and Engineering Facility at the OU. The *ion source* electrodes (see Fig. 7.2) are supported by four pillars which are mounted on a $DN160CF$ zero-length reducer flange (stainless steel $316LN$), which is placed between the *main* and the *reflectron vacuum chamber* (see Fig. 7.1). The distances within the *ion source* are the same as in the *Compact MPI/EII experimental set-up* and they were provided by KORE technology. The *ion source* electrodes and pillars are made of titanium, while the grids are made of stainless steel (gold grids, preferable to avoid any magnetisation, proved to be too fragile for practical use in this experiment). Unlike in the *Compact MPI/EII experimental set-up*, the backplate electrode is not a solid disk (see Fig. 3.3); a stainless steel grid is used instead in order to enable the desorbed molecules enter the interaction region (see Fig. 7.2).

After passing through the backplate grid of the ion source, the desorbed molecules interact with electrons produced by the home-built pulsed electron gun for DEA or EII experiments. In both cases the electron beam current is monitored by a home-built Faraday cup and Helmholtz coils are used to collimate the beam (magnetic field $\sim 6\,mT$). The EG, Fc and Helmholtz coils were all designed by Prof. E. Krishnakumar (Tata Institute of Fundamental Research Mumbai and former Marie Curie visiting professor at the OU) and built by C. Hall and his colleagues from the Research Design and Engineering Facility at the OU. More details on the EG and the Fc are given in Section 7.4.2. The UV laser beam arrangement for MPI experiments is described in Section 7.4.3.

Analogously to the *Compact MPI/EII experiment*, ions formed after the interaction of the desorbed molecules with electrons/UV laser beam are extracted by the electric field produced by applying a voltage pulse ($+380\,V$ in DEA experiments and $-380\,V$ in EII/MPI experiments) to the extraction electrode, then accelerated to about $2\,keV$ and deflected by X and Y deflectors in order to direct them into a detector (analogous to Fig. 3.3). For DEA experiments, the EG has to be pulsed such that there is no temporal overlap of the electron beam and the ion extraction field established by the pulsed extraction electrode, in order to avoid extracting electrons from the interaction region onto the detector (for more details on pulsing the EG see Section 7.4.2.3.1). After passing through the deflectors,

ions then travel through the field-free region (FFR), are decelerated in the retarding field and reflected to pass through the FFR again before reaching a micro-channel plate (MCP) detector. As in the *Compact MPI/EII experimental set-up*, the pre-amplified ion signals are timed using a Fast ComTec *P*7887 time-to-digital conversion (TDC) card with 250 *ps* minimum bin size. Data are collected using a LabVIEW acquisition system developed by M. Ryszka (the same system as used for the *Compact MPI/EII experimental set-up*, see Section 3.2.2).

7.3 *Stark deflection mode*

As mentioned in Section 7.1, *Stark deflection* is not exploited in this PhD thesis, therefore we will describe the *Stark deflection set-up* here only very briefly. It should be noted though that the molecular beam from the *Stark deflection set-up* was used for optimising the performance of the *New DEA/EII/MPI experimental set-up*, notably the pulsing of the EG and the mass spectrometer as discussed in Sections 7.4.2.3.1 and 7.4.4. In addition, the MPI experiments on uridine presented in Chapter 6 showing the evidence for thermally driven isomeric transitions highlight the importance of developing methods to produce gas-phase neutral targets that are pure not only in terms of eliminating thermal decomposition but also in terms of structure. This may be achievable in the future by seeding molecules from ILTD in a supersonic expansion or noble gas atoms for *Stark deflection*.

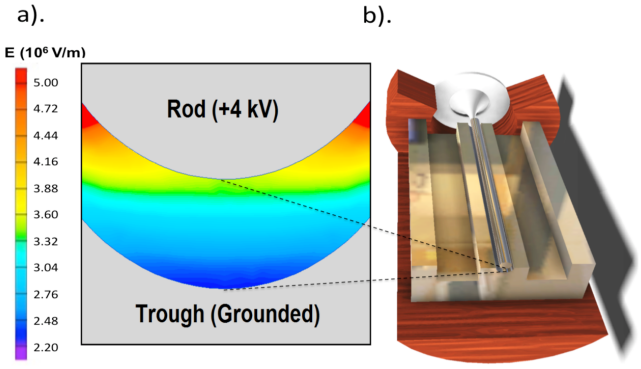

Fig. 7.4: Two-wire *Stark deflector* built by J. Küpper and co-workers at DESY. a) Cross-sectional view of the *Stark deflector* showing the electric field strength with 4 *kV* applied to the rod and b) 3*D* drawing of the *Stark deflector* (adapted from [58]).

The *Stark deflector* (see Fig. 7.4) employs a strong electric field gradient to deflect molecules and/or clusters in supersonic molecular beams based on their *effective dipole moment*-to-mass ratio. In order to achieve controlled deflection a rotationally cold molecular beam has to be produced. In high rotational states the specific rotational state occupied by a polar molecule dominates its deflection and hence Stark deflection be-

comes a much less effective tool for separating out different molecular structures in the beam [57, 58]. Therefore, extensive pumping is applied in the *expansion chamber* (up to $4000 ls^{-1}$ compared with $500 ls^{-1}$ in most experiments using the *Compact MPI/EII experimental set-up*) in combination with a differential pumping stage (*intermediate chamber* pumped at $\sim 500 ls^{-1}$) (see Fig. 7.1). Despite the importance of rotational cooling, a CW expansion is applied because DEA experiments will require high pulsing frequencies of the electron beam and mass spectrometer (typically several tens of kHz) in order to achieve reasonable signal-to-noise ratios (S/Ns) in practical acquisition times. To our knowledge no commercial supersonic expansion nozzle can be pulsed at such high frequencies and in any case the cooling benefit is reduced as the pulsing frequency is increased, raising the residual pressure in the expansion chamber.

The CW expansion of Ar, He or Kr in the *Stark deflection set-up* is seeded with the molecules of interest (either liquids or solids vaporised by *conventional* heating) in essentially the same way as in the *Compact MPI/EII experimental set-up* (see Section 3.2.2 for more details). The beam passes through three skimmers (see Fig. 7.1) before reaching the Stark deflector (built by J. Küpper and co-workers at Deutsches Elektronen-Synchrotron - DESY). The Stark deflector deflects polar species vertically (see Fig. 7.4). The beam then passes through a flexible nipple which connects the *deflection chamber* to the gate valve. This is kept open in the *Stark deflection* experiments. Afterwards the beam passes through the *cross vacuum chamber* where a movable skimmer is used to sample different parts of the beam and then it enters the interaction region of the *main vacuum chamber* where it interacts with electrons (DEA/EII) or photons (MPI). The resultant ions are detected using the reflectron TOF mass spectrometer as described in Section 7.2.2. It should be noted that in order for the *Stark deflected* beam system to be compatible with the new chamber, the flexible nipple, the gate valve and the *cross vacuum chamber* had to be designed and built.

7.4 Design, development, testing and optimisation of the *New DEA/EII/MPI experimental set-up*

7.4.1 The indirect laser-induced thermal desorption system

The design of this ILTD system was modified for the *New DEA/EII/MPI experimental set-up* as follows (see Fig. 7.5):

1. The most important change is that the foil is separate from the backplate, which means a negative bias voltage can be applied to the foil. The bias voltage prevents

electrons in DEA and EII experiments from hitting the sample in its solid state (powder) by repelling them from the foil. This is essential for excluding any contribution of such interactions in the measured mass spectra as well as for preserving the sample molecules intact prior sublimation.

2. Heating tapes mounted on the outside of the *main vacuum chamber* will be used during ILTD measurements to heat the whole chamber to $80 - 90\,^{\circ}C$ to prevent condensation of the *indirect laser-induced thermally* desorbed molecules on the grids of the *ion source* and subsequently the interaction of the electrons with the solid-state targets. Therefore, the volatilisation of molecules will not be *"pure"* ILTD, but it will be a combination of *conventional heating* to moderate temperatures and *"standard"* ILTD. Due to increased sample temperature induced by heating of the chamber, we are expecting to use much lower desorption laser powers than in ILTD experiments. The *baseline* temperature of the foil (i.e. when the desorption laser is turned off) will be estimated using a thermocouple (OMEGA Engineering) attached to the sample holder. During the measurements we will regularly monitor the temperature of the *ion source* using this thermocouple.

3. The static foil holder is replaced by a rotatable one, which has the following advantages:

    - It provides 29-times larger surface area for sample deposition and therefore longer measurement times. This is particularly valuable for DEA measurements in view of the long acquisition times expected. Furthermore, the relevant flange's position at the bottom of the experiment makes its removal and installation relatively awkward so minimising the frequency of these interventions is desirable.
    - After using a given desorption laser power, the foil can be rotated to provide a completely fresh sample without breaking the vacuum and opening the experimental system. In the case of the ILTD system in the *Compact MPI/EII experimental set-up*, it is necessary to open the experimental system and change the sample to make sure we can desorb from a completely fresh spot unaffected by previous measurements. This is due to relatively small sample deposition area and limited control over changing the laser spot position.

4. The use of fibre optics to direct the desorption laser light onto the foil makes the optical alignment much easier and safer. As the desorption laser and the optics needed to focus the light into the optical fibre are located on an optical bench relatively far from the vacuum chambers, the risk of unintentionally disrupting the

alignment is reduced. To the best of our knowledge, fibre optics have not been previously used for ILTD experiments. It should be noted that the suitability of readily-available fibres and associated optical components for typical ILTD CW beams is very different to that required for pulsed infrared (IR) beams. Therefore, a commercial system outside of its normal specifications had to be tested as a part of the design process.

5. The foil holder is mounted horizontally, which was made possible by the fibre optics system. The horizontal orientation was essential because both the pulsed UV laser and molecular beams are horizontal. If the foil holder had been mounted vertically, the pulsed UV laser beam would have needed to be directed upwards at some stage, which would not be safe nor practical. In addition, the horizontal orientation reduces the risk of powder falling from the foil. By contrast, in the *Compact MPI/EII experimental set-up* the foil is mounted vertically just above a turbomolecular pump which has to be therefore protected by inserting an arc-shaped piece of copper sheet below the *ion source* to prevent any dislodged powder falling into the pump.

6. A *DN*100*CF* viewport on the side of the *main vacuum chamber* allows us to check the state of the sample (i.e. whether it has been depleted or not).

7.4.1.1 The rotatable foil holding system

The rotatable foil holding system is attached to the bottom *DN*160*CF* flange of the *main vacuum chamber* as outlined in Fig. 7.2 and 7.5. It consists of a mechanical rotary feedthrough (stainless steel 304, moved away from the chamber by inserting a 316*LN DN*40*CF* full nipple), a titanium bar and a titanium *sandwich system* with a stainless steel foil. The titanium bar and the *sandwich system* were built with the help of A. Jones from Research Design and Engineering Facility at the OU. The rotary feedthrough allows controlled rotation of the foil. The titanium bar is attached to the rotary feedthrough using a polyether ether ketone (PEEK) piece of studding and a ceramic washer, in order to electrically-insulate the rotary feedthrough from the bias voltage which is applied to the titanium bar (and hence also to the *sandwich system* with the stainless steel foil). The *sandwich system* used for attaching the foil is similar to the one used in the ILTD system for the *Compact MPI/EII experimental set-up*, i.e. the foil is gripped between two titanium parts as shown in Fig. 7.6. The gap in the bottom titanium ring (see Fig. 7.5) allows the CW laser beam to irradiate the foil and therefore to desorb the sample molecules attached to the opposite side of the foil in the same way as described in Section 3.2.3.3. It should be noted that sample is not spread around the whole surface of the foil, but only on the reverse side of the parts which can be irradiated by the desorption laser (see Fig. 7.6 c)).

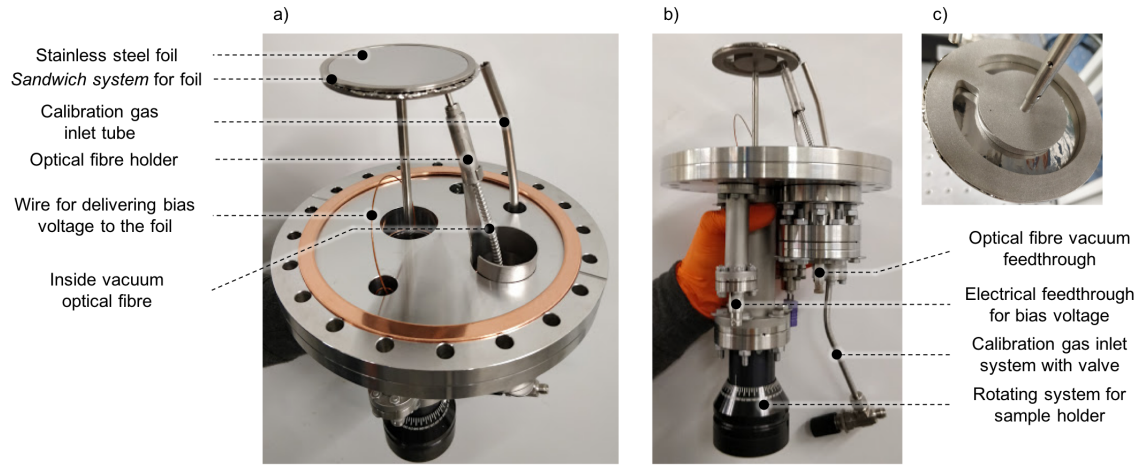

Fig. 7.5: a) and b) pictures of the bottom flange of the *main vacuum chamber* showing the new indirect laser-induced thermal desorption source (without sample on the foil), the system for applying bias voltage to the foil and the calibration gas inlet system. c) Detailed view from below of the *sandwich system* holding a stainless steel foil.

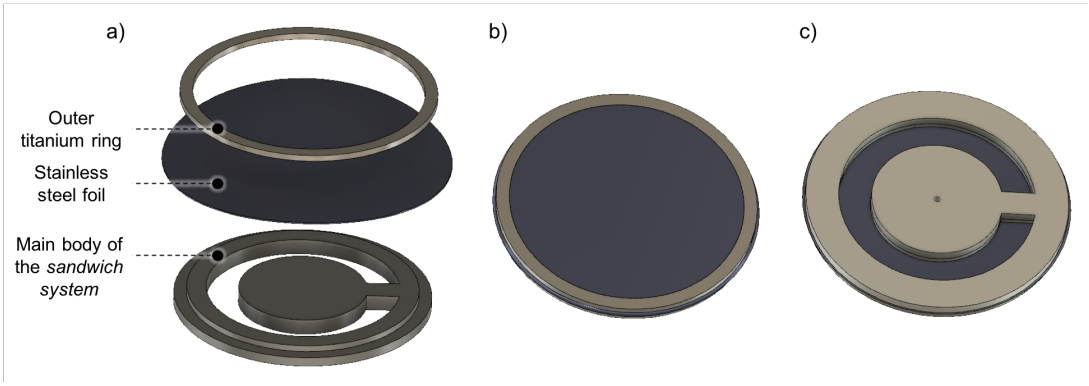

Fig. 7.6: *Sandwich system* for the foil: a) in the process of assembling; b) top view (assembled) and c) bottom view (assembled).

7.4.1.2 The fibre optics arrangement

The same laser (CW diode laser $DLM-445-1000$, Eksma Optics, $445\,nm$, the maximum power $1.28\,W$) is used to desorb the molecules from the foil as in the ILTD system in the *Compact MPI/EII experimental set-up*. The major difference is in the way the laser beam enters the vacuum chamber and reaches the stainless steel foil. While in the *Compact MPI/EII experimental set-up*, the desorption laser beam enters the chamber via a viewport, in the *New DEA/EII/MPI experimental set-up* a fibre optics arrangement is used instead. The schematic diagram of the fibre optics arrangement is depicted in Fig. 7.7. Briefly, the desorption laser beam is reflected by two broadband dielectric mirrors positioned at approximately 45° to the beam propagation before reaching a lens. The lens focuses the light to an appropriate beam width to enter the *outside vacuum optical fibre* component.

The light then passes through a vacuum feedthrough for optical fibres and the *inside vacuum optical fibre* component. The CW laser light exits the optical fibre via a *SMA*905 termination, which is positioned approximately 3 *mm* underneath the stainless steel foil as shown in Fig. 7.5 a) and b). All of the fibre optics components were provided by Anglia Instruments and contain stainless steel (304). Specifications of individual optical components are mentioned in Fig. 7.7.

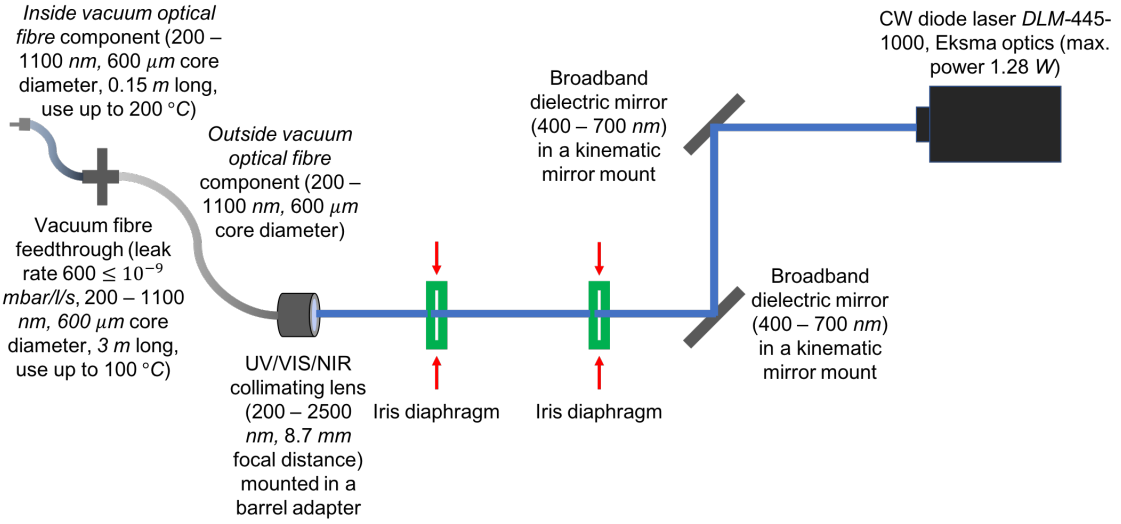

Fig. 7.7: Schematic diagram of the fibre optics arrangement of the ILTD system for the *New DEA/EII/MPI experimental set-up* in the Molecular Clusters Laboratory at the OU.

Optical fibres are typically used in the IR range of the electromagnetic spectrum, notably for telecommunications. In our application, 445 *nm* laser light of relatively high maximum CW power of 1.28 *W* is used. Optical fibres for high-power applications normally use air-gap-ferrule technology to connect the terminals instead of energy-absorbing materials such as epoxies. However, air-gap-ferrule technology is not vacuum-compatible and therefore inside vacuum fibres and feedthroughs for the fibres normally use *epoxy* to connect the terminals. At 445 *nm* there is a high risk of burning the epoxy, causing it to vaporise and deposit a residue on the face of the connector (private communication with D. Farrer, technical support engineer from Thorlabs). Therefore to test the suitability of the fibre optics for our application, the first tests were run on a test kit provided by Anglia Instruments, which consisted of a collimating lens, an optical fibre and a vacuum fibre feedthrough. We passed the desorption laser beam at its maximum power through these components for an hour. The test kit was checked under a microscope by the company before and after our test and no obvious damage due to high power of 445 *nm* laser beam was observed. The test kit was then returned and new fibre optics has been installed and aligned as shown in Fig. 7.7.

A set of two broadband dielectric mirrors and two iris diaphragms are used to allow fine alignment of the desorption laser with the *outside vacuum optical fibre* component (see Fig. 7.7). The alignment is done as follows:

1. The initial alignment of the mirrors is achieved by placing a laser pointer in the place of the collimating lens, shinning the laser pointer light through the two iris diaphragms with minimum possible opening and tuning the mirror positions until the laser pointer beam enters the opening of the desorption laser.

2. The laser pointer is replaced by a collimating lens and the position of the mirrors is finely tuned until the desorption laser beam passes through the two iris diaphragms and the collimating lens.

3. The *outside vacuum optical fibre* component is connected to the collimating lens and a UNO laser power meter (Gentec-EO) is used to measure the power of the desorption laser beam after the *outside vacuum optical fibre* component. The desorption laser is kept at low powers ($\approx 0.01\,W$) in order to protect the optical fibre from potential damage if the alignment is not optimal. Fine-tuning of the mirrors positions can be performed while watching the response of the desorption laser power.

7.4.1.3 Testing and optimisation of the ILTD system

The following tests have been already made on the new ILTD system:

1. Vacuum tests
   The flange with the ILTD source (the rotatable foil holding system, the vacuum fibre feedthrough and the *inside vacuum optical fibre* component), the system for applying a bias voltage on the foil, the calibration gas inlet system (for more details see Section 7.4.2.1) as well as a feedthrough for thermocouple (see point 2. in Section 7.4.1) has been installed in the *main vacuum chamber* and vacuum-tested. The electrical feedthroughs and the feedthroughs for thermocouple and calibration gas are made of stainless steel 304 separated from the flange by 316*LN DN*16*CF* full nipples. The calibration gas tube inside vacuum is made of titanium.

2. $445\,nm$ transmission tests
   The average transmission of the $445\,nm$ light through the collimating lens is only around $72 \pm 2\,\%$ due to a small defect. The combined transmission of the $445\,nm$ light through the *outside vacuum optical fibre* component, the vacuum fibre feedthrough and the *inside vacuum optical fibre* component is $88 \pm 1\,\%$. Therefore the maximum power deliverable to the foil under vacuum using the current desorption laser and fibre optics arrangement is $0.65\,W$. This is above the desorption laser

powers applied in the vast majority of the measurements presented in Chapter 6 (e.g. $0.49\,W$ in the Fig. 6.2 experiments).

3. Uridine desorption tests
   The fibre optics arrangement has been successfully used for desorbing uridine from the foil. This was tested by placing uridine sample on the foil and irradiating the foil under vacuum which resulted in blank spots indicating that all molecules were desorbed.

The tests above show that the new ILTD system can be used to produce similar targets to the ones we have studied in the *Compact MPI/EII experimental set-up*. However, it should also be noted that the planned experiments using the electron beams will be carried out in a heated chamber (as explained in Section 7.4.1) so in fact we expect lower desorption laser powers to be required.

7.4.2 The electron beam

The electron beam in the *New DEA/EII/MPI experimental set-up* is produced by a home-built thermionic emission EG and the electron beam current is measured using a home-built Fc. The key advantage of using the home-built EG is that the same EG has been previously proven to give high current (i.e. from hundreds of *pA* up to a maximum of about $2\,nA$ during the pulses [314]) even at low energy. The current from this type of EG typically only begins to drop below $5\,eV$ and DEA resonances have been studied successfully using this system down to $\sim 1\,eV$ [314]. For DEA experiments high electron currents are essential as DEA typically have low cross sections (for comparison Feil et al. [181] measured maximum total cross section for EII of uracil of about $16\times10^{-20}\,m^2$ around $100\,eV$ and for DEA of about $25\times10^{-22}\,m^2$ around $1\,eV$) and it is not possible to maintain a dense target using ILTD over very long periods due to the thinness of condensed sample layer. Furthermore, the target densities of the Stark-deflected beams will be very low. In addition, the collimating magnetic field makes it robust and convenient to work with even when residual magnetic and electric fields cannot be eliminated entirely. This reduces cost and complexity of the experiment. This disadvantage of the design is that it has no *"monochromator"* function. Therefore the energy resolution can be no better than the thermal (Maxwell-Boltzmann) distribution of the hot filament. At the temperatures required for thermionic emission from tungsten ($\sim 2200\,^{\circ}C$), this corresponds to an energy resolution of about $\pm 0.5\,eV$. Higher resolution than this would be extremely valuable in DEA studies but improved resolution necessarily comes at the expense of beam current. This will be targeted after it has been established that the method can work with high electron beam currents.

The only modification to the design of the EG was adding an extension to the front part of the EG (see Fig. 7.2) which fits between the backplate grid and the extraction electrode of the *ion source* (approximately 5 *mm* overlap) and therefore helps to shield the electrons from the electric fields generated by other electrodes of the *ion source*, mainly the focusing electrode (see Fig. 3.3). A similar extension is used for the Fc. It should be noted that without these extensions turning on the mass spectrometer voltages led to complete loss of the current measured on the Fc, while with the extensions the corresponding drop in the current measured on the Fc was never greater than 0.1 μA. New holding systems were designed to mount the EG and the Fc in the *main vacuum chamber* as indicated in Fig. 7.2. In both cases, the holding system consists of a titanium plate and four titanium rods attached to *DN*100*CF* flanges (stainless steel 316*LN*). The external housing of the EG is attached to the plate which is then mounted to the four rods and enables the EG to be moved closer/further from the centre of the chamber. The Fc can be moved in an equivalent manner. The separation between the exit of the EG and the entrance of the Fc is kept at around 8 *cm*.

7.4.2.1 Principles of operation of the electron gun and the Faraday cup

A schematic diagram of the EG and the Fc is shown in Fig. 7.8.

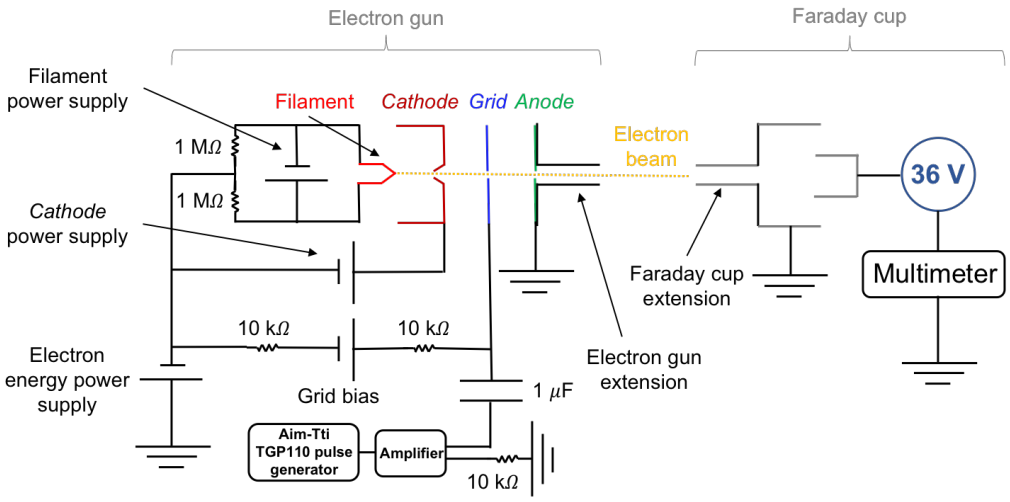

Fig. 7.8: Schematic diagram of the EG and the Fc. *Cathode* aperture (1.5 *mm*, *grid* aperture 1 *mm*, *anode* aperture 1.5 *mm*, electron gun extension aperture 4 *mm*, Faraday cup extension aperture 3 *mm*, separation between *cathode* and *grid* apertures 2.9 *mm* and separation between *grid* and *anode* apertures 4 *mm* (adapted from [314]).

Briefly, a current of about 2.2 A is passed through the tungsten filament (A & J Scientific) which leads to thermionic emission. Two 1 $M\Omega$ resistors are connected parallel to the filament (in a so-called Wheatstone bridge configuration) to ensure that the tip of the

filament is at the same potential as the point between the two resistors. The electrons emitted by the filament are extracted by the *cathode* in the forward direction, then pass through the *grid* towards anode which is grounded and therefore positive with respect to the filament, *cathode* and *grid*. An $Aim-TTiEX752M$ power supply is used to supply voltage for electron beam energy. The filament, *cathode* and *grid* are floated at this voltage with respect to ground, but an offset still needs to be applied because the voltage across the filament means that the filament tip will not be at the float voltage. The electrons will have energy equal to the potential difference between the filament tip and ground. Therefore, it will be necessary to calibrate the electron beam energy and this will be performed using an effusive flow of calibration gas (see Section 7.4.2.1). An $ISO-TECHIPS1603D$ power supply is used to supply current for the filament, and $Aim-TTiEX752M$ and *FARNELL LS* $30-10$ supply voltages for *cathode* and *grid*, respectively.

To align the electrons produced by the filament an external magnetic field is applied which is generated by a pair of water-cooled Helmholtz coils (see Fig. 7.2, designed by Prof. E. Krishnakumar and built by C. Hall and his colleagues from Research Design and Engineering Facility at the OU). This magnetic field is essential as without applying the magnetic field, no beam current is measured on the Fc. Normally, a current of $4.5A$ supplied by *GW INSTEKSPS* -606 power supplies passes through the coils (335 turns, radius $\approx 22\,cm$) producing a magnetic field of approximately $6\,mT$, which was measured using a $GM04$ gaussmeter with a transverse probe (Hirst Magnetic Instruments). The Fc is placed opposite the EG at the end of the interaction region and is connected to a $36V$ power supply (i.e. four $9V$ batteries) to attract the electrons. The electron current on the Fc is measured using a $U1232A$ Handheld Digital Multimeter (Keysight Technologies, sensitivity $0.01\,\mu A$).

7.4.2.1.1 The calibration gas inlet system

As noted above, the absolute electron energy scale has to be calibrated to account for the voltage across the filament as well as for possible minor effects on electron energies by any stray fields in the interaction volume. Often such calibration is based on a well-known resonance for the formation of O^- from O_2 by DEA, at $6.5\,eV$ [315]. Therefore, a calibration gas inlet system was built in the *New DEA/EII/MPI experimental set-up* as shown in Fig. 7.5 a) and b). The system consists of a stainless steel tube ($1/4\,in$ inner diameter) welded in the $DN16CF$ flange. A Lewvac $FLV-16CFR$ fine control leak valve (flow adjustable from 10^{-3} to $10^{-11}\,mbar\,ls^{-1}$) is attached at the end of the outside part of the tube to regulate the calibration gas flow. The inner part has a titanium tube

(6 *mm* inner diameter) attached at the end to minimise possible magnetisation close to the electron beam. The titanium tube is bent in the way to direct the calibration gas towards the centre of the interaction region of the TOF mass spectrometer as shown in Fig. 7.5 a) and b).

7.4.2.2 Testing and optimisation of the electron gun performance at 70 *eV* for electron impact ionisation experiments

As mentioned in Section 7.2, MPI and EII experiments represent a natural starting point for the optimisation of the *New DEA/EII/MPI experimental set-up*. Therefore, the performance of the EG was first optimised for EII experiments without pulsing of the electron beam. Pulsing of the electron beam is not essential for EII because the electrons are not attracted into the MS in cation detection mode. However, it will degrade the effective electron energy resolution in the measurement. An electron beam energy of 70 *eV* was chosen for this optimisation work because this is a standard energy in EII experiments as it is close to energy of maximum EII cross section for most molecules in spectral libraries. It generally causes significant fragmentation of molecules and at this energy small changes in the electron energy do not significantly affect the fragmentation pattern. Furthermore, high energy electrons are deviated less by stray fields and collimated more effectively by the magnetic field from the Helmholtz coils so optimising at 70 *eV* is more readily-achievable as a first step than optimising at DEA energies.

Prior to this optimisation work, stray magnetic fields had to be minimised as effectively as possible. As already mentioned in Section 7.2.1 replacing the bolts, nuts and washers significantly improved the collimation of the electron beam. The electron current was measured on the Fc systematically after adding new components in the chamber one by one. The pumps as well as pressure gauges were kept as far as possible from the electron beam. The *"weak points"* of the *main vacuum chamber* with respect to the use of materials that can be magnetised (mainly stainless steel 304, although we do not have a full breakdown of the materials in some of these components) are the stainless steel foil mounted on the sample holder, stainless steel grids, X and Y deflectors, fibre optics components, viewports for the UV laser beam and a *DN*100*CF* viewport (at the end of the molecular beam path) which enables to visually check the alignment of the EG and Fc as well as the state of the sample. The Helmholtz coil positions were adjusted to correct for the potential effect of the above-mentioned components on the trajectory of the electron beam. The Helmholtz coils positions were adjusted by moving the coils closer/further to the chamber and by changing the angle between the coil plane and the axis of the chamber parallel to the propagation of the magnetic field. The coil placed closer to the EG had a

bigger effect on the resultant Fc current than the one closer to the Fc. Fine-adjustment was achieved by tightening and/or releasing the screws which allow tilting of the coils after adding any new component in the chamber. The position of the coils was normally not significantly affected by adding new parts in the vacuum chamber. It should be noted though that the position of the coils had to be adjusted also after opening the chamber to adjust the position of EG or the Fc, replace the EG filament, or make any changes to the ILTD source including replenishing the sample on the foil. This is because the ILTD flange can only be removed by first removing a Helmholtz coil and the fine adjustment systems of the Helmholtz coils, the EG and the Fc do not have a scale to enable a return to exactly the same position. Therefore each intervention of this kind requires a new optimisation of the Helmholtz coil positions.

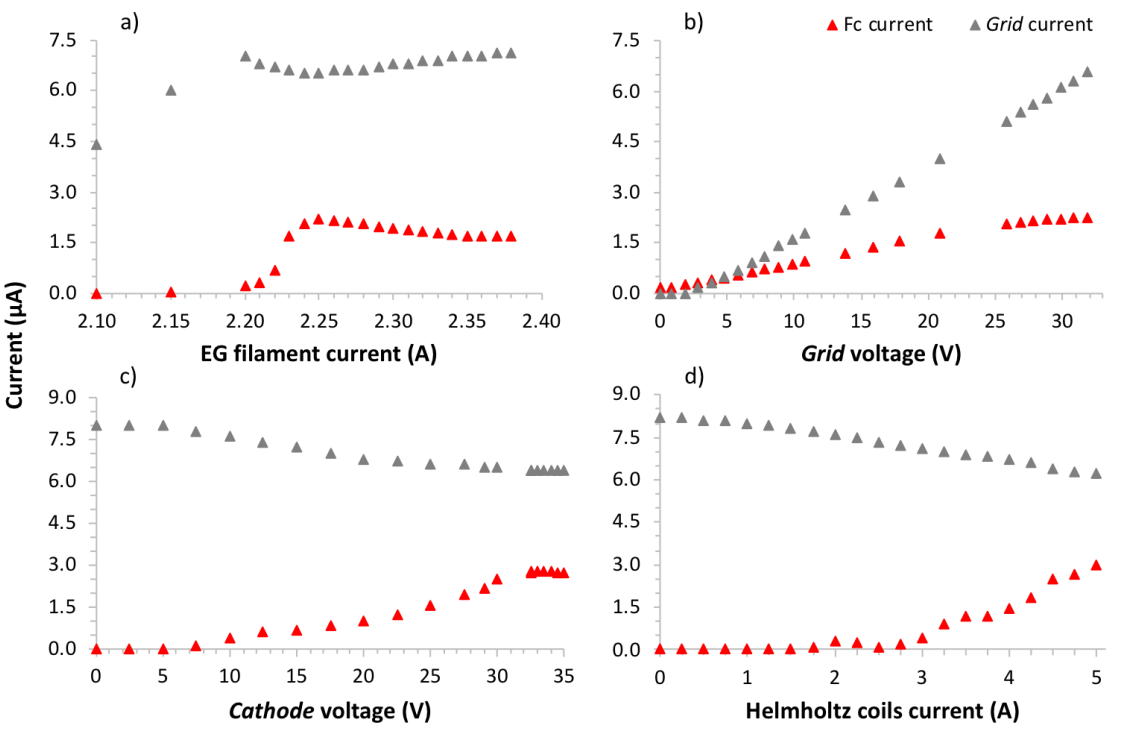

Fig. 7.9: Optimisation of the electron gun (EG) performance at $70\,eV$. The electron beam current measured on the Fc and the *grid* current (red and grey data points, respectively) as a function of a) current supplied to the EG filament (*cathode* voltage $29\,V$ and *grid* voltage $31.8\,V$ with respect to $-70\,V$, Helmholtz coils current $4.5\,A$); b) voltage supplied to the *grid* with respect to $-70\,V$ (EG filament current $2.25\,A$, *cathode* voltage $29\,V$ with respect to $-70\,V$, Helmholtz coils current $4.5\,A$); c) voltage supplied to the *cathode* with respect to $-70\,V$ (EG filament current $2.25\,A$, *grid* voltage $31.8\,V$ with respect to $-70\,V$, Helmholtz coils current $4.5\,A$) and d) current supplied to the Helmholtz coils (EG filament current $2.25\,A$, *cathode* voltage $29\,V$ and *grid* voltage $31.8\,V$ with respect to $-70\,V$).

The optimisation of the EG performance was carried out as follows (see Fig. 7.9)

1. The current on the Fc was optimised as a function of the current supplied to the EG

filament (see red data points in Fig. 7.9 a)).

The voltages on the *cathode* and *grid* were set to $29V$ and $31.8V$ (based on preliminary search of the parameter space) with respect to $-70V$ (electron energy power supply). The position of the Helmholtz coils was adjusted prior to this optimisation process and the current was set to $4.5A$. The maximum Fc current was achieved for the EG filament current of $2.25A$. It should be noted that all of the plots in Fig. 7.9 show also how the current on the *grid* evolves with the EG settings (see grey data points). We can see in Fig. 7.9 a) that the electron current measured on the *grid* is higher compared to the one on the Fc in the whole range of the EG filament currents, i.e. the majority of electrons does not leave the EG. The maximum current on the *grid* does not follow the maximum current on the Fc. The difference between the *grid* and the Fc currents is smallest at $2.25A$, where the latter one reaches maximum. We assume that increasing the emission of electrons from the filament by increasing EG filament current above $2.25A$ results in space charge starting to have a negative effect on the number of electrons leaving the gun and then reaching the Fc. The filament current was not increased above $2.38A$ to avoid damaging the filament.

2. The current on the Fc was optimised as a function of the *grid* voltage with respect to $-70V$ (see red data points in Fig. 7.9 b)).

   The EG filament current was set to $2.25A$ (maximum current on the Fc in Fig. 7.9 a)), the voltage on the *cathode* was set to $29V$ with respect to $-70V$ and the current on the Helmholtz coils was set to $4.5A$. It should be noted that both Fc and *grid* current were increasing with increasing voltage on the *grid* in the measured data range (0 to $31.8V$ with respect to $-70V$). The maximum current on the Fc and on the *grid* was limited by the maximum output voltage of the power supply. The Fc current is beginning to flatten out at the end of our range, so we do not expect to gain much more Fc current by continuing to increase the *grid* voltage beyond the range of our power supply.

3. The current on the Fc was optimised as a function of the *cathode* voltage with respect to $-70V$ (see red data points in Fig. 7.9 c)).

   The EG filament current was set to $2.25A$ (maximum current on the Fc in Fig. 7.9 a)), the voltage on the *grid* was set to $31.8V$ with respect to $-70V$ (maximum current on the Fc in Fig. 7.9 b)) and the current on the Helmholtz coils was set to $4.5A$. The current on the Fc increased with increasing voltage on the *cathode* from 0 to $33.5-34V$ where it reached the maximum and then started decreasing again (although only subtly). The current on the *grid* evolved in the opposite way, slowly decreasing until the voltage on the *cathode* reached $30V$ and then showed

constant behaviour. Increasing the *cathode* voltage to more positive values helps to pull electrons away from the filament. When the voltage on the *cathode* gets more positive than $2.2V$ with respect to the *grid*, electrons are *attracted back* to the *cathode* and the current on the Fc begins to drop.

4. The current on the Fc was optimised as a function of the current passing through the Helmholtz coils (see red data points in Fig. 7.9 d)).

   The EG filament current was set to $2.25A$ (maximum current on the Fc in Fig. 7.9 a)), the voltage on the *grid* was set to $31.8V$ with respect to $-70V$ (maximum current on the Fc in Fig. 7.9 b)) and the voltage on the *cathode* was set to $33.5V$ with respect to $-70V$ (maximum current on the Fc in Fig. 7.9 c)). Increasing the current which passes through the Helmholtz coils resulted in stronger magnetic field, which helped to collimate the electron beam, hence increasing current on the Fc and decreasing current on the *grid*. Comparing the evolution of the current on the *grid* and the Fc suggests that the magnetic field is not essential for the electrons to pass through the *cathode*, but it is essential for directing the electrons to leave the EG. It should be noted that further increasing the current in the Helmholtz coils and hence the magnetic field would be risky as it could result in damaging the coils and/or permanently magnetising some parts in the chamber. Therefore, to avoid the above mentioned complications the coils were normally operated at $4.5A$.

   The optimisation of the EG performance at $70eV$ resulted in the Fc currents of around $3\mu A$. This is comparable with the currents obtained by other groups using a similar design of the EG (private communication with I. Jana, [314]). The EG was successfully used in $70eV$ electron impact ionisation experiments on methanol seeded in He which are presented in Section 7.4.4.

7.4.2.3 Testing and optimisation of the electron gun performance for DEA experiments

Two key steps were taken to prepare the experimental system for DEA experiments: pulsing of the EG and installing the calibration gas inlet system. These are discussed in more detail below.

7.4.2.3.1 Pulsing of the electron gun

In DEA experiments, the TOF mass spectrometer will be operated with positive voltages on the mass spectrometer electrodes and the MCP). In order to avoid extracting electrons onto the MCP (which would have the effect of significantly shortening its lifetime), the

extraction electrode (see Fig. 3.3) and the EG will be pulsed in such a way that the beam will be turned off during the ion extraction pulses. Pulsing of the EG is achieved by pulsing its *grid* component (see Fig. 7.8). The pulsing scheme of the EG *grid* and the ion extraction electrode is illustrated in Fig. 7.10 a).

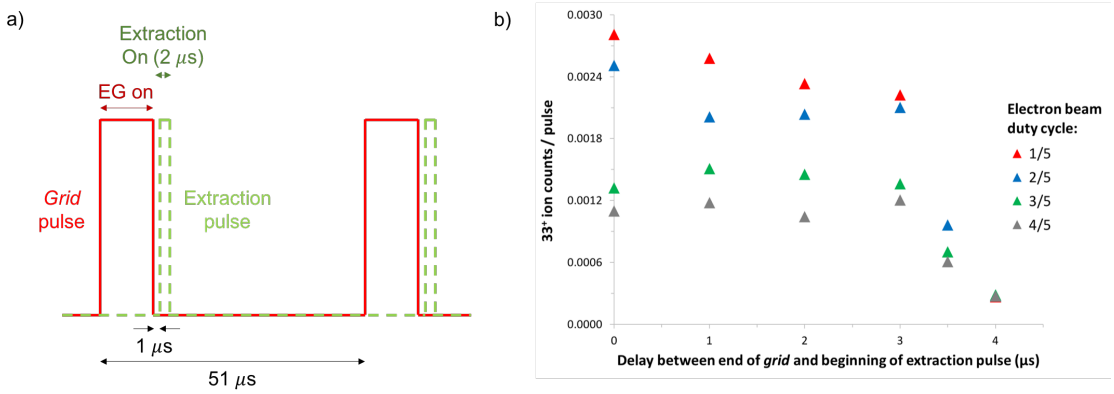

Fig. 7.10: a) Pulsing scheme for the *grid* of the EG. b) $m/z\,33$ ion signal in EII experiments on methanol (molecular beam, average sample temperature $23\,^{\circ}C$, electron energy $70\,eV$, pressure of He $1.1\,bar$) as a function of the *grid* pulse – extraction pulse delay and of the duty cycle of the *grid* pulse (i.e. EG *grid* pulse time/pulsing period). The pulsing period and the extraction pulse width were fixed at $51\,\mu s$ and $2\,\mu s$, respectively.

When the EG pulse is off, the voltage on the EG *grid* is kept at a value that ensures that electrons do not leave the EG. This can be confirmed by measuring the current on the EG *grid*. For example, Fig. 7.9 b) shows that EG *grid* current is $\sim 0\,\mu A$ (to within the sensitivity of the multimeter) when the EG *grid* voltage is equal to the electron beam voltage. A positive pulse then needs to be applied to the EG *grid* to allow electrons to leave the gun (as evidenced by the non-zero *grid* current) and reach the interaction region (as evidenced by the Fc current). For this purpose, an $Aim-TTi\,TGP110$ pulse generator is used to generate $+10\,V$ (maximum amplitude) pulses, which are then amplified to the desired value by a home-built amplifier (R. Seaton and his colleagues from Intra-Faculty Electronics and Computing Facility at the OU). During the EG *grid* pulse (see Fig. 7.10 a)) electrons leave the EG and interact with molecules, and this coincides with the extraction electrode of the mass spectrometer being grounded so neither electrons nor ions are extracted onto the MCP detector. After the end of the EG *grid* pulse, a delay is applied to allow the voltage on the *grid* to return to the *"electron beam off"* value and to allow all the emitted electrons to leave the interaction region. After this delay, the extraction pulse is applied to extract ions from the interaction region. The pulsing frequency is normally set to $19,607\,Hz$. This is currently limited by the maximum frequency of the *BEHLKE GHTS* 30 pulser, which supplies pulses to the power supply for the extraction electrode ($+380\,V$ in DEA experiments and $-380\,V$ in EII/MPI experiments).

The electron beam duty cycle (EG grid pulse time/pulsing period) and the delay between the EG *grid* pulse and the extraction pulse were tested in EII experiments on methanol in a molecular beam (MB) produced in the *Stark deflection set-up*. As the main goal of the electron gun testing was to enable EII experiments with the best possible S/N, the signal intensity in EII experiments is a more relevant parameter to use in such tests than, for example, the current on the Fc. Methanol was evaporated at room temperature and seeded in $1.1\,bar$ of He. The supersonic molecular beam from the *Stark deflection set-up* then interacted with $70\,eV$ electrons. The duty cycle of the EG and the delay between the *grid* pulse and the extraction pulse were tested based on the signal of $m/z\,33$ ion (the fragment ion from the MB with the best S/N), which is a fragmentation product of methanol clusters (protonated methanol). A fragment ion was chosen for this testing instead of the He^+ signal because fragment ions will leave the interaction region quicker due to kinetic energy release and hence will be more sensitive to the delay. As shown in Fig. 7.10 b) the $m/z\,33$ signal intensity was measured as a function of the delay between the *grid* pulse and the extraction pulse in steps of $1\,\mu s$ for four different duty cycles ($1/5$ to $4/5$). The strongest signals were obtained for the duty cycle $1/5$. Normally, we would expect the signal to be flat or increase with increasing duty cycle. The observed behaviour might be caused by instabilities in the electron beam related to a dissipation/accumulation of space charge or possibly charging on the insulator elements or even residual condensed molecules (or *dirt*) within the gun. Alternatively, charging of insulators or thin layers of condensed molecules outside the gun could play a role. As expected, the shorter the delay, the stronger the signal. However, in order to eliminate the presence of electrons in the interaction region during the ion extraction, we keep the delay set to $1\,\mu s$ as indicated in Fig. 7.10 a).

7.4.3 The UV laser beam

Designing and building the optical system to deliver the UV pulses into the experiment was complicated by:

1. limited space and no optical bench in between the *Compact MPI/EII experimental set-up* and the *main vacuum chamber* of the *New DEA/EII/MPI experimental set-up*,

2. close proximity of the Helmholtz coils and their support/adjustment structures to the windows of the chamber,

3. angular and positional offset of the laser beam path through the two chambers (see Fig. 7.11).

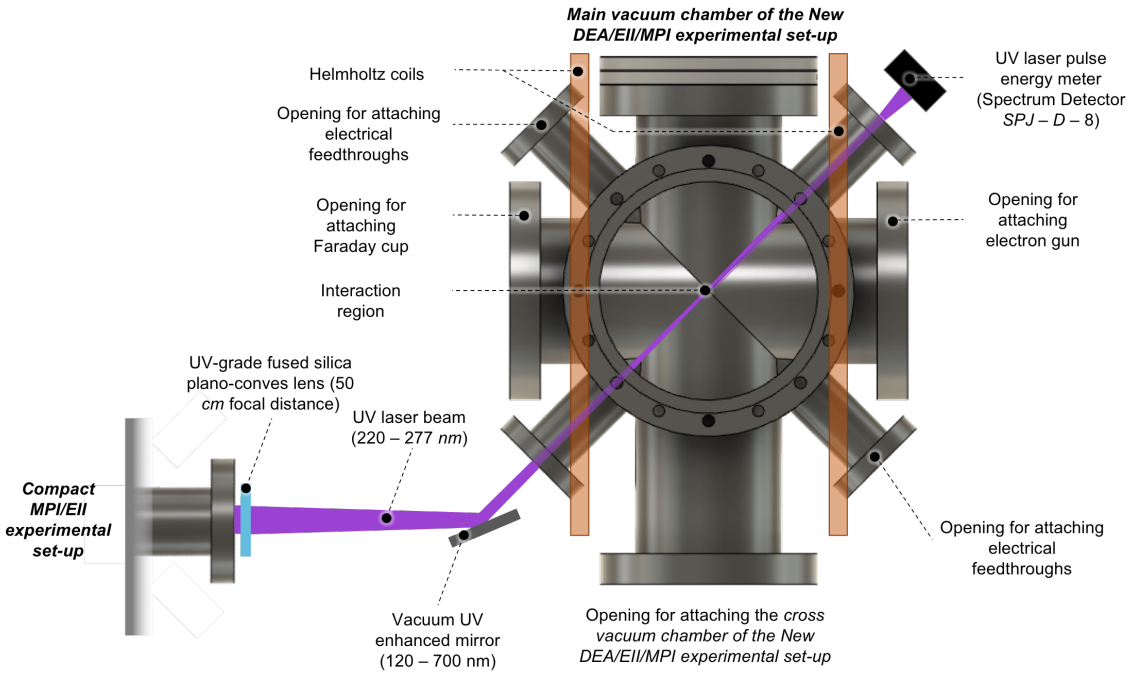

Fig. 7.11: The schematic diagram (above view) of the angular and positional offset of the UV laser beam path through the *Compact MPI/EII experimental set-up* and *New DEA/EII/MPI experimental set-up*.

The same UV laser beam that is used for the experiments in the *Compact MPI/EII experimental set-up* (for more details see Section 3.2.4) is also used in the *New DEA/EII/MPI experimental set-up*. After the UV laser beam passes through the *interaction chamber* of the *Compact* apparatus, a UV-grade fused silica plano-convex lens (50 cm focal distance) and a vacuum UV enhanced mirror ($120 - 700\,nm$, average reflectance $\geq 88\,\%$) are placed in the path of the UV laser beam to focus and direct the beam into the interaction region of the TOF mass spectrometer of the *New DEA/EII/MPI experimental set-up*. The angle between the UV laser beam propagation direction and the axis of the imaginary line connecting the centre of the viewport with the centre of the interaction region of the *main vacuum chamber* is 135°.

7.4.3.1 Testing and optimisation of the experimental set-up for multi-photon ionisation experiments

The UV-grade fused silica plano-convex lens on a slider and the vacuum UV enhanced mirror were aligned for MPI experiments in the *New DEA/EII/MPI experimental set-up*. Custom mounting parts were commissioned for the optics from the Research Design and Engineering Facility at the OU. The alignment was made by adjusting the position (vertical translation stage with micrometer adjustment) and angle (kinematic mount) of the mirror so that it enters the *main vacuum chamber* through the centre of a *DN*40*CF* viewport and leaves the chamber through the centre of a viewport on the opposite side of the chamber.

A laser pulse energy meter (Spectrum Detector $SPJ-D-8$) was installed to measure the energy of the UV laser pulses after passing through the *main vacuum chamber*. Fine optimisation of the lens and mirror positions will be done in the future based on observing the response of the signal intensities in the MPI experiments.

7.4.4 Optimisation of the time-of-flight mass spectrometer

The *ion source* of the mass spectrometer designed by A. Rebelo (a PhD student in the Molecular Clusters Laboratory at the OU) based on the one obtained from KORE Technology is shown in Fig. 7.12. The flight tube and the reflectron part of the mass spectrometer were obtained from KORE Technology.

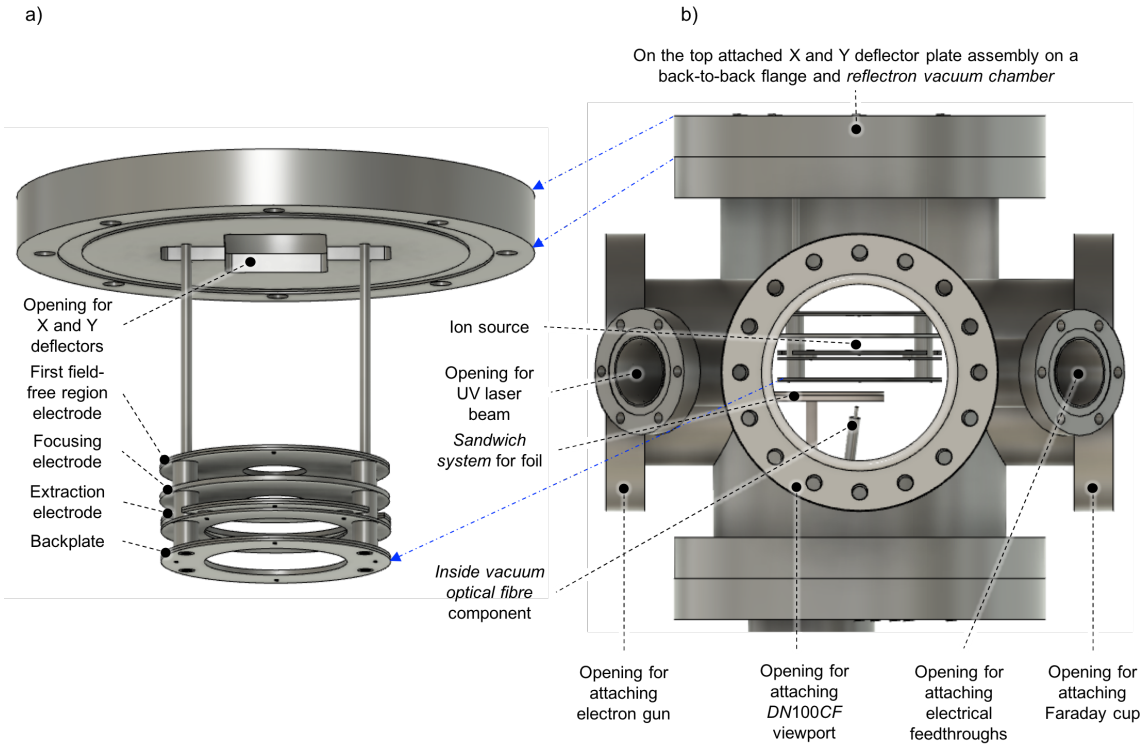

Fig. 7.12: a) The *ion source* of the mass spectrometer designed by A. Rebelo and b) the *ion source* mounted on the *main vacuum chamber* (the molecular beam would come out of the page towards the reader in this diagram).

The functioning of the re-designed mass spectrometer was tested in EII ($70\,eV$) experiments on methanol seeded in a supersonic expansion of He. The mass spectrometer voltages were optimised to enhance the relative contribution of the methanol parent/fragment ions and methanol clusters fragment ions signal compared to the background ion signal (primarily water and hydrocarbon molecules that diffused in the *main vacuum chamber* before and during the pumping down stage) and signals coming from molecules scattered in the *main vacuum chamber*. The EII mass spectrum obtained with optimised mass spectrometer

voltages is shown in Fig. 7.13. The peaks with $1\,m/z$ difference can be clearly separated in the mass spectrum in Fig. 7.13 and those above the background level have been previously reported in the literature on methanol/methanol clusters [316, 317]. The strongest peak in the mass spectrum $m/z\,33$ reached a count rate of $0.003\,counts/pulse$, which corresponds to $52.17\,counts/s$ in the present experimental conditions. It should be noted that signal rates can be increased at the expense of mass resolution by adjusting the mass spectrometer voltages, notably the reflection voltage, which was set to $-350\,V$ in the present experiment. Additional compensation for lower count rates in DEA experiments can be achieved by longer acquisition times. The first tests of the experiment for MPI-TOF will be carried out by my colleagues in the Molecular Clusters Group imminently.

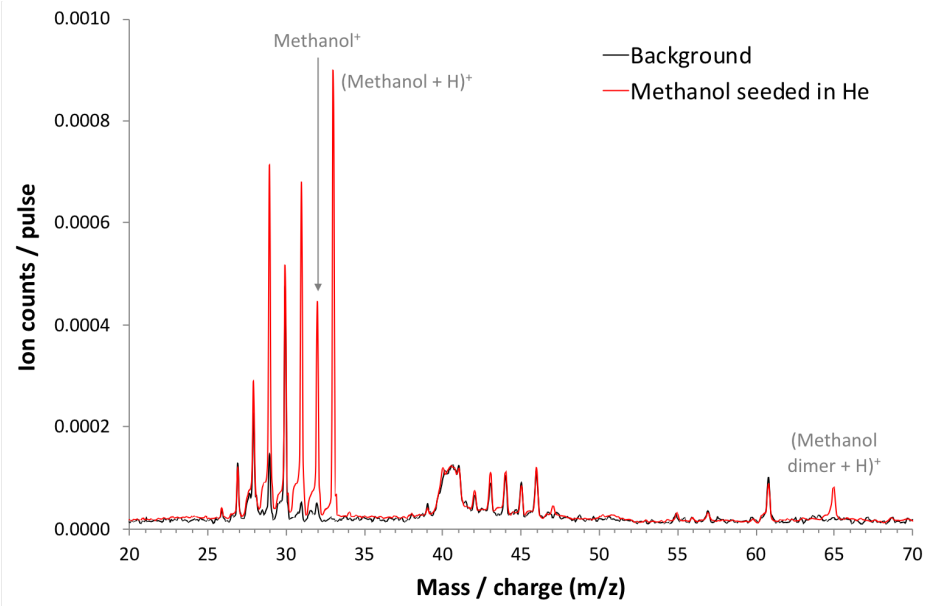

Fig. 7.13: EII mass spectrum of methanol (molecular beam, average sample temperature $23\,^{\circ}C$, electron energy $70\,eV$, pulsed electron beam - $1/5$ duty cycle, $1\,\mu s$ delay between the *grid* pulse of the EG and the extraction pulse, pulsing frequency $19,607\,Hz$, average Fc current $0.84\,\mu A$, pressure of He $1.1\,bar$).

7.5 Summary and outlook

This chapter explains the motivation behind building the *New DEA/EII/MPI experimental set-up* in the Molecular Clusters Laboratory at the OU. In addition to a general description of the experiment, detailed information is provided on the design and principles of operation of the indirect laser-induced thermal desorption system, the home-built thermionic emission EG and the Fc. It should be noted that the literature for DEA on laser-desorbed targets is extremely sparse and nobody has ever done an electron collision experiment on an ILTD target. In addition, nobody has ever combined DEA with *Stark deflection*.

Optimisation of the experimental set-up is on-going. Up to now, the following challenges have been addressed and the following progress has been achieved:

1. Challenge: Producing ILTD targets without any electron interactions with condensed molecules.

    - An original design solution has been devised based on hiding biased foil behind a grid and combining conventional heating with ILTD.
    - The ILTD source (the rotatable foil holding system, the vacuum fibre feed-through and the *inside vacuum optical fibre* component) has been built and installed in the *main vacuum chamber* and no leaking/degassing was observed.
    - The desorption laser and fibre optics was aligned. The arrangement was successfully used for desorbing uridine under vacuum at ambient temperature $23\,^{\circ}C$.

2. Challenge: Producing pulsed electron beams with high currents.

    - The EG and the Fc were installed, Helmholtz coils position was optimised and stray electric and magnetic fields were successfully reduced.
    - The current (continuous mode) measured on the Fc at beam energy $70\,eV$ up to $\sim 4\,\mu A$, in line with the optimised performance of electron guns with the same design in experiments by Krishnakumar and co-workers.
    - Pulsing of the EG was set up as well as tested and optimised based on signal intensities in electron impact ionisation experiments ($70\,eV$) on methanol seeded in He.

3. Challenge: Optimising the mass spectrometer for *Stark deflection* experiments.

    - The *cross vacuum chamber* and the *main vacuum chamber* were aligned with the *Stark deflection experimental set-up*.
    - The mass spectrometer was tested and optimised for electron impact ionisation experiments ($70\,eV$) on targets produced in molecular beam.

4. Challenge: Optimising the experimental set-up for MPI experiments.

    - The vacuum UV enhanced mirror and the UV-grade fused silica plano-convex lens were positioned and aligned for the UV laser beam to pass through the centre of the interaction region of the *ion source*.

The further work on the *New MPI/EII/EA experimental set-up* in *indirect laser-induced thermal desorption mode* will continue as follows:

1. Multi-photon ionisation experiments on uridine produced by indirect laser-induced thermal desorption. This will involve the following optimisations:

    - Fine tuning of the mirror and lens positions based on the signal intensities in MPI mass spectra.
    - Optimisation of the mass spectrometer for targets produced by ILTD.

2. Electron impact ionisation experiments on uridine produced by indirect laser-induced thermal desorption. This will involve the following:

    - Testing the electron beam performance and the EII background levels in a heated chamber and possibly adopting a more localised heating system (e.g. a halogen lamp) and/or testing how low the chamber could be heated to prevent condensation of key ILTD molecules on the grid.

3. Dissociative electron attachment experiments:

    - Characterisation and optimisation of the EG performance at low energies ($< 20\,eV$).
    - Optimisation of the mass spectrometer when operating in negative mode.
    - Calibration of the electron beam energy using O_2 targets.
    - DEA experiments on *ILT*-desorbed nucleosides.

7.6 Contributions by co-workers

Dr. S. Eden proposed the idea of building a new experimental system combining the EG, Fc, and Helmholtz coil hardware belonging to Prof. E. Krishnakumar and Prof. N. J. Mason with the Molecular Clusters Group's reflectron MS, UV laser for MPI, Stark deflection/MB system, and a new ILTD source. I then worked closely with Dr. S. Eden and A. Rebelo on devising the overall design for the experiment before we divided responsibility for detailed design and construction work between us. I designed and built the support frame for the new experimental system and installed the *main vacuum chamber* and Helmholtz coils working with D. Mészáros (an internship student in the Molecular Clusters Laboratory at the OU). I installed the *reflectron vacuum chamber* and aligned the new system with the *Stark deflection set-up* working with A. Rebelo (a PhD student in the Molecular Clusters Laboratory). I designed the support system for the turbomolecular pump attached to the *cross vacuum chamber* and built and installed it with the help from T. Hajj (an internship student in the Molecular Clusters Laboratory at the OU). I also designed the bottom flange arrangement of the *main vacuum chamber* as well as the new

indirect laser-induced thermal desorption system. I devised, aligned and optimised the fibre optics arrangement for the ILTD system. Both the EG and the Fc were designed by Prof. E. Krishnakumar and built by C. Hall and his colleagues from the Research Design and Engineering Facility at the OU. Prof. E. Krishnakumar also provided valuable advice, notably with respect to shielding the electron beam from electric fields within the mass spectrometer. The electronics for the EG was built by ourselves (based on the diagrams provided by Prof. E. Khrishnakumar) with the support from D. Pound from Intra-Faculty Electronics and Computing Facility at the OU. I designed the holding system for the EG and the Fc. I worked on installing and optimising of the EG and the Fc mainly with A. Rebelo, D. Mészáros, Dr. K. Nixon (a visiting researcher in the Molecular Clusters Laboratory at the OU), I. Jana (an internship student in the Velocity Map Imaging Laboratory at the OU) and T. Hajj. A. Rebelo designed and built the new *ion source* and provided drawings shown in Fig. 7.12. I worked on the optimisation of the new *ion source* mainly with A. Rebelo. Building of the *New DEA/EII/MPI experimental set-up* was supported substantially by the Research Design and Engineering Facility at the OU. In particular, C. Hall and K. Dewar provided advice on materials and design of individual components, T. Jones built the ILTD source, the EG and Fc holding systems and the extension for the EG and M. Abbott built the *ion source* and the plate which is part of the support system for the turbomolecular pump attached to the *cross vacuum chamber*. All of the design work was supported by Dr. S. Eden.

Chapter 8

Conclusions and outlook

This PhD thesis is centred on applying the *bottom-up* approach in the study of radiation-induced processes in nucleic acids. In this context it reports on multi-photon ionisation experiments on nucleosides as well as on the development of a new experimental set-up for dissociative electron attachment experiments on *indirect laser-induced thermally* desorbed nucleoside targets. The thesis also showcases the recent advances of the OU Molecular Clusters Group's experiment to probe complex metastable fragmentation pathways of excited molecular ions. This chapter first highlights the most important contributions of the thesis (see Section 8.1) and then provides a more thorough summary of the outcomes of Chapters 3 to 7 (see Section 8.2). It finishes with a short overall summary and some proposals for future experiments and development work (see Section 8.3).

8.1 Highlights

Here we present four major outcomes of this PhD thesis:

1. This work provides the first full experimental evidence showing that indirect laser-induced thermal desorption (ILTD) can be used to produce intense neutral gas-phase targets of nucleosides (in this case uridine, 2′-deoxyuridine and 5-methyluridine) without thermal degradation. This clarifies the value of ILTD as a tool in the *bottom-up* approach in the study of radiation-induced processes to nucleic acids. In our MPI-TOF experiments, it enabled to progress one step further in complexity from nucleobases to nucleosides. However, our observations of some thermal decomposition of thymidine indicate that nucleosides are already at the threshold of thermal lability that we can study effectively using this technique. This highlights the importance of *target decomposition/reactivity* tests for nucleosides and larger species as well as the need to continue developing and testing methods for the production of intact neutral gas-phase targets of thermally labile biomolecules.

2. The contribution above laid foundations for developing a unique experimental system for probing dissociative electron attachment processes to nucleoside targets produced by ILTD. DEA has been up till now limited mainly to smaller biomolecules such as nucleobases and sugars. A further strength of the apparatus is its versatility as it enables also multi-photon ionisation and electron impact ionisation experiments in the same conditions. In addition to probing molecular targets produced by ILTD, the experiment was built to probe targets produced in a molecular beam which can be structurally purified by Stark selection prior the interaction with electrons/photons.

3. The multi-photon ionisation experiments on uridine produced in the gas-phase by ILTD provide evidence supporting changes in the population of uridine isomers as a function of ILTD conditions. In addition, these experiments are, to the best of our knowledge, the first ones showing that the excited state dynamics and photostability of uridine are sensitive to the isomeric form of the molecule immediately prior to photo-excitation. Indeed, we are not aware of any previous experimental evidence for isomer-dependent radiosensitivity of any nucleoside. This result highlights the importance of experiments with greater control over the neutral target structures.

4. The Matlab simulation developed for the analysis of metastable dissociation results from reflectron time-of-flight mass spectrometer has significantly enhanced the capability of the Molecular Clusters Group to analyse complex metastable fragmentation pathways.

8.2 Summary of conclusions from Chapters 3 to 7

8.2.1 Chapter 3: Experimental

Chapter 3 presented the previously built *Compact MPI/EII experimental set-up* in the Molecular Clusters Laboratory at the OU and my contributions towards the enhancement of the system, which we can summarise as follows:

- A new *ion source* was built and tested.

- A new indirect laser-induced thermal desorption system was set-up, which involved installing a more powerful desorption laser and optimising the alignment with the aim of improving the signal-to-noise ratio in multi-photon ionisation experiments.

- The performance of the Nd:YAG/dye laser system was characterised and optimised. Most importantly, this gave us a new level of control over laser pulse energy fluctuations as a function of energy and wavelength.

- A Matlab simulation was developed for analysing metastable dissociation results measured using reflectron time-of-flight mass spectrometer (TOF-MS). Compared to the previous approach of the Molecular Clusters Group, the simulation enabled analysis of much more complex metastable fragmentation patterns.

8.2.2 Chapter 4: Fragmentation pathways of excited 3-aminophenol ions

Chapter 4 presented the results of multi-photon ionisation experiments (225 and 270 nm) on 3-aminophenol (3-AP) seeded in a supersonic helium beam. The technique of mapping ion detection using reflectron TOF-MS against flight-time and reflection voltage in combination with the Matlab simulation was used to elucidate complex metastable fragmentation pathways of excited 3-aminophenol$^+$. The key findings can be summarised as follows:

- A rich array of metastable dissociation channels of multi-photon ionised 3-AP was detected. 18 channels were identified in the MPI experiments at 225 nm with the help of the Matlab simulation, which showcases the capability of this approach for the elucidation of complex metastable fragmentation patterns.

- A sequential fragmentation route: 3-AP$^+$ $(m/z\,109) \rightarrow HCO + C_5H_6N^+$ $(m/z\,80) \rightarrow$ $\rightarrow CNH + C_4H_5{}^+$ $(m/z\,53) \rightarrow C_2H_2 + C_2H_3{}^+$ $(m/z\,27)$ was detected and assigned with the help of Density Functional Theory (DFT) calculations performed by my collaborator Dr. J.-C. Poully.

- Extensive hydrogen scrambling accompanying metastable dissociation of 3-AP was revealed both theoretically as well as experimentally. DFT calculations showed that numerous atomic rearrangements preceded each of the fragmentation steps in the above-mentioned sequential fragmentation pathway. The experimental evidence was based on detecting a double hydrogen loss channel (H_2 or two separate atoms) from an excited fragment ion of 3-AP. Previous experimental observations of double hydrogen loss from excited fragment ions are very rare in the literature.

- Comparison of our MPI experiments at 225 and 270 nm revealed strong wavelength effects on the metastable dissociation pattern. In particular, the first metastable dissociation step of the excited parent ion ($m/z\,109 \rightarrow 80$) was much stronger at 270 nm than at 225 nm. We argue that this strong wavelength dependence is most likely linked to the level of vibrational excitation of the electronically excited neutral prior its ionisation.

- Comparison of our complementary experiments for the estimation of vapour pressure of 3-aminophenol and thymine suggests the unusually strong signals of multi-photon ionised 3-AP and hence the rich metastable fragmentation pattern are unlikely to be explained only by high target densities. We expect electronic excited state absorption cross sections and/or dynamics to be at least partially responsible for very efficient multi-photon ionisation of 3-aminophenol in the present conditions.

8.2.3 Chapter 5: Indirect laser-induced thermal desorption for the production of intact gas-phase nucleobase, nucleoside and nucleotide targets

Chapter 5 addressed one of the major experimental challenges of the *bottom-up* approach to study the radiation response of nucleic acids, which is producing neutral gas-phase targets with adequate number densities of thermally labile molecules without *target degradation*. The suitability of ILTD for the production of intact gas-phase targets of the most thermally labile nucleobase guanine, nucleosides uridine, thymidine, 2′-deoxyuridine and 5-methyluridine, as well as nucleotide uridine 5′-monophosphate was investigated. The outcomes of this chapter are summarised below:

- The multi-photon ionisation experiments on guanine and uridine produced in the gas-phase by *conventional* heating in a carrier gas showed that nucleobases are at the limit of thermal lability that can be studied using the OU molecular beam system.

- The chapter provided evidence that the ILTD can be successfully used for producing an intact gas-phase guanine with sufficient density to study very weak MPI channels, including metastable fragmentation.

- Potential thermal decomposition of nucleosides uridine, thymidine, 2′-deoxyuridine and 5-methyluridine produced in the gas-phase was investigated by studying the ratio of base/hydrogenated base ions signal with increasing desorption laser power. This study showed that the above-mentioned nucleosides can be produced in the gas-phase by ILTD without *target decomposition/reactivity* with the exception of thymidine. The experiments on thymidine suggested that some thermal decomposition occurs even at relatively low desorption laser powers. This result suggests that nucleosides are already at the threshold for how far we can go in the production of intact progressively more thermally labile nucleic acid constituents using ILTD and highlights the need for thorough tests of *target degradation* to accompany experimental studies of radiation-induced fragmentation processes.

- The experiments on uridine 5′-monophosphate suggest that the same sample preparation procedure which was applied for the ILTD experiments on nucleobases and nucleosides is not suitable for nucleotides. Therefore, the sample preparation procedure might need to be optimised for different species in order to avoid changing their chemical/physical properties prior sublimation.

8.2.4 Chapter 6: Multi-photon ionisation experiments on *indirect laser-induced thermally* desorbed uridine

Chapter 6 presented the results of multi-photon ionisation ($222 - 265\,nm$) experiments on uridine produced by ILTD. The key result obtained is the first experimental evidence supporting changes in the population of different isomers of uridine as a function desorption conditions. The main outcomes of the chapter can be summarised as follows:

- The multi-photon ionisation experiments on uridine at $225\,nm$ indicate that the ribose moiety has a stabilising effect with respect to the CO loss channel that had been observed in previous MPI experiments on isolated uracil.

- The $222 - 265\,nm$ MPI experiments on uridine show that ILTD conditions dramatically affect the production of sugar-unit ions ($m/z\,133$) via a critical process in an electronically excited state of neutral uridine with a wavelength threshold at $250\,nm$.

- The experimental observation above was rationalised in terms of changes in the population of uridine isomers in *ILT*-desorbed targets. This was supported by DFT calculations which indicated that isomeric transitions of uridine can happen at noticeably lower temperatures than decomposition. This result supports the importance of developing methodologies for the production of intact and structurally pure gas-phase targets.

8.2.5 Chapter 7: *New DEA/EII/MPI experimental set-up* for probing *indirect laser-induced thermally* desorbed or *Stark deflected* molecules

Chapter 7 presented the new experimental set-up which was developed to study dissociative electron attachment (DEA), electron impact ionisation (EII) and multi-photon ionisation (MPI) processes using reflectron time-of-flight mass spectrometry under the same experimental conditions. The system was built with the main motivation to carry out DEA experiments on nucleoside targets produced in the gas-phase by ILTD in order to extend the knowledge on low-energy electron interaction processes from nucleobases to

nucleosides. An additional motivation is to perform EII and MPI experiments on uridine with the same target conditions and thus strengthen the interpretations presented in Chapter 6. The new apparatus was connected to the previously built *Stark deflection set-up* which extends the capability of the new system to carry out experiments also on targets seeded in molecular beams. Moreover, this opens the possibility of *Stark selection* prior the interaction with electrons or photons. The key achievements in developing and testing the new apparatus are listed below:

- The new experimental system was designed and completely built. The key work involved setting-up and installing a new ILTD system, installing a home-built electron gun and Faraday cup, building and installing a new *ion source*, installing Helmholtz coils and aligning the new apparatus with the previously built *Stark deflection set-up*.
- A new version of the ILTD system was built which has improved design compared to the one in the *Compact MPI/EII experimental set-up*. Notably, a rotatable foil holding system is used which enables longer measurement times. In addition, a fibre optics arrangement was designed and built for directing of the desorption laser beam onto the foil inside of a vacuum chamber. The system was successfully tested for desorbing uridine under vacuum.
- Electron gun performance was optimised for electron impact ionisation experiments at $70\,eV$. The pulsing of the EG was tested and optimised in EII experiments on methanol seeded in He.
- A new system of optics was installed to align the UV laser beam for MPI experiments in the new set-up.
- The TOF-MS was optimised for EII ($70\,eV$) experiments on targets in molecular beams.

8.3 Overall summary and outlook

The current work has addressed the issue of thermal lability of nucleosides which has not been fully explored in the literature of gas-phase experiments on progressively more complex neutral nucleic acid constituents. The thesis brought detailed insights into the applicability of ILTD for the production of intact neutral gas-phase nucleoside targets of uridine, thymidine, $2'$-deoxyurdine and 5-methyluridine. This has opened up plenty of opportunities for future experiments including dissociative electron attachment experiments for which a new experimental system has been built. In addition, the experiments also showed limitations of the technique, which should in turn inspire further experimental

work towards enhancing methodologies to bring neutral thermally labile biomolecules into the gas-phase. The experiments on *indirect laser-induced thermally* desorbed uridine have not only shown evidence for interesting neutral electronic excited state dynamics, but also indicated that such dynamics as well as associated fragmentation pathways can be strongly dependent on the initial isomeric form of the molecule. This highlights the importance of developing methods which can separate different isomeric structures from a mixture of isomers produced in the gas-phase. The metastable dissociation experiment has proved capable of elucidating complex metastable fragmentation pathways which can be exploited in the future for tracing the origin of products resulting from sequential fragmentation routes of large biomolecules.

We propose the following steps to build on the research in this thesis:

1. Indirect laser-induced thermal desorption of nucleosides:

    - Testing the suitability of ILTD for the production of intact neutral gas-phase targets of the remaining RNA/DNA nucleosides (adenosine, guanosine and cytidine). This has a potential to provide adequate targets for DEA, but also MPI and EII experiments which can be studied in the newly developed system at the OU once the optimisation and testing of the new set-up has been completed. Such experiments are likely to provide further insights into how bonding of the sugar molecule affects the radiation response of neutral nucleobases isolated in the gas-phase as well as how the site-specific chemical modification affects the response of nucleosides which could be used as a tool to mimic the response of larger RNA/DNA constituents.
    - Investigating the effect of the foil properties (material and thickness) as well as sample thickness on the thermal decomposition of thymidine produced in the gas-phase by ILTD has a potential to enhance the robustness of the technique even for more fragile biomolecules.
    - Testing and optimising the system (mentioned only very briefly in this thesis) for seeding the *ILT*-desorbed molecules in cold molecular beams. If a reasonable pick-up efficiency is achieved, the system can be tested on thymidine for whether rapid cooling in supersonic beams can affect the thermal decomposition threshold. Analogously to the point above, this could extend the applicability of ILTD for more fragile species.

2. Indirect laser-induced thermal desorption of nucleotides:

    - Optimising the sample preparation procedure for ILTD of nucleotides could

potentially extend the range of biomolecules which can be produced intact in the gas-phase by ILTD. We propose the following steps for the optimisation:

- Trying to dry off solvent molecules by placing the sample holder in a vacuum desiccator prior exposing it to high vacuum of the experimental chamber and/or testing different solvents.
- Designing and testing alternative sample holding arrangement which does not require use of any solvents. For example, a rougher foil surface may be amenable to producing a lightly-adhered layer by *dry packing*. The horizontal orientation of the foil in the new experiment will be valuable in this case.

3. S^+ ($m/z\,133$) fragment ion production from *ILT*-desorbed uridine:

   - Carrying out multi-photon ionisation and electron impact ionisation experiments on uridine produced by ILTD in the same experimental conditions should help to strengthen the interpretations presented in Chapter 6 of this PhD thesis, i.e. that the increased production of $m/z\,133$ fragment ions with increasing desorption laser power in the MPI experiments at $225\,nm$ is linked to a critical process happening in the neutral electronic excited state of uridine. Accordingly, our prediction is that the ratio of S^+/total ion production by EII will be essentially independent of the desorption laser power.
   - Carrying out rotational spectroscopy experiments on uridine produced by ILTD should bring more insights into how changing the desorption laser power affects the production of ground state isomers of uridine in the gas-phase.
   - Carrying out time-resolved photoion yield experiments on uridine in coincidence with photoelectron-energy analysis compared with dynamics calculations of several different isomers of uridine should help to understand which electronic excited state(s) of uridine are involved in the S^+ production.
   - In the future, seeding *ILT*-desorbed uridine in the molecular beam for *Stark deflection* should enable to probe radiation response of uridine with control over relative populations of different isomers in the target.
   - If we can achieve the production of intact neutral gas-phase 5′-UMP, it will be interesting to see effect of the phosphate group on MPI production of S^+ ions as well as on other fragment ion channels that may or may not have any dependence on neutral electronic excited state dynamics.

4. Optimisation and testing of the *New DEA/EII/MPI experimental set-up*:

- The following action has to be taken to enable multi-photon ionisation experiments on targets produced by ILTD:
  - Optimising the performance of the mass spectrometer for the targets produced by ILTD.
  - Fine tuning of the optics alignment for the UV beam based on signal intensities in the MPI mass spectra.
- The following action has to be taken to further enable electron impact ionisation experiments on targets produced by ILTD:
  - Fully test and optimise the electron beam in the heated chamber ($80 - 90\,^{\circ}C$).
- The following action has to be taken to further enable dissociative electron attachment experiments on targets produced by ILTD:
  - Optimising the EG performance at low electron beam energies $< 20\,eV$.
  - Optimising the mass spectrometer in the negative ion detection mode.
  - Calibrating the absolute electron energy scale of low-energy electron beam, which can be done based on the well-known resonances from DEA experiments to O_2 targets.

8.4 Final remarks

Studying UV- and electron impact-induced dynamics of neutral RNA/DNA subunits in the gas-phase has potential to provide important insights into the radiosensitivity in nucleic acids. This PhD thesis has shown that the intricacy of the experimental work escalates very quickly with increasing size of biomolecules. In addition to investigating thermal lability, structural purity of increasingly large gas-phase biomolecules is an important point which should be addressed in the future experiments.

Bibliography

[1] Nano-scale insights in ion beam cancer therapy (nano-IBCT). COST action, 2010-2014.

[2] Advanced radiotherapy, generated by exploiting nanoprocesses and technologies (FP7 ITN ARGENT). COST action, 2014.

[3] H. L. Barks, R. Buckley, G. A. Grieves, E. Di Mauro, N. V. Hud, and T. M. Orlando. Guanine, adenine, and hypoxanthine production in UV-irradiated formamide solutions: Relaxation of the requirements for prebiotic purine nucleobase formation. *ChemBioChem*, 11(9):1240–1243, 2010.

[4] Origins, evolution of life on earth, and in the universe (ORIGINS). `https://www.cost.eu/actions/TD1308/#tabs|Name:overview`, 2014. [Online; accessed 15-March-2019].

[5] C. Meinert, I. Myrgorodska, P. de Marcellus, T. Buhse, L. Nahon, S. V. Hoffmann, L. Le S. d'Hendecourt, and U. J. Meierhenrich. Ribose and related sugars from ultraviolet irradiation of interstellar ice analogs. *Science*, 352(6282):208–212, 2016.

[6] C. T. Middleton, K. de La Harpe, C. Su, Y. K. Law, C. E. Crespo-Hernández, and B. Kohler. DNA excited-state dynamics: From single bases to the double helix. *Annual Review of Physical Chemistry*, 60(1):217–239, 2009.

[7] V. G. Stavros and J. R. R. Verlet. Gas-phase femtosecond particle spectroscopy: A bottom-up approach to nucleotide dynamics. *Annual Review of Physical Chemistry*, 67(1):211–232, 2016.

[8] J.-C. Poully, J. Miles, S. De Camillis, A. Cassimi, and J. B. Greenwood. Proton irradiation of DNA nucleosides in the gas phase. *Physical Chemistry Chemical Physics*, 17(11):7172–7180, 2015.

[9] O. Ghafur, S. W. Crane, M. Ryszka, J. Bockova, A. Rebelo, L. Saalbach, S. De Camillis, J. B. Greenwood, S. Eden, and D. Townsend. Ultraviolet relaxation dy-

namics in uracil: Time-resolved photoion yield studies using a laser-based thermal desorption source. *The Journal of Chemical Physics*, 149(3):034301(1–13), 2018.

[10] M. Gargaud, W. M. Irvine, R. Amils, J. Cernicharo, Q. Henderson, J. Cleaves II, D. L. Pinti, D. Rouan, T. Spohn, S. Tirard, and M. Viso. *Encyclopedia of Astrobiology*. Springer, 2015.

[11] I. Martincorena, K. M. Raine, M. Gerstung, K. J. Dawson, K. Haase, P. Van Loo, H. Davies, M. R. Stratton, and P. J. Campbell. Universal patterns of selection in cancer and somatic tissues. *Cell*, 171(5):1029–1041, 2017.

[12] L. A. Pray. Discovery of DNA structure and function: Watson and Crick. *Nature Education*, 1(1):100, 2008.

[13] J. Kohanoff, M. McAllister, G. A. Tribello, and B. Gu. Interactions between low energy electrons and DNA: A perspective from first-principles simulations. *Journal of Physics: Condensed Matter*, 29(38):383001(1–29), 2017.

[14] M. Barbatti, A. C. Borin, and S. Ullrich. *Photoinduced phenomena in nucleic acids I: Nucleobases in the Gas Phase and in Solvents*. Springer, 2014.

[15] D. M. York and T.-S. Lee. *Multi-scale Quantum Models for Biocatalysis*. Springer, 2009.

[16] S. Ptasińska, P. Candori, S. Denifl, S. Yoon, V. Grill, P. Scheier, and T. D. Märk. Dissociative ionization of the nucleosides thymidine and uridine by electron impact. *Chemical Physics Letters*, 409(3-4):270–276, 2005.

[17] J. Kopyra. Low energy electron attachment to the nucleotide deoxycytidine monophosphate: Direct evidence for the molecular mechanisms of electron-induced DNA strand breaks. *Physical Chemistry Chemical Physics*, 14(23):8287–8289, 2012.

[18] B. Barc, M. Ryszka, J. Spurrell, M. Dampc, P. Limão-Vieira, R. Parajuli, N. J. Mason, and S. Eden. Multi-photon ionization and fragmentation of uracil: Neutral excited-state ring opening and hydration effects. *The Journal of Chemical Physics*, 139(24):244311(1–10), 2013.

[19] M. Folkard, B. Brocklehurst K. M. Prise and, , and B. D. Michael. DNA damage induction in dry and hydrated DNA by synchrotron radiation. *Journal of Physics B*, 32(11):2753–2761, 1999.

[20] B. Boudaiffa, P. Cloutier, D. Hunting, M. A. Huels, and L. Sanche. Resonant formation of DNA strand breaks by low-energy (3 to 20eV) electrons. *Science*, 287(5458):1658–1660, 2000.

[21] A. Solov'yov. *Nanoscale Insights into Ion-Beam Cancer Therapy*. Springer, 2017.

[22] O. Desouky, N. Ding, and G. Zhou. Targeted and non-targeted effects of ionizing radiation. *Journal of Radiation Research and Applied Sciences*, 8(2):247–254, 2015.

[23] F. D. Lewis, X. Liu, J. Liu, S. E. Miller, R. T. Hayes, and M. R. Wasielewski. Direct measurement of hole transport dynamics in DNA. *Nature*, 406(6791):51–53, 2000.

[24] D. Becker and M. D. Sevilla. 3 - The chemical consequences of radiation damage to DNA. *Advances in Radiation Biology*, 17:121–180, 1993.

[25] B. H. Yun, Y. A. Lee, S. K. Kim, V. Kuzmin, A. Kolbanovskiy, P. C. Dedon, N. E. Geacintov, and V. Shafirovich. Photosensitized oxidative DNA damage: From hole injection to chemical product formation and strand cleavage. *Journal of the American Chemical Society*, 129(30):9321–9332, 2007.

[26] M. Ryszka, R. Pandey, C. Rizk, J. Tabet, B. Barc, M. Dampc, N. J. Mason, and S. Eden. Dissociative multi-photon ionization of isolated uracil and uracil-adenine complexes. *International Journal of Mass Spectrometry*, 396:48–54, 2016.

[27] F. L. Gates. A study of the bactericidal action of ultra violet light: I. The reaction to monochromatic radiations. *The Journal of General Physiology*, 13(2):231–248, 1929.

[28] W. J. Schreier, P. Gilch, and W. Zinth. Early events of DNA photodamage. *Annual Review of Physical Chemistry*, 66(1):497–519, 2015.

[29] M. Barbatti, A. J. A. Aquinoa, and H. Lischka. The UV absorption of nucleobases: Semi-classical *ab initio* spectra simulations. *Physical Chemistry Chemical Physics*, 12(19):4959–4967, 2010.

[30] W. B. Demore, S. P. Sandler, D. M. Golden, R. F. Hampson, M. J. Kurylo, C. J. Howard, A. R. Ravishankara, C. E. Kolb, and M. J. Molina. *Chemical Kinetics and Photochemical Data for Use in Stratospheric Modelling*. Jet Propulsion Laboratory Publication 97-4, 1997.

[31] International Agency for Research on Cancer. *IARC Monographs on the Evaluation of Carcinogenic Risks to Humans*. International Agency for Research on Cancer, 2012.

[32] N. d. N. Rodrigues and V. G. Stavros. From fundamental science to product: A bottom-up approach to sunscreen development. *Science Progress*, 101(1):8–31, 2018.

[33] R. P. Rastogi, Richa, A. Kumar, M. B. Tyagi, and R. P. Sinha. Molecular mechanisms of ultraviolet radiation-induced DNA damage and repair. *Journal of Nucleic Acids*, 6551:592980(1–32), 2010.

[34] F. R. de Gruijl and J. C. van der Leun. Environment and health: 3. Ozone depletion and ultraviolet radiation. *Canadian Medical Association Journal*, 163(7):851–855, 2000.

[35] L. Mullen. Shining light on life's origin. `http://www.astrobio.net/origin-and-evolution-of-life/shining-light-on-lifes-origin/`, 2003. [Online; accessed 05-December-2019].

[36] C. S. Cockell. Biological effects of high ultraviolet radiation on early Earth – a theoretical evaluation. *Journal of Theoretical Biology*, 193(4):717–729, 1998.

[37] L. J. Rothschild. The influence of UV radiation on protistan evolutions. *Journal of Eukaryotic Microbiology*, 46(5):548–555, 1999.

[38] W. Gilbert. Origin of life: The RNA world. *Nature*, 319(6055):618, 1986.

[39] S. A. Benner, A. D. Ellington, and A. Tauer. Modern metabolism as a palimpsest of the RNA world. *Proceedings of the National Academy of Sciences of the United States of America*, 86(18):7054–7058, 1989.

[40] G. F. Joyce. The antiquity of RNA-based evolution. *Nature*, 418(6894):214–221, 2002.

[41] J. P. Dworkin, A. Lazcano, and S. L. Miller. The roads to and from the RNA world. *Journal of Theoretical Biology*, 222(1):127–134, 2003.

[42] R. F. Gesteland, T. R. Cech, and J. F. Atkins. *The RNA World*. Cold Spring Harbor Laboratory Press, 2006.

[43] S. De Camillis, J. Miles, G. Alexander, O. Ghafur, I. D. Williams, D. Townsend, and J. B. Greenwood. Ultrafast non-radiative decay of gas-phase nucleosides. *Physical Chemistry Chemical Physics*, 17(36):23643–23650, 2015.

[44] C. Canuel, M. Mons, F. Piuzzi, B. Tardivel, I. Dimicoli, and M. Elhanine. Excited states dynamics of DNA and RNA bases: Characterization of a stepwise deactivation pathway in the gas phase. *The Journal of Chemical Physics*, 122(7):074316(1–6), 2005.

[45] D. Nachtigallová, A. J. A. Aquino, J. J. Szymczak, M. Barbatti, P. Hobza, and H. Lischka. Nonadiabatic dynamics of uracil: Population split among different decay mechanisms. *The Journal of Physical Chemistry A*, 115(21):5247–5255, 2011.

[46] S. Matsika, C. Zhou, M. Kotur, and T. C. Weinacht. Combining dissociative ionization pump-probe spectroscopy and *ab initio* calculations to interpret dynamics and control through conical intersections. *Faraday Discussions*, 153:247–260, 2011.

[47] S. Ullrich, T. Schultz, M. Z. Zgierskia, and A. Stolow. Electronic relaxation dynamics in DNA and RNA bases studied by time-resolved photoelectron spectroscopy. *Physical Chemistry Chemical Physics*, 6(10):2796–2801, 2004.

[48] P. M. Girard, S. Francesconi, M. Pozzebon, D. Graindorge, P. Rochette, R. Drouin, and E. Sage. UVA-induced damage to DNA and proteins: Direct versus indirect photochemical processes. *Journal of Physics: Conference Series*, 261:012002(1–10), 2011.

[49] R. Brem, M. Guven, and P. Karran. Oxidatively-generated damage to DNA and proteins mediated by photosensitized UVA. *Free Radical Biology and Medicine*, 107:101–109, 2017.

[50] E. Alizadeh, T. M. Orlando, and L. Sanche. Biomolecular damage induced by ionizing radiation: The direct and indirect effects. *Annual Review of Physical Chemistry*, 66:379–398, 2015.

[51] S. M. Pimblott and J. A. LaVerne. Production of low-energy electrons by ionizing radiation. *Radiation Physics and Chemistry*, 76(8–9):1244–1247, 2007.

[52] D. J. Haxton, Z. Zhang, H-D. Meyer, T. N. Rescigno, and C. W. McCurdy. Dynamics of dissociative attachment of electrons to water through the $^2B_1$ metastable state. *Physical Review A*, 69:062714(1–16), 2004.

[53] D. Dehareng and G. Dive. Vertical ionization energies of α-L-amino acids as a function of their conformation: An *ab initio* study. *International Journal of Molecular Sciences*, 5(11):301–332, 2004.

[54] M. Taherkhani, A. Armentano, J. Černý, and K. Müller-Dethlefs. Threshold ionization spectroscopic investigation of supersonic jet-cooled, laser-desorbed tryptophan. *Chemical Physics Letters*, 657:142–147, 2016.

[55] H.-C. Hsu and C.-K. Ni. Vacuum ultraviolet single-photon postionization of amino acids. *Applied Sciences*, 8(5):301–332, 2018.

[56] B. Barć. *Hydrated clusters of nucleic acid bases in supersonic beams probed by multiphoton ionization (MPI) mass spectrometry*. PhD thesis, The Open University, Milton Keynes, United Kingdom, 2013.

[57] M. Ryszka. *Radiation induced processes in biomolecules and clusters in controlled beams*. PhD thesis, The Open University, Milton Keynes, United Kingdom, 2016.

[58] R. K. Pandey. *UV induced processes in biomolecules, hydrated clusters and Stark deflected beams*. PhD thesis, The Open University, Milton Keynes, United Kingdom, 2017.

[59] J. Tabet, S. Eden, S. Feil, H. Abdoul-Carime, B. Farizon, M. Farizon, S. Ouaskit, and T. D. Märk. Absolute total and partial cross sections for ionization of nucleobases by proton impact in the Bragg peak velocity range. *Physical Review A*, 82(2):022703, 2010.

[60] H. W. Jochims, M. Schwell, H. Baumgärtel, and S. Leach. Photoion mass spectrometry of adenine, thymine and uracil in the 6–22 eV photon energy range. *Chemical Physics*, 314(1-3):263–282, 2005.

[61] S. Denifl, S. Ptasińska, M. Probst, J. Hrušák, P. Scheier, and T. D. Märk. Electron attachment to the gas-phase DNA bases cytosine and thymine. *Journal of Physical Chemistry A*, 108(31):6562–6569, 2004.

[62] S. Denifl, S. Ptasińska, G. Hanel, B. Gstir, M. Probst, P. Scheier, and T. D. Märk. Electron attachment to gas-phase uracil. *The Journal of Chemical Physics*, 120(14):6557–6565, 2004.

[63] H. Abdoul-Carime, J. Langer, M. A. Huels, and E. Illenberger. Decomposition of purine nucleobases by very low energy electrons. *The European Physical Journal D*, 35(2):399–404, 2005.

[64] M. Y. Choi and R. E. Miller. Four tautomers of isolated guanine from infrared laser spectroscopy in helium nanodroplets. *Journal of the American Chemical Society*, 128(22):7320–7328, 2006.

[65] A. N. Zavilopulo, O. B. Shpenik, and A. S. Agafonova. Electron impact ionization of gas-phase guanine near the threshold. *Journal of Physics B*, 42(2):025101(1–6), 2009.

[66] E. P. Mansson, S. De Camillis, M. C. Castrovilli, M. Galli, M. Nisoli, F. Calegari, and J. B. Greenwood. Ultrafast dynamics in the DNA building blocks thymidine and thymine initiated by ionizing radiation. *Physical Chemistry Chemical Physics*, 19(30):19815–19821, 2017.

[67] V. B. Delchev. Computational (DFT and TD DFT) study of the electron structure of the tautomers/conformers of uridine and deoxyuridine and the processes of intramolecular proton transfers. *Journal of Molecular Modeling*, 16(4):749–757, 2010.

[68] R. So and S. Alavi. Vertical excitation energies for ribose and deoxyribose nucleosides. *Journal of Computational Chemistry*, 28(11):1776–1782, 2007.

[69] H. D. Flosadóttir, B. Ómarsson, I. Bald, and O. Ingólfsson. Metastable decay of DNA components and their compositions – a perspective on the role of reactive electron scattering in radiation damage. *The European Physical Journal D*, 66(13):1–20, 2012.

[70] J. Kočišek, B. Sedmidubská, S. Indrajith, M. Fárník, and J. Fedor. Electron attachment to microhydrated deoxycytidine monophosphate. *The Journal of Physical Chemistry B*, 122(20):5212–5217, 2018.

[71] N. D. N. Rodrigues, N. C. Cole-Filipiak, M. D. Horbury, M. Staniforth, T. N. V. Karsili, Y. Peperstraete, and V. G. Stavros. Photophysics of the sunscreen ingredient menthyl anthranilate and its precursor methyl anthranilate: A bottom-up approach to photoprotection. *Journal of Photochemistry and Photobiology A: Chemistry*, 353:376–384, 2018.

[72] S. Boldissar and M. S. de Vries. How nature covers its bases. *Physical Chemistry Chemical Physics*, 20(15):9701–9716, 2018.

[73] S. A. Carey and R. J. Sundberg. *Advanced Organic Chemistry*. Kluwer Academic Publishers, 2002.

[74] S. S. Zumdahl. *Chemistry*. D. C. Heath and Company, 1986.

[75] J. M. Hollas. *Modern Spectroscopy*. John Willey & Sons, Ltd, 2004.

[76] W. Demtröder. *Atoms, Molecules and Photons*. Springer, 2010.

[77] J. P. Gallivan and D. A. Dougherty. Cation-π interactions in structural biology. *Proceedings of the National Academy of Sciences of the United States of America*, 96(17):9459–9464, 1999.

[78] C. R. Martinez and B. L. Iverson. Rethinking the term "pi-stacking". *Chemical Science*, 3(7):2191–2201, 2012.

[79] R. L. Johnston. *Atomic and Molecular Clusters*. CRC Press, 2002.

[80] S. L. Boyd and R. J. Boyd. A density functional study of methanol clusters. *Journal of Chemical Theory and Computation*, 3(1):54–61, 2007.

[81] B. Wardle. *Principles and Applications of Photochemistry*. John Wiley & Sons, Ltd, 2009.

[82] E. G. Lewars. *Computational Chemistry*. Springer, 2016.

[83] J. Franck and E. G. Dymond. Elementary processes of photochemical reactions. *Transactions of the Faraday Society*, 21:536–542, 1926.

[84] E. Condon. A theory of intensity distribution in band systems. *Physical Review*, 28(6):1182–1201, 1926.

[85] J. H. Gross. *Mass Spectrometry*. Springer, 2017.

[86] M. Born and R. Oppenheimer. Zur Quantentheorie der Molekeln. *Annalen der Physik*, 389(20):457–484, 1927.

[87] M. Nisoli, P. Decleva, F. Calegari, A. Palacios, and F. Martín. Attosecond electron dynamics in molecules. *Chemical Reviews*, 117(16):10760–10825, 2017.

[88] C. D. Lin, A.-T. Le, C. Jin, and H. Wei. *Attosecond and Strong-Field Physics*. Cambridge University Press, 2018.

[89] L. Piela. *Ideas of Quantum Chemistry*. Elsevier, 2014.

[90] A. L. Sobolewski and W. Domcke. *Ab initio* studies on the photophysics of the guanine-cytosine base pair. *Physical Chemistry Chemical Physics*, 6(10):2763–2771, 2004.

[91] G. A. Worth and L. S. Cederbaum. Mediation of ultrafast electron transfer in biological systems by conical intersections. *Chemical Physics Letters*, 338(4):219–223, 2001.

[92] S. Matsika. Radiationless decay of excited states of uracil through conical intersections. *The Journal of Physical Chemistry A*, 108(37):7584–7590, 2004.

[93] A. Mozumder and Y. Hatano. *Charged Particle and Photon Interactions with Matter*. CRC Press, 2003.

[94] J. C. Lindon, G. E. Tranter, and J. L. Holmes. *Encyclopedia of Spectroscopy and Spectrometry: Part 1, (A - L)*. Academic Press, 2000.

[95] C. M. Marian. Spin–orbit coupling and intersystem crossing in molecules. *Wiley Interdisciplinary Reviews: Computational Molecular Science*, 2:187–203, 2012.

[96] J. A. Barltrop and J. D. Coyle. *Excited States in Organic Chemistry*. Wiley & Sons Ltd, 1975.

[97] N. J. Masona, P. Limão Vieira, S. Eden, P. Kendall, S. Pathak, A. Dawes, J. Tennyson, P. Tegeder, M. Kitajima, M. Okamoto, K. Sunohara, H. Tanaka, H. Cho, S. Samukawa, S. V. Hoffmann, D. Newnham, and S. M. Spyrou. VUV and low energy electron impact study of electronic state spectroscopy of CF_3I. *International Journal of Mass Spectrometry*, 223-224(1-3):647–660, 2003.

[98] M. Barbatti, A. J. A. Aquinoa, J. J. Szymczak, D. Nachtigallová, P. Hobzac, and H. Lischka. Relaxation mechanisms of UV-photoexcited DNA and RNA nucleobases. *Proceedings of the National Academy of Sciences of the United States of America*, 107(50):21453–21458, 2010.

[99] J. Morellec, D. Normand, and G. Petite. Resonance shifts in the multiphoton ionization of cesium atoms. *Physical Review A*, 14(1):300–312, 1976.

[100] S. H. Nam, H. S. Park, J. K. Song, and S. M. Park. Photoinduced dynamics of hydrated adenine clusters. *The Journal of Physical Chemistry A*, 111(18):3480–3484, 2007.

[101] C. Weickhardt, F. Moritz, and J. Grotemeyer. Multiphoton ionization mass spectrometry: Principles and fields of application. *European Journal of Mass Spectrometry*, 2(3):151–160, 1996.

[102] I. Schechter, H. Schröder, and K. L. Kompa. A simplified method for absolute MPI cross-section measurements. Application to three-photon non-resonant ionization of Xe at $266\,nm$. *Chemical Physics Letters*, 194(1-2):128–134, 1992.

[103] P. B. Corkum. Plasma perspective on strong-field multiphoton ionization. *Physical Review Letters*, 71(13):1994–1997, 1993.

[104] R. Schinke. *Photodissociation Dynamics*. Cambridge University Press, 1993.

[105] S. Schlemmer, T. Giesen, H. Mutschke, and C. Jäger. *Laboratory Astrochemistry*. Wiley-VCH, 2015.

[106] T. D. Märk and G. H. Dunn. *Electron Impact Ionisation*. Springer-Verlag Wien GmbH, 1985.

[107] L. G. Christophorou. *Electron-molecule Interactions and their Applications*. Academic Press, Inc., 1984.

[108] P. J. M. van der Burgt, S. Finnegan, and S. Eden. Electron impact fragmentation of adenine: Partial ionization cross sections for positive fragments. *The European Physical Journal D*, 69(173):1–8, 2015.

[109] I. I. Fabrikant, S. Eden, N. J. Mason, and J. Fedor. *Advances In Atomic, Molecular, and Optical Physics*. Academic Press, 2017.

[110] K. Aflatooni, A. M. Scheer, and P. D. Burrow. Total dissociative electron attachment cross sections for molecular constituents of DNA. *The Journal of Chemical Physics*, 125(5):054301(1–5), 2006.

[111] K. Aflatooni, A. M. Scheer, and P. D. Burrow. Dissociative electron attachment in uracil: Total anion yield. *Chemical Physics Letters*, 408(4-6):426–428, 2005.

[112] S. Gohlke, H. Abdoul-Carime, and E. Illenberger. Dehydrogenation of adenine induced by slow ($< 3\,eV$) electrons. *Chemical Physics Letters*, 380(5–6):595–599, 2003.

[113] M. T. Bowers. *Gas Phase Ion Chemistry*. Academic Press, Inc., 1979.

[114] B. Barc, M. Ryszka, J.-C. Poully, E. Jabbour Al Maalouf, Z. el Otella, J. Tabet, R. Parajuli, P. J. M. van der Burgt, P. Limão-Vieira, P. Cahillane, M. Dampc, N. J. Mason, and S. Eden. Multi-photon and electron impact ionisation studies of reactivity in adenine–water clusters. *International Journal of Mass Spectrometry*, 365–366:194–199, 2014.

[115] R. Pandey, M. Ryszka, T. da Fonseca Cunha, M. Lalande, M. Dampc, P. Limão-Vieira, N. J. Mason, J.-C. Poully, and S. Eden. Threshold behavior in metastable dissociation of multi-photon ionized thymine and uracil. *Chemical Physics Letters*, 684:233–238, 2017.

[116] R. Pandey, M. Lalande, M. Ryszka, P. Limão-Vieira, N. J. Mason, J.-C. Poully, and S. Eden. Stabilities of nanohydrated thymine radical cations: Insights from multi-photon ionization experiments and ab initio calculations. *The European Physical Journal D*, 71(190):1–8, 2017.

[117] M. D. Morse. *Methods of Experimental Physics: Atomic, Molecular, and Optical Physics*. Academic Press, Inc., 1996.

[118] J. Ross. *Advances in Chemical Physics: Molecular Beams, Volume 10*. John Wiley & Sons, Inc., 1966.

[119] J. C. Lindon, G. E. Tranter, and J. L. Holmes. *Encyclopedia of Spectroscopy and Spectrometry: Part 2 (M - Z)*. Academic Press, 2000.

[120] C. R. Calvert, L. Belshaw, M. J. Duffy, O. Kelly, R. B. King, A. G. Smyth, T. J. Kelly, J. T. Costello, D. J. Timson, W. A. Bryan, T. Kierspel, P. Rice, I. C. E. Turcu, C. M. Cacho, E. Springate, I. D. Williamsa, and J. B. Greenwood. LIAD-fs scheme for studies of ultrafast laser interactions with gas phase biomolecules. *Physical Chemistry Chemical Physics*, 14(18):6289–6297, 2012.

[121] P. J. M. van der Burgt, M. A. Brown, J. Bockova, A. Rebelo, M. Ryszka, J.-C. Poully, and S. Eden. Fragmentation processes of ionized 5-fluorouracil monomers and clusters. *The European Physical Journal D*, 73(8):184(1–13), 2019.

[122] *Pulsed dye laser*. Laser- und Plasmatechnik GmbH, 2006.

[123] Sirah Lasertechnik GmbH. SHG. `http://www.sirah.com/laser/frequency-conversion/shg`, 2019. [Online; accessed 17-September-2019].

[124] I. Bald, H. D. Flosadóttir, B. Ómarsson, and O. Ingólfsson. Metastable fragmentation of a thymidine-nucleotide and its components. *International Journal of Mass Spectrometry*, 313:15–20, 2012.

[125] J. M. Rice, G. O. Dudek, and M. Barber. Mass spectra of nucleic acid derivatives. Pyrimidines. *Journal of the American Chemical Society*, 87(20):4569–4576, 1965.

[126] A. Mauracher, S. Denifl, A. Edtbauer, M. Hager, M. Probst, O. Echt, T. D. Märk, P. Scheier, T. A. Field, and K. Graupner. Metastable anions of dinitrobenzene: Resonances for electron attachment and kinetic energy release. *The Journal of Chemical Physics*, 133(24):244302(1–9), 2010.

[127] W. F. Haddon and F. W. McLafferty. Metastable ion characteristics. Measurements with a modified time-of-flight mass spectrometer. *Analytical Chemistry*, 41(1):31–36, 1969.

[128] A. G. Shard and I. S. Gilmore. Analysis of metastable ions in the ToF-SIMS spectra of polymers. *International Journal of Mass Spectrometry*, 269(1-2):85–94, 2008.

[129] J. M. L'Hermite, F. Rabilloud, P. Labastie, and F. Spiegelman. Evidence for trimers evaporation in silver bromide clusters. *The European Physical Journal D*, 16(1):77–80, 2001.

[130] I. S. Gilmore and M. P. Seah. Static SIMS: Metastable decay and peak intensities. *Applied Surface Science*, 144-145(1-4):26–30, 1999.

[131] J. M. L'Hermite, L. Marcou, F. Rabilloud, and P. Labastie. A new method to study metastable fragmentation of clusters using a reflectron time-of-flight mass spectrometer. *Review of Scientific Instruments*, 71(5):2033–2037, 2000.

[132] J. M. L'Hermite, F. Rabilloud, L. Marcou, and P. Labastie. Metastable fragmentation of silver bromide clusters. *The European Physical Journal D*, 14(3):323–330, 2001.

[133] C. R. Ponciano, F. E. Ávalos, A. Rentería, and E. F. Da Silveira. Analysis of metastable decay by time-of-flight coincidence and kinetics energy measurements. *International Journal of Mass Spectrometry*, 209(2-3):197–208, 2001.

[134] A. Vredenborg, W. G. Roeterdink, C. A. De Lange, and M. H. M. Janssen. Revealing femtosecond multiphoton induced multichannel molecular ionization and fragmentation dynamics by photoelectron–photoion coincidence imaging. *Chemical Physics Letters*, 478(1-3):20–27, 2009.

[135] J.-C. Poully, V. Vizcaino, L. Schwob, R. Delaunay, J. Kocisek, S. Eden, J. Y. Chesnel, J. Rangama A. Méry, L. Adoui, and B. Huber. Formation and fragmentation of protonated molecules after ionization of amino acid and lactic acid clusters by collision with ions in the gas phase. *ChemPhysChem*, 16(11):2389–2396, 2015.

[136] A. R. Milosavljević, V. Z. Cerovski, F. Canon, M. L. Ranković, N. Škoro, L. Nahon, and A. Giuliani. Energy-dependent UV photodissociation of gas-phase adenosine monophosphate nucleotide ions: The role of a single solvent molecule. *The Journal of Physical Chemistry Letters*, 5(11):1994–1999, 2014.

[137] T. W. Shannon and F. W. McLafferty. Identification of gaseous organic ions by the use of "metastable peaks"[1]. *Journal of the American Chemical Society*, 88(21):5021–5022, 1966.

[138] R. E. Continetti. Photoelectron-photofragment coincidence studies of dissociation dynamics. *International Reviews in Physical Chemistry*, 17(2):227–260, 1998.

[139] R. G. Cooks, J. H. Beynon, R. M. Caprioli, and G. R. Lester. *Metastable Ions*. Elsevier, 1973.

[140] S. Feil, K. Gluch, S. Denifl, F. Zappa, O. Echt, P. Scheier, and T. D. Märk. Metastable dissociation and kinetic energy release of helium clusters upon electron impact ionization. *International Journal of Mass Spectrometry*, 252(2):166–172, 2006.

[141] S. Ishiuchi, M. Sakai, K. Daigoku, K. Hashimoto, and M. Fujii. Hydrogen transfer dynamics in a photoexcited phenol/ammonia (1 : 3) cluster studied by picosecond time-resolved UV-IR-UV ion dip spectroscopy. *The Journal of Chemical Physics*, 127(23):234304(1–8), 2007.

[142] N. J. Kim, Y. S. Kim, G. Jeong, T. K. Ahn, and S. K. Kim. Hydration of DNA base cations in the gas phase. *International Journal of Mass Spectrometry*, 219(1):11–21, 2002.

[143] E. Bruzzi, G. Raggi, R. Parajuli, and A. J. Stace. Experimental binding energies for the metal complexes $[Mg(NH_3)_n]^{2+}$, $[Ca(NH_3)_n]^{2+}$, and $[Sr(NH_3)_n]^{2+}$ for $n = 4$–20 determined from kinetic energy release measurements. *The Journal of Physical Chemistry A*, 118(37):8525–8532, 2014.

[144] M. Shinozaki, M. Sakai, S. Yamaguchi, T. Fujioka, and M. Fujii. S_1–S_0 electronic spectrum of jet-cooled m-aminophenol. *Physical Chemistry Chemical Physics*, 5(22):5044–5050, 2003.

[145] V. Yatsyna, D. J. Bakker, R. Feifel, A. M. Rijs, and V. Zhaunerchyk. Aminophenol isomers unraveled by conformer-specific far-IR action spectroscopy. *Physical Chemistry Chemical Physics*, 18(8):6275–6283, 2016.

[146] National Institute of Advanced Industrial Science and Technology (AIST). Spectral database for organic compounds SDBS. `https://sdbs.db.aist.go.jp/sdbs/cgi-bin/direct_frame_top.cgi`, 1999. [Online; accessed 01-May-2019].

[147] National Institute of Standards and Technology. Phenol, 3-amino-. `https://webbook.nist.gov/cgi/cbook.cgi?ID=C591275&Mask=200#Mass-Spec`, 2014. [Online; accessed 06-May-2019].

[148] F. Filsinger, J. Küpper, G. Meijer, J. L. Hansen, J. Maurer, J. H. Nielsen, L. Holmegaard, and H. Stapelfeldt. Pure samples of individual conformers: The separation of stereoisomers of complex molecules using electric fields. *Angewandte Chemie International Edition*, 48(37):6900–6902, 2009.

[149] C. Unterberg, A. Gerlach, A. Jansen, and M. Gerhards. Structures and vibrations of neutral and cationic 3- and 4-aminophenol. *Chemical Physics*, 304(3):237–244, 2004.

[150] M. H. Palmer, T. Ridley, S. V. Hoffmann, N. C. Jones, M. Coreno, M. de Simone, C. Grazioli, M. Biczysko, A. Baiardi, and P. Limão-Vieira. Interpretation of the vacuum ultraviolet photoabsorption spectrum of iodobenzene by *ab initio* computations. *The Journal of Chemical Physics*, 142(13):134302, 2015.

[151] PubChem. 3-Aminophenol. `https://pubchem.ncbi.nlm.nih.gov/compound/3-Aminophenol#section=Top`, 2010. [Online; accessed 20-May-2019].

[152] G. W. Thomson. The Antoine equation for vapor-pressure data. *Chemical Reviews*, 38(1):1–39, 1946.

[153] R. C. Rodgers and G. E. Hill. Equations for vapour pressure versus temperature: Derivation and use of the Antoine equation on a hand-held programmable calculator. *British Journal of Anaesthesia*, 50(5):415–424, 1978.

[154] D. Ferro, L. Bencivenni, R. Teghil, and R. Mastromarino. Vapour pressures and sublimation enthalpies of thymine and cytosine. *Thermochimica Acta*, 42(1):75–83, 1980.

[155] J. Tabet, S. Eden, S. Feil, H. Abdoul-Carime, B. Farizon, M. Farizon, S. Ouaskit, and T. D. Märk. Absolute molecular flux and angular distribution measurements to characterize DNA/RNA vapor jets. *Nuclear Instruments and Methods in Physics Research B*, 268(15):2458–2466, 2010.

[156] J. M. S. Fonseca, N. Gushterov, and R. Dohrn. Vapour pressures of selected organic compounds down to 1 *mPa*, using mass-loss Knudsen effusion method. *The Journal of Chemical Thermodynamics*, 73:148–155, 2014.

[157] R. Kendler, F. Dreisbach, R. Seif, S. Pollak, and M. Petermann. Measuring low vapor pressures employing the Knudsen effusion technique and a magnetic suspension balance. *Review of Scientific Instruments*, 90(5):055105(1–8), 2019.

[158] C. G. De Kruif and C. H. D. Van Ginkel. Torsion-weighing effusion vapour-pressure measurements on organic compounds. *The Journal of Chemical Thermodynamics*, 9(8):725–730, 1977.

[159] J. Nishimura, T. Numata, H. Ogasawara, and Y. Sakanoue. Static method to measure vapor pressure in the temperature range below $1100k$. *Review of Scientific Instruments*, 56(12):2306–2309, 1985.

[160] T. B. Douglas and R. F. Krause Jr. Evaluation of a simple static method for measuring vapor pressure. *The Journal of Chemical Thermodynamics*, 9(6):511–522, 1977.

[161] S. Kim, W. Lee, and D. Herschbach. Cluster beam chemistry: Hydration of nucleic acid bases; ionization potentials of hydrated adenine and thymine. *The Journal of Physical Chemistry A*, 100(19):7933–7937, 1996.

[162] K. W. Choi, J. H. Lee, and S. K. Kim. Ionization spectroscopy of a DNA base: Vacuum-ultraviolet mass-analyzed threshold ionization spectroscopy of jet-cooled thymine. *Journal of the American Chemical Society*, 127(45):15674–15675, 2005.

[163] K. Khistyaev, K. B. Bravaya, E. Kamarchik, O. Kostko, M. Ahmed, and A. I. Krylov. Proton transfer in nucleobases is mediated by water. *Faraday Discussions*, 150:313–330, 2011.

[164] L. Belau, K. R. Wilson, S. R. Leone, and M. Ahmed. Vacuum-ultraviolet photoionization studies of the microhydration of DNA bases (guanine, cytosine, adenine, and thymine). *The Journal of Physical Chemistry A*, 117(31):7562–7568, 2007.

[165] K. Watanabe and Murray Zelikoff. Absorption coefficients of water vapor in the vacuum ultraviolet. *Journal of the Optical Society of America*, 43(9):753–755, 1953.

[166] J. M. Rice and G. O. Dudek. Mass spectra of nucleic acid derivatives. II. Guanine, adenine, and related compounds. *Journal of the American Chemical Society*, 89(11):2719–2725, 1966.

[167] C. Ottinger. Metastable ions in the mass spectra of propane and deuterated propanes. *The Journal of Chemical Physics*, 47(4):1452–1457, 1967.

[168] K. Gluch, E. Szot, A. Gruszecka, M. Szymańska-Chargot, J. Cytawa, and L. Michalak. Kinetic energy release and mean life time of metastable ions produced from C_3H_3N. *Vacuum*, 83(1):S20–S23, 2009.

[169] S. Feil, O. Echt, K. Gluch, V. G. Hasan, S. Matt-Leubner, T. Tepnual, V. Grill, A. Bacher, P. Scheier, and T. D. Märk. Metastable dissociation of doubly charged ions produced from toluene: Kinetic energy release upon charge separation and H_2 elimination. *Chemical Physics Letters*, 411(4-6):366–372, 2005.

[170] J. Roithová, D. Schröder, P. Gruene, T. Weiske, and H. Schwarz. Structural aspects of long-lived $C_7H_8{}^{2+}$ dications generated by the electron ionization of toluene. *The Journal of Physical Chemistry A*, 110(9):2970–2978, 2006.

[171] M. J. Frisch, G. W. Trucks, H. B. Schlegel, G. E. Scuseria, M. A. Robb, J. R. Cheeseman, G. Scalmani, V. Barone, B. Mennucci, G. A. Petersson, H. Nakatsuji, M. Caricato, X. Li, H. P. Hratchian, A. F. Izmaylov, J. Bloino, G. Zheng, J. L. Sonnenberg, M. Hada, M. Ehara, K. Toyota, R. Fukuda, J. Hasegawa, M. Ishida, T. Nakajima, Y. Honda, O. Kitao, H. Nakai, T. Vreven, J. A. Montgomery Jr., J. E. Peralta, F. Ogliaro, M. Bearpark, J. J. Heyd, E. Brothers, K. N. Kudin, V. N. Staroverov, R. Kobayashi, J. Normand, K. Raghavachari, A. Rendell, J. C. Burant, S. S. Iyengar, J. Tomasi, M. Cossi, N. Rega, J. M. Millam, M. Klene, J. E. Knox, J. B. Cross, V. Bakken, C. Adamo, J. Jaramillo, R. Gomperts, R. E. Stratmann, O. Yazyev, A. J. Austin, R. Cammi, C. Pomelli, J. W. Ochterski, R. L. Martin, K. Morokuma, V. G. Zakrzewski, G. A. Voth, P. Salvador, J. J. Dannenberg, S. Dapprich, A. D. Daniels, Ö. Farkas, J. B. Foresman, J. V. Ortiz, J. Cioslowski, and D. J. Fox. *Gaussian 09, Revision A.02*. Wallingford, 2016.

[172] M. Sodupe, A. Oliva, and J. Bertran. Theoretical study of the ionization of phenol-water and phenol-ammonia hydrogen-bonded complexes. *The Journal of Physical Chemistry A*, 101(48):9142–9151, 1997.

[173] J. Bertran, A. Oliva, L. Rodriguez-Santiago, and M. Sodupe. Single versus double proton-transfer reactions in Watson-Crick base pair radical cations. A theoretical study. *Journal of the American Chemical Society*, 120(32):8159–8167, 1998.

[174] A. Kumar and M. D. Sevilla. Influence of hydration on proton transfer in the guanine-cytosine radical cation ($G^{\bullet+}$-C) base pair: A density functional theory study. *The Journal of Physical Chemistry B*, 113(33):11359–11361, 2009.

[175] W. Y. Sohn, M. Kim, S. S. Kim, Y. D. Park, and H. Kang. Solvent-assisted conformational isomerization and the conformationally-pure REMPI spectrum of 3-aminophenol. *Physical Chemistry Chemical Physics*, 13(15):7037–7042, 2011.

[176] J. Bockova, A. Rebelo, M. Ryszka, R. Pandey, T. da Fonseca Cunha, P. Limão-Vieira, N. J. Mason, J.-C. Poully, and S. Eden. Mapping the complex metastable

fragmentation pathways of excited 3-aminophenol$^+$. *International Journal of Mass Spectrometry*, 442:95–101, 2019.

[177] S. Kanvah, J. Joseph, and G. B. Schuster. Oxidation of DNA: Damage to nucleobases. *Accounts of Chemical Research*, 43(2):280–287, 2009.

[178] M. D. Stapels, J.-C. Cho, S. J. Giovannoni, and D. F. Barofsky. Proteomic analysis of novel marine bacteria using MALDI and ESI mass spectrometry. *Journal of Biomolecular Techniques*, 15(3):191–198, 2004.

[179] B. Bothner and G. Siuzdak. Electrospray ionization of a whole virus: Analyzing mass, structure, and viability. *ChemBioChem*, 5(3):258–260, 2004.

[180] E. Forsberg, M. Fang, and G. Siuzdak. Staying alive: Measuring intact viable microbes with electrospray ionization mass spectrometry. *Journal of The American Society for Mass Spectrometry*, 28(1):14–20, 2017.

[181] S. Feil, K. Gluch, S. Matt-Leubner, P. Scheier, J. Limtrakul, M. Probst, H. Deutsch, K. Becker, A. Stamatovic, and T. D. Märk. Partial cross sections for positive and negative ion formation following electron impact on uracil. *Journal of Physics B*, 37(15):3013–3020, 2004.

[182] L. Li and D. M. Lubman. Resonance enhanced multiphoton ionisation of nucleosides by using pulsed-laser desorption in supersonic beam mass spectrometry. *International Journal of Mass Spectrometry and Ion Processes*, 88(2-3):197–210, 1989.

[183] M. S . Wilson and J. A. McCloskey. Chemical ionization mass spectrometry of nucleosides. Mechanisms of ion formation and estimations of proton affinity. *Journal of the American Chemical Society*, 97(12):3436–3444, 1975.

[184] P. O. P. Ts'o. *Basic Principles in Nucleic Acid Chemistry*. Academic Press, Inc., 1974.

[185] S. M. Hecht, A. S. Gupta, and N. J. Leonard. Mass spectra of ribonucleoside components of tRNA. II. *Analytical Biochemistry*, 38(1):230–251, 1970.

[186] A. Dasgupta and A. Wahed. *Clinical Chemistry, Immunology and Laboratory Quality Control*. Elsevier, 2014.

[187] J. Li, C. Li, and S. M. Smith. *Hormone Metabolism and Signaling in Plants*. Academic Press, 2017.

[188] H. Pang, K. H. Schram, D. L. Smith, S. P. Gupta, L. B. Townsend, and J. A. McCloskey. Mass spectrometry of nucleic acid constituents. Trimethylsilyl derivatives of nucleosides. *The Journal of Organic Chemistry*, 47(20):3923–3932, 1982.

[189] J. A. McCloskey. *Methods in Enzymology*. Academic Press, Inc., 1990.

[190] J. L. Little. Artifacts in trimethylsilyl derivatization reactions and ways to avoid them. *Journal of Chromatography A*, 844(1-2):1–22, 1999.

[191] P. Markush, P. Bolognesi, A. Cartoni, P. Rousseau, S. Maclot, R. Delaunay, A. Domaracka, J. Kocisek, M. C. Castrovilli, B. A. Huber, and L. Avaldi. The role of the environment in the ion induced fragmentation of uracil. *Physical Chemistry Chemical Physics*, 18(25):16721–16729, 2016.

[192] B. F. Minaev, M. I. Shafranyosh, Y Y. Svida, M. I. Sukhoviya, I. I. Shafranyosh, G. V. Baryshnikov, and V. A. Minaeva. Fragmentation of the adenine and guanine molecules induced by electron collisions. *The Journal of Chemical Physics*, 140(17):175101(1–15), 2014.

[193] M. V. Muftakhov and P. V. Shchukin. Resonant electron capture by uridine and deoxyuridine molecules: Fragmentation with charge transfer. *Rapid Communications in Mass Spectrometry*, 33(5):482–490, 2019.

[194] J. M. Rice and G. O. Dudek. Mass spectra of uridine and pseudouridine: Fragmentation patterns characteristic of a carbon-carbon nucleosidic bond. *Biochemical and Biophysical Research Communications*, 35(3):383–388, 1969.

[195] H. Levola, K. Koosera, E. Rachlewb, E. Nommistec, and E. Kukk. Fragmentation of thymidine induced by ultraviolet photoionization and thermal degradation. *International Journal of Mass Spectrometry*, 353:7–11, 2013.

[196] H. Levola, K. Kooser, E. Itälä, and E. Kukk. Comparison of VUV radiation induced fragmentation of thymidine and uridine nucleosides – the effect of methyl and hydroxyl groups. *International Journal of Mass Spectrometry*, 370:96–110, 2014.

[197] S. Maclot, R. Delaunay, D. G. Piekarski, A. Domaracka, B. A. Huber, L. Adoui, F. Martín, M. Alcamí, L. Avaldi, P. Bolognesi, S. Díaz-Tendero, and P. Rousseau. Determination of energy-transfer distributions in ionizing ion-molecule collisions. *Physical Review Letters*, 117(7):073201(1–6), 2016.

[198] E. Itälä, K. Kooser, E. Rachlew, H. Levola, D. T. Ha, and E. Kukk. Gas-phase study on uridine: Conformation and X-ray photofragmentation. *The Journal of Chemical Physics*, 142(19):194303–(1–8), 2015.

[199] E. Itälä, M. A. Huels, E. Rachlew, K. Kooser, T. Hägerth, and E. Kukk. A comparative study of dissociation of thymidine molecules following valence or core photoionization. *Journal of Physics B*, 46(21):215102(1–9), 2013.

[200] K. L. Wells, D. J. Hadden, M. G. D. Nix, and V. G. Stavros. Competing $\pi\sigma^\star$ states in the photodissociation of adenine. *The Journal of Physical Chemistry Letters*, 1(6):993–996, 2010.

[201] G. M. Roberts and V. G. Stavros. The role of $\pi\sigma^\star$ states in the photochemistry of heteroaromatic biomolecules and their subunits: Insights from gas-phase femtosecond spectroscopy. *Chemical Science*, 5(5):1698–1722, 2014.

[202] S. Matsika, M. Spanner, M. Kotur, and T. C. Weinacht. Ultrafast relaxation dynamics of uracil probed via strong field dissociative ionization. *Journal of Physical Chemistry A*, 117(48):12796–12801, 2013.

[203] N. L. Evans and S. Ullrich. Wavelength dependence of electronic relaxation in isolated adenine using UV femtosecond time-resolved photoelectron spectroscopy. *The Journal of Physical Chemistry*, 114(42):11225–11230, 2010.

[204] K. Kosma, Ch. Schröter, E. Samoylova, I. V. Hertel, and T. Schultz. Excited-state dynamics of cytosine tautomers. *Journal of the American Chemical Society*, 131(46):16939–16943, 2009.

[205] S. Yamazaki and T. Taketsugu. Nonradiative deactivation mechanisms of uracil, thymine, and 5-fluorouracil: A comparative ab initio study. *Journal of Physical Chemistry A*, 116(1):491–503, 2012.

[206] S. Perun and A. L. Sobolewski. Conical intersections in thymine. *Journal of Physical Chemistry A*, 110(49):13238–13244, 2006.

[207] M. Staniforth and V. G. Stavros. Recent advances in experimental techniques to probe fast excited-state dynamics in biological molecules in the gas phase: Dynamics in nucleotides, amino acids and beyond. *Proceedings of the Royal Society A*, 469(2159):20130458(1–23), 2013.

[208] K. B. Bravaya, O. Kostko, S. Dolgikh, A. Landau, M. Ahmed, and A. I. Krylov. Electronic structure and spectroscopy of nucleic acid bases: Ionization energies,

ionization-induced structural changes, and photoelectron spectra. *The Journal of Physical Chemistry A*, 114(46):12305–12317, 2010.

[209] E. Nir, Ch. Plützer, K. Kleinermanns, and M. S. de Vries. Properties of isolated DNA bases, base pairs, and nucleosides examined by laser spectroscopy. *The European Physical Journal D*, 20(3):317–329, 2002.

[210] T. Bergen, X. Biquard, A. Brenac, F. Chandezon, B. A. Huber, D. Jalabert, H. Lebius, M. Maurel, E. Monnand, J. Opitz, A. Pesnelle, B. Pras, C. Ristori, and J. C. Rocco. Multiply charged cluster ion crossed-beam apparatus: Multi-ionization of clusters by ion impact. *Review of Scientific Instruments*, 70(8):3244–3253, 1999.

[211] S. Ptasińska, S. Denifl, S. Gohlke, P. Scheier, E. Illenberger, and T. D. Märk. Decomposition of thymidine by low-energy electrons: Implications for the molecular mechanisms of single-strand breaks in DNA. *Angewandte Chemie International Edition*, 45(12):1893–1896, 2006.

[212] CAMECA. Introduction to SIMS. `https://www.cameca.com/products/sims/technique`, 2014. [Online; accessed 24-April-2019].

[213] N. B. Cech and C. G. Enke. Practical implications of some recent studies in electrospray ionization fundamentals. *Mass Spectrometry Reviews*, 20(6):362–387, 2001.

[214] I. Peña, S. Mata, A. Martín, C. Cabezas, A. M. Daly, and J. L. Alonso. Conformations of D-xylose: The pivotal role of the intramolecular hydrogen-bonding. *Physical Chemistry Chemical Physics*, 15(41):18243–18248, 2013.

[215] Z. Huang, T. Ossenbrüggen, I. Rubinsky, M. Schust, D. A. Horke, and J. Küpper. Development and characterization of a laser-induced acoustic desorption source. *Analytical Chemistry*, 90(6):3920–3927, 2018.

[216] F. W. Crow, K. B. Tomer, M. L. Gross, J. A. McCloskey, and D. E. Bergstrom. Fast atom bombardment combined with tandem mass spectrometry for the determination of nucleosides. *Analytical Chemistry*, 139(1):243–262, 1984.

[217] S. E. Unger, A. E. Schoen, R. G. Cooks, D. J. Ashworth, J. D. S. Gomes, and C. Chang. Identification of modified nucleosides by secondary-ion mass spectrometry. *The Journal of Organic Chemistry*, 46(23):4765–4769, 1981.

[218] K. H. Schram. Mass spectrometry: Applications in the analysis of nucleosides, nucleotides and oligonucleotides. *Nucleosides and Nucleotides*, 9(3):311–317, 1990.

[219] H. R. Schulten and H. D. Becke. High resolution field desorption mass spectrometry – I: Nucleosides and nucleotides. *Organic Mass Spectrometry*, 7(7):861–867, 1973.

[220] E. Dodbiba, Z. Breitbach, E. Wanigasekara, T. Payagala, X. Zhang, and D. W. Armstrong. Detection of nucleotides in positive-mode electrospray ionization mass spectrometry using multiply-charged cationic ion-pairing reagents. *Analytical and Bioanalytical Chemistry*, 398(1):367–376, 2010.

[221] A. E. Countermana, A. E. Hilderbranda, C. A. Srebalus Barnesa, and D. E. Clemmer. Formation of peptide aggregates during ESI: Size, charge, composition, and contributions to noise. *Journal of the American Society for Mass Spectrometry*, 12(9):1020–1035, 2001.

[222] S. Medhe. Ionization techniques in mass spectrometry: A review. *Mass Spectrometry and Purification Techniques*, 4(1):1–6, 2018.

[223] S. Banerjee and S. Mazumdar. Electrospray ionization mass spectrometry: A technique to access the information beyond the molecular weight of the analyte. *International Journal of Analytical Chemistry*, 2012(8):1–40, 2012.

[224] I. V. Chernushevich and B. A. Thomson. Collisional cooling of large ions in electrospray mass spectrometry. *Analytical Chemistry*, 76(6):1754–1760, 2004.

[225] F. W. McLafferty. Neutralization-reionization mass spectrometry. *International Journal of Mass Spectrometry and Ion Processes*, 118–119:221–235, 1992.

[226] J. L. Seymour, E. A. Syrstad, C. C. Langley, and F. Tureček. Neutralization–reionization of ions produced by electrospray instrument design and initial data. *International Journal of Mass Spectrometry*, 228:687–702, 2003.

[227] R. J. Levis. Laser desorption and ejection of biomolecules from the condensed phase into the gas phase. *Annual Review of Physical Chemistry*, 45(1):483–518, 1994.

[228] F. J. Vastola, A. J. Pirone, and B. E. Knox. *Proceedings of the ASTM Committee E-14*. Dalas, 1966.

[229] R. C. Beavis, J. Lindner, and J. Grotemeyer E. W. Schlag. Sample-matrix effects in infrared laser neutral desorption, multiphoton-ionization mass spectrometry. *Chemical Physics Letters*, 146(3-4):310–314, 1988.

[230] F. Piuzzi, M. Mons, I. Dimicoli, B. Tardivel, and Q. Zhao. Ultraviolet spectroscopy and tautomerism of the DNA base guanine and its hydrate formed in a supersonic jet. *Chemical Physics*, 270(1):205–214, 2001.

[231] I. Peña, C. Cabezas, and J. L. Alonso. The nucleoside uridine isolated in the gas phase. *Angewandte Chemie International Edition*, 54(10):2991–2994, 2015.

[232] M. Karas, D. Bachmann, U. Bahr, and F. Hillenkamp. Matrix-assisted ultraviolet laser desorption of non-volatile compounds. *International Journal of Mass Spectrometry and Ion Processes*, 78:53–68, 1987.

[233] R. A. Meyers. *Encyclopedia of Analytical Chemistry*. John Wiley & Sons Ltd, 2000.

[234] V. V. Golovlev, S. L. Allman, W. R. Garrett, N. I. Taranenko, and C. H. Chen. Laser-induced acoustic desorption. *International Journal of Mass Spectrometry and Ion Processes*, 169-170:69–78, 1997.

[235] A. N. Krutchinsky and B. T. Chait. On the nature of the chemical noise in MALDI mass spectra. *Journal of the American Society for Mass Spectrometry*, 13(2):129–134, 2002.

[236] M. A. Posthumus, H. L. C. Meuzelaar P. G. Kistemaker, M. C. Ten, and N. de Brauw. Laser desorption-mass spectrometry of polar nonvolatile bio-organic molecules. *Analytical Chemistry*, 50(7):985–991, 1978.

[237] M. Taherkhani, M. Riese, M. Benyezzar, and K. Müller-Dethlefs. A novel experimental system of high stability and lifetime for the laser-desorption of biomolecules. *Review of Scientific Instruments*, 81(6):063101(1–6), 2010.

[238] E. Nir, K. Kleinermanns, and M. S. de Vries. Pairing of isolated nucleic-acid bases in the absence of the DNA backbone. *Nature*, 408(6815):949–951, 2000.

[239] E. Nir, P. Imhof, K. Kleinermanns, and M. S. de Vries. REMPI spectroscopy of laser desorbed guanosines. *Journal of the American Chemical Society*, 122(33):8091–8092, 2000.

[240] B. Lindner and U. Seydel. Laser desorption mass spectrometry of nonvolatiles under shock wave conditions. *Analytical Chemistry*, 57(4):895–899, 1985.

[241] L. Belshaw, F. Calegari, M. J. Duffy, A. Trabattoni, L. Poletto, M. Nisoli, and J. B. Greenwood. Observation of ultrafast charge migration in an amino acid. *The Journal of Physical Chemistry Letters*, 3(24):3751–3754, 2012.

[242] R. C. Shea, S. C. Habicht, W. E. Vaughn, and H. I. Kenttämaa. Design and characterization of a high-power laser-induced acoustic desorption probe coupled with a Fourier transform ion cyclotron resonance mass spectrometer. *Analytical Chemistry*, 79(7):2688–2694, 2007.

[243] S. C. Habicht, L. M. Amundson, P. Duan, N. R. Vinueza, and H. I. Kenttämaa. Laser-induced acoustic desorption coupled with a linear quadrupole ion trap mass spectrometer. *Analytical Chemistry*, 82(2):608–614, 2007.

[244] W. P. Peng, Y. C. Yang, M. W. Kang, Y. K. Tzeng, Z. Nie, H. C. Chang, W. Chang, and C. H. Chen. Laser-induced acoustic desorption mass spectrometry of single bioparticles. *Angewandte Chemie International Edition*, 45(9):1423–1426, 2006.

[245] I. Bald, I. Dabkowska, and E. Illenberger. Probing biomolecules by laser-induced acoustic desorption: Electrons at near zero electron volts trigger sugar–phosphate cleavage. *Journal of the American Society for Mass Spectrometry*, 47(44):8518–8520, 2008.

[246] A. V. Zinovev, I. V. Veryovkin, J. F. Moore, and M. J. Pellin. Laser-driven acoustic desorption of organic molecules from back-irradiated solid foils. *Analytical Chemistry*, 79(21):8232–8241, 2007.

[247] Z. Huang, D. A. Horke, and J. Küpper. Laser-induced acoustic desorption of thermally stable and unstable biomolecules. *arXiv:1811.05925*, 2018.

[248] P. Arrowsmith, M. de Vries, H. Hunziker, and H. Wendt. Pulsed laser desorption near a jet orifice: Concentration profiles of entrained perylene vapor. *Applied Physics B*, 46(2):165–173, 1988.

[249] J. Kopyra, A. Kellerb, and I. Bald. On the role of fluoro-substituted nucleosides in DNA radiosensitization for tumor radiation therapy. *RSC Advances*, 4(13):6825–6829, 2014.

[250] N. S. Hush and A. S. Cheung. Ionization potentials and donor properties of nucleic acid bases and related compounds. *Chemical Physics Letters*, 34(1):11–13, 1975.

[251] D. Dougherty and S. P. McGlynn. Photoelectron spectroscopy of carbonyls. Biological molecules. *The Journal of Chemical Physics*, 67(3):1289–1290, 1977.

[252] D. Dougherty, E. S. Younathan, R. Voll, S. Abdulnur, and S. P. McGlynn. Photoelectron spectroscopy of some biological molecules. *JournaI of Electron Spectroscopy and Related Phenomena*, 13(3):379–393, 1978.

[253] J. Lin, C. Yu, S. Peng, I. Akiyama, K. Li, L. K. Lee, and P. R. LeBreton. Ultraviolet photoelectron studies of the ground-state electronic structure and gas-phase tautomerism of hypoxanthine and guanine. *The Journal of Physical Chemistry*, 84(9):1006–1012, 1980.

[254] O. Plekan, R. Richter V. Feyer, M. Coreno, M. de Simone, K. C. Prince, and V Carravetta. Photofragmentation of guanine, cytosine, leucine and methionine. *Chemical Physics*, 334(1-3):53–63, 2007.

[255] I. L. Zaytseva, A. B. Trofimov, J. Schirmer, O. Plekan, V. Feyer, R. Richter, M. Coreno, and K. C. Prince. Theoretical and experimental study of valence-shell ionization spectra of guanine. *The Journal of Physical Chemistry A*, 113(52):15142–15149, 2009.

[256] A. Ostroverkh, A. Zavilopulo, and O. Shpenik. Ionization of guanine, adenine and thymine molecules by electron impact. *The European Physical Journal D*, 73(38):1–11, 2019.

[257] J. Zhou, O. Kostko, C. Nicolas, X. Tang, L. Belau, M. S. de Vries, and M. Ahmed. Experimental observation of guanine tautomers with VUV photoionization. *The Journal of Physical Chemistry A*, 113(17):4829–4832, 2009.

[258] E. Nir, L. Grace, B. Brauer, and M. S. de Vries. REMPI spectroscopy of jet-cooled guanine. *Journal of the American Chemical Society*, 121(20):4896–4897, 1999.

[259] E. Nir, Ch. Janzen, P. Imhof, K. Kleinermanns, and M. S. de Vries. Guanine tautomerism revealed by UV–UV and IR–UV hole burning spectroscopy. *The Journal of Chemical Physics*, 115(10):4604–4611, 2001.

[260] W. Chin, M. Mons, I. Dimicoli, F. Piuzzi, B. Tardivel, and M. Elhanine. Tautomer contributions to the near UV spectrum of guanine: Towards a refined picture for the spectroscopy of purine molecules. *The European Physical Journal D*, 20(3):347–355, 2002.

[261] M. Mons, I. Dimicoli, F. Piuzzi, B. Tardivel, and M. Elhanine. Tautomerism of the DNA base guanine and its methylated derivatives as studied by gas-phase infrared and ultraviolet spectroscopy. *The Journal of Physical Chemistry A*, 106(20):5088–5094, 2002.

[262] J. L. Alonso, I. Peña, J. C. López, and V. Vaquero. Rotational spectral signatures of four tautomers of guanine. *Angewandte Chemie International Edition*, 48(33):6141–6143, 2009.

[263] K. Biemann and J. A. McCloskey. Application of mass spectrometry to structure problems. VI. Nucleosides. *Journal of the American Chemical Society*, 84(10):2005–2007, 1962.

[264] D. L. Smith, K. H. Schram, and J. A. McCloskey. The negative ion mass spectra of selected nucleosides. *Biological Mass Spectrometry*, 10(4):269–275, 1983.

[265] National Institute of Standards and Technology. Uridine. `http://webbook.nist.gov/cgi/cbook.cgi?ID=C58968&Mask=200#Mass-Spec`, 2014. [Online; accessed 01-May-2019].

[266] D. Almeida, F. Ferreira da Silva, J. Kopyra, G. García, and P. Limão-Vieira. Anion formation in gas-phase potassium–uridine collisions. *International Journal of Mass Spectrometry*, 365–366:243–247, 2014.

[267] M. V. Muftakhov and P. V. Shchukin. Resonant electron capture by uridine. *Journal of Analytical Chemistry*, 68(14):1200–1204, 2013.

[268] M. V. Muftakhov and P. V. Shchukin. Destruction of peptides and nucleosides in reactions with low-energy electrons. *Technical Physics*, 63(5):747–758, 2018.

[269] P. V. Shchukin, M. V. Muftakhov, and R. V. Khatymov. Dissociative capture of thermal electrons by ribose and deoxyribose. *Mass-Spektrometriya*, 10(3):158–166, 2013.

[270] C. Meola, S. Boccardi, and G. Carlomagno. *Infrared Thermography in the Evaluation of Aerospace Composite Materials*. Woodhead Publishing, 2016.

[271] P. Cheng, Y. Li, S. Li, M. Zhang, and Z. Zhou. Collision-induced dissociation (CID) of guanine radical cation in the gas phase: An experimental and computational study. *Physical Chemistry Chemical Physics*, 12(18):4667–4677, 2010.

[272] J. Leszczynski. *Computational Molecular Biology*. Elsevier, 1999.

[273] H. Sugiyama and I. Saito. Theoretical studies of gg-specific photocleavage of DNA via electron transfer: Significant lowering of ionization potential and 5'-localization of HOMO of stacked GG bases in B-form DNA. *Journal of the American Chemical Society*, 118(30):7063–7068, 1996.

[274] C. M. Marian. The guanine tautomer puzzle: Quantum chemical investigation of ground and excited states. *The Journal of Physical Chemistry A*, 111(8):1545–1553, 2007.

[275] P. Colarusso, K. Zhang, B. Guo, and P. F. Bernath. The infrared spectra of uracil, thymine, and adenine in the gas phase. *Chemical Physics Letters*, 269(1-2):39–48, 1997.

[276] R. N. Casaes, J. B. Paul, R. P. McLaughlin, R. J. Saykally, and T. van Mourik. Infrared cavity ringdown spectroscopy of jet-cooled nucleotide base clusters and water complexes. *The Journal of Physical Chemistry A*, 108(50):10989–10996, 2004.

[277] F. Inagaki, M. Tasumi, and T. Miyazawa. Structures and populations of conformers of nucleoside monophosphates in aqueous solution. I. General methods of conformation search with lanthanide-ion probes and spin-coupling constants and application to uridine-5′-monophosphate. *Biopolymers*, 17(2):267–289, 1987.

[278] T. Hajj. Seeding DNA nucleosides in supersonic beams for laser and electron irradiation experiments. Master's thesis, (based on a research internship at the Open University), Lebanese University, 2019.

[279] A. S. Chatterley, A. S. Johns, V. G. Stavros, and J. R. R. Verlet. Base-specific ionization of deprotonated nucleotides by resonance enhanced two-photon detachment. *The Journal of Physical Chemistry A*, 117(25):5299–5305, 2013.

[280] D. Strzelecka, S. Chmielinski, S. Bednarek, J. Jemielity, and J. Kowalska. Analysis of mononucleotides by tandem mass spectrometry: Investigation of fragmentation pathways for phosphate- and ribose-modified nucleotide analogues. *Scientific Reports*, 7(8931):1–12, 2017.

[281] A. M. Lesk. Why does DNA contain thymine and RNA uracil? *Journal of Theoretical Biology*, 22(3):537–540, 1969.

[282] B. K. Duncan and J. H. Miller. Mutagenic deamination of cytosine residues in DNA. *Nature*, 287(5782):560–561, 1980.

[283] H. Yu, J. A. Sanchez-Rodriguez, M. Pollum, C. E. Crespo-Hernández, S. Mai, P. Marquetand, L. Gonzálezc, and S. Ullrich. Internal conversion and intersystem crossing pathways in UV excited, isolated uracils and their implications in prebiotic chemistry. *Physical Chemistry Chemical Physics*, 18(30):20168–20176, 2016.

[284] M. Ligare, F. Siouri, O. Bludsky, D. Nachtigallová, and M. S. de Vries. Characterizing the dark state in thymine and uracil by double resonant spectroscopy and quantum computation. *Physical Chemistry Chemical Physics*, 17(37):24336–24341, 2015.

[285] M. Richter, S. Mai, P. Marquetand, and L. González. Ultrafast intersystem crossing dynamics in uracil unravelled by *ab initio* molecular dynamics. *Physical Chemistry Chemical Physics*, 16(44):24423–24436, 2014.

[286] M. Merchán, R. González-Luque, T. Climent, L. Serrano-Andrés, E. Rodríguez, M. Reguero, and D. Peláez. Unified model for the ultrafast decay of pyrimidine nucleobases. *The Journal of Physical Chemistry B*, 110(51):26471–26476, 2006.

[287] B. B. Brady, L. A. Peteanu, and D. H. Levy. The electronic spectra of the pyrimidine bases uracil and thymine in a supersonic molecular beam. *Chemical Physics Letters*, 147(6):538–543, 1988.

[288] S. Denifl, B. Sonnweber, G. Hanel, P. Scheier, and T. D. Märk. Threshold electron impact ionization studies of uracil. *International Journal of Mass Spectrometry*, 238(1):47–53, 2004.

[289] B. Coupier, B. Farizon, M. Farizon, M. J. Gaillard, F. Gobet, N. V. de Castro Faria, G. Jalbert, S. Ouaskit, M. Carré, B. Gstir, G. Hanel, S. Denifl, L. Feketeova, P. Scheier, and T. D. Märk. Inelastic interactions of protons and electrons with biologically relevant molecules. *The European Physical Journal D*, 20(3):459–468, 2002.

[290] J. Tabet, S. Eden, S. Feil, H. Abdoul-Carime, B. Farizon, M. Farizon, S. Ouaskit, and T. D. Märk. $20-150-keV$ proton-impact-induced ionization of uracil: Fragmentation ratios and branching ratios for electron capture and direct ionization. *Physical Review A*, 81(1):012711(1–10), 2010.

[291] J. de Vries, R. Hoekstra, R. Morgenstern, and T. Schlathölter. C^{q+}-induced excitation and fragmentation of uracil: Effects of the projectile electronic structure. *Journal of Physics B*, 35(21):4373–4381, 2002.

[292] M. Imhoff, Z. Deng, and M. A. Huels. Ionizing fragmentation of uracil and 5-bromouracil by electron impact in gas phase and hyperthermal Ar^+ ion irradiation in condensed phase. *International Journal of Mass Spectrometry*, 262(1-2):154–160, 2007.

[293] National Institute of Standards and Technology. Uracil. `https://webbook.nist.gov/cgi/inchi?ID=C66228&Mask=200#Mass-Spec`, 2014. [Online; accessed 12-July-2019].

[294] A. N. Zavilopulo, O. B. Shpenik, and A. N. Mylymko amd V. Yu. Shpenik. Mass spectrometry of D-ribose molecules. *International Journal of Mass Spectrometry*, 441:1–7, 2019.

[295] National Institute of Standards and Technology. D-ribose. `https://webbook.nist.gov/cgi/cbook.cgi?ID=C50691&Mask=200#Mass-Spec`, 2014. [Online; accessed 12-July-2019].

[296] L. Sadr-Arani, P. Mignon, H. Chermette, and T. Douki. Theoretical and experimental study of the fragmentation of protonated uracil. *Chemical Physics Letters*, 605-606:108–114, 2014.

[297] National Institute of Standards and Technology. D-erythro-Pentose, 2-deoxy-. `https://webbook.nist.gov/cgi/cbook.cgi?ID=C533675&Units=SI&Mask=200#Mass-Spec`, 2014. [Online; accessed 26-January-2020].

[298] H. W. Jochims, M. Schwell, J.-L. Chotin, M. Clemino, F. Dulieu, H. Baumgärtel, and S. Leach. Photoion mass spectrometry of five amino acids in the $6-22\,eV$ photon energy range. *Chemical Physics*, 298(1-3):279–297, 2004.

[299] G. Giorgi, M. Anzini, A. Cappelli, F. Corelli, and S. Vomero. Characterization and differentiation of heterocyclic isomers. Part 2*. Mass spectrometry and molecular orbital calculations on pyrrolo$[1,2-a][1,4]$benzodiazepin-4-one, -6-one, and -4,6-dione. *Journal of the American Society for Mass Spectrometry*, 7(7):653–663, 1996.

[300] M. J. Abplanalp, S. Gobi, and R. I. Kaiser. On the formation and the isomer specific detection of methylacetylene (CH_3CCH), propene (CH_3CHCH_2), cyclopropane ($c-C_3H_6$), vinylacetylene (CH_2CHCCH), and 1,3-butadiene ($CH_2CHCHCH_2$) from interstellar methane ice analogues. *Physical Chemistry Chemical Physics*, 21(10):5378–5393, 2019.

[301] M. J. Abplanalp and R. I. Kaiser. On the formation of complex organic molecules in the interstellar medium: Untangling the chemical complexity of carbon monoxide–hydrocarbon containing ice analogues exposed to ionizing radiation via a combined infrared and reflectron time-of-flight analysis. *Physical Chemistry Chemical Physics*, 21(31):16949–16980, 2019.

[302] D. Qasim, G. Fedoseev, T. Lamberts, K.-J. Chuang, J. He, S. Ioppolo, J. Kästner, and H. Linnartz. Alcohols on the rocks: Solid-state formation in a $H_3CC{\equiv}CH + OH$

cocktail under dark cloud conditions. *ACS Earth and Space Chemistry*, 3(6):986–999, 2019.

[303] R. Larralde, M. P. Robertson, and S. L. Miller. Rates of decomposition of ribose and other sugars: Implications for chemical evolution. *Proceedings of the National Academy of Sciences of Sciences of the United States of America*, 92(18):8158–8160, 1995.

[304] E. J. Cocinero, A. Lesarri, P. Écija, F. J. Basterretxea, J.-U. Grabow, J. A. Fernández, and F. Castaño. Ribose found in the gas phase. *Angewandte Chemie International Edition*, 51(13):3119 –3124, 2012.

[305] N. J. Mason, B. Nair, S. Jheeta, and E. Szymańska. Electron induced chemistry: A new frontier in astrochemistry. *Faraday Discussions*, 168:235–247, 2014.

[306] I. Bald, H. D. Flosadóttir, J. Kopyra, E. Illenberger, and O. Ingólfsson. Fragmentation of deprotonated D-ribose and D-fructose in MALDI—Comparison with dissociative electron attachment. *International Journal of Mass Spectrometry*, 280(1-3):190–197, 2009.

[307] A. Mauracher, S. Denifl, A. Aleem, N. Wendt, F. Zappa, P. Cicman, M. Probst, T. D. Märk, P. Scheier, H. D. Flosadóttir, O. Ingólfsson, and E. Illenberger. Dissociative electron attachment to gas phase glycine: Exploring the decomposition pathways by mass separation of isobaric fragment anions. *Physical Chemistry Chemical Physics*, 9(42):5680–5685, 2007.

[308] H. Abdoul-Carime, C. König-Lehmann, J. Kopyra, B. Farizon, M. Farizon, and E. Illenberger. Dissociative electron attachment to amino-acids: The case of leucine. *Chemical Physics Letters*, 477(4-6):245–248, 2009.

[309] I. Bald. *Low energy electron induced reactions in gas phase biomolecules*. PhD thesis, Freie Universität Berlin, Berlin, Germany, 2007.

[310] M. Haranczyk and M. Gutowski. Valence and dipole-bound anions of the most stable tautomers of guanine. *Journal of the American Chemical Society*, 127(2):699–706, 2005.

[311] RMI Titanium Company. TITANIUM ALLOY GUIDE. `https://www.spacematdb.com/spacemat/manudatasheets/TITANIUM%20ALLOY%20GUIDE.pdf`, 2000. [Online; accessed 30-Oct-2019].

[312] VACOM Vakuum Komponenten & Messtechnik GmbH. Materials. https://www.vacom.de/en/products/standard-components/materials, 2018. [Online; accessed 30-Oct-2019].

[313] Engineering ToolBox. Permeability. https://www.engineeringtoolbox.com/permeability-d_1923.html, 2016. [Online; accessed 30-Oct-2019].

[314] E. Szymańska Skolimowska. *Dissociative electron attachment and dipolar dissociation processes in organic molecules found in the interstellar medium*. PhD thesis, The Open University, Milton Keynes, United Kingdom, 2014.

[315] D. Nandi, V. S. Prabhudesai, E. Krishnakumar, and A. Chatterjee. Velocity slice imaging for dissociative electron attachment. *Review of Scientific Instruments*, 76(5):053107(1–8), 2005.

[316] National Institute of Standards and Technology. Methyl alcohol. https://webbook.nist.gov/cgi/cbook.cgi?ID=C67561&Mask=200#Mass-Spec, 2018. [Online; accessed 03-November-2019].

[317] U. Buck and F. Huisken. Infrared spectroscopy of size-selected water and methanol clusters. *Chemical Reviews*, 100(11):3863–3890, 2000.

[318] T. H. Dunning. Gaussian basis sets for use in correlated molecular calculations. I. The atoms boron through neon and hydrogen. *The Journal of Chemical Physics*, 90(2):1007–1023, 1989.

[319] Y. Zhao, N. E. Schultz, and D. G. Truhlar. Functional with broad accuracy for metallic and nonmetallic compounds, kinetics, and noncovalent interactions. *The Journal of Chemical Physics*, 123(16):161103(1–4), 2005.

[320] D. Bakowies. Assessment of density functional theory for thermochemical approaches based on bond separation reactions. *The Journal of Physical Chemistry A*, 117(1):228–243, 2013.

Appendix A

Matlab scripts for the analysis of metastable dissociation data

A.1 Matlab script for visualisation of experimental data

```
%% Import data from spreadsheet
% Script for importing data from the following spreadsheet:
%
%    Workbook: /.../Directory/.../data_metastable.xlsx,
%    Worksheet: Sheet1.

%% Import the data
[~, ~, raw] = xlsread('/.../Directory/.../data_metastable.xlsx','Sheet1');
% ".../Directory/..." specifies the path to the MS Excel workbook
% "data_metastable.xlsx".

raw = raw(G_i:G_f,b_i:b_f); % Specifies range of the data we want to plot,
% i.e. raws "G_i" to "G_f" and comlumns "b_i" to "b_f".
raw(cellfun(@(x) ~isempty(x) && isnumeric(x) && isnan(x),raw)) = {''};

%% Replace non-numeric cells with NaN
R = cellfun(@(x) ~isnumeric(x) && ~islogical(x),raw); % Find non-numeric cells.
raw(R) = {NaN}; % Replace non-numeric cells.

%% Create output variable
datametastable = reshape([raw{:}],size(raw));
% "datametastable" is the matrix of data imported from MS Excel workbook
% "data_metastable.xlsx".

%% Clear temporary variables
clearvars raw R;
```

Fig. A.1: Matlab script *"import_data.m"* for importing experimental data (commands are in black and magenta, the explanation of individual commands is in green).

```
%% Create a contour plot of imported data
% Script for creating a contour plot of the matrix "datametastable":

X = linspace(b_i, b_f, n); % Generates n points, where the spacing between the points is
    % (b_f - b_i)/(n); where:
    % [b_i; b_f] is the range of the time bins we want to plot,
    % n is the number of data points between b_i and b_f (equals to number of columns
    % in the matrix "datametastable").
Y = linspace(G_i, G_f, m); % Generates m points, where the spacing between the points is
    % (G_f - G_i)/(m); where:
    % [G_i; G_f] is the range of reflection voltages we want to plot,
    % "m" is the number of data points between G_i and G_f (equals to number of rows
    % in the matrix "datametastable").

contour(X, Y, datametastable, l) % Plots a contour plot of matrix "datametastable", where:
    % - "X" and "Y" are the coordinates for the values in "datametastable",
    % - the contour lines are displayed at "l" automatically chosen levels (heights).
```

```
%% Contour plot design
caxis([c_i, c_f]) % Sets colourmap limits.

set(gca,'FontSize',28); % Sets fontsize "28" in the contour plot.
set(gca,'box','off') % Remove border line around the plot.
set(gca,'TickDir','out'); % Tick marks to be on the outside of the plot.

xticks([b_1 b_2 b_3 b_4 b_5 b_6]); % Specifies x-axis tick values.
xticklabels({'t_1', 't_2', 't_3', 't_4', 't_5', 't_6'}) % Specifies x-axis tick labels.
yticks([G1 G2 G3]); % Specifies y-axis tick values.
yticklabels({'-G1', '-G2', '-G3'}) % Specifies y-axis tick labels.
xlabel('Time (ns)', 'FontSize', 32) % Labels x-axis and sets the fontsize "32"
                                    % for the label.
ylabel('Reflection voltage (V)', 'FontSize',32) % Labels y-axis and sets
                                                % the fontsize "32" for the label.

    % Contour plot colour settings
    set(gcf, 'Color', 'w')
set(gca,'Color','b',...
        'XColor','k',...
        'YColor','k')
     colormap(jet);

    % Colourmap legend
     h = colorbar;
set(h, 'ylim', [c_i, c_f]); % Sets colourbar limits.
colorbar('Ticks',[c_1, c_2, c_3, c_f],...  % Specifies colourbar tick values.
         'TickLabels',{'c_1','c_2','c_3', '\geq c_f'})  % Specifies colourbar
                                                        % tick labels.
```

Fig. A.2: Matlab script *"contour_plot.m"* for creating a contour plot from the matrix of experimental data imported using a script in Fig. A.1 (commands are in black, blue and magenta, the explanation of individual commands is in green).

A.2 Matlab script for simulation of metastable dissociations

```
%% Create a scatter plot of candidate dissociations

timebin = 32; % Specifies the size of time bins in the experimental data,
              % i.e. each time bin corresponds to 32 ns.

%% Candidate metastable ion characteristics
% First estimate precursor and product ion masses of candidate metastable dissociations.

% First band
for mass1 = 109 % Parent ion mass [amu].
    mass2 = 42; % Intermediate ion mass [amu],
                % i.e. mass of ion before entering the FFR.
    mass3 = 16; % Detected ion mass [amu].
    k = (V_FrM_1 - G_i)/step; % Specifies the number of iterations,
    % i.e. the number of different reflection voltages for which we calculate
    % the flight-time of this particular candidate dissociation.
    % "V_FrM_1" is the cut-off voltage of the first fragment ion resulting
    % from metastable dissociation,
    % G_i is the lowest absolute value of reflection volatage that
    % we want to inlcude in the metastable dissociation map.
in_FFR_for_loop % The calculation of the flight-times is done
% by "in_FFR_for_loop.m" Matlab script.
end

band = ttotalns_3; % The total flight-time calculated by "in_FFR_for_loop" script.
length = (V_FrM_1 - G_i)/step; % Specifies the number of data points we want to plot
                               % (in this case the same as the number of iterations).
scatter(band(1:length)/timebin,V6(1:length), '.', 'r'); hold on; % Creates a scatter
% plot with red data points at the locations specified by the vectors
% "band(1:length)/timebin" and  "V6(1:length)". The total flight-time is divided
% by the size of time bins used in experiments in order to get the same units
% for the comparison with the experimental contour plot.

% Second band
for mass1 = 109 % Parent ion mass [amu].
    mass2 = 53; % Intermediate ion mass [amu],
                % i.e. mass of ion before entering FFR.
    mass3 = 27; % Detected ion mass [amu].
    k = (V_FrM_2 - G_i)/step; % Specifies the number of iterations,
    % i.e. the number of different reflection voltages for which we calculate
    %the flight-time of this particular candidate dissociation.
    % "V_FrM_2" is the cut-off voltage of the second metastable fragment ion resulting
    % from metastable dissociation
    % G_i is the lowest absolute value of reflection volatage that
    % we want to inlcude in the 2D map.
in_FFR_for_loop % The calculation of the flight-times is done
% by "in_FFR_for_loop.m" Matlab script.
end

band = ttotalns_3; % The total flight-time calculated by "in_FFR_for_loop" script.
length = (V_FrM_2 - G_i)/step; % Specifies the number of data points we want to plot
                               % (in this case the same as the number of iterations).
scatter(band(1:length)/timebin,V6(1:length), '.', 'r'); hold on; % Creates a scatter
% plot with red data points at the locations specified by the vectors
% "band(1:length)/timebin" and "V6(1:length)". The total flight-time is divided
% by the size of time bins used in experiments in order to get the same units
% for the comparison with the experimental contour plot.

% Etc.
```

Fig. A.3: Matlab script *"results.m"* for creating a scatter plot of flight-times at different reflection voltages for candidate dissociations (commands are in black, blue and magenta, the explanation of individual commands is in green).

```
%% Scatter plot design
% Scatter plot colour settings
set(gcf, 'Color', 'w')
set(gca,'Color','b',...
        'XColor','k',...
        'YColor','k')

axis([b_i b_f G_i G_f]) % Defines the rage of x and y axes we want to plot
                        % (the same as in experimental contour plot).

xticks([b_1 b_2 b_3 b_4 b_5 b_6]); % Specifies x-axis tick values.
xticklabels({'t_1','t_2','t_3','t_4','t_5','t_6'}) % Specifies x-axis tick labels.

yticks([G1 G2 G3]); % Specifies y-axis tick values.
yticklabels({'-G1', '-G2','-G3'}) % Specifies y-axis tick labels.

xlabel('Time (ns)') % Labels x-axis.
ylabel('Reflection voltage [V]') % Labels y-axis.
```

Fig. A.4: Matlab script *"results.m"* for creating a scatter plot of flight-times at different reflection voltages for candidate dissociations (commands are in black, blue and magenta, the explanation of individual commands is in green); continued.

```
%% For loop to calculate flight-times at "k" different values of reflection volatge with the step of 10 V

for i = 1:k
    step = 10; % Specifies the reflection voltage difference between two successive calculated data points.
    V6(i) = G_i+i*step; % "V6(i)" is the absolute value of reflection voltage at i-th step of calculation,
                        % G_i is the lowest absolute value of reflection volatage we want to inlcude in the map.

%% Distances within mass spectrometer (distances are a trade seceret of Kore Technology)
z1 = ...; % From ion source backplate to ion production [m].
d1 = ...; % From ion source backplate to extraction electrode [m].
d2 = ...; % From extraction electrode to focusing electrode [m].
d3 = ...; % From focusing electrode to ion source FFR electrode [m].
d4 = ...; % From first FFR electrode to second FFR electrode [m].
d5 = ...; % From second FFR electrode to reflectron retard electrode [m].
d6 = ...; % From reflectron retard electrode to reflectron reflect electrode [m].
d7 = ...; % From second FFR electrode to FFR electrode in front of the detector [m].
d8 = ...; % From FFR electrode in front of the detector to the detector [m].
d_add = ...; % Additional distance within the detector [m].

%% Mass spectrometer voltages

% All of the MS voltages are negative. The calculations below use their absolute values.

V1 = 0; % Absolute value of ion source backplate volatge [V].
V2 = 380; % Absolute value of extraction electrode voltage [V].
V3 = 1143; % Absolute value of focusing electrode voltage [V].
V4 = 2040; % Absolute value of field-free region voltage [V].
V7 = 5000; % Absolute value of post-acceleration voltage [V].
```

Fig. A.5: Matlab script *"in_ffr_for_loop.m"* for the calculation of total time ions spend in reflectron MS (commands are in black and blue, the explanation of individual commands is in green).

```
%% Correction for the changes in reflectron retard voltage with the changes in reflection voltage

% As reflectron retard and reflection voltage are supplied by a voltage divider unit which contains a resistor chain,
% a big change in the reflection voltage will result in a change in reflectron retard voltage
% (e.g. 50 V change in the reflection voltage will result in up to 0.15% change of the refectron retard voltage).
% Different outputs have to be used to supply reflection voltage between
% <-700 V; 0V> and <-700 V; -1200V> and thus two differenet correction functions have to be used:

if i <= 70
    % Reflectron retard voltage as a function of reflection voltage when the reflection voltage is in the range <-700 V; 0V>.
    V5(i) = f_1(V6(i)); % Specify function "f_1".
else % Reflectron retard voltage as a function of reflection voltage when the reflection voltage is in the range <-1200V; -700 V>.
    V5(i) = f_2(V6(i)); % Specify function "f_2".
end

charge1 = 1; % Charge of parent ion [au].
charge2 = 1; % Charge of intermediate ion [au].
charge3 = 1; % Charge of detected ion [au].

% Ion characteristics [SI units]
mass1kg = mass1*(1.673*10^-27); % Mass of parent ion [kg].
mass2kg = mass2*(1.673*10^-27); % Mass of intermediate ion [kg].
mass3kg = mass3*(1.673*10^-27); % Mass of detected ion [kg].
```

Fig. A.6: Matlab script *"in_ffr_for_loop.m"* for the calculation of total time ions spend in reflectron MS (commands are in black and blue, the explanation of individual commands is in green); continued.

```
%% Calculation of time-of-flight at different stages of reflectron TOF-MS

% Calculated field strengths
EZ1_1 = (V2-V1)/(d1); % Extraction field [Vm-1].
EZ1_2 = (V2-V1)/(d1); % Extraction field [Vm-1].
EZ1_3 = (V2-V1)/(d1); % Extraction field [Vm-1].

EZ2_1 = (V3-V2)/d2; % Extraction electrode to focusing electrode [Vm-1].
EZ2_2 = (V3-V2)/d2; % Extraction electrode to focusing electrode [Vm-1].
EZ2_3 = (V3-V2)/d2; % Extraction electrode to focusing electrode [Vm-1].

EZ3_1 = (V4-V3)/d3; % Focusing electrode to FFR [Vm-1].
EZ3_2 = (V4-V3)/d3; % Focusing electrode to FFR [Vm-1].
EZ3_3 = (V4-V3)/d3; % Focusing electrode to FFR [Vm-1].

EZ4_1 = (V5(i)-V4)/d5; % FFR to reflectron retard [Vm-1].
EZ4_2 = (V5(i)-V4)/d5; % FFR to reflectron retard [Vm-1].
EZ4_3 = (V5(i)-V4)/d5; % FFR to reflectron retard [Vm-1].

EZ5_1(i) = (V6(i)-V5(i))/d6; % Reflectron retard to reflect [Vm-1].
EZ5_2(i) = (V6(i)-V5(i))/d6; % Reflectron retard to reflect [Vm-1].
EZ5_3(i) = (V6(i)-V5(i))/d6; % Reflectron retard to reflect [Vm-1].

EZ6_1 = (V7-V4)/d8; % Second FFR grid to detector [Vm-1].
EZ6_2 = (V7-V4)/d8; % Second FFR grid to detector [Vm-1].
EZ6_3 = (V7-V4)/d8; % Second FFR grid to detector [Vm-1].
```

Fig. A.7: Matlab script *"in_ffr_for_loop.m"* for the calculation of total time ions spend in reflectron MS (commands are in black, the explanation of individual commands is in green); continued.

```
% Calculated ion time in extraction field
AEZ1_1 = (EZ1_1*charge1*(1.602*10^-19))/mass1kg; % Acceleration [ms-2].
AEZ1_2 = (EZ1_2*charge2*(1.602*10^-19))/mass2kg; % Acceleration [ms-2].
AEZ1_3 = (EZ1_3*charge3*(1.602*10^-19))/mass3kg; % Acceleration [ms-2].

vzfEZ1_1 = ((vinitial1z^2)+(2*AEZ1_1*((d1-zi))))^0.5; % z velocity after acceleration [ms-1].
vzfEZ1_2 = ((vinitial2z^2)+(2*AEZ1_2*((d1-zi))))^0.5; % z velocity after acceleration [ms-1].
vzfEZ1_3 = ((vinitial3z^2)+(2*AEZ1_3*((d1-zi))))^0.5; % z velocity after acceleration [ms-1].

% Solved at^2+bt+c=0
a1_1 = 0.5*AEZ1_1; % a
a1_2 = 0.5*AEZ1_2; % a
a1_3 = 0.5*AEZ1_3; % a

b1_1 = vinitial1z; % b
b1_2 = vinitial2z; % b
b1_3 = vinitial3z; % b

c1_1 = (-1)*(d1-zi); % c
c1_2 = (-1)*(d1-zi); % c
c1_3 = (-1)*(d1-zi); % c

tZ1_1 = ((-b1_1)+((((b1_1)^2)-(4*a1_1*c1_1))^0.5))/(2*a1_1); % Time travelling in field for parent ion [s].
tZ1_2 = ((-b1_2)+((((b1_2)^2)-(4*a1_2*c1_2))^0.5))/(2*a1_2); % Time travelling in field for intermediate ion [s].
tZ1_3 = ((-b1_3)+((((b1_3)^2)-(4*a1_3*c1_3))^0.5))/(2*a1_3); % Time travelling in field for detected ion [s].
```

Fig. A.8: Matlab script *"in_ffr_for_loop.m"* for the calculation of total time ions spend in reflectron MS (commands are in black, the explanation of individual commands is in green); continued.

```
% Calculated ion time between extraction electrode and focusing electrode
AEZ2_1 = (EZ2_1*charge1*(1.602*10^-19))/mass1kg; % Acceleration [ms-2].
AEZ2_2 = (EZ2_2*charge2*(1.602*10^-19))/mass2kg; % Acceleration [ms-2].
AEZ2_3 = (EZ2_3*charge3*(1.602*10^-19))/mass3kg; % Acceleration [ms-2].

vzfEZ2_1 = ((vzfEZ1_1^2)+(2*AEZ2_1*d2))^0.5; % z velocity after acceleration [ms-1].
vzfEZ2_2 = ((vzfEZ1_2^2)+(2*AEZ2_2*d2))^0.5; % z velocity after acceleration [ms-1].
vzfEZ2_3 = ((vzfEZ1_3^2)+(2*AEZ2_3*d2))^0.5; % z velocity after acceleration [ms-1].

% Solved at^2+bt+c=0
a2_1 = 0.5*AEZ2_1; % a
a2_2 = 0.5*AEZ2_2; % a
a2_3 = 0.5*AEZ2_3; % a

b2_1 = vzfEZ1_1; % b
b2_2 = vzfEZ1_2; % b
b2_3 = vzfEZ1_3; % b

c2_1 = (-1)*(d2); % c
c2_2 = (-1)*(d2); % c
c2_3 = (-1)*(d2); % c

tZ2_1 = ((-b2_1)+((((b2_1)^2)-(4*a2_1*c2_1))^0.5))/(2*a2_1); % Time travelling in field for parent ion [s].
tZ2_2 = ((-b2_2)+((((b2_2)^2)-(4*a2_2*c2_2))^0.5))/(2*a2_2); % Time travelling in field for intermediate ion [s].
tZ2_3 = ((-b2_3)+((((b2_3)^2)-(4*a2_3*c2_3))^0.5))/(2*a2_3); % Time travelling in field for detected ion [s].
```

Fig. A.9: Matlab script *"in_ffr_for_loop.m"* for the calculation of total time ions spend in reflectron MS (commands are in black, the explanation of individual commands is in green); continued.

```
% Calculated ion time between focusing electrode and first FFR electrode
AEZ3_1 = (EZ3_1*charge1*(1.602*10^-19))/mass1kg; % Acceleration [ms-2].
AEZ3_2 = (EZ3_2*charge2*(1.602*10^-19))/mass2kg; % Acceleration [ms-2].
AEZ3_3 = (EZ3_3*charge3*(1.602*10^-19))/mass3kg; % Acceleration [ms-2].

vzfEZ3_1 = ((vzfEZ2_1^2)+(2*AEZ3_1*d3))^0.5; % z velocity after acceleration [ms-1].
vzfEZ3_2 = ((vzfEZ2_2^2)+(2*AEZ3_2*d3))^0.5; % z velocity after acceleration [ms-1].
vzfEZ3_3 = ((vzfEZ2_3^2)+(2*AEZ3_3*d3))^0.5; % z velocity after acceleration [ms-1].

% Solved at^2+bt+c=0
a3_1 = 0.5*AEZ3_1; % a
a3_2 = 0.5*AEZ3_2; % a
a3_3 = 0.5*AEZ3_3; % a

b3_1 = vzfEZ2_1; % b
b3_2 = vzfEZ2_2; % b
b3_3 = vzfEZ2_3; % b

c3_1 = (-1)*(d3); % c
c3_2 = (-1)*(d3); % c
c3_3 = (-1)*(d3); % c

tZ3_1 = ((-b3_1)+((((b3_1)^2)-(4*a3_1*c3_1))^0.5))/(2*a3_1); % Time travelling in field for parent ion [s].
tZ3_2 = ((-b3_2)+((((b3_2)^2)-(4*a3_2*c3_2))^0.5))/(2*a3_2); % Time travelling in field for intermediate ion [s].
tZ3_3 = ((-b3_3)+((((b3_3)^2)-(4*a3_3*c3_3))^0.5))/(2*a3_3); % Time travelling in field for detected ion [s].


% FFR time - first direction
tZdrift1_1 = d4/vzfEZ3_1; % Time travelling in FFR (first time) for parent ion [s].
tZdrift1_2 = d4/vzfEZ3_2; % Time travelling in FFR (first time) for intermediate ion [s].
tZdrift1_3 = d4/vzfEZ3_2; % Time travelling in FFR (first time) for detected ion [s].
```

Fig. A.10: Matlab script *"in_ffr_for_loop.m"* for the calculation of total time ions spend in reflectron MS (commands are in black, the explanation of individual commands is in green); continued.

```
% Calculated ion time between second FFR electrode and reflectron retard
AEZ3a_1 = (EZ4_1*charge1*(1.602*10^-19))/mass1kg; % Acceleration [ms-2].
AEZ3a_2 = (EZ4_2*charge2*(1.602*10^-19))/mass2kg; % Acceleration [ms-2].
AEZ3a_3 = (EZ4_3*charge3*(1.602*10^-19))/mass3kg; % Acceleration [ms-2].

vzfEZ3a_1 = ((vzfEZ3_1^2)+(2*AEZ3a_1*d5))^0.5; % z velocity after acceleration [ms-1].
vzfEZ3a_2 = ((vzfEZ3_2^2)+(2*AEZ3a_2*d5))^0.5; % z velocity after acceleration [ms-1].
vzfEZ3a_3 = ((vzfEZ3_2^2)+(2*AEZ3a_3*d5))^0.5; % z velocity after acceleration [ms-1].

% Solved at^2+bt+c=0
a3a_1 = 0.5*AEZ3a_1; %a
a3a_2 = 0.5*AEZ3a_2; %a
a3a_3 = 0.5*AEZ3a_3; %a

b3a_1 = vzfEZ3_1; %b
b3a_2 = vzfEZ3_2; %b
b3a_3 = vzfEZ3_2; %b

c3a_1 = (-1)*(d5); %c
c3a_2 = (-1)*(d5); %c
c3a_3 = (-1)*(d5); %c

tZ3a_1 = ((-b3a_1)+((((b3a_1)^2)-(4*a3a_1*c3a_1))^0.5))/(2*a3a_1); % Time travelling in field for parent ion [s].
tZ3a_2 = ((-b3a_2)+((((b3a_2)^2)-(4*a3a_2*c3a_2))^0.5))/(2*a3a_2); % Time travelling in field for intermediate ion [s].
tZ3a_3 = ((-b3a_3)+((((b3a_3)^2)-(4*a3a_3*c3a_3))^0.5))/(2*a3a_3); % Time travelling in field for detected ion [s].
```

Fig. A.11: Matlab script *"in_ffr_for_loop.m"* for the calculation of total time ions spend in reflectron MS (commands are in black, the explanation of individual commands is in green); continued.

```
% Calculating ion time between reflectron retard and v=0
AEZ4_1(i) = (EZ5_1(i)*charge1*(1.602*10^-19))/mass1kg; % Acceleration [ms-2].
AEZ4_2(i) = (EZ5_2(i)*charge2*(1.602*10^-19))/mass2kg; % Acceleration [ms-2].
AEZ4_3(i) = (EZ5_3(i)*charge3*(1.602*10^-19))/mass3kg; % Acceleration [ms-2].

DPPR_1(i) = ((vzfEZ3a_1)^2)/((-2)*AEZ4_1(i)); % Distance penetrated past retard for parent ion [m].
DPPR_2(i) = ((vzfEZ3a_2)^2)/((-2)*AEZ4_2(i)); % Distance penetrated past retard for intermediate ion [m].
DPPR_3(i) = ((vzfEZ3a_3)^2)/((-2)*AEZ4_3(i)); % Distance penetrated past retard for detected ion [m].

% Solved at^2+bt+c=0
a4_1(i) = 0.5*AEZ4_1(i); %a
a4_2(i) = 0.5*AEZ4_2(i); %a
a4_3(i) = 0.5*AEZ4_3(i); %a

b4_1 = vzfEZ3a_1; %b
b4_2 = vzfEZ3a_2; %b
b4_3 = vzfEZ3a_3; %b

c4_1(i) = (-1)*(DPPR_1(i)); %c
c4_2(i) = (-1)*(DPPR_2(i)); %c
c4_3(i) = (-1)*(DPPR_3(i)); %c

tZ4_1(i) = -vzfEZ3a_1/AEZ4_1(i); % Time slowing in field [s].
tZ4_2(i) = -vzfEZ3a_2/AEZ4_2(i); % Time slowing in field [s].
tZ4_3(i) = -vzfEZ3a_3/AEZ4_3(i); % Time slowing in field [s].


% FFR time - second direction
tZdrift2_1 = d7/vzfEZ3_1; % Time in FFR (second time) for parent ion [s].
tZdrift2_2 = d7/vzfEZ3_2; % Time in FFR (second time) for intermediate ion [s].
tZdrift2_3 = d7/vzfEZ3_2; % Time in FFR (second time) for detected ion [s].
```

Fig. A.12: Matlab script *"in_ffr_for_loop.m"* for the calculation of total time ions spend in reflectron MS (commands are in black, the explanation of individual commands is in green); continued.

```
% Calculated ion time between grid at end of FFR and the detector
AEZ3b_1 = (EZ6_1*charge1*(1.602*10^-19))/mass1kg; % Acceleration [ms-2].
AEZ3b_2 = (EZ6_2*charge2*(1.602*10^-19))/mass2kg; % Acceleration [ms-2].
AEZ3b_3 = (EZ6_3*charge3*(1.602*10^-19))/mass3kg; % Acceleration [ms-2].

vzfEZ3b_1 = ((vzfEZ3_1^2)+(2*AEZ3b_1*d8))^0.5; % z velocity after acceleration [ms-1].
vzfEZ3b_2 = ((vzfEZ3_2^2)+(2*AEZ3b_2*d8))^0.5; % z velocity after acceleration [ms-1].
vzfEZ3b_3 = ((vzfEZ3_2^2)+(2*AEZ3b_3*d8))^0.5; % z velocity after acceleration [ms-1].

% Solved at^2+bt+c=0
a3b_1 = 0.5*AEZ3b_1; % a
a3b_2 = 0.5*AEZ3b_2; % a
a3b_3 = 0.5*AEZ3b_3; % a

b3b_1 = vzfEZ3_1; % b
b3b_2 = vzfEZ3_2; % b
b3b_3 = vzfEZ3_2; % b

c3b_1 = (-1)*(d8); % c
c3b_2 = (-1)*(d8); % c
c3b_3 = (-1)*(d8); % c

tZ3b_1 = ((-b3b_1)+((((b3b_1)^2)-(4*a3b_1*c3b_1))^0.5))/(2*a3b_1); % Time accelerating in field for parent ion [s].
tZ3b_2 = ((-b3b_2)+((((b3b_2)^2)-(4*a3b_2*c3b_2))^0.5))/(2*a3b_2); % Time accelerating in field for intermediate ion [s].
tZ3b_3 = ((-b3b_3)+((((b3b_3)^2)-(4*a3b_3*c3b_3))^0.5))/(2*a3b_3); % Time accelerating in field for detected ion [s].
```

Fig. A.13: Matlab script *"in_ffr_for_loop.m"* for the calculation of total time ions spend in reflectron MS (commands are in black, the explanation of individual commands is in green); continued.

```
% Total TOF in microseconds the ions spend before reaching the detector
ttotalus_1(i) = (tZdrift2_1+(2*tZ4_1(i))+(2*tZ3a_1)+tZdrift1_1+tZ3_1+tZ2_1+tZ1_1+tZ3b_1)*(1000000); % For parent ion [us].
ttotalus_2(i) = (tZdrift2_2+(2*tZ4_2(i))+(2*tZ3a_2)+tZdrift1_2+tZ3_2+tZ2_2+tZ1_2+tZ3b_2)*(1000000); % For intermediate ion [us].
ttotalus_3(i) = (tZdrift2_3+(2*tZ4_3(i))+(2*tZ3a_3)+tZdrift1_3+tZ3_2+tZ2_2+tZ1_2+tZ3b_3)*(1000000); % For detected ion [us].

% t_add - the extra time ions spend in the detector
t_add_1 = (d_add/vzfEZ3b_1)*10^9; % Additional time parent ion spends in the detector [ns].
t_add_2 = (d_add/vzfEZ3b_2)*10^9; % Additional time intermediate ion spends in the detector [ns].
t_add_3 = (d_add/vzfEZ3b_3)*10^9; % Additional time detected ion spends in the detector [ns].


% Total TOF in nanoseconds
ttotalns_1(i)=(ttotalus_1(i)*1000)+t_add_1+t_const; % Total time for parent ion [ns].
ttotalns_2(i)=(ttotalus_2(i)*1000)+t_add_2+t_const; % Total time for intermediate ion [ns].
ttotalns_3(i)=(ttotalus_3(i)*1000)+t_add_3+t_const; % Total time for detected ion [ns].
end


%Results
V6;
ttotalns_3;
```

Fig. A.14: Matlab script *"in_ffr_for_loop.m"* for the calculation of total time ions spend in reflectron MS (commands are in black and blue, the explanation of individual commands is in green); continued.

A.3 Matlab script for the superposition of experimental and simulated *maps*

```
%% Superposition of experimental and simulated maps

trial_contour; % Experimental contour plot.
hold on;
results; % Simulated scatter plot.
```

Fig. A.15: Matlab script *"superimpose.m"* for the superposition of the experimental contour plot created by *"contour_plot.m"*, see Appendix A.1, and the simulated scatter plot created by *"results.m"* and *"in_ffr_for_loop.m"*, see Appendix A.2, (commands are in black and magenta, the explanation of individual commands is in green).

Appendix B

DFT optimisations of selected uridine isomers and possible pairs of dissociation products

As a starting point for subsequent calculations of neutral ground-state energy barriers and optimised structure and energy of dissociation product pairs, A. Rebelo, PhD student in the Molecular Clusters Laboratory at the OU, ran DFT optimisations of structures at $0\,K$ with input geometries close to those of the lowest-energy isomers of uridine that had been reported in the literature [67, 68, 231]. All the energies reported below have been calculated at $0\,K$ and have not been corrected by the vibrational zero-point energy. The absence of negative frequencies was checked to ensure that the optimised structures are indeed energy minima and not saddle points. The Minessota functional $M05$ [318] and the Dunning's double zeta basis set [319] augmented with diffuse functions ($M05/aug-cc-pVDZ$) were used throughout the calculations. The combination of this functional with this basis set shows good performance in estimating atomisation energies and heats of formation [320]. A restricted formalism was employed for closed-shell species whereas open-shell species (radicals) were described by unrestricted wavefunctions. The spin contamination of radicals was monitored to avoid inclusion of higher spin states in the wavefunction. The maximum value was 0.7506, meaning that the wavefunctions are mostly free from contamination and hence suitable to use in the calculations. All the calculations were performed using the default algorithms of Gaussian 09 [171].

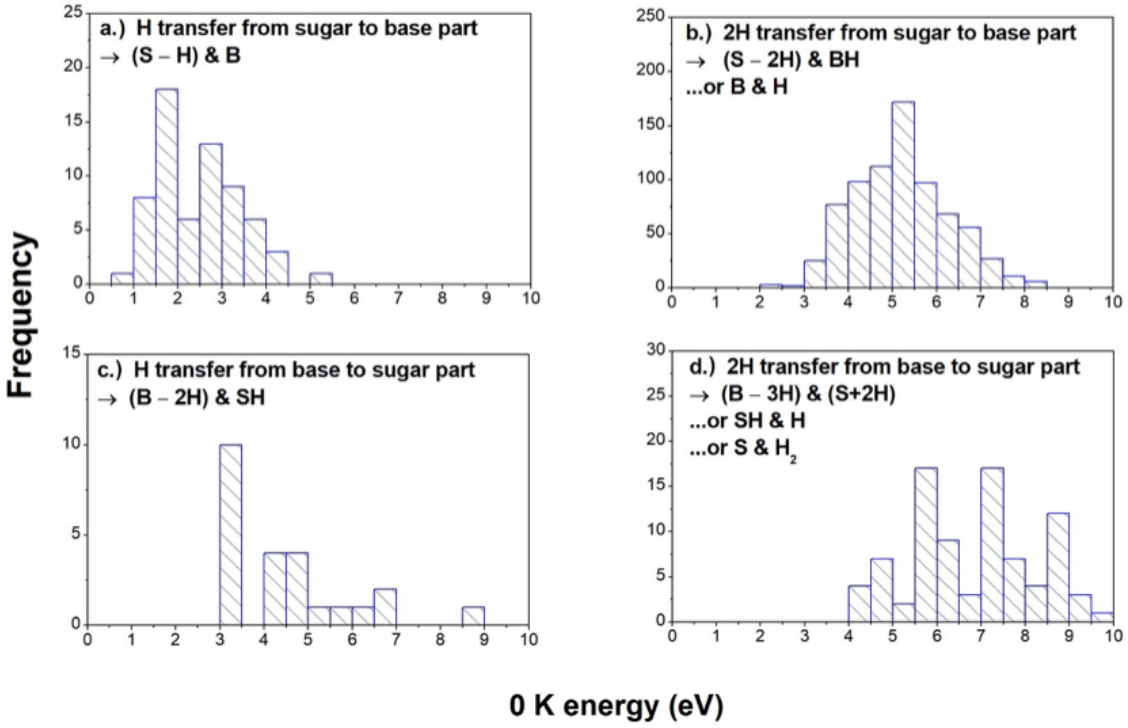

Fig. B.1: Histograms showing energy differences between *conformer 1* of uridine and the summed energies of optimised product-pairs that can be produced by glycosidic bond cleavage of uridine. The histograms are grouped according to the number of hydrogens transferred from the molecule's sugar part (S, 133 amu) to its base part ((B–H), 111 amu) or vice versa. The dissociation products are noted on the panels using the nomenclature described in Section 5.2.4.

Fig. B.1 shows that by-far the lowest-energy calculated product-pairs of glycosidic bond cleavage are produced by single hydrogen transfer from the sugar to the base part of uridine. The resulting lowest-energy optimised B and $(S-H)$ pair is shown schematically in Fig. B.2 and has 0.63 eV greater energy than *conformer 1*, as noted in Section 6.3.1. Fig. B.1 shows multiple energies corresponding to product-pairs whose optimisations began with different possible hydrogen transfers during glycosidic bond cleavage. By contrast, only a single optimisation of the S and $B-H$ product-pair was carried out with the assumption that these are produced by a simple cleavage of the glyosidic bond without any reciprocal hydrogen transfers. The resultant optimised S and $(B-H)$ pair has 3.61 eV greater energy than *conformer 1* and is shown schematically in Fig. B.2 b). This large minimum energy difference appears to be broadly consistent with the experimental evidence in Section 6.3.2 that the observed m/z133 ions are not caused by thermal decomposition.

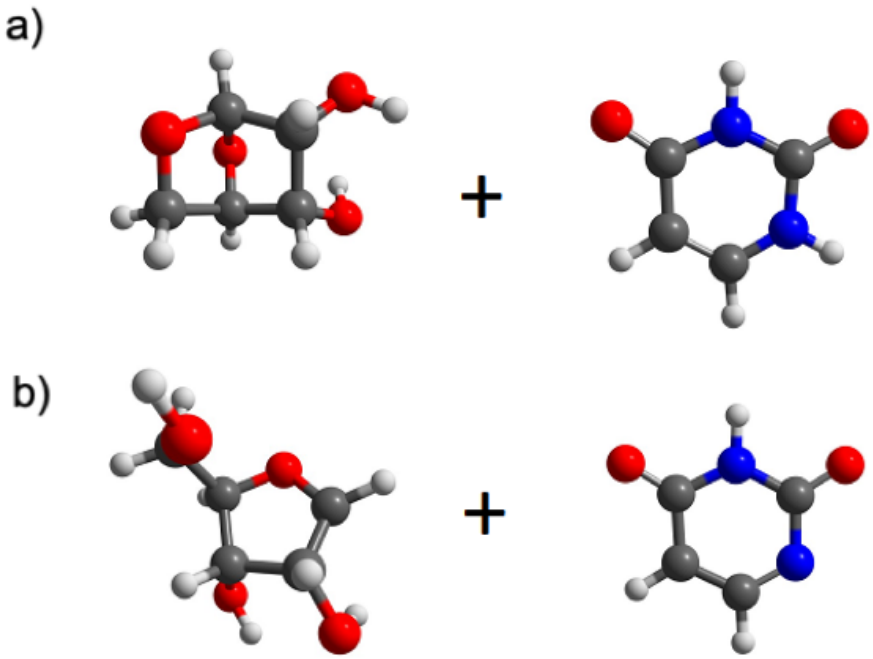

Fig. B.2: a) The lowest-energy optimised product-pair following glycosidic bond cleavage of *conformer 1* with single hydrogen transfer from the sugar to the base parts of uridine (i.e. giving uracil and an $(S-H)$ isomer). b) The optimised product-pair following glycosidic bond cleavage of *conformer 1* without any hydrogen transfer between the sugar and base parts (i.e. giving dehydrogenated uracil and an *S* isomer).

Appendix C

Proof of publication

THE JOURNAL OF CHEMICAL PHYSICS **149**, 034301 (2018)

Ultraviolet relaxation dynamics in uracil: Time-resolved photoion yield studies using a laser-based thermal desorption source

Omair Ghafur,[1,a)] Stuart W. Crane,[1,a)] Michal Ryszka,[2] Jana Bockova,[2] Andre Rebelo,[2,3] Lisa Saalbach,[1] Simone De Camillis,[4] Jason B. Greenwood,[4] Samuel Eden,[2,b)] and Dave Townsend[1,5,b)]

[1]*Institute of Photonics and Quantum Sciences, Heriot-Watt University, Edinburgh EH14 4AS, United Kingdom*
[2]*School of Physical Sciences, The Open University, Walton Hall, Milton Keynes MK7 6AA, United Kingdom*
[3]*CEFITEC, Departamento de Física, FCT–Universidade NOVA de Lisboa, P-2829-516 Caparica, Portugal*
[4]*School of Mathematics and Physics, Queen's University Belfast, Belfast BT7 1NN, United Kingdom*
[5]*Institute of Chemical Sciences, Heriot-Watt University, Edinburgh EH14 4AS, United Kingdom*

(Received 11 April 2018; accepted 15 June 2018; published online 17 July 2018)

Wavelength-dependent measurements of the RNA base uracil, undertaken with nanosecond ultraviolet laser pulses, have previously identified a fragment at $m/z = 84$ (corresponding to the $C_3H_4N_2O^+$ ion) at excitation wavelengths ≤232 nm. This has been interpreted as a possible signature of a theoretically predicted ultrafast ring-opening occurring on a neutral excited state potential energy surface. To further investigate the dynamics of this mechanism, and also the non-adiabatic dynamics operating more generally in uracil, we have used a newly built ultra-high vacuum spectrometer incorporating a laser-based thermal desorption source to perform time-resolved ion-yield measurements at pump wavelengths of 267 nm, 220 nm, and 200 nm. We also report complementary data obtained for the related species 2-thiouracil following 267 nm excitation. Where direct comparisons can be made (267 nm), our findings are in good agreement with the previously reported measurements conducted on these systems using cold molecular beams, demonstrating that the role of initial internal energy on the excited state dynamics is negligible. Our 220 nm and 200 nm data also represent the first reported ultrafast study of uracil at pump wavelengths <250 nm, revealing extremely rapid (<200 fs) relaxation of the bright $S_3(^1\pi\pi^*)$ state. These measurements do not, however, provide any evidence for the appearance of the $m/z = 84$ fragment within the first few hundred picoseconds following excitation. This key finding indicates that the detection of this specific species in previous nanosecond work is not directly related to an ultrafast ring-opening process. An alternative excited state process, operating on a more extended time scale, remains an open possibility. *Published by AIP Publishing.*
https://doi.org/10.1063/1.5034419

I. INTRODUCTION

Over the past two decades, the relaxation dynamics of electronically excited DNA and RNA nucleobases following ultraviolet (UV) irradiation have attracted considerable attention.[1–5] This has largely been motivated by a desire to better understand various photochemical/photophysical pathways that potentially damage living organisms (through the formation of lesions in critical macromolecules) or, alternatively, provide rapid and efficient routes for the harmless dissipation of excess energy (so-called "photo-protection" mechanisms). Many experimental studies have focused on isolated species in the gas phase, providing an instructive "bottom up" starting point for developing detailed insight into such pathways, free from perturbations due to the surrounding environment (e.g., solvation and/or clustering effects). This approach also provides benchmarks for complimentary *ab initio* theoretical studies undertaken with high-level computational chemistry methodologies able to capture the dynamics of decay pathways.

Based on the above rationale, the pyrimidine RNA base uracil has been the subject of numerous gas-phase spectroscopy and dynamics studies across the ~220-270 nm UV absorption region.[6–15] This sizable body of work, supported by an extensive theoretical input,[16–30] has started to reveal a complex picture of competing non-radiative decay pathways occurring on femtosecond to nanosecond time scales. These include internal conversion (IC) from the optically prepared $S_2(^1\pi\pi^*)$ state direct to the S_0 ground state and also IC from $S_2(^1\pi\pi^*)$ to the lower-lying $S_1(^1n\pi^*)$ state, which can then subsequently relax to S_0 or, alternatively, undergo intersystem crossing to the triplet manifold. A more detailed overview of the substantial literature describing these various processes is omitted here in the interests of brevity. The reader is, however, directed to the work of Richter *et al.* for a more expanded perspective, which includes instructive graphical summaries of the various relaxation schemes proposed to date.[17] At this point, we limit our outline to briefly highlighting theoretically predicted ultrafast (i.e., sub-picosecond) excited state ring-opening mechanisms that served as the initial

[a)]O. Ghafur and S. W. Crane contributed equally to this work.
[b)]Authors to whom correspondence should be addressed: d.townsend@hw.ac.uk and s.p.eden@open.ac.uk

Fig. C.1: Front page of publication [9]. The time-resolved ion yield measurements on uracil mentioned in Section 6.2.3 were published in [9].

International Journal of Mass Spectrometry 442 (2019) 95–101

Contents lists available at ScienceDirect

International Journal of Mass Spectrometry

journal homepage: www.elsevier.com/locate/ijms

Mapping the complex metastable fragmentation pathways of excited 3-aminophenol$^+$

J. Bockova [a], A. Rebelo [a, b], M. Ryszka [a], R. Pandey [a], T. da Fonseca Cunha [b], P. Limão-Vieira [b], N.J. Mason [a, d], J.C. Poully [c], S. Eden [a, *]

[a] School of Physical Sciences, The Open University, Walton Hall, Milton Keynes, MK7 6AA, UK
[b] Laboratório de Colisões Atómicas e Moleculares, CEFITEC, Departamento de Física, FCT - Universidade NOVA de Lisboa, P-2829-516, Caparica, Portugal
[c] CEA/CNRS/ENSICAEN/Université de Caen Normandie) Boulevard Becquerel, 14070 Caen, France
[d] School of Physical Sciences, Ingram Building, University of Kent, Canterbury, CT2 7NH, UK

ARTICLE INFO

Article history:
Received 27 December 2018
Received in revised form
22 March 2019
Accepted 12 May 2019
Available online 14 May 2019

Keywords:
Metastable fragmentation
Reflectron time-of-flight mass spectrometry
3-Aminophenol
DFT calculations
Sequential fragmentation
Double hydrogen loss

ABSTRACT

This work applies the technique of mapping ion detection using a reflectron mass spectrometer against flight-time and reflection voltage to elucidate the complex metastable fragmentation pattern of the biomolecular ion 3-aminophenol$^+$ (3-AP$^+$, $C_6H_7NO^+$). Multi-photon ionization experiments revealed the excited ion's fragmentation routes for the first time and comparisons with calculated flight-times enabled 18 different μs-timescale dissociations to be assigned. These included the rare observation of a double hydrogen loss channel from a fragment ion. DFT calculations provided further insights into the most prominent apparent fragmentation sequence: 3-AP$^+$ (m/z 109) → HCO + $C_5H_6N^+$ (m/z 80) → CNH + $C_4H_5^+$ (m/z 53) → C_2H_2 + $C_2H_3^+$ (m/z 27).

1. Introduction

The dissociation processes of biomolecules, notably the subunits of DNA and proteins, have attracted considerable attention in recent years with the motivation of better understanding the nanoscale mechanisms by which ionizing radiation can initiate damage in biological material [1–4]. Mass spectrometry studies of metastable ions are valuable to identify sequential fragmentation pathways because they simultaneously define ion mass before and after dissociation. Furthermore, metastable dissociation experiments have revealed distinct fragmentation patterns of different molecular isomers [5]. This is of considerable interest because biological function is often highly sensitive to molecular conformation. Metastable dissociation experiments can also provide information on fragment ion energetics, as the microsecond-order time delay implies that the vibrational energy of the precursor ion was very close to the relevant dissociation barrier [6]. Such studies are particularly prevalent in research into the structure and stabilities of molecular clusters [7–12]. This paper showcases the capability of a reflectron mass spectrometry experiment at the Open University (OU) to probe complex metastable fragmentation patterns. The subject of the study is multi-photon ionized 3-aminophenol (3-AP) and the data interpretations are enhanced by DFT calculations.

Aminophenol (C_6H_7NO) shares the same phenol group as the amino acid tyrosine and is also closely related to the neurotransmitter dopamine [13]. It is therefore somewhat surprising that the experimental and theoretical work in the literature on the electronic states, ionic states, and fragmentation of 3-AP is extremely sparse. Shinozaki et al. [13] performed resonance enhanced multi-photon ionization (REMPI) experiments on 3-AP in the photon energy range 4.2–4.6 eV, as well as laser induced fluorescence (LIF) measurements and quantum chemical calculations to support their assignments of vibronic structure. 3-AP exists in approximately equal populations of *cis*- and *trans*-conformers in the gas phase [13] and Shinozaki et al.'s REMPI assignments enabled Küpper, Meijer and co-workers to demonstrate the complete separation of these conformers in Stark-deflected pulsed beams [14]. More recently, Yatsyna et al. [15] have performed infrared action spectroscopy

* Corresponding author.
E-mail address: s.p.eden@open.ac.uk (S. Eden).

https://doi.org/10.1016/j.ijms.2019.05.006
1387-3806/

Fig. C.2: Front page of publication [176]. The results presented in Sections 4.3, 4.5 and 4.6 were published in [176].

Eur. Phys. J. D (2019) 73: 184
https://doi.org/10.1140/epjd/e2019-100107-7

THE EUROPEAN PHYSICAL JOURNAL D

Regular Article

Fragmentation processes of ionized 5-fluorouracil in the gas phase and within clusters*

Peter J. M. van der Burgt[1,a], Michael A. Brown[1], Jana Bockova[2], André Rebelo[2,3], Michal Ryszka[2], Jean-Christophe Poully[4], and Sam Eden[2]

[1] Department of Experimental Physics, National University of Ireland Maynooth, Maynooth, Co. Kildare, Ireland
[2] School of Physical Sciences, The Open University, Walton Hall, Milton Keynes MK7 6AA, United Kingdom
[3] Laboratório de Colisões Atómicas e Moleculares, CEFITEC, Departamento de Física, FCT – Universidade NOVA de Lisboa, 2829-516 Caparica, Portugal
[4] CIMAP UMR 6252 (CEA/CNRS/ENSICAEN/Université de Caen Normandie), Boulevard Becquerel, 14070 Caen Cedex 5, France

Received 26 February 2019 / Received in final form 14 June 2019
Published online 27 August 2019

Abstract. We have measured mass spectra for positive ions produced from neutral 5-fluorouracil by electron impact at energies from 0 to 100 eV. Fragment ion appearance energies of this (radio-)chemotherapy agent have been determined for the first time and we have identified several new fragment ions of low abundance. The main fragmentations are similar to uracil, involving HNCO loss and subsequent HCN loss, CO loss, or FCCO loss. The features adjacent to these prominent peaks in the mass spectra are attributed to tautomerization preceding the fragmentation and/or the loss of one or two additional hydrogen atoms. A few fragmentions are distinct for 5-fluorouracil compared to uracil, most notably the production of the reactive moiety CF^+. Finally, multiphoton ionization mass spectra are compared for 5-fluorouracil from a laser thermal desorption source and from a supersonic expansion source. The detection of a new fragment ion at 114 u in the supersonic expansion experiments provides the first evidence for a clustering effect on the radiation response of 5-fluorouracil. By analogy with previous experiments and calculations on protonated uracil, this is assigned to NH_3 loss from protonated 5-fluorouracil.

1 Introduction

5-fluorouracil is a significant chemotherapy drug whose action is primarily associated with inhibiting the synthesis of thymidine and thus DNA replication. Furthermore, it is well established that the substitution of thymine with a 5-halouracil in the genetic sequence of cellular DNA during replication in the presence of these dopants leads to greater sensitivity to ionizing radiation [1–3]. In view of the generally rapid replication of cancerous cells compared with healthy cells, this provides a strong basis for the use of halouracil radiosensitizers in radiotherapy. However, the nanoscale interactions of halouracil molecules with ionizing radiation have not been characterized fully to date. This limits our understanding of how the presence of these molecules can affect the earliest physical-chemical stages of the radiation response of DNA. When high-energy ionizing radiation passes through biological tissue it produces a large amount of secondary electrons, mostly with energies below 30 eV, and these electrons are very effective in causing DNA strand breaks [4–7]. For this reason, low-energy electron impact studies of radiosensitizers such as 5-fluorouracil are of particular relevance. The present work is the most detailed experimental study of the dissociative ionization of 5-fluorouracil to date, and includes the first determinations of fragment ion appearance energies. This article also provides the first insights on the effects of clustering on the molecule's radiation response, as a simple first approximation for a condensed environment.

To our knowledge, the only previous electron ionization mass spectrum of 5-fluorouracil in the literature [8] was recorded in the gas-phase at 70 eV electron impact without any proposed fragment assignments. A mass spectrum of 5-fluorouracil following single ionization by 100 keV proton collisions was presented by Champeaux et al. [9] and was compared with equivalent measurements on 5-XU where X = C, Br, and I. In addition to focusing on X^+ loss, Champeaux et al. [9] noted comparable channels for the procution of XCH^+, XC_2H^+, XC_2OH^+, and $5\text{-}XU^+$ minus HNCO in all four molecules. No other single ionization products were identified or discussed and X^+ production

* Contribution to the Topical Issue "Dynamics of Systems on the Nanoscale (2018)", edited by Ilko Bald, Ilia A. Solov'yov, Nigel J. Mason and Andrey V. Solov'yov

[a] e-mail: peter.vanderburgt@mu.ie

Fig. C.3: Front page of publication [121]. The MPI experiments on 5-fluorouracil mentioned in Section 5.4.1 were published in [121].